Synthesis and Characterization of Engineered Carbon-based Nanoparticles by Arc-discharge Plasma

Mohammad Reza Sanaee

Synthesis and Characterization of Engineered Carbon-based Nanoparticles by Arc-discharge Plasma

Presented by Mohammad Reza Sanaee

Director and Tutor: Prof. Dr. Enric Bertran Serra

Departament de Física Aplicada i Òptica

PhD program: Nanosciences

Barcelona, May 2015

I would like to dedicate this PhD dissertation to:
my late Grandmother who taught me invaluable lessons in life with endless love and glow;
to my kind and wonderful parents who have believed in my potential and inspired me to continue my education and for their enormous contribution to getting me where I am today; and
to my loving sister, Reyhaneh who is very special in kindness and have never left my side.

Preface

PhD research study was initiated in September 2011 in FEMAN Group after the author obtained his Official MSc degree in Nanoscience and Nanotechnology with “Excellent Average Grade Point, 9.2 out of 10”, distinguished by the University. Master thesis carried out at the Pharmacy and Pharmaceutical Technology Department in partial fulfillment of the requirements for the Official MSc degree at University of Barcelona.

The PhD research study was initiated by studying and doing laboratory work towards synthesis of carbon based materials, particularly Core@Shell nanoparticles by arc discharge method under the supervision of Prof. Dr. Enric Bertran.

This work was partially financed by the MICYN of Spanish Government, under contract MAT2010 20468, and by AGAUR of Generalitat de Catalunya, under contracts 2009SGR00185 and 2014SGR0948.

Since the last two decades, arc discharge technique leads to the discovery of two important carbon based materials, nanotubes and fullerenes. However, the formation of nanomaterials by thermal plasma still remains poorly understood and need further investigation. The focus in this study is on synthesis of carbon based nanoparticles by arc discharge method, particularly carbon encapsulated iron nanoparticles in the form of Core@Shell nanostructure. An arc discharge reactor that was patented by FEMAN group was used with slight modification. The growth processes were elucidated through many experiments and characterizations. Precise control over carbon encapsulated iron nanoparticles were addressed. In addition, a new carbon encapsulated multi iron nanoparticles is introduced. The results have been lead to new elements for understanding the growth mechanism of iron core and carbon shell nanostructure. In order to improve the synthesis process, a new modified arc discharge reactor was developed and implemented. Two new materials are prepared through a new facile synthetic method; carbon nanoparticles decorated by fullerenes and spherical porous carbon microparticles. Last but not least, in this research medical application requirements have been taken into account to prepare suitable nanoparticle.

Thesis is divided into four main chapters as shown in the following flow chart:

Thesis Flow Chart

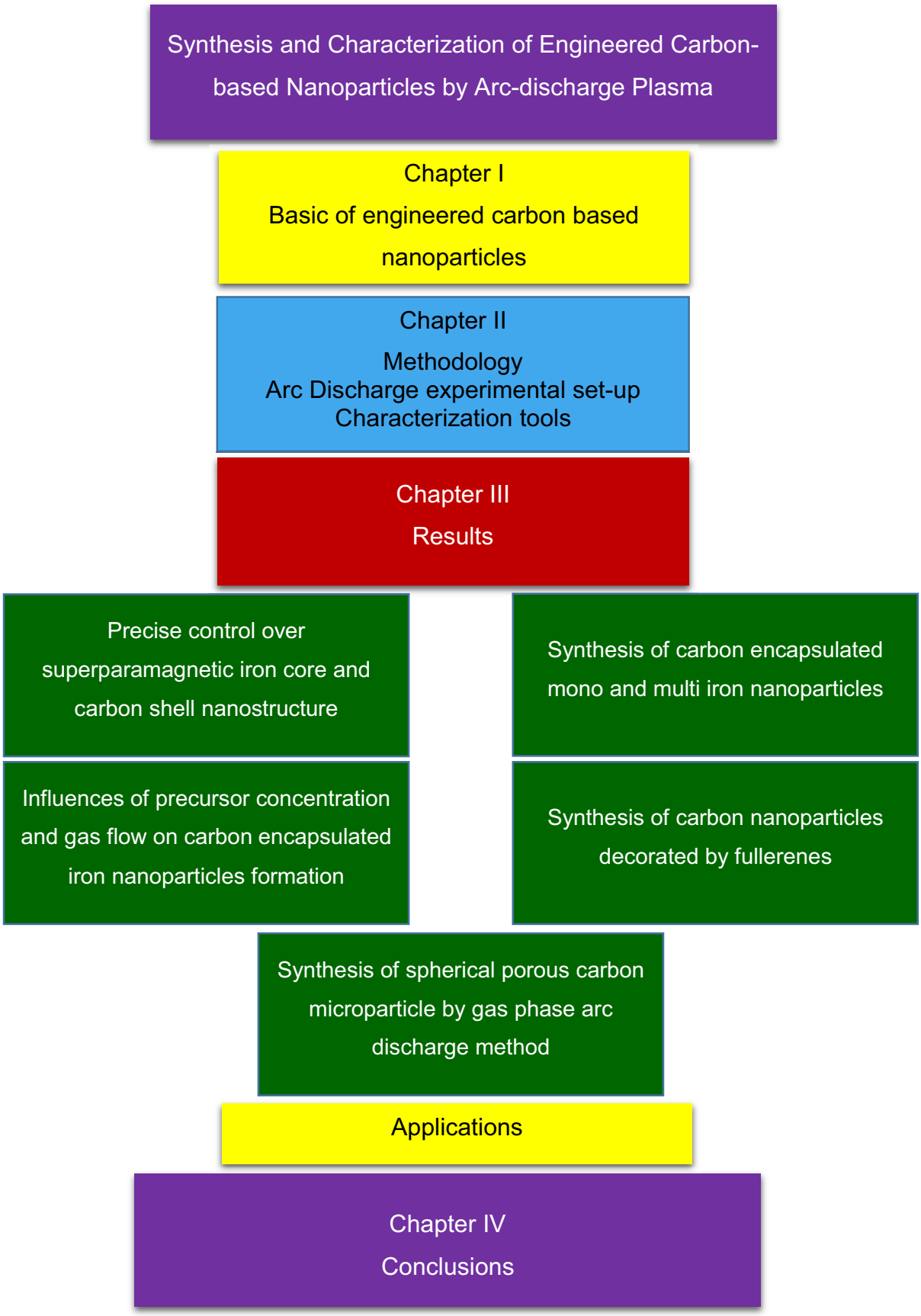

Chapter I consists of an introduction to nanotechnology, core@shell nanoparticles and related theories. This chapter is also devoted to state of the art of carbon based nanoparticles growth formation and most common synthesis methods. In addition, potential applications are described. Chapter II describes methodology, two arc discharge experimental set-up and also describes all characterization tools employed for the morphological and magnetic properties of obtained nanoparticles. In this chapter design and implementation of a new gas phase arc discharge reactor is described in details. Chapter III consists of five sections. The first section demonstrates how to synthesis and engineer core@shell nanostructure of carbon encapsulated iron nanoparticles based on desired application. Second section describes the synthesis of spherical and oval shaped iron nanoparticles as well as a new carbon encapsulated multi iron nanoparticles. Third section, describes the synthesis of carbon encapsulated iron nanoparticle by a new gas phase arc discharge reactor. In forth section with respect to the medical application requirements, carbon nanoparticles decorated by fullerenes are synthesized. Fifth section introduces a new spherical porous carbon microparticle and its potential applications. Sixth section devoted to the potential applications. Finally, chapter IV includes the main conclusions of study.

Acknowledgements

This thesis would certainly have not been possible without the support of many individuals.

I would like to express my deep and sincere gratitude to my supervisor Prof. Dr. Enric Bertran for his unbelievable kindness and encouragement during my study. Without doubt his kind efforts, support and smart guidance were the main factors in achieving the results of this research. I truly thank my supervisor for the creative and enjoyable atmosphere in my research work in FEMAN group laboratory excellently leading by him.

I acknowledge Dr. Sonia Estrade, Dr. Lluís Yedra, Dr Joan Mendoza, Dr. Tariq Jawhari and Dr. Núria Clos from Centres Científics i Tecnològics of the Universitat de Barcelona (CCIT-UB) for their kind cooperation.

My thanks goes to all PhD students, especially Stefanos Chaitoglou and to all kind Professors in FEMAN group and Department of Applied Physics and Optics.

I take the opportunity to express my thankfulness to the coordinators Dr. Albert Cirera Hernandez, Dr. Albert Romano-Rodriguez and former coordinator Dr. Amilcar Labarta for their great management of the PhD program in Nanoscience. Especially want to thank the secretary teams of Department of Applied Physics and Optics and Faculty of Physics, Ms. Maria Teresa Fraile Sanchez, Ms. Mireia Ortiz Ferrer, Ms.Teresa Torrejon Alabau, Mr. Jordi Sola Antolin and Ms. Silvia Rovira for their sincere cooperation.

I am also very grateful to my kind parents, my farther Prof. Dr. Samad Sanaee for his scientific comments and financial supports, my mother Maryam Seyf for her encouragements and spiritual supports and my sister Dr. Reyhaneh Sanaee for her scientific comments particularly in medicine field.

Contents

Figure List

Table List

I. Basic of carbon based nanoparticles

In this chapter, an overview to nanotechnology, core@shell nanoparticles and related theories are described. The state-of-the-art knowledge of core@shell nanoparticles synthesis techniques and formation mechanism are addressed. Moreover, potential applications of carbon-based nanoparticles are presented.

1.1

1.2 Intro to Nanotechnology

Nanotechnology definition given by scientific organizations are described as:

American Heritage Dictionary: The science and technology of building electronic circuits and devices from single atoms and molecules (Heritage, 2000).

National Nanotechnology Initiative (2006), “Nanotechnology is the understanding and control of matter at dimensions of roughly 1 to 100 nanometers, where unique phenomena enable novel applications. Encompassing nanoscale science, engineering and technology, nanotechnology involves imaging, measuring, modeling, and manipulating matter at this length scale.” (Weiss, 2006).

NASA: The creation of functional materials, devices and systems through control of matter on the nanometer length scale (1-100 nanometers), and exploitation of novel phenomena and properties (physical, chemical, biological) at that length scale (Mnyusiwalla, 2003).

In fact, nanotechnology can be found in nature. From the beautiful colors of some butterflies and moths (arises from nanostructure on the wings) to the stunning cups and metallic materials made by world ancient empires such as Persians 1000 BC, Egypt, Roman AD 400.

1.2.1 Nanotechnology in ancient history

After 20 years, studies of Iranian researchers in Chogha Zanbil and Pasargadae historical sites led into tracing nanotechnology in these two World Heritage Sites (Afrazeh, 2007). According to Afrazeh, two nanotechnology techniques were implemented in Chogha Zanbil Ziggurat including nanoparticles, which attract harmful rays from mobiles, which are employed in structures, and nanoparticles, which are used in colors. He further explained that Iranians succeeded in inventing a new atomic order in Chogha Zanbil some 3000 years ago which was quite different with the natural elements of its surrounding area. Regarding the implementation of this technique in Chogha Zanbil, most probably this cover was used in holy chambers and the music halls of this monument. The studies further revealed that contrary to previous beliefs, what connected the metal part of monuments in Pasargadae historical site to the stones were not bronze joints but it was the new metal's atomic structure. This new technique is considered very important in strengthening the monument and its long term survival. Today many developed countries such as the United States and Japan are using this high technique for making a protective covers in an attempt to reduce the harmful effects of mobile rays on users' brains. An apparent similarity can be seen between this technique and what was practiced during the first millennium BC in Chogha Zanbil. The large Chogha Zanbil temple is one of the ancient monuments of Iran which has been registered on UNESCO World Heritage List. There are a number of relatively famous examples of ancient artefacts, which were created using nanocomposites. The Lycurgus cup, for example, is a stunning decorative Roman treasure from about AD400; it is made of a glass that changes colour when light is shone through it. The glass contains gold-silver alloyed nanoparticles, which are distributed in such a way to make the glass look green in reflected light but, when light passes through the cup, it reveals a brilliant red (Museum, 2012). These historic structures are the results of hundreds of years of trial and error experimentation with craftsmen passing their skills and know-how down through generations. Nanotechnologists can also now build on this ancient wisdom. But they benefit from a modern understanding of the behavior of atoms and molecules along with state-of-the-art fabrication tools and analytical instruments to achieve exciting new products and devices in a fraction of the time (Museum, 2012).

1.2.2 Nanotechnology in Nature

Fern Wickson offered conceptual framework that can assist in the advance of reflective technology development and transparent policy debate (Wickson, 2008). Scientists often invoke comparisons with nature when discussing developments in nanotechnology, but the relationship between the two is more complex than it first appears, and can be broken down into nine different narratives (Narratives of nature and nanotechnology) as the following: 1- Nanotechnology as nature, 2- Nanotechnology using nature, 3- Nanotechnology inspired by nature, 4- Nanotechnology improving on nature, 5- Nanotechnology transgressing nature, 6- Nanotechnology restricted by nature, 7- Nanotechnology controlling nature, 8- Nanotechnology threatening nature, 9- Nanotechnology treating nature (Wickson, 2008).

In principle, the ultimate results of this research study leads to the synthesis of magnetic and porous carbon based nanoparticles as the material and tool for biomedical applications and therefore fall into narrative of nanotechnology treating nature. Currently, we are in a battle with a dangerous and destructive diseases such as cancers, and nanotechnology is then presented as a tool that can help us win control. This work is to support medical and other applications of nanotechnology specifically aimed to prepare carbon based nanoparticles.

1.2.3 Nanotechnology in 20th century

The concept of nanotechnology is attributed to Nobel prize winner Richard Feynman who gave a very famous, visionary in 1959 (published in 1960) during one of his lectures, saying: "the principles of physic, as far as I can see, do not speak against the possibility of maneuvering things atom by atom" (Feynman, 1960). At the time, Feynman's words were received as pure science fiction". Today, we have instruments that allow precisely what Feynman had predicted: creating structures by moving atoms individually. In fact, his speech was an invitation to enter a new field of physics. He described the problem of manipulating and controlling things on a small scale. He gave

an example of writing Encyclopedia Britannica on a head of a pin to support his principles. These principles will be discussed in this report.

Feynman (1959) suggested writing only the information content in a code of dots and dashes. Today's computers are using the same structure and pattern, which are called binary codes. He described his idea of writing Encyclopedia Brittanica on a head of a pin. He said let us represent a dot by a small spot of one metal, the next dash, by an adjacent spot of another metal, and so on. Suppose, to be conservative that a bit of information is going to require a little cube of atoms (5, 5, 5), that is 125 atoms. Perhaps we need a hundred and some odd atoms to make sure that the information is not lost through diffusion, or through some other process.

Indeed, Feynman opened a new window to the scientists. Today, his idea has come into reality. The most important idea that Feynman emphasized is that atoms on small scale behave significantly different from behaving on a large scale. This important point has actually provided many new opportunities in various fields of sciences. By studying atoms in a small world and rearranging the atoms, as Feynman had predicted, many researchers have done several studies such as miniaturizing the computers, the marvelous biological systems and many other fields. Today, scientists from different disciplines are doing various researches at nanoscale and some have come into reality and even commercializing phase and many other in the process of developing the new ideas and opportunities. We expect to have much more wonderful applications in coming future based on this idea.

1.3 Core@Shell nanoparticles

Global statistical data analysis shows meaningful interest for the synthesis of core@shell nanoparticles. A statistical data analysis is presented in Figure 1.3-1 to show the increasing trend of published research papers in this area. These were collected from "Web of Science™, Thomas Reuters" using the keyword "core/shell nanoparticles".

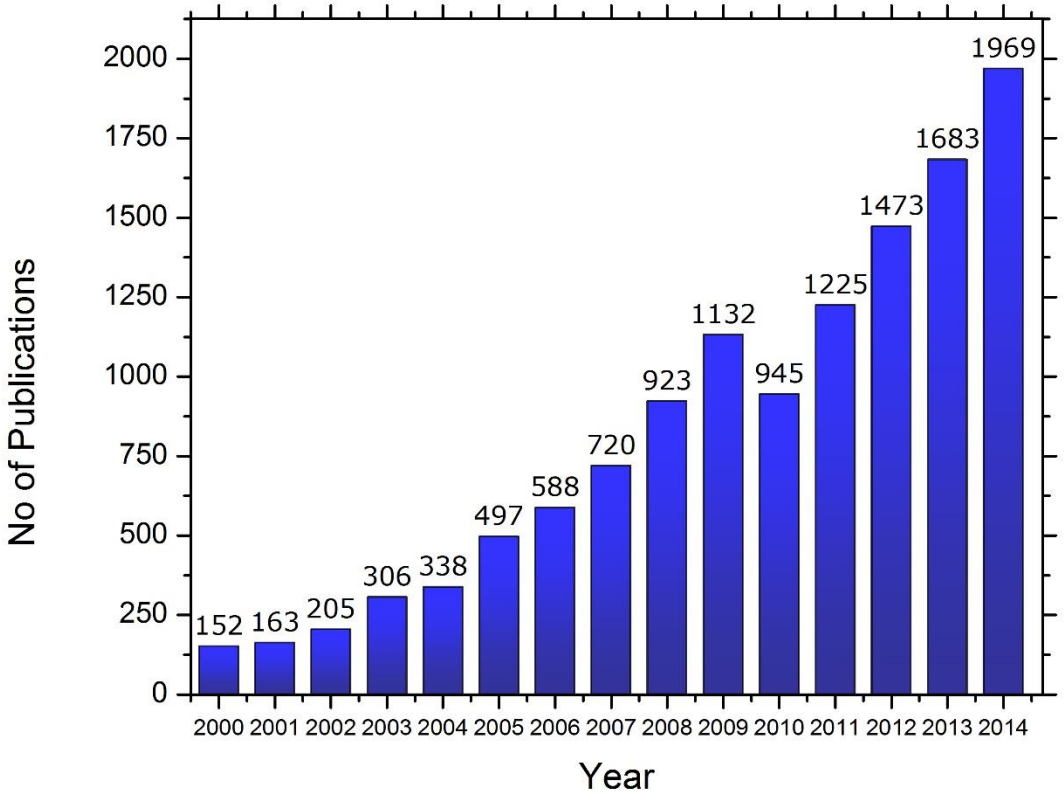

Figure 1.3-1. The number of published papers over the years shows an increase and interest in research activities for synthesis of core/shell nanoparticles since years 2000 to 2014 around the world. The decrease number of publications in 2010 is probably due to the global financial crisis; 9 May 2010 marked the point at which the focus of concern switched from the private sector to the public sector (Moniruzzaman, 2014).

Different classes of core@shell nanoparticles are shown schematically in Figure 1.3-2 (Ghosh Chaudhuri and Paria, 2011). Concentric spherical core@shell nanoparticles are the most common, where a simple spherical core particle is completely coated by

a shell of a different material, core@shell nanoparticles in this study falls into categories of (a) and (c) in Figure 1.3-2.

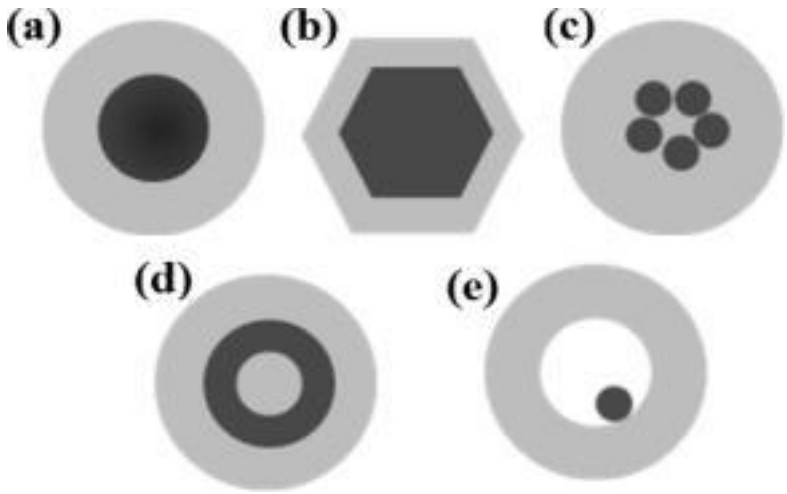

Figure 1.3-2. Showing different types of core@shell nanoparticles Different core/shell nanoparticles: (a) spherical core/shell nanoparticles; (b) hexagonal core/shell nanoparticles; (c) multiple small core materials coated by a single shell material; (d) nanomatryushka material; (e) movable core within hollow shell material (Ghosh Chaudhuri and Paria, 2011).

The properties of nanoparticles are size dependent and are also linked with the actual shape. For example, certain properties of magnetic nanocrystals such as the blocking temperature, magnetic saturation, and permanent magnetization are all dependent on particle size, but the coercivity of the nanocrystals totally depends on the particle shape because of surface anisotropy effects (Song and Zhang, 2004, Chen, 2005). Different shaped magnetic nanocrystals possess tremendous potential in helping our fundamental understanding of not only magnetism but also technological applications in the field such as high-density information storage; Other nanoparticle physical and chemical properties such as catalytic activity and selectivity, electrical and optical properties, and melting point are also all highly shape dependent (Song and Zhang, 2004).

Magnetic nanoparticles are being of great interest because of their unique properties especially in drug delivery, hyperthermia, magnetic resonance imaging and cell separation. In many clinical situations, medication doses are oversized as a result of impaired drug absorption or tissue unspecific delivery (Ruiz-Hernandez, 2011). The

ultimate goal of magnetically controlled drug delivery and drug therapy is to selectively delivering drug molecules to the diseased site without a concurrent increase in its level in healthy tissues.

Although there have been many significant developments in the synthesis of magnetic nanoparticles, maintaining the stability of these particles for a long time is an important issue. Stability is a crucial requirement for almost any application of magnetic nanoparticles. Especially pure metals, such as Fe, Co, and Ni and their metal alloys, are very sensitive to oxidation by air and other oxidizing agents. Thus, the main difficulty for the use of pure metals or alloys arises from their instability towards oxidation. Therefore, it is necessary to develop efficient strategies to improve the chemical stability of magnetic nanoparticles. The most straightforward method seems to be protection by a layer, which is impenetrable, so that oxygen cannot reach the surface of the magnetic particles (Rashid, 2011). The stabilization and protection of the particles are often closely associated with each other. Although to date most studies have been focused on the development of polymer or silica protective coatings, recently carbon-coated magnetic nanoparticles are receiving more attention, because carbon-based materials have many advantages over polymer or silica, such as high chemical and thermal stability, better conductivity, as well as biocompatibility of carbon-based materials (Taylor, 2010a, Lu, 2007). Thus, carbon is a suitable and preferable candidate to form a shell around a pure metal for the synthesis of core@shell nanostructure. It is noteworthy that in many cases the protecting shells not only stabilize the nanoparticles, but can also be used for further functionalization, for instance with other nanoparticles or various ligands, depending on the desired application (Bakthavathsalam, 2013).

One of the important goals of nanotechnology is to control the matter at nanoscale. The size control is crucial for almost all potential applications of nanoparticles. Many studies have been conducted and examined the role of nanoparticle sizes from biomedical to sensor applications of nanoparticles (Santoro, 2014, Santo, 2014, Mohamud, 2013, Liu, 2012, Zeng, 2012, Hwang, 2012, Li, 2011, Tonezzer and Hieu, 2012, Kreyling, 2006, Gaumet, 2008, Shah, 2014, Rao, 2015). Concerning drug delivery applications, Decuzzi in a valuable review answered to this question: Does

geometry really matter? They concluded that, the characterization of the endothelial biodiversity and the precise control of size and shape in micro/nanofabrication have promoted a paradigm shift in the systemic administration of particulate systems for biomedical applications: both geometry and surface physicochemical properties contribute substantially to the optimal design of the particulate system; geometry affects the transport and biodistribution of the particles, at the vascular level; the strength of adhesion and the internalization rate at the cellular level; geometry favors particle accumulation in proximity of the blood vessels (margination dynamics) to better sense endothelial wall biodiversity; geometry affects the strength of adhesion to cells improving target specificity; geometry influences the rate of internalization discriminating between particles for nuclear delivery (rapid internalization) and particles for vascular targeting (no internalization) (Decuzzi, 2009).

Consequently, in this research study the objective is to develop an approach to control the synthesis of carbon encapsulated iron nanoparticles (CEINPs) in the form of core@shell nanostructure. Accordingly, understanding and revealing the growth mechanism of carbon encapsulated iron nanoparticles is necessary by doing characterization. Furthermore, engineering of suitable carbon based nanoparticles for biomedical applications has been also considered.

1.3.1 Core@Shell nanoparticles synthesis: State of the art

So far, smart strategies have been employed to prepare carbon encapsulated iron, nickel, cobalt and magnetic oxides nanoparticles including detonation synthesis, chemical vapour deposition, combustion synthesis, hydrothermal process, microwave plasma synthesis and arc discharge. The state of the art of above techniques have been investigated to choose a proper technique to achieve the objectives of this study. In contrast, each of these synthesis methods has particular advantages according to their applications and uses. Herein, some of their importance and properties are highlighted. In an important research study Luo clearly suggests that their detonation synthesis route is capable of producing a variety of nanocrystalline particles, such as Fe-based oxides, graphite coated Fe, Fe-based carbides and their mixtures (Luo, 2012). Typical detonation experiment explosive vessel is shown in Figure 1.3-3.

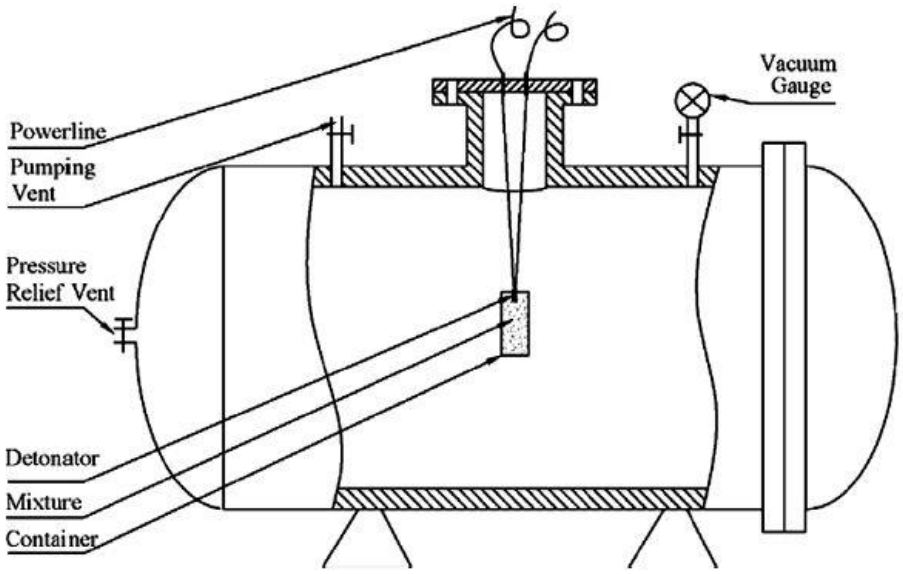

Figure 1.3-3. Schematic of a typical explosion vessel (Ning, 2009).

As described by Ning the homemade composite explosive was packed in a thin plastic column bag with the density of approximate 1.69 g/cm^3 as explosive precursors. First, the explosion vessel was pumped into vacuum state to - 0.1 MPa by a vacuum equipment (VSTX-1850); and then nitrogen gas was filled into the explosion vessel when the air meter coming back to normal pressure. Last, the charge was initiated by a non-electric detonator in nitrogen gas. The nitrogen gas was used in detonation process, which provided an effective mean of cooling detonation products and thus reduced the reuniting of obtained nanoparticles. According to their analysis, graphite coated Fe particles have a broad range from 8 to 40 nm in diameter and therefor control over size distribution still remains a challenge (Ning, 2009). Moreover, according to the TEM images in Figure 1.3-4 the quality of carbon coated iron-based composite nanoparticles by denotation method is not favorable.

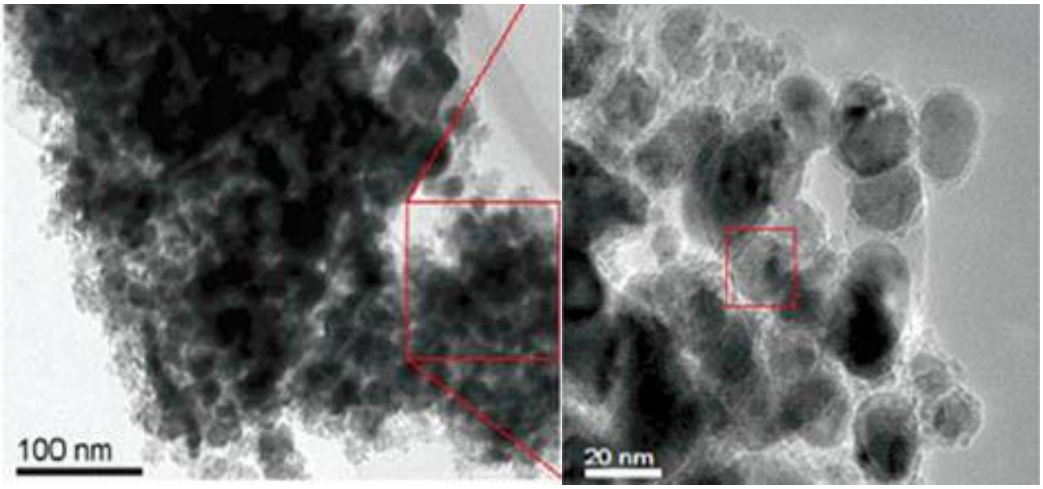

Figure 1.3-4. Amorphous carbon coated Fe-based nanoparticles (Luo, 2012).

Chemical vapor deposition (CVD) is a common technique for synthesis of graphene and also carbon coated iron nanoparticles. The CVD equipment is shown in Figure 1.3-5. As described by El-Gend the corresponding metallocene is sublimated in a thermostated chamber at 95° C (Figure 1.3-5) and transported using argon gas (1400 sccm) into the reactor. The injection into the reactor is realized by a copper nozzle system through a ceramic insulated water-cooled steel tube. The water cooling is necessary to avoid the metallocene decomposition before entering the reactor.

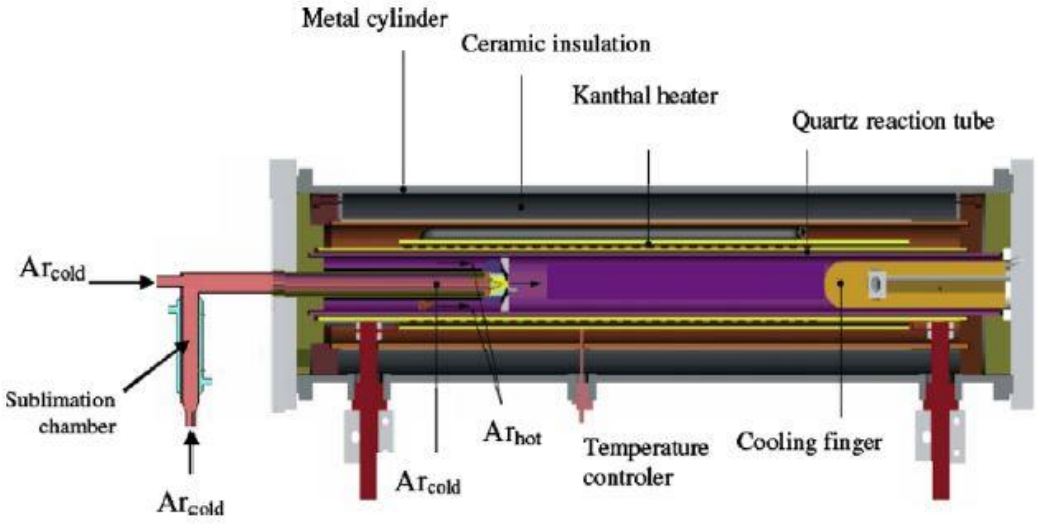

Figure 1.3-5. Schematic of high pressure chemical vapour deposition equipment (El-Gendy, 2009).

El-Gendy used above CVD process and obtained carbon coated iron nanoparticles with core average size of 16 nm by CVD (El-Gendy, 2009). According to the given

magnetic analysis the particles show a blocking temperature above 400 K and hence their superparamagnetic behavior is only evidenced and applicable above room and body temperature. In addition, the size distribution of carbon coated iron nanoparticles is broad by using this method as shown in TEM image (a) and size distribution histogram (b) of Figure 1.3-6.

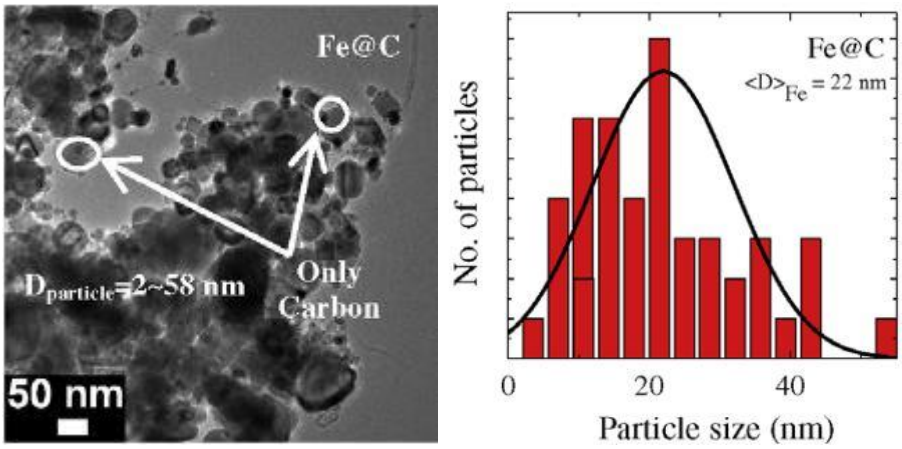

(a) (b)

Figure 1.3-6. TEM image of carbon coated iron nanoparticles obtained by CVD method (El-Gendy, 2009).

Combustion synthesis is an autothermal process having inherent advantages, including the use of low cost materials and the simplicity of the production protocol (Huczko, 2003, Huczko, 2005, Bystrzejewski, 2007). As described by Borysiuk typical procedures of a combustion synthesis are as following: the starting reactants were prepared in the form of a 2 cm in diameter pellet (5 g) made of the mixture of fine powders and compressed at 10 MPa. The pellet was placed in a graphite crucible and ignited by an electrically heated reaction promoter. The combustion synthesis was carried out under Ar (0.5 MPa) atmosphere in a calorimetric bomb in order to monitor the heat of reaction. The thermolysis of NaN_3 and chlorocarbon mixtures was also performed as a reference test. The collected raw products were sequentially pre-purified by water and ethanol to remove residual soluble impurities, e.g., NaCl. The pre-purified products from test 2 and 4 were subjected to further purification procedure to remove not-encapsulated iron and iron carbide nanocrystallites. However, this method seems not suitable for encapsulating metallic nanoparticles by carbon. Borysiuk produced and compared carbon encapsulated iron nanoparticles (CEINPs)

by using both arc plasma and combustion synthesis methods (Borysiuk, 2008). According to their experiments the combustion sample has much higher content of carbon, indicating that the Fe particles were not covered by a graphite layer totally, and were dissolved in the etching process. In contrast the Fe-containing particles are much more abundant in arc-plasma samples and they are covered by thicker graphite layers, effectively protecting them during the etching process. A hydrothermal process has been reported by Wang.The synthesis of Fe and Fe@Au magnetic nanoparticles was accomplished using a sequential synthesis technique afforded by reverse micelles (Wang, 2006). They found that only Fe nanoparticles did not favor the formation of CEINPs due to the oxidation of Fe nanoparticle by H_2O during the reaction (Wang, 2006). Moreover, this chemical approach may not be environmentally friendly.

The use of emerging microwave-assisted chemistry techniques in conjunction with benign reaction media is dramatically reducing chemical waste and reaction times in several organic syntheses and chemical transformations. The rapid synthesis of organic compounds in microwave oven is reported by Gedye and their results demonstrate that ions in the reaction mixture alter the heating rate of the microwave reactions (Gedye, 1988).

Microwave plasma synthesis of carbon-supported ultrafine metal particles have been done by Brenner (Brenner, 1997). They have used microwave to excited plasma. According to their results microwave plasma decomposition of metal carbonyls has been used to synthesize a series of carbon-supported monometallic (Fe, Co) and bimetallic (Co-Mo) materials. The average metal particle diameters in all cases were less than 10 nm. By using 10% H_2/Ar instead of pure Ar as a carrier gas, the mean particle diameters could be decreased to less than 2 nm. The microwave generator in these experiments was a continuously variable, 2.2 kW magnetron (2.45 GHz) operated at 500 W (measured by a directional coupler and a Hewlett Packard 435B power meter). Schematic of microwave plasma dissociation apparatus is described in Figure 1.3-7.

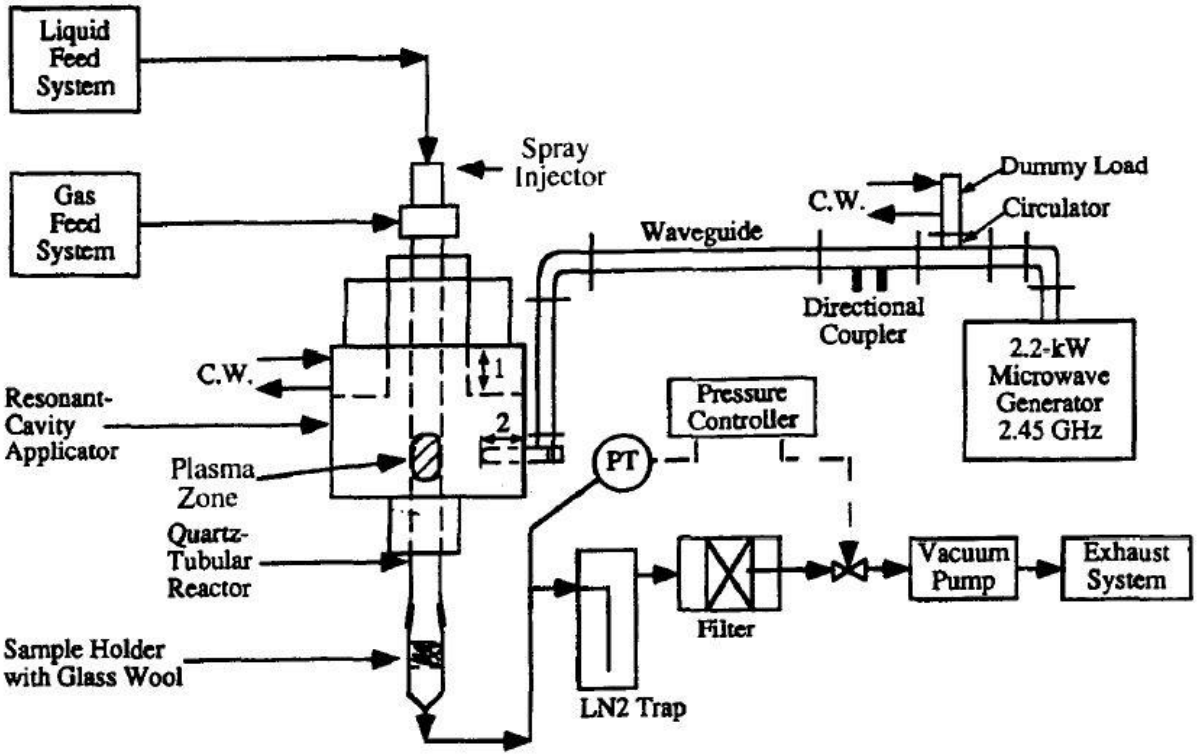

Figure 1.3-7. Schematic of microwave plasma dissociation apparatus (Brenner, 1997)

Microwave-assisted synthesis of aluminum nitride, simple and attractive route to submicrometer AlN powder is reported based on the use of microwave radiation (Ramesh and Rao, 1995). Microwave rapid synthesis of nanoporous Fe_3O_4 magnetic microsphere, has been successfully applied by the way of microwave heating. The average size of Fe_3O_4 microspheres is ~100nm and shows well-dispersed quality in aqueous solution (Yang, 2009).

In a study, Ai developed a facile microwave-assisted ethylene glycol approach to synthesize Fe_3O_4 nanoroses in the presence of the PEO-PPO-PEO block copolymer (P123) (Ai, 2010). Obtained particles by microwave-assisted method are not in spherical form as shown in Figure 1.3-8 TEM images. Spherical shape of nanoparticles are important for drug delivery due to the fact that movement of spherical nanoparticles are smooth in fluid.

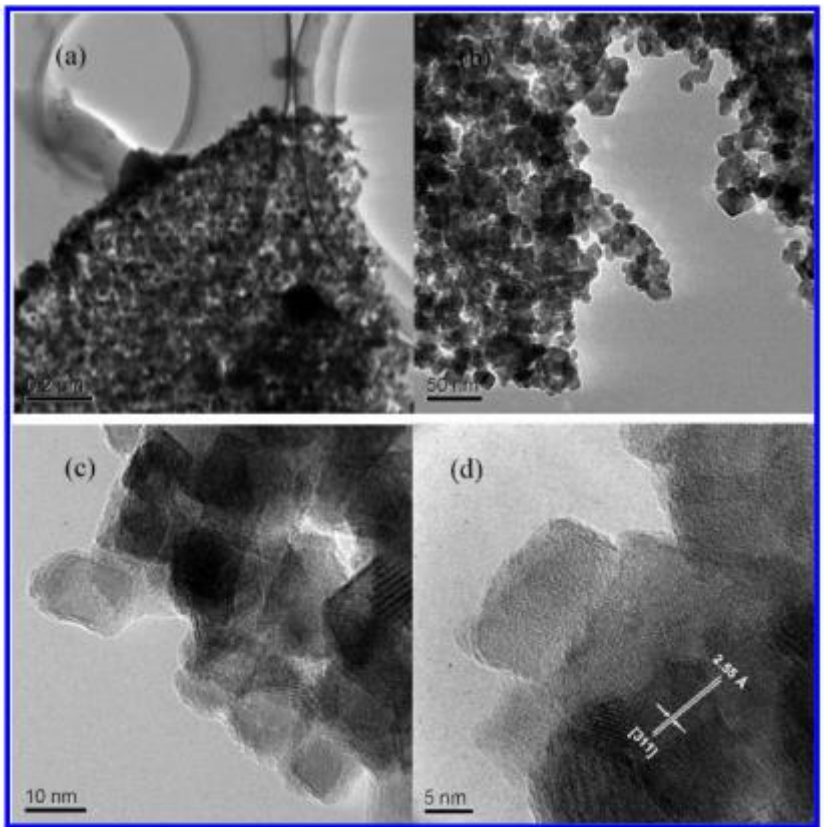

Figure 1.3-8. TEM images of low magnification (a, b), high magnification (c), and HRTEM images (d) of the rose-like nanocrystalline Fe_3O_4 superstructures obtained after 30 min of reaction (Ai, 2010).

Parada reported core@shell structures of Ni/NiO in “Microwave assisted synthesis and magnetic study of nanosized Ni/NiO materials” (Parada, 2006). By using a domestic microwave furnace and depending on the nickel precursor used, either tetrahydrated nickel acetate or dihydrated nickel formate, different nanosized materials are obtained: Ni/NiO composites, Ni metal, or NiO. The acetate leads to core-shell composites: Ni on the outside and NiO on the inside, while the formate behaves oppositely, yielding the metal that is progressively oxidized in air, the shell being in this case NiO. All these materials show ferromagnetic behavior but not superparamagnetic.

A review of the literature clearly shows that the majority of reports are focused on inorganic materials rather than organics. Inorganic materials can be broadly classified into three different groups, (i) metal, (ii) metal or metalloid oxide, and (iii) metal chalcogenide and metal salt. Herein, the synthesis methods for carbon encapsulated iron nanoparticles (CEINPs) have been discussed briefly. As described each of mentioned methods has its own weakness and strength.

Arc discharge method is simple, cost effective rapid technique that can easily be carried out. Different modified arc discharge reactor designs have been made at laboratory scale. High yield, large-scale, and cost-efficient approaches to such nanostructures should not only boost fundamental research but will also foster industrial applications, e.g., lubrication technology. Such a reaction environment can effectively lead to cooling of the reactants and intensification of the coalescence processes, leading to novel nano structures (Lange, 2003). Lange carried out detailed studies of the C arc-discharge process in water. Figure 1.3-9 illustrates their arc discharge design. They have demonstrated the production of well-crystallized nano-onions, nanotubes, fully or partly filled with crystallized metal encapsulates by using arc discharge in water successfully. They concluded that the yield and quality of the products are comparable to those obtained using He as the gas phase and the temperature and C_2 abundance in water are higher than those associated with standard carbon arc discharge under He. C_2 radicals facilitate carbon nanotube growth, akin to the mechanism proposed for a standard gas phase carbon arc discharge. Their study has shown that water arc-discharge technology simplifies the traditional He discharge for carbon nanotube production no special equipment, vacuum or gas are needed. Furthermore, this technique facilitates the collection of products from the water surface, rather than from the whole of the dusty reaction chamber (Lange, 2003). However, it should be noted that collecting and filtering this volume of water is difficult and time consuming.

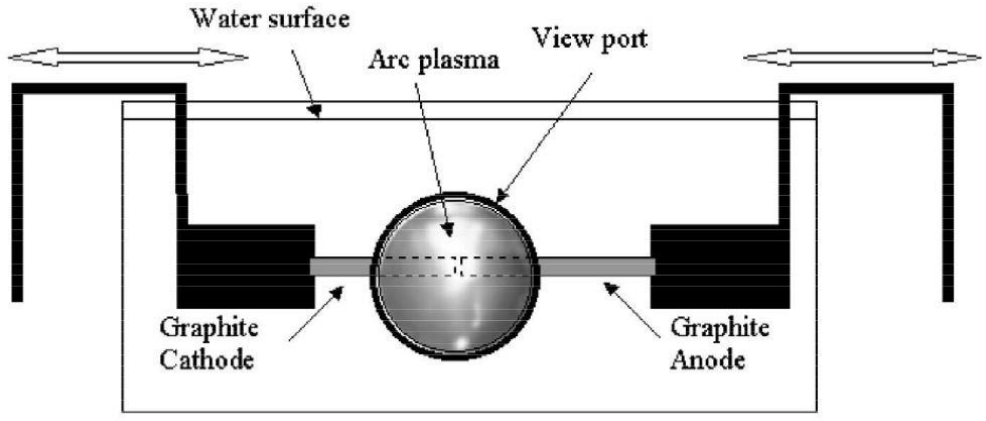

Figure 1.3-9. Electrodes arrangement for arc discharge in water (Lange, 2003).

Graphite encapsulated metal (GEM) nanocrystal is a core-shell structured nanomaterial, which is capable of surviving in severe environments, such as strong-

acid or strongly-oxidizing conditions (Lo, 2011). Many researches have proven GEM to be useful for its potential multiple applications. However, as they mentioned there is a serious problem: its low production rate hinders future research on possible applications. In this case, the arc discharge setup for GEM synthesis is presented in Figure 1.3-10.

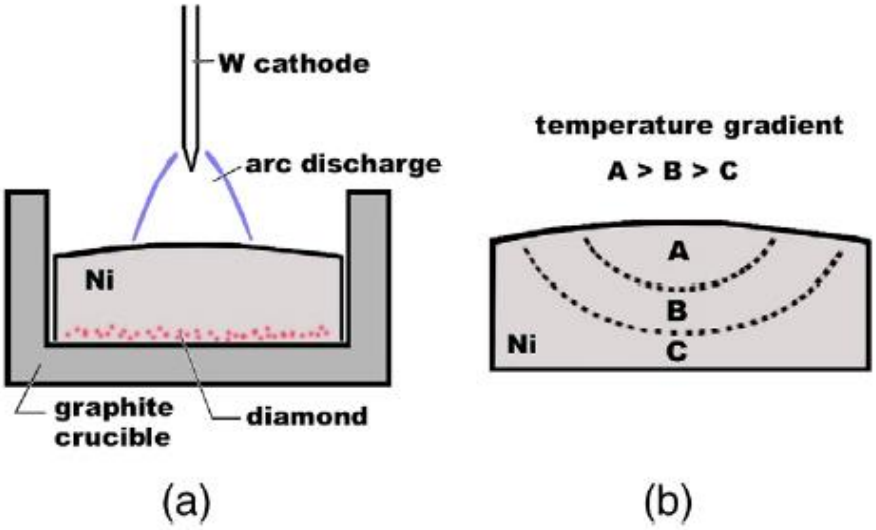

Figure 1.3-10. (a) The schematic of an arc-discharge setup. The diamond particles dissolved in melted nickel in the first 5 min period. (b) The temperature gradient was established during arc-discharge, where the temperature at zone A is higher than at zone B, and zone C is at lowest temperature (Teng, 2009).

Although the tungsten arc-discharge method produces more GEM nanoparticles than all the other methods do, the production rate remains unsatisfactory (Lo, 2011). Their work demonstrates, as attested by experimental evidence, how an alumina piece can effectively change the temperature profile in the crucible and facilitate the synthesis of GEM in a tungsten arc-discharge system. As a result, the as-made production rate approximately quadruples.

Aguilo-Aguayo designed two arc-discharge plasma in FEMAN group. The first reactor experimental setup was developed during the Master's thesis. The reactor consisted of three main parts as shown in Figure 1.3-11.

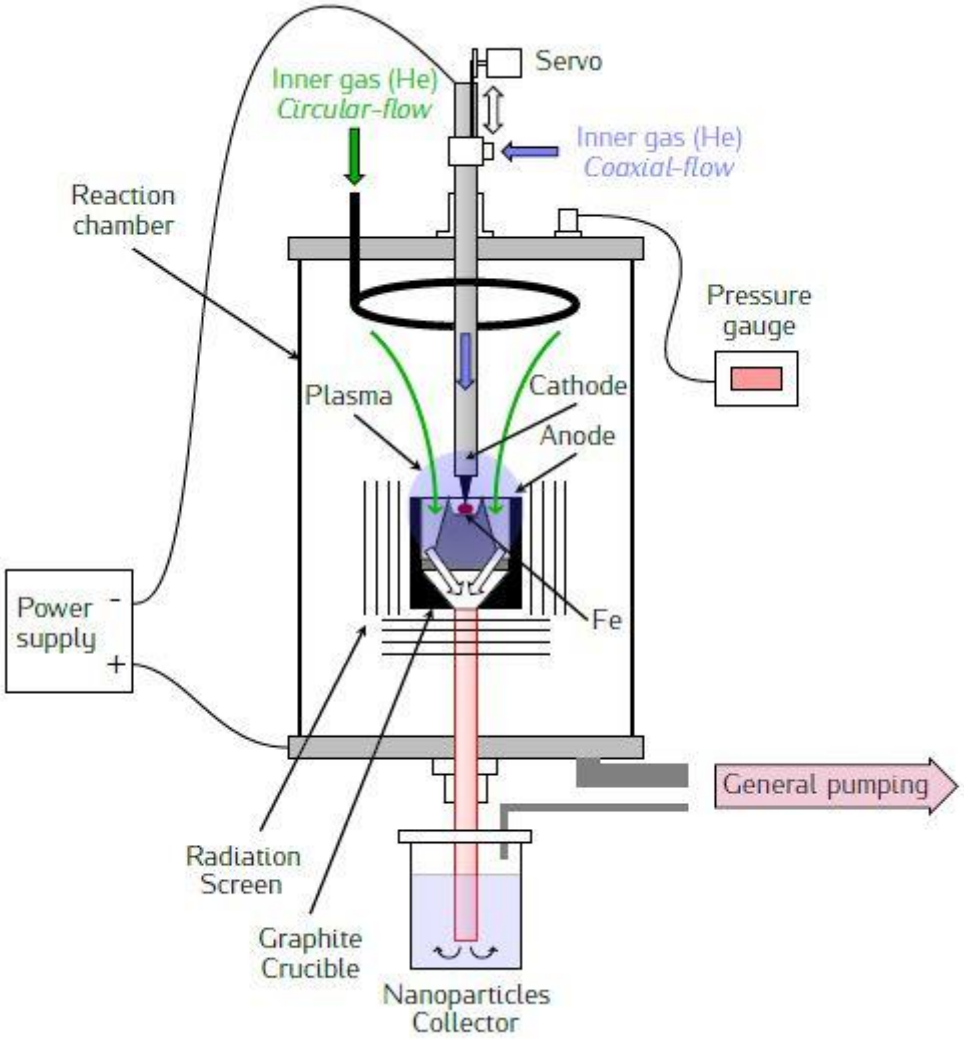

Figure 1.3-11. Schematic drawing of the conventional arc-discharge plasma method reactor (Aguilo-Aguayo, 2012).

A common problem with the arc method is the instability in the arc. In order to improve the stability of the plasma, which was crucial to obtain smaller core sizes as well as smaller standard deviations, Aguilo-Aguayo decided to use a metal precursor made of an organometallic compound in a liquid state instead of solid Fe precursor. The precursor injection in that system was completely new in the arc discharge plasma technology and allowed to improve the quality of nanoparticles (smaller sizes, narrowest size distribution), to better control the Fe composition and carbon encapsulation, to obtain higher yield of nanoparticles than the previous reactor as well as to work at atmospheric pressures and thus reducing the costs related to the vacuum system. In addition, they improved the operation procedure to collect nanoparticles

and manipulate them in solution, which is the safest mode. Due to the advantages of this reactor with some modifications it is employed for further research in this study. The details are explained in the experimental setup reactor.

Common challenges for synthesis of carbon encapsulated iron nanoparticles are improving uniformity, enhancing coating protection and controlling particles compositions, shape and core/shell sizes. In addition, due to the lack of comprehensive understanding of the optimal parameters and formation mechanism most of the current fabrication process are empirical, which means a large number of experimental trials are required to optimize any given process. Arc discharge method is simple, cost effective rapid technique that can easily be carried out. However, maintaining and or increasing quality in parallel with quantity of nanoparticles needs to be improved by arc discharge method. In addition, plasma instability, high temperature and chemical pollution during the process are drawbacks examples of arc discharge technique. Adequate control over synthesis parameters are essential, and are directly depends on the design of the reactor.

1.4 Nanothermodynamics

It is well known that thermodynamics and statistical mechanic, our principal theoretical tools for understanding the physic and behavior of material systems, are mainly based on the assumption that the system under consideration is infinitely large and, therefore, the system is essentially uniform at equilibrium even if it has multiple phases; uniformity in this context is the uniformity of thermodynamic function in the system (Amer, 2010). Common thermodynamic functions include: pressure, temperature, chemical potential, internal energy and free energy. If the uniformity condition of thermodynamic functions is not met, then system is considered as a small system. For small thermodynamic systems the quasi-thermodynamic assumption, sometimes called the point thermodynamic approximation, assumes that is possible to define unique and useful thermodynamic functions for the system at a point (Amer, 2010). It should be noted that the mechanical behavior of small systems is an anomalous phenomenon that has attracted the attention of many researches and is still under investigation (Zhang, 2008, Meyers, 2006, Desai and Haque, 2007).

1.4.1 Surface energy of nanoparticles

Restriction of electrons in one or more dimension translates into quantum confinement; in other words, especially in the case of metals, a continuum of electronic states no longer exists (Zhao, 2014). The size dependent evaporation of free Ag nanoparticles shows that the Kelvin effect is verifiable at nanoscale and Nanda pridected a surface energy value for Ag nanoparticles to be 7.2 $J.m^{-2}$ (Nanda, 2003). Hence, there is a linear relationship between the onset of evaporation temperature and reciprocal particle size.

When nanoparticles present spherical shape, they display liquid-like behavior showing specific properties associated to fluids (example, pressure) (Aguilo-Aguayo, 2012). Energy of cohesion of a homogenous fluid is equal to twice the value of the surface tension. Surface tension then is also called surface excess energy (Hornyak, 2011). This means that there is extra free energy available to drive chemical or physical process on the surface.

The surface energy (tension) is equal to:

$$\gamma = \left(\frac{\delta G}{\delta A}\right)$$

Where G is the Gibbs free energy in joules and A is the area in square meters. G is negative, or spontaneous, when surface area decreased and is positive, requiring energy input, when surface area is increased (Hornyak, 2011).

1.4.2 Kelvin equation

Vapor pressure at the liquid-vapor interface is influenced by pressure, and if pressure is applied (e.g., by an inert gas to the surface of a liquid in equilibrium with its vapor), the vapor pressure, p, of the liquid is increased. The Kelvin equation is:

$$p = p_0 e^{V_m \Delta P / RT}$$

Where p_0 is the vapor pressure of the liquid under standard conditions and $V_m$is the molar volume of the liquid, R is gas constant and T is temperature.

The Kelvin equation gives us a free pass into the nanodomain and the key component is the radius term *r* in the denominator; as *r* gets smaller, the vapor pressure of the droplet becomes larger and larger (Hornyak, 2011). The Kelving equation explains the growth of water droplets in the atmosphere and the condensation of cold gases in nanopores by surface area methods such as BET and BJH.

The value for pressure difference of a spherical surface was independently deducted in 1805 by Thomas Young (1772-1829) and Pierre Simon de Laplace (1749-1827), and is represented in the Young-Laplace equation (Zhong, 2013):

$$P\alpha - P\beta = \gamma \left(\frac{1}{R_1} + \frac{1}{R_2}\right)$$

The Kelvin equation describes the transition of molecules from a liquid phase to a gas phase, which can also be applied to the transition of molecules from a solid phase (drug particle) to a liquid phase (Jacobs and Müller, 2002).

As Yonemoto explained we consider the equilibrium state where the gas and liquid phases coexist and temperature is constant. The gas–liquid interface is a flat surface and, so in this situation, the amount of evaporated liquid from the gas phase to the liquid phase is determined by the relationship between the saturated vapor pressure and ambient pressure if the temperature is constant. The vapor in the ambient pressure is decreased to less than the saturated vapor pressure (Yonemoto and Kunugi, 2011). This is formulated by considering the changes in chemical potential thermodynamically. The same discussion is applied to a bubble and droplet. However, a bubble or droplet has a curvature. The vapor pressure of a droplet takes a different value when the interface has a curvature. The concrete equation is as follows (Butt, 2006):

$$\ln\left(\frac{P_k}{P^*}\right) = \frac{2H\sigma V_m}{\mathrm{R}T}$$

In this equation, P^* and P_k represent the vapor pressures where the gas–liquid interface is flat and with a curvature, respectively. H [1/m^3] is mean curvature, σ [N/m] is surface tension coefficient, V_m [m^3/kg] is specific volume, R [J/kg K] is the ideal gas constant, and T [K] is the temperature. This equation is mainly derived based on both the Gibbs–Duhem equation and Young-Laplace equation from the thermodynamic point of view.

1.4.3 Lattice parameters

It is well known that the lattice parameters of metallic nanoparticles contract with decreasing particle size (Qi, 2003). Figure 1.4-1 illustrates rearrangement in a primitive-C material (Hornyak, 2011).

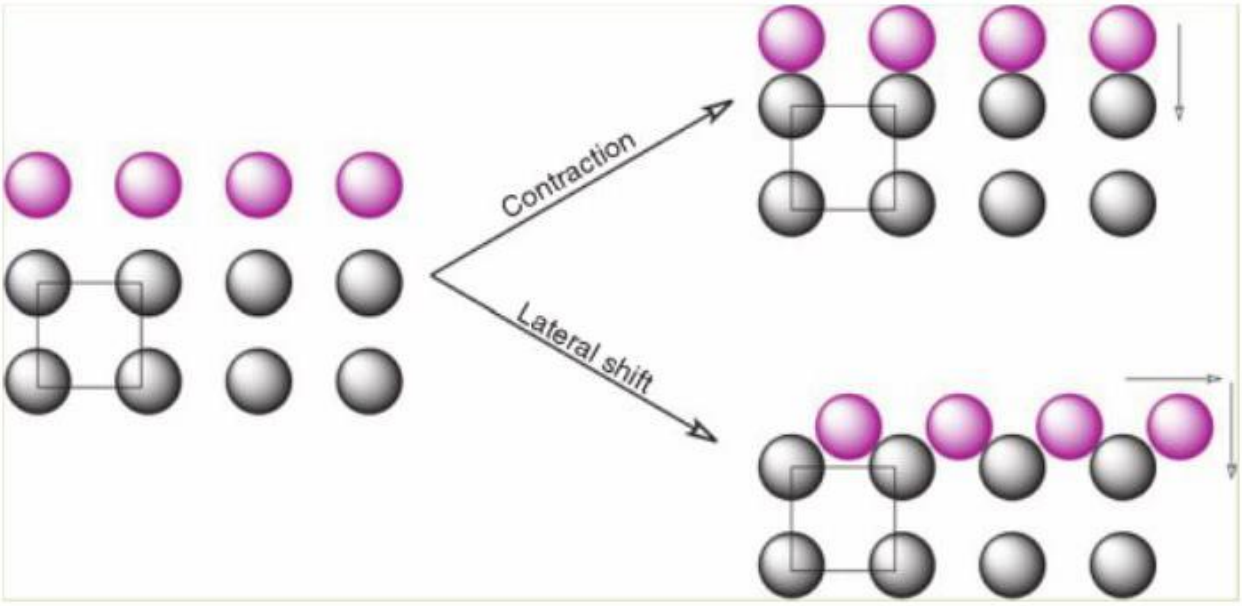

Figure 1.4-1. Restructuring of a simple cubic surface is shown. The coordination of a surface atom is reduce from 6 to 5 (one broken bond forming one dangling bond); for this reason, the surface atom is drawn inward in order to compensate for the lost bond. In this case, the overall structure remains relatively the same and there is only inward shift of the surface atom lattice (Hornyak, 2011).

Lattice contraction is not just a surface phenomenon as the whole of the nanoparticle may experience diminishing of its natural lattice constant; if more bonds are broken, as in the case of atoms with higher levels of coordination, the surface is actually restructured (Hornyak, 2011).

Wang have developed a general method to account for size effect on the lattice parameters of nanoparticles (Wang, 2003). It should be noted that in their method, it is assumed that a large spherical particle is changed into *n* smaller identical spherical nanoparticles, which results in the increase of the total surface energy. Accordingly, the following equation is a general formulation accounting for size and shape effects on the lattice parameters of nanoparticles.

$$\frac{\Delta a}{a} = -\frac{1}{1+K\,.\,d\,.\propto^{\frac{1}{2}}}$$

a is the lattice parameter of bulk material and Δa is the difference between the lattice parameter of nanoparticle and that of the corresponding bulk material. d is the particle diameter; the $\mathrm{K} = \frac{G}{2\gamma_0}$ where G is shear modulus.

1.5 Quantum confinement effect

A quantum well is a potential well that confines particles, which were originally free to move in three to two dimensions, forcing them to occupy a planar region (Choi and Pyun, 2008). Quantum wells are formed in semiconductors by having a material, like gallium arsenide sandwiched between two layers of a material with a wider gap, like aluminum arsenide (Yin, 2012). Coated spheres with thin shells may serve as quantum wells because different potential energies are related to different refractive indices (Choi and Pyun, 2008). The effects of quantum confinement take place when the quantum well thickness becomes comparable to the de Broglie wavelength of the carriers (electrons and holes), leading to energy levels termed sub-bands, i.e. the carriers can only have discrete energy values (Bogue, 2010).

The dependence of spectral position and absolute value of surface plasmon extinction maximum on the particle radius and material of core and shell are analysed in the visible region by Kachan (Kachan and Ponyavina, 2001). Accordingly, the effect of absorbed energy redistribution between external and internal surface plasmons is established to be a change in the ratio of dielectric core/matrix refractive indices. The light intensity on any light absorbing surfaces is subject to fluctuations, which are similar to the shot noise observed in the photoelectronic devices, and so suggested that this noise from numerical computation be modeled to be the real thermal fluctuations of photon density on the particle surface (Choi and Pyun, 2008). Si nanocrystallites with the size less than 4.8 nm are characterized by a quantum confinement effect and named as quantum dots (QDs); PL bands of Si QDs have peak energies higher than Si band gap at 300K (E_G = 1.12 eV), which allows attributing them to radiative transitions between quantum confined levels localized inside of Si NCs

(Hernandez, 2007). As explained by Roduner an important threshold is reached when the gap between the highest occupied and the lowest unoccupied state (called the Kubo gap) equals thermal energy (Roduner, 2006). When electrons get thermally excited across the Kubo gap, a low temperature insulator becomes a semiconductor and at higher temperatures a metal; and also magnetic properties of small clusters can change dramatically. This non-metal-to-metal transition can take place within a single incompletely filled band, or when two bands begin to overlap because of band broadening. The catalytic activity and selectivity are highly dependent on the shape, size, and surface structure of supported metal NPs as well as oxides (Zhang, 2014). Quite often, the discontinuous behavior of quantum size effects is superimposed on a smoothly scaling slope, which also reflects the size of the quantized system (Roduner, 2006, Ghosh, 2011).

1.6 Magnetic nanoparticles theoretical background

The fundamental motivation for the fabrication and study of nanoscale magnetic materials is the dramatic change in magnetic properties that occurs when the critical length governing some phenomenon (magnetic, structural, etc.) is comparable to the nanoparticle or nanocrystal size (Leslie-Pelecky and Rieke, 1996).

The following description are derived from paper published by Leslie-Pelecky (Leslie-Pelecky and Rieke, 1996). Changes in the magnetization of a material occur via activation over an energy barrier. Each physical mechanism responsible for an energy barrier has an associated length scale. The fundamental magnetic lengths are the crystalline anisotropy length, I_K, the applied field length, I_H, and the magnetostatic length, I_S, which are defined as the following:

$$I_K = \sqrt{J/K}$$

$$I_H = \sqrt{2J/HM_S}$$

$$I_S = \sqrt{J/2\pi M_S^2}$$

K is the anisotropy constant of the bulk material due to the dominant anisotropy and J is the exchange within a grain. If more than one type of barrier is present, magnetic properties are dominated by the shortest characteristic length. For most common magnetic materials, these lengths are on the order of 1-100 nm. For example, nickel at 1000 Oe and room temperature has lengths$l_S = 8\ nm$, $l_K = 45\ nm$, and $l_H = 19\ nm$.

Figure 1.6-1 schematically illustrates a hysteresis loop (magnetization vs field). The application of a sufficiently large magnetic field causes the spins within a material to align with the field. The maximum value of the magnetization achieved in this state is called the saturation magnetization, M_s. As the magnitude of the magnetic field decreases, spins cease to be aligned with the field, and the total magnetization decreases. In ferromagnets, a residual magnetic moment remains at zero field. The value of the magnetization at zero field is called the remanent magnetization, M_r. The ratio of the remanent magnetization to the saturation magnetization, M_r/M_s, is called the remanence ratio and varies from 0 to 1. The coercive field H_c is the magnitude of the field that must be applied in the negative direction to bring the magnetization of the sample back to zero. The shape of the hysteresis loop is especially of interest for magnetic recording applications, which require a large remanent magnetization, moderate coercivity, and (ideally) a square hysteresis loop.

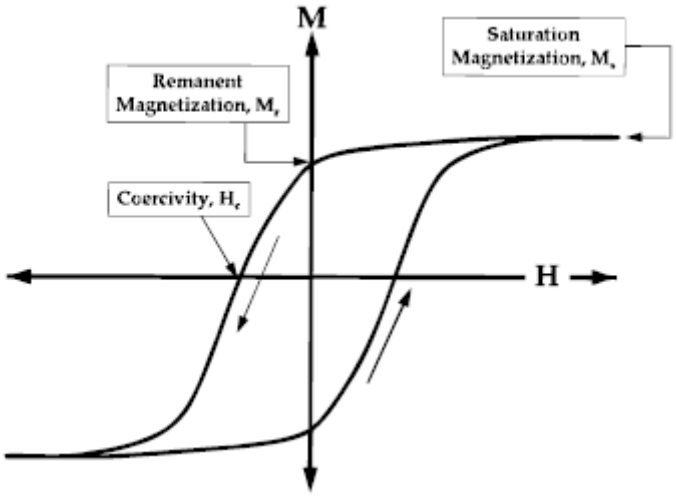

Figure 1.6-1. Important parameters obtained from a magnetic hysteresis loop. The saturation magnetization, M_s, remanent magnetization, M_r, and coercivity, H_c, are shown (Leslie-Pelecky and Rieke, 1996).

1.6.1 Classical theories of paramagnetism

Paramagnetic materials have a small, positive susceptibility to magnetic fields. These materials are slightly attracted by a magnetic field and the material does not retain the magnetic properties when the external field is removed. Paramagnetic properties are due to the presence of some unpaired electrons, and from the realignment of the electron paths caused by the external magnetic field. Paramagnetic materials include magnesium, molybdenum, lithium, and tantalum.

The first systematic measurements of the susceptibility of a large number of substances over an extended range of temperature were made by Pierre Curie in 1895 (Curie, 2013). He found that the mass susceptibility x_m was independent of temperature for diamagnetic, but that it varied inversely with the absolute temperature for paramagnetic (Cullity and Graham, 2011):

$$x_m = C/T.$$

This relation is called the Curie law, C is the Curie constant per gram and T is temperature. It was later shown that the Curie law is only a special case of a more general law, called the Curie–Weiss law (Cullity and Graham, 2011):

$$x_m = C/(T - \theta),$$

Here θ is a constant, with the dimensions of temperature, for any one substance, and equal to zero for those substances, which obey Curie's law.

The following description is derived from a book written by Cullity (Cullity and Graham, 2011). Curie's measurements on paramagnetics went without theoretical explanation for 10 years, until Langevin in 1905 took up the problem in the same paper in which he presented his theory of diamagnetism. Qualitatively, his theory of paramagnetism is simple. He assumed a paramagnetic to consist of atoms, or molecules, each of which has the same net magnetic moment μ, because all the spin and orbital moments

of the electrons do not cancel out. In the absence of an applied field, these atomic moments point at random and cancel one another, so that the magnetization of the specimen is zero. When a field is applied, there is a tendency for each atomic moment to turn toward the direction of the field; if no opposing force acts, complete alignment of the atomic moments would be produced and the specimen as a whole would acquire a very large moment in the direction of the field. But thermal agitation of the atoms opposes this tendency and tends to keep the atomic moments pointed at random. The result is only partial alignment in the field direction, and therefore a small positive susceptibility. The effect of an increase in temperature is to increase the randomizing effect of thermal agitation and therefore to decrease the susceptibility.

1.6.2 Superparamagnetic

Each particle has a magnetic moment $\mu = M_s V$ and, if a field is applied, the field will tend to align the moments of the particles, whereas thermal energy will tend to misalign them (Cullity and Graham, 2011). This is just like the behavior of a normal paramagnetic, with one notable exception. The magnetic moment per atom or ion in a normal paramagnetic is only a few Bohr magnetons. But a spherical particle of iron 50A° in diameter contains 5560 atoms and has the relatively enormous moment of (5560)(2.2) = 12,000 μ_B. As a result, Bean coined the very apt term superparamagnetism to describe the magnetic behavior of such particles (Bean and Livingston, 1959).

Understanding the correlation between magnetic properties and nanostructure involves cooperative efforts between chemists, physicists, and materials scientists to study both fundamental properties and potential applications; the correlation between nanostructure and magnetic properties suggests a classification of nanostructure morphologies (Leslie-Pelecky and Rieke, 1996). The classification shown in Figure 1.6-2 is designed to emphasize the physical mechanisms responsible for the magnetic.

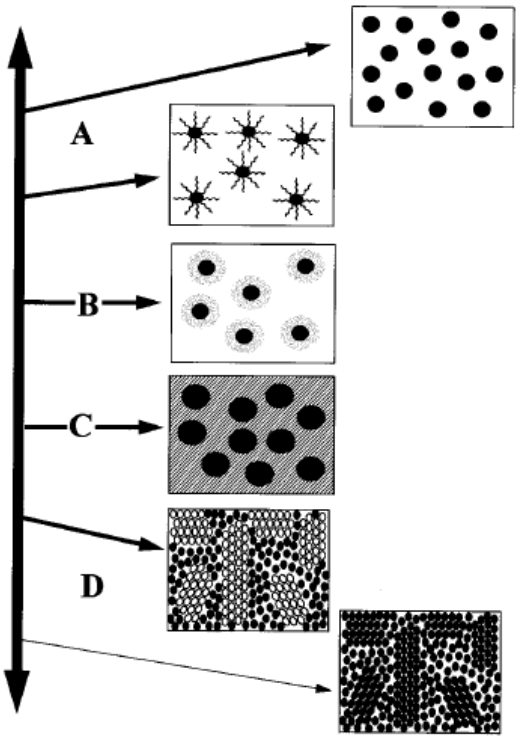

Figure 1.6-2. Schematic representation of the different types of magnetic nano-structures. Type-A materials include the ideal ultrafine particle system, with interparticle spacing large enough to approximate the particles as non-interacting. Ferro-fluids, in which magnetic particles are surrounded by a surfactant preventing interactions, are a sub group of Type-A materials. Type-B materials are ultrafine particles with a core@shell morphology. Type-C nanocomposites are composed of small magnetic particles embedded in a chemically dissimilar matrix. The matrix may or may not be magnetoactive. Type-D materials consists of small crystallites dispersed in a noncrystalline matrix. The nanostructure may be two-phase, in which nanocrystallites are a distinct phase from the matrix, or the ideal case in which both the crystallites and the matrix are made of the same material (Leslie-Pelecky and Rieke, 1996).

1.7 Growth formation of carbon based nanoparticles

In this study, arc discharge technique have been used for the synthesis of carbon based nanoparticles. Although a number of variations exist for gas phase synthesis processes, they all have in common the fundamental aspects of particle formation mechanisms that occur once the product species are generated (Varga and Kröll). Nucleation is the process of random generation of nanoscopically small formation of the new phase that have the ability for irreversible overgrowth to macroscopic sizes (Cabriolu, 2012). It is the very first step of the vapor deposition process. The properties of the material grown in the vapor deposition process at the nucleation stage influence the properties of the final product. Hence, control over the process while the nucleation of the vapor occurs is important.

According to Gibbs, the reversible work, W, required to form the critical nucleus of the new phase is (Joshi, 2008):

$$W = \Delta G^0 = A \cdot \gamma_T - V(P_j - P_v)$$

A, V are area and volume, respectively, of the specific energy of a specially chosen discrete surface, which is the dividing line between the old and new phase. P_j is the pressure of the new bulk phase. P_v is the pressure of the parent phase. γ_T is the surface tension. There are two types of nucleation process: homogenous nucleation and heterogeneous nucleation. The homogeneous nucleation is described by the classical theory developed by Becker and Döring (Becker and Döring, 1935). The classical formula provides a simple method of estimating the size of the energy barrier to nucleation and the critical cluster size. A serious rival to the classical theory is that presented by Lothe and Pound; who dispense with many of the assumptions made by Becker and Döring and who, in addition, argue that the translational and rotational energies of the droplet as it moves through the system are significant contributions to the estimation of the energy of formation (Moody and Attard, 2002). Predicting nucleation rates for real experimental substances is either impossible due to lack of realistic interaction models between real molecules, or enormous computational costs and for most practical purposes, classical nucleation theory is still the only means of predicting nucleation rates and critical cluster sizes (Vehkamäki, 2006). Gas to particle

conversion refers to the production of condensed particles from individual atoms or molecules in the gas phase; the particle formation is then driven by the cooling of a supersaturated vapor (Chazelas, 2006). Our experiments results explained how the cooling rate, which is regulated by thermal conductivity of the gas, effects the iron particle sizes. The nucleation event is very sensitive to the supersaturation ratio S, defined by the following equation (Friedlander, 1983):

$$S = \frac{P_i}{P_s(T)}$$

Where P_i is the partial pressure of the gaseous reactant and $P_s(T)$ the corresponding saturated vapor pressure. When this supersaturation ratio becomes larger than unity, nucleation can occur (Chazelas, 2006).

As explained Pomogailo in the general case, the change of Gibbs energy, *ΔG*, in the system under formation of a new phase nucleus can be presented by the sum of two component, the first of them denotes system properties in the macrovolume and makes allowance for lessening of the Gibbs energy, $(\Delta G_j)_{macr}$, during formation of the new phase nucleus (Pomogailo and Kestel'man, 2006). This formation incorporates j atoms and is characterized by difference, $\Delta\mu$, in the chemical potentials between the metastable maternal phase and environment, and between the new stable phase and the nucleus

$$(\Delta G_j)_{macr} = -j\,(\mu_e - \mu_n) = -j\Delta\mu$$

Where μ_e and $\mu_n$are the chemical potentials of the environment and nucleus, correspondingly for one atom and $\Delta\mu$ is the variation of chemical potential (J/atom)

The value $\Delta\mu$ can be expressed through the parameters being measured. The simplest questions for $\Delta\mu$ for a number of cases of isotropic homogeneous phase formation characterize vapor condensation as well as crystallization of single component particles from a solution, melt or during boiling.

Let the nucleus of the new phase consisting of j atoms be spherical with radius $R_j = (3j\Omega/4\pi)^{1/3}$, so it can be written that $\left(\Delta G_j\right)_{micr} = 4\pi R_j^2$. Then the total change of Gibbs, energy during formation of a single spherical nucleus will be:

$$\Delta G_j = \left(\Delta G_j\right)_{macr} + \left(\Delta G_j\right)_{micr} = 4\pi R_j^3 \Delta\mu/3\Omega + 4\pi R_j^2/\gamma\ .$$

This condition is valid for the following radius of the critical nucleus

$$R_{j,cr} = 2\Omega\gamma/\Delta\mu.$$

The number of atoms in this critical nucleus will be, correspondingly,

$$j_{cr} = 4\pi R_j^3 \Delta\mu/3\Omega = 32\pi\Omega^2(\gamma/\Delta\mu)^3/3$$

The energy barrier to be overcome at formation of a new phase will be

$$\Delta G_{j,cr} = 16\pi\ (\Omega/\Delta\mu)^2\ \gamma^3/3.$$

The energy barrier constitutes one third of the surface energy of the critical nucleus according to Gibbs.

The system potential will diminish for an ensemble of atoms having $R_j < R_{j,cr}$, so aggregates less than $R_{j,cr}$, will disintegrate, whereas aggregates with $R_j > R_{j,cr}$, show growth that lessens the energy of the system, the nuclei will be just these particles. Let us estimate the characterstics size of a critical nucleus. To condense from vapor, high temperatures and supersaturation are needed for metal containing particles. These conditions can be modeled by the method of impact tubes, so, for iron [14] at $T = 1600K, s = P/P_0 = 3040, \gamma = 1.8.10^{-4}\mathrm{J/cm^2}$, we have $\Delta\mu = k_A T ln(P/P_0) \approx 9.10^{-20}\ \mathrm{J}.$ At $\Omega = 10^{-23}\mathrm{cm}^3$ we get $R_{j,cr} = 2\Omega\gamma/\Delta\mu \approx 0.47\ nm$. The critical

nucleus of this size contains about 33 atoms of Fe (Pomogailo and Kestel'man, 2006). It should be noted that the nucleation process become stable when their critical energy barrier is more than ΔG_{cr}.

Ostwald ripening is an observed phenomenon in solid solutions or liquid sols that describes the change of an inhomogeneous structure over time, i.e., small crystals or sol particles dissolve, and redeposit onto larger crystals or sol particles (McNaught and McNaught, 1997). The Ostwald-ripening process typically leads to a coarsening of the size distribution, and hence in nanocrystal synthesis one usually aims to suppress it by having excess precursors in solution and at long times, Ostwald ripening leads to a decreased number of particle domains (Mokari, 2005). In Ostwald ripening mechanism smaller crystals transfer and exchange atoms and form larger nanoparticle as shown in Figure 1.7-1. Ostwald ripening phenomena can occur in solid, liquid or gas phase (Hornyak, 2011, Mokari, 2005).

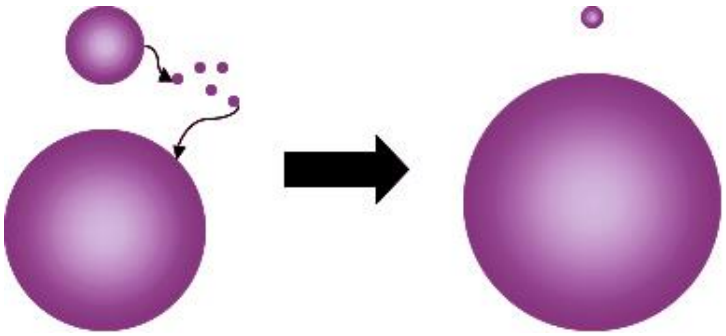

Figure 1.7-1. Schematic of the Ostwald-ripening process.

Mainly, nanoparticles properties depend strongly on their size distribution and morphology. In the results chapter an approach to control the sizes of carbon encapsulated iron nanoparticles are described, which shed new light on the fundamental processes that govern growth mechanism. In gas phase reactors, the final characteristics of particulate products are determined by fluid mechanics and particle dynamics within a few milliseconds at the early stages of the synthesis process; as described by Gutsch within this short time frame, three major formation mechanisms dominate the particle formation (Gutsch, 2002):

1st, Chemical reaction of the precursor leads to the formation of product monomers by nucleation or direct inception, and to the growth of particles by reaction of precursor molecules on the surface of newly formed particles; this is called surface growth. The influences of precursor, which shows surface growth and leads to the formation of fullerenes molecules on carbon nanoparticles surface, are demonstrated in the section entitled: “Synthesis of carbon nanoparticles decorated by fullerenes”.

2nd, Coagulation is an intrinsic mechanism, which inevitably occurs at high particle concentrations and therefore in all industrial aerosol processes. Particles dispersed in a fluid move randomly due to Brownian motion and collide with each other along their trajectories. Assuming strong adhesive forces, characteristic for small particles, or chemical bonds, these collisions result in coagulation. As explained by Gutsch with increasing residence time, the expected advancing degree of aggregation can clearly be seen. As the residence time of the droplets in the plasma is very short it is important that the droplet sizes are small in order to obtain complete evaporation (Kruis, 1998). Residence time is the period that the nucleus of the precursor is spending inside the plasma zone. The time that gas atoms and precursor radicals stay inside the plasma zone depends on the gas flow rate. The estimation of residence time and its influence on particle size are described in section entitled: “Influences of precursor concentration and gas flow on carbon encapsulated iron nanoparticles formation”.

3rd Coalescence and fusion are sufficiently fast in the high temperature zones of the reactor to effect a reduction in the level of aggregation or even the formation of spherical particles due to sintering processes. Our investigation revealed the coalescence effect and for the first time leads to the formation of multi iron nanoparticles in carbon shell, the mechanisms, influence of coalescence on particle formation, growth, and final morphology are described in section of “Synthesis of carbon encapsulated mono and multi iron nanoparticles”.

1.7.1 Carbon coating formation mechanism: State of the art

Most of the theories regarding the formation of carbon based nanomaterials such as carbon encapsulated iron nanoparticles are developed from the suggested mechanisms about the formation of carbon nanotubes using plasma method. Carbon nanotubes use metal nanoparticles as catalysts for their growth (Huang, 2004, Zhang, 2015).

Vapor-liquid-solid (VLS) is the most popular theory model for the explanation of carbon nanotubes growth (Baker, 1989, Baker, 1972). The VLS mechanism circumvents this by introducing a catalytic liquid alloy phase, which can rapidly adsorb a vapor to supersaturation levels, and from which crystal growth can subsequently occur from nucleated seeds at the liquid–solid interface (Chaturvedi and Dave, 2013).

Later in 1976. Oberlin proposed a growth model related to the surface diffusion of carbon species on the catalyst particle. An association of metal and hydrocarbon nucleates and diffuses on the clean Fe particle surface (which they assume is “liquid-like”) and eventually dissociates at the contact angle between the particle and the substrate, thus producing the beginning of a carbon shell. New metal hydrocarbon species dissociate on its edge and the carbon layers develop by lateral growth, following the external surface of the catalyst. Such a lateral growth exerts a force strong enough to lift up the catalyst particle above the surface of the substrate (Laurent, 1998). Ding [Ding and Bolton, 2006] showed by thermodynamic analysis that a metal particle only needs to be highly carbon supersaturated to nucleate carbon islands and illustrate graphically three kinds of carbon condensed C atom *(C_C)*, dissolved C atom *(C_D)* and precipitated C atom *(C_P)* as shown in Figure 1.7-2.

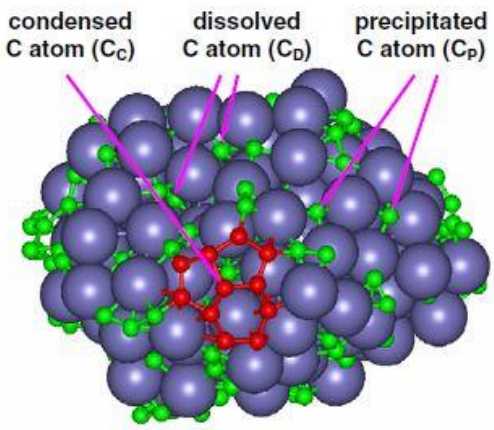

Figure 1.7-2. Illustration of the three kinds of carbon C atoms used in the thermodynamic model of SWNT nucleation on the catalyst particle surface: carbon atoms that have condensed (coalesced) to form the graphitic island, C_C; carbon atoms that have precipitated on the particle surface but do not form part of the island, C_P; and carbon atoms that are dissolved in the catalyst particle, C_D. The large spheres are metal atoms and the carbon atoms are shown as ball-and-stick models (Ding and Bolton, 2006).

According to the Saito growth model, carbon and metal catalysts are evaporated in an arc discharge plasma, when catalytic particles cool down enough then the carbon atoms are segregated onto the surface due to the decreasing of solubility of carbon with the decreasing temperature; and additional carbon atoms from the vapor phase helps the growth of tubular structures (Saito, 1994).

Saito revealed that the rare-earth metals with low vapor pressures, Sc, Y, La, Ce, Pr, Nd, Gd, Tb, Dy, Ho, Er, Tm, and Lu, were encapsulated in the form of carbides, whereas volatile Sm, Eu, and Yb metals were not; and for iron-group metals, particles in metallic phases (α-Fe, γ-Fe; hcp-Co, fcc-Co; fcc-Ni) and in a carbide phase (M_3C, where M is a metal like Fe, Co, Ni) were wrapped in graphitic carbon. Hence, they proposed that core@shell nanoparticles growth with a liquid core coated by a graphite shell, which then segregates and solidifies (Saito, 1995). Similar growth mechanism were explained by authors (Majetich, 1994, Scott and Majetich, 1995); they suggested that firstly magnetic material and carbon are atomized in the plasma zone and collide and nucleate into clusters in the supersaturated vapor. Afterward, by phase segregation particles are deposited on surfaces within the reactor. Formation of the carbon coating metal nanoparticle graphically is shown in Figure 1.7-3. In addition, according to their analysis the size distribution of the samples depends on the steepness of the nanoparticles cooling curve during the growth formation.

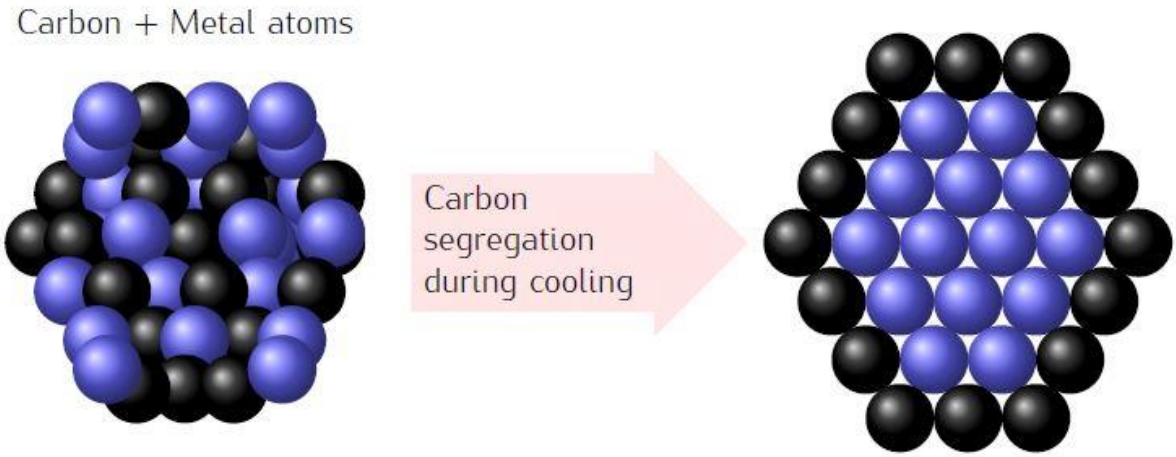

Figure 1.7-3. The blue color represents metal and the black ones are the carbon. Shows the formation of the carbon coating by phase segregation during the cooling of the liquid metal nanoparticle (Majetich, 1994).

Extensive research have been done by Seraphin and co-workers, in their study twenty elements were code posited with carbon in an arc discharge between graphite electrodes (Seraphin, 1996). The products fall into four categories:

(1) Elements that can be encapsulated in the form of their carbides (B, V, Cr, Mn, Y, Zr, Nb, Mo);

(2) Elements that are not encapsulated but tolerate the formation of graphitic carbon cages (Cu, Zn, Pd, Ag, Pt);

(3) Elements that form stable carbides, competing with and pre-empting the carbon supply for the graphitic cage formation (Al, Si, Ti, W); and

(4) the iron-group metals (Fe, Co, Ni) that stimulate the formation of single-walled tubes and strings of nanobeads in the conventional arc discharge condition, and produce the nanometer-size carbon-coated ferromagnetic particles in a modified arc discharge in which metals are in molten form in graphite crucible anodes exposed to a helium jet stream.

They commented that it is apparent that the physical properties such as vapor pressure, melting and boiling points, the completeness of the electronic shells of the elements, or their heat of carbide formation are not sufficient to explain the selectivity of the encapsulation without exceptions.

Borysiuka studied carbon encapsulated Fe nanoparticles synthesis by arc discharge method (Borysiuk, 2008). As they commented, their results cannot be explained by the use of one of the proposed models. Relatively high content of the carbide indicates that at least part of the particles nucleates from the vapor phase. That is nucleation of either liquid nano-droplets or graphite nanocrystals. In both cases, the graphite is crystallized first, during cooling down to 1252 ^{0}C, i.e. to the congruent melting point of Fe_3C (Bystrzejewski, 2009, Coey, 2002). Without strong experimental evidence they commented that it is improbable that theααFe or even perhaps γγFe nanoparticles grew from the vapor phase under heavy or even dominating presence of carbon.

Results from excellent and extensive research studies of Aguilo-Aguayo showed that the arc current was the most influential arc discharge reactor parameter. Optical emission spectroscopy studies for the plasma characterization in the modified arc discharge reactor pointed out the relation of the plasma temperature to the arc current used (Aguilo-Aguayo, 2012). Their results showed the importance of the temperature in this kind of technology and its important role on the growth of nanoparticles, determining the cooling rate and hence, the residence time of nanoparticles.

So far, from the proposed models it is not yet possible to predict the growth formation of core@shell nanoparticles. Despite the strong industrial and scientific interest in synthesis of nanoparticles by thermal plasmas, the growth mechanism of the nanoparticles remains poorly understood. Due to the lack of comprehensive understanding of the optimal parameters and formation mechanism most of the current fabrication process are empirical, which means a large number of experimental trials are required to optimize any given process (Shigeta and Murphy, 2011).

1.8 Potential applications

There are wide range of applications for carbon based materials such as carbon encapsulated iron nanoparticle, porous carbon microparticles and carbon nanoparticles decorated by fullerenes.

Taylor presented the effects of acidic treatments based on HCl, HNO_3 and H_2SO_4 on carbon encapsulated iron nanoparticles highlighting the impact on their magnetic and surface properties and they have shown that acidic treatments based on HNO_3 can be successfully applied for the generation of carboxylic groups on the surface of the nanoparticles. Using methylamine as a model, it was demonstrated that these functional groups can be used for further functionalization with amino-containing biomolecules via diimide-activated amidation (Taylor, 2010a). Later Taylor have shown that the surface functionalization with carboxylic functionalities allows their loading with the drug cisplatin, which is released in saline solutions and hence the use of carbon-encapsulated nanoparticles makes feasible the application of metallic iron as an agent for magnetic fluid hyperthermia (Taylor, 2010b). Grudzinski studied cytotoxicity evaluation of carbon-encapsulated iron nanoparticles in melanoma cells and dermal fibroblasts (Grudzinski, 2013).

Large porous particles, characterized by geometric sizes larger than 5 μm and mass densities around 0.1 g/cm^3 or less, have achieved recent popularity as carriers of drugs to the lungs for local and systemic applications; they have combined advantages of reduced macrophages uptake, improved dispensability and enhanced delivery efficiency. It is because the large porous microparticles possess small aerodynamic diameter due to its reduced density and prevention of phagocytosis by macrophages owing to its large geometric size (Wan, 2012) (Tsapis, 2002). Tsapis have combined the drug release and delivery potential of nanoparticle systems with the ease of flow, processing, and aerosolization potential of large porous particle systems by spray, drying solutions of polymeric and nonpolymeric NPs into extremely thin-walled macroscale structures. They concluded that NPs appear to be robust drug delivery systems that may be useful for encapsulating drugs of varying chemistry and molecular weight into biodegradable nanoparticles, thereby combining the persistence

advantages of nanoparticles with the delivery convenience of large porous particle. Their ultimate practical utility for drug and gene delivery requires incorporation of drug, exploration of the use of other biocompatible materials, and delivery to human and animals (Tsapis, 2002, Hartono, 2014).

Fullerene materials have received wide attention due to their biomedical applications such as photodynamic therapy, magnetic resonance imaging and also their capability to act as ‘radical sponges’ in various schemes (Wang, 2014, Partha and Conyers, 2009, McBride, 2015). Huang studied antimicrobial photodynamic therapy with decacationic monoadducts and bisadducts of [70] fullerene: in vitro and in vivo and proposed that the attachment of an additional deca(tertiary-ethylenylamino) malonate arm to C70 allowed the moiety to act as a potent electron donor and increased the generation yield of hydroxyl radicals under UVA illumination (Huang, 2014). Moreover, fullerenes are known to function as good radical sponges that can make possible a variety of radical addition reactions (Gunji, 2014). Shi developed a fullerene-based tumor targeting multi-functional magnetic nanocomposite, by using C60-IONP-PEG-FA. C60-IONP-PEG-FA showed neglectable toxicity both in vitro and in vivo, the nanoparticles could serve not only as a powerful tumor diagnostic agent, but also as a strong photosensitizer and powerful agent for photothermal ablation of tumor (Shi, 2014b).

II. Methodology

This chapter consists of two main sections: Arc Discharge experimental set-up and Characterization tools. Liquid phase arc discharge reactor were utilized for further investigation on synthesis of carbon encapsulated iron nanoparticles. The reactor details are described in section 2.1.1. Investigation results by using liquid phase arc discharge reactor are presented in two sections: 3.1 and 3.2 of results chapter. Afterward, drawbacks of liquid phase arc discharge reactors were identified such as very low synthesis yield. Consequently, to overcome those drawbacks a new modified arc discharge reactor were designed and implemented and named as gas phase arc discharge reactor and the details are described in section 2.1.2. New reactor not only improved the synthesis process of carbon encapsulated iron nanoparticle (section 3.3) but also leads to the synthesis of two new materials carbon nanoparticles decorated by fullerenes and spherical porous carbon microparticles, which are described in sections: 3.4 and 3.5, respectively. Moreover, gas phase arc discharge reactor increased production yield dramatically. As recently in an important review, Wang commented that spherical nanocarbon materials have properties that make the promising as nano-medicines and therapeutic agents and major limitations of realizing the practical applications of fullerenes are high cost and low production yield. It will be important to develop a large scale method for the synthesis and purification of these structures (Wang, 2014). According to the accurate weight measurements provided by BET analysis (data available in appendix B) and superconducting quantum interference device, mass estimation of new gas phase arc discharge reactor (using collection system described in section 2.1.2.3) shows synthesis rate of 0.1 mg/min, whereas liquid phase arc discharge reactor synthesis yield estimation shows synthesis rate of 0.025 mg/min, averagely. Moreover, new precursor delivery system allowed continuous synthesis, which increases the synthesis yield and can run for hours. Liquid phase arc discharge reactor runs for no more than 10 minutes per day due to the time needs to cool down and more importantly electrodes deform due to the high temperature, which have negative effect on plasma shape and uniform formation of nanoparticles.

Nanoparticles synthesis of 0.1 mg/min is sufficient for laboratory scale, especially for drug delivery experiments. For example Yu functionalized superparamagnetic iron oxide nanoparticles with doxorubicin (an anticancer) for combined cancer imaging and therapy In Vivo (Yu, 2008a). To validate the therapeutic efficacy they randomly sorted mice into five groups (n=5-7) and treated each group with reagents that contains 12.5 mg Fe Kg^{-1}. This means that new gas phase reactor, can synthesis 12.5 mg of carbon encapsulated iron nanoparticles in 125 minutes continuously in a single day, approximately. In comparison, the liquid phase arc discharge reactor can run 10 minutes per day, and it takes 50 days to synthesis 12.5 mg of carbon encapsulated iron nanoparticles. The new gas phase Arc Discharge reactor design are described in section 2.1.2.

Second section of this chapter is description regarding characterization tools that have been employed to study morphological and magnetic properties of obtained nanoparticles. In this study, advanced characterization tools were provided from Centers Cientific i Tecnologics (CCiT), Universitat de Barcelona (UB).

2.1 Arc Discharge experimental set-up

State of the art of core@shell nanoparticles synthesis techniques including detonation, chemical vapour deposition, combustion, hydrothermal, microwave plasma and arc discharge are described in section 1.2.1. By comparing the results of obtained nanoparticles from those synthesis techniques, as explained in section 1.2.1, it is concluded that best technique for the synthesis of carbon based materials, particularly core@shell nanoparticles is arc discharge technique. Arc discharge is a well-known technique for producing carbon materials at nano and micro scale. The arc discharge phenomenon was first described in 1902, as a “special fluid with electrical properties”, by Vasily V. Petrov (Shea, 1983). Sir Humphry Davy first demonstrated the arc early in the nineteenth century by transmitting an electric current through two touching carbon rods and then pulling them a short distance apart. He is credited with naming the arc.

Since the last two decades arc discharge technique leads to the discovery of important carbon materials. In 1991, W. Krätschmer and D. R. Huffman obtained fullerene

carbon structure from the carbon soot produced from two high-purity graphite electrodes by igniting an arc discharge between them in an inert atmosphere (Krätschmer and Huffman, 1992). In 1991 for the first time the nanotubes were observed in the carbon soot of graphite electrodes during an arc discharge, by using a current of 100 Amperes that was intended to produce fullerenes (Iijima, 1991). The differences in arc discharge specifics at various locations on the inside of the plasma cord lead to the growth of different carbon structures (Koprinarov, 1997).

2.1.1 Liquid phase arc discharge reactor

Arc discharge is one of the most convenient methods to generate the thermal plasma, which is characterized by the high energy content and the local thermal equilibrium state. In this study, a modified arc discharge reactor was used for producing carbon encapsulated iron nanoparticle (CEINPs). The experimental setup details are described by Noemi Aguilo-Aguayo (Aguilo-Aguayo, 2012). The novelty of the reactor was delivering precursor in liquid phase and its design was patented (Bertran, 2012). In order to change specific parameters its design was slightly changed. Here in, the reactor set up are briefly explained.

The apparatus used to produce carbon encapsulated iron nanoparticles (CEINPs) nearly monodisperse superparamagnetic NPs consists of four parts, as it is shown in Figure 2.1-1: The reaction chamber, the gas entrance and vacuum control, a pair of electrodes anode-cathode and precursor injector.

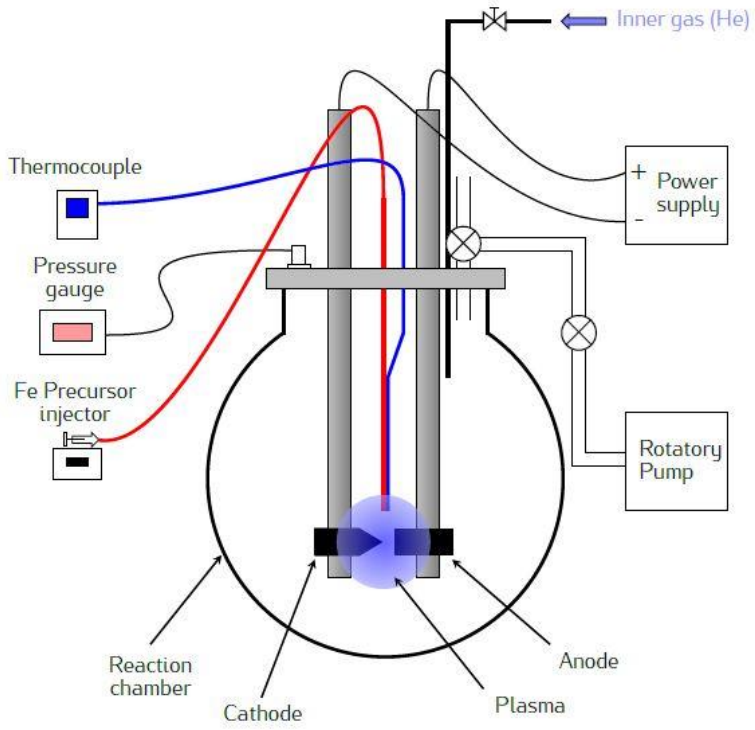

Figure 2.1-1. Schematic drawing of the arc discharge reactor set-up used in our experiments for the production of CEINPs (Aguilo-Aguayo, 2012).

In order to control the gas flow precisely, the reactor equipped with two special micro valves. Unlike previous experiments on this reactor, in order to avoid changes in process temperature inside the glass chamber a water bath was not used.

Two 99.99 % pure graphite rode served as anode and cathode inside the process chamber. Cathode graphite rode was sharpening at an angle near to 20° and placed perpendicular to the anode electrode. The synthesis and collection process was taken place inside a spherical glass chamber. In order to ensure the absence of oxygen a rotary vane pump was used for making vacuum inside the glass chamber up to a pressure of 1 Pa, afterward, Ar and/or He and/or N_2 gas mixtures with proportions of 100%, 75%, 50% and 25% were introduced at set flow rate. The pressure was always kept at near atmospheric pressure condition by a micro valve connected to a pump. An arc was generated between anode and cathode by a programmable constant power supply, which was set at 40 A for each production run of 5 or 10 min. Precursor consisted of ferrocene (0.5 wt%) dissolved in isooctane. Ferrocene is a solid organometallic compound, which should be dissolved to use in a liquid state. A syringe pump along with an injector regulated the droplets flow of precursor to the plasma

zone (droplet flow rate 1 ml/min). Finally, obtained particles were separated through a magnetic filtration as shown in Figure 2.1-2.

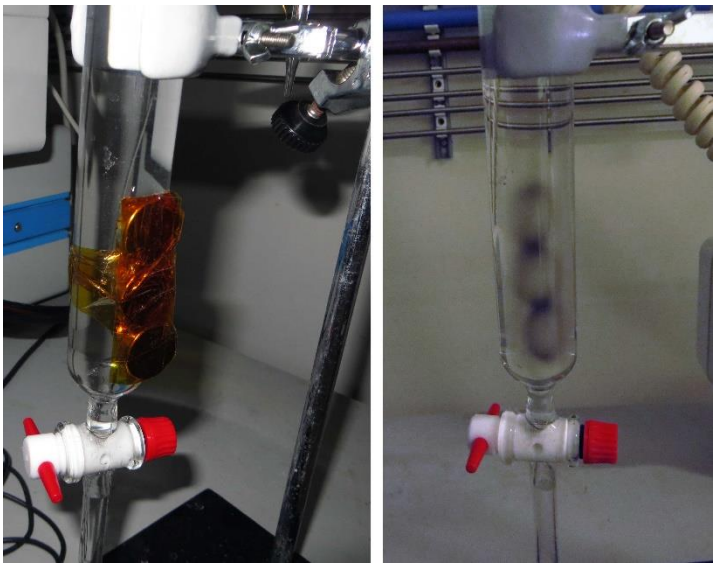

Figure 2.1-2. Magnetic nanoparticles filtered from solution by placing magnets on glass surface.

It should be noted that proper parameters such as current, flow rate, precursor composition were set constant according to the previous published research on this reactor (Aguilo-Aguayo, 2010, Aguilo-Aguayo, 2013, Bertran, 2012). The experimental results and discussion by using liquid phase reactor are explained in results chapter.

Five tips are proposed in appendix A to modify and improve the liquid phase arc discharge equipment.

2.1.2 Gas phase Arc Discharge reactor

The weaknesses of liquid phase reactor design such as air leakage, current discharge, electrodes re-shape and residency time to high temperature during the experiment and particles collection process have been identified. Extensive research and sessions were conducted within FEMAN group to study different aspect and possibilities for designing a new reactor. Eventually, entirely new reactor have been designed and installed. Figure 2.1-3 shows our effort during making the new reactor. New generation reactor not only solved the weaknesses of previous ones, also opens the possibility to

perform synthesis run for hours in order to produce enough amounts of nanoparticles. It should be noted that the increase in production yield is in proportional to amount of precursor usage.

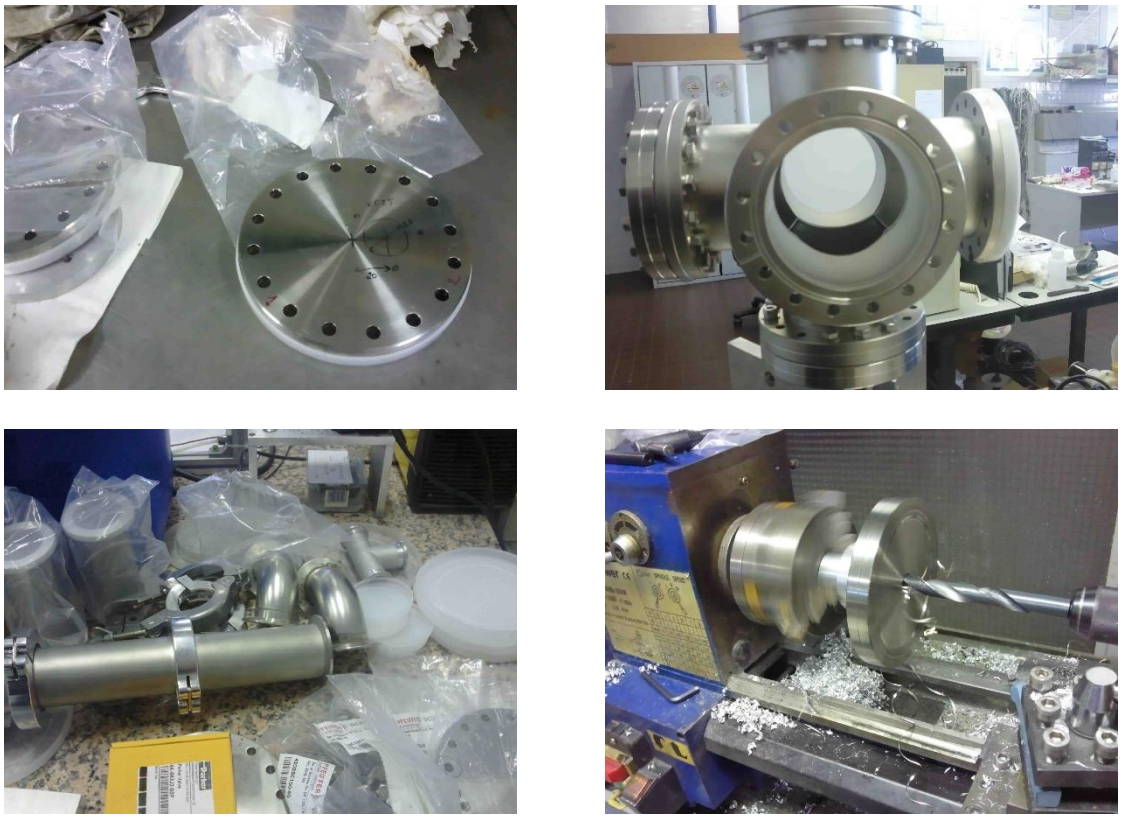

Figure 2.1-3. Images taken during the making new reactor.

New reactor consists of the following major parts:

a) Gas flow controller and distribution

Residence time of gas atoms and precursor radicals staying inside the plasma zone depends on gas flow rate; and influence the morphology of CEINPs; the gas flow effects are discussed in III. Results part, section 3.3 Accordingly, gas flow and its distribution is important therefore two main gas flows are dedicated in the new design; one for delivering the precursor to the plasma zone and the other one to help and maintain the laminar flow.

b) Bubbling system for delivering precursor

Delivering the precursor to the plasma zone in liquid phase caused instability of plasma. Moreover, it was not possible to delivery all the precursor by gravity to the plasma zone; and always some amount of precursor remained inside the glass chamber due to the vacuum system and also the metal needle on top of the plasma. More importantly it was not possible to control the quantity of precursor to the plasma zone precisely; because after a short while of process due to the high temperature the precursor droplets were evaporated before reaching to the plasma zone.

All of these disadvantages were overcome by introducing a new delivery system, which we called it bubbling system. In this new system, a gas flow inside the liquid precursor delivers the micro droplet to the plasma zone. The bubbling system is shown in Figure 2.1-4. In this way, the delivery amount can be regulated by gas flow, evaporation rate of the precursor and temperature. In comparison of liquid phase, the bubbling system minimizes the deformation of carbon electrodes; and there won't be waste of precursor.

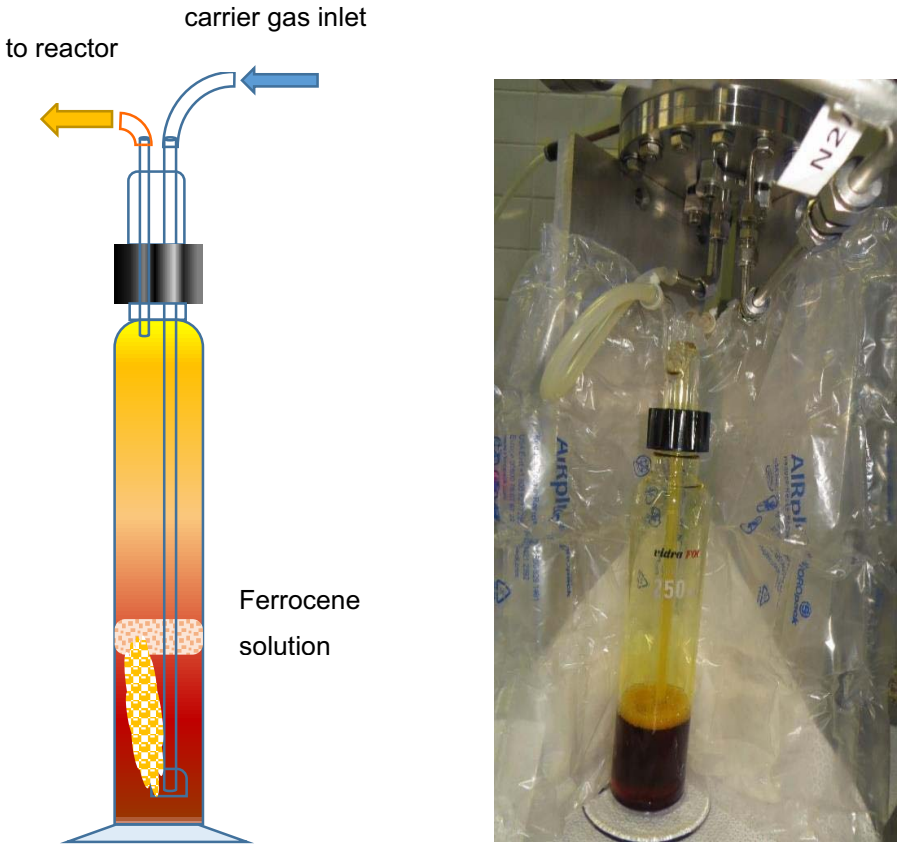

Figure 2.1-4. This is the bubbling system, the gas flow cross the liquid precursor.

c) Programmer power supply

A plasma is achieved by making a gas conduct electricity by providing a potential difference across two electrodes. A programmable power supply can keep the electric current constant while the voltage changes by demand. The electric current regulates the temperature and the plasma size as well. This is important because the arc plasma uses are, vaporizing the material and the formation of carbon particles.

d) Vacuum pump and pressure monitoring sensor

Since one the objective of this research is to avoid iron oxidation; it is important to do the vacuum prior to the synthesis process. In addition, since the pressure affects the

plasma attribute; the new reactor was equipped with a pressure sensor inside the reactor and also two special micro valves for regulating the gas flow and keeping the outlet constant for keeping constant the pressure inside the reactor.

e) Electrodes movement system

The deformation of electrodes has a negative effect on plasma size and stability and also prevent long process duration. One of the parameters that effect the plasma shape is the angel between electrodes and plasma should be generated on top of a ceramic tube, which deliver the precursor by gas flow. The new electrodes are perpendicular to each other precisely. The anode electrode is an arm carbon cylinder, which can be rotated during the process, and the cathode arm is also movable back and forward but without rotation. Figure 2.1-5 show the electrodes after a production process. In this way, the plasma size and stability can be kept for a long time; and allowed us to study other parameters, which affect the growth and formation of carbon material by this arc discharge method.

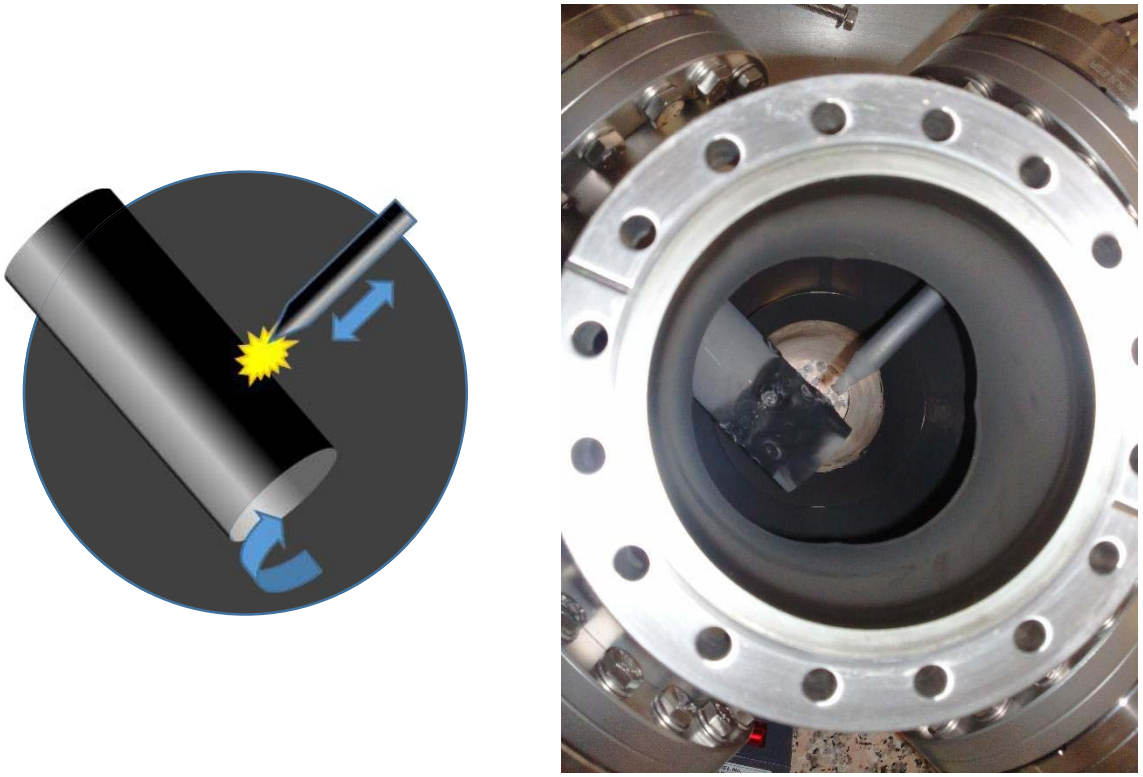

Figure 2.1-5. Moving the carbon electrodes (rotation and back and forward) during the production run helped us to keep stable plasma conditions.

f) Particle collection system

In three main steps we could modify the old particle collection system:

1st Gas phase reactor based on laminar flow and liquid nitrogen,
2nd Gas phase reactor based on turbulent and filter and
3rd Gas phase reactor based on glass beads.

Each of these modifications has particular advantages.

2.1.2.1 Gas phase reactor based on laminar flow and liquid nitrogen

The two path for gas flows allowed us to regulate the flow in order to achieve the laminar flow; therefore after the growth, nanoparticles cross a U shaped tube to reach to a glass cup, which is impressed in liquid nitrogen. Figure 2.1-6 shows the reactor design. Very low temperature of liquid nitrogen helps to trap the nanoparticles inside the glass and do not allowed them to escape to the gas outlet. In this system the gas flow has a practical role in the formation of nanoparticles; for this reason we have chosen effects of gas flow as our objective investigation from this design. Such a design and using liquid nitrogen can extend the production run. In the results chapter influences of different gas flows on formation of CEINPs are explained.

Figure 2.1-6. This is the gas phase reactor based on laminar flow and liquid nitrogen. The collection glass is putted inside a liquid nitrogen box; and so the nanoparticles trapped inside the glass before the gas outlet.

2.1.2.2 Gas phase reactor based on turbulent and filter

In order to collect the nanoparticles more efficient we come up with an idea of making a turbulent flow and a filter for collection. Therefor a special column was designed to produce a turbulence passing through a paper filter. Figure 2.1-7 shows the perforated stainless steel column used for particle collection. In our test we used clean room tissue for test; and nanoparticles were successfully collected. However, particles became trapped inside the filter material and the process of extracting the nanoparticles from the filter showed a low efficiency.

Figure 2.1-7. This stainless steel column was prepared for collecting the particles by making turbulent and capturing them by a paper filter.

2.1.2.3 Gas phase reactor based on glass beads

In order to optimize the collection of nanoparticles collection new process based on glass beads was used. Hundreds of glass beads were placed on a support mesh on top of the plasma zone, just after the growth of the nanoparticles so that, the particles dragged by the gas flow would necessarily pass through pearls. The large surface of the spherical glass beads (5 mm diameter) was sufficient to significantly increase the collection of nanoparticles. Figure 2.1-8 shows the glass beads and the mesh support. After each synthesis run, the glass beads were put inside a sonication bath and therefore nanoparticles were easily dispersed in ethanol from the glass beads surfaces. This approach not only collect the nanoparticles efficiently also minimize possible pollution and impurity. Carbon aerogel, carbon encapsulated iron nanoparticles and carbon nanoparticles carrying fullerene molecules on the surface were obtained by using this reactor design and are explained in the results chapter.

Figure 2.1-8. The 5 mm diameter glass beads plus the support mesh are shown in the two images.

2.2 Chemical vapor deposition method for graphene growth by using CEINPs

Chemical vapor deposition (CVD) in clean room condition and sputtering reactor were utilized for using CEINPs for the graphene growth. The experimental setup details of CVD and sputtering reactor are described in the Víctor Manuel Freire Soler doctorate thesis (Freire Soler, 2014). The CVD parameters were set as: 750^0C and 1020^0C; the growth duration 20 minutes with 40 sccm CH_4 and 10 sccm H_2 at low pressure.

2.3 Characterization tools

Characterization tools accelerated research studies especially in the field of nanotechnology.

SEM and TEM technologies are extensively used in materials science, but despite being well known techniques, we have considered appropriate give a very brief description of them, in particular, a description of the most important features of the specific instruments of the CCiT-UB that we have used in this thesis, highlighting their peculiarities and associated techniques (EDX, SAED, EELS), from the point of view of their usefulness for observing and analyzing the nanoparticles. Also, in order to complete the description of the other advanced tools that have been used to study our samples, we have considered to briefly describe the analysis techniques such as Raman, SQUID and BET.

2.3.1 Scanning Electron Microscopy (SEM)

The wavelength became the limiting factor in light microscopes for this reason electron microscope was developed. Because electrons have much shorter wavelengths, enabling better resolution. Since their development in the early 1950's, scanning electron microscopes have developed new areas of study in the medical and physical science communities (Schweitzer, 2014). The SEM uses a focused beam of high-energy electrons to generate a variety of signals at the surface of solid specimens (Malik and Singh, 2010). Carbon is a good conductive itself and SEM technique illustrate nice images for morphological study. All our samples have been characterized by SEM.

2.3.1.1 SEM principles

Figure 2.3-1 shows the basic components of a SEM and its description is as the following (Hafner, 2007):

A source (electron gun) of the electron beam, which is accelerated down the column;

A series of magnetic lenses (condenser and objective), which act to control the diameter of the beam as well as to focus the beam on the specimen;

A series of apertures (micron-scale holes in metal film), which the beam passes through and which affect properties of that beam; controls for specimen position (x,y,z-height) and orientation (tilt, rotation);

An area of beam/specimen interaction that generates se veral types of signals that can be detected and processed to produce an image or spectra;

And all of the above maintained at high vacuum levels (the value of the upper column being greater than the specimen chamber).

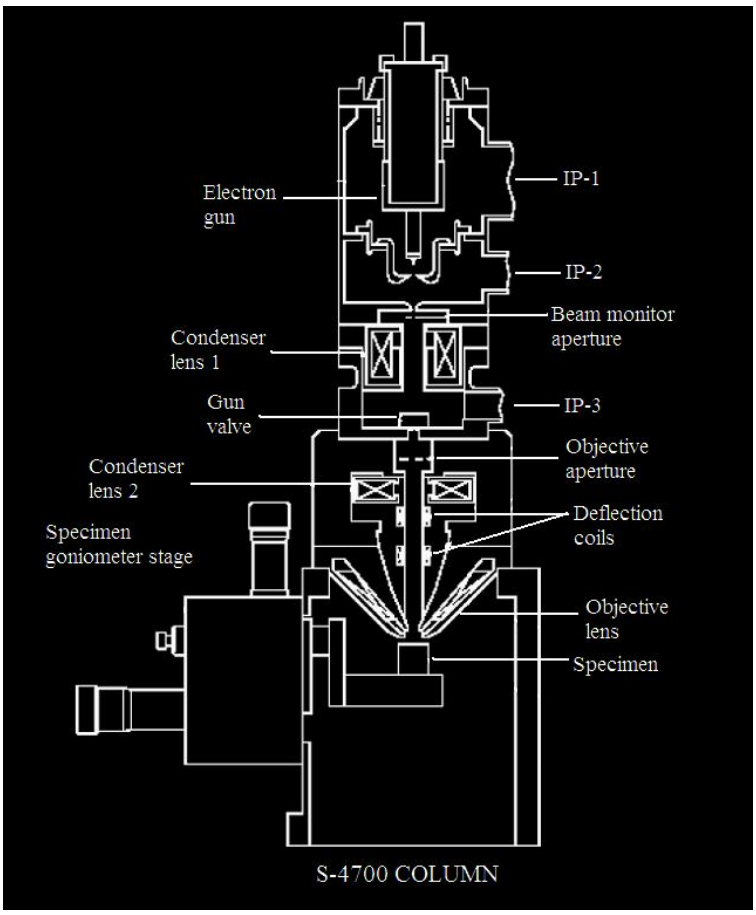

Figure 2.3-1. Basic components of a SEM (Hafner, 2007).

In order to produce images the electron beam is focused into a fine probe in vacuum condition and scan across the surface of the specimen with the help of scanning coils. The incident electron beam loses some energy at each point on the specimen that is

converted into emission of secondary electrons, back-scattered electrons, characteristic X-rays, light and heat and the display maps the varying intensity of any of these signals to generate the image (Weder, 2010).

2.3.1.2 Energy-Dispersive X-Ray Spectroscopy

Energy-Dispersive X-Ray Spectroscopy (EDS) systems are typically integrated into a SEM. EDS systems include a sensitive x-ray detector, a liquid nitrogen for cooling, and software to collect and analyze energy spectra; the detector is mounted in the sample chamber of the main instrument at the end of a long arm, which is itself cooled by liquid nitrogen; the most common detectors are made of Si(Li) crystals that operate at low voltages to improve sensitivity, but recent advances in detector technology make available so-called "silicon drift detectors" that operate at higher count rates without liquid nitrogen cooling (Nazarov, 2011).

An EDS detector contains a crystal that absorbs the energy of incoming x-rays by ionization, yielding free electrons in the crystal that become conductive and produce an electrical charge bias; the X-ray absorption thus converts the energy of individual X-rays into electrical voltages of proportional size; the electrical pulses correspond to the characteristic X-rays of the element (Nazarov, 2011).

By EDS carbon element have been detected for carbon nanoparticles and graphene; however it should be noted that due to the carbon low atomic number the EDS carbon peaks were weak in the case of graphene or in some cases it was not possible to detect correctly.

2.3.2 High-Resolution Transmission Electron Microscopy (HRTEM)

The Transmission Electron Microscopy (TEM) and HRTEM operates on the same basic principles as the light microscope but uses electrons instead of light. TEM and HRTEM images taken by the Jeol JEM 2100 and the Hitachi MT800 (equipped with Bruker XFlash detector 4010) of the CCiT-UB were used for the analysis of our samples extensively. TEM provide us information regarding carbon and metal

structures; more importantly fullerene molecules have been detected by HRTEM. In addition, nanoparticles statistical information of size distribution relies on TEM and HRTEM images for both metal and carbon species.

2.3.2.1 TEM principles

In transmission electron microscope (TEM), the source of illumination is a beam of electrons of very short wavelength, emitted from a tungsten filament at the top of a cylindrical column of about 2 m high (Williams and Carter, 2009). The electron column shown in Figure 2.3-2 consists of an electron gun and set of 5 or more electromagnetic lenses operating in vacuum. The three main components of TEM are: the illumination system, the objective lens/stage, and the imaging system.

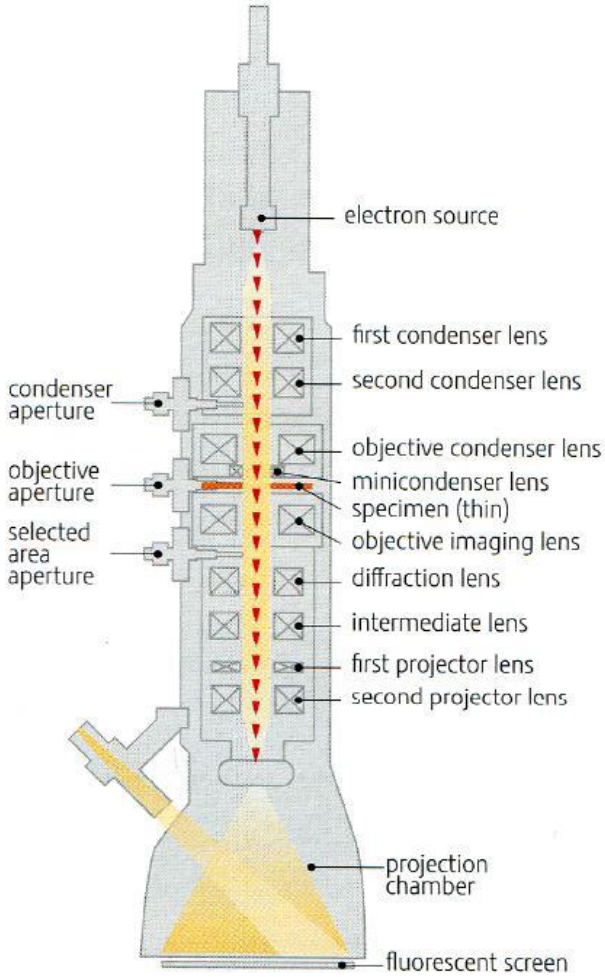

Figure 2.3-2. Illustration of the main parts of a typical TEM (Williams and Carter, 2009).

The illumination system comprises the gun and the condenser lenses and it takes the electrons from the source and transfer them to the specimen. The electron beam is accelerated to an energy in the range 20 - 1000 keV in the electron gun and then the electron beam passes through a set of condenser lenses in order to produce a beam of electrons with ~~a~~ desired diameter (Williams and Carter, 2009). The illumination system can be operated in two principal modes: parallel beam and convergent beam. The first mode is used primarily for TEM imaging and selected area diffraction, while the second is used mainly for scanning imaging, analysis via X-ray and electron spectrometry, and convergent beam electron diffraction.

The objective lens and the specimen holder/stage system is the heart of the TEM (Williams and Carter, 1949). Here is where all of the beam-specimen interactions take place and the two fundamental TEM operations occur, namely, the creation of the various images and diffraction patterns (DP) that are subsequently magnified for viewing and recording (Williams and Carter, 1949).

The imaging system uses several lenses to magnify the image or the DP produced by the objective lens and to focus these on the viewing screen or computer display via a detector, charge-coupled device, or TV camera (Williams and Carter, 1949).

2.3.3 Electron energy loss spectroscopy (EELS)

Electron energy-loss spectroscopy (EELS) is an analytical technique that measures the change in kinetic energy of electrons after they have interacted with a specimen (Egerton, 2009). In this research we have used TEM Jeol model JEM 2010F (equipped with GIF spectrometer) of the CCiT-UB. The reason behind using EELS technique is investigating about the existence of metal oxide in carbon material.

2.3.3.1 EELS principles

Inelastic scattering of electrons or Electron Energy Loss Spectroscopy (EELS) is the most versatile technique for the investigation of vibrational modes on surfaces in vacuum (Ibach, 2006b). The following descriptions are derived from the book entitled:

“Physics of Surfaces and Interfaces” (Ibach, 2006a). The energy resolution of present-day spectrometers is as high as 1 meV; all vibration modes from the low frequency vibrations of physical adsorption rare-gas atoms to the internal vibrations of molecules are accessible in a single scan; furthermore, one can probe phonons in the entire Brillouin zone; by varying the electron energy, different scattering mechanisms can be employed, leading to different selection rules for the inelastic scattering.

The width of the energy distribution of electrons from thermal, field emission or photoemission cathodes is at least 200 meV. Energy selectors are required to make electrons useful for inelastic scattering from phonons. A second energy selector is required for the analysis of the scattered electrons.

The combined resolution of the electron monochromator and analyzer must be in the low meV range. Electrostatic deflector type selectors, as opposed to magnetic deflectors are used exclusively, because of the difficulty to shield magnetic fields effectively. Figure 2.3-3 displays a typical experimental set-up of an electron spectrometer. An electron spectrometer comprises the electron emission system, two monochromators, lenses to image the exit slit of the monochromator onto the sample and further onto the analyzer entrance slit, two analyzers and a channeltron electron multiplier. In the interest of an optimum intensity of the signal, perfect as possible images of each aperture onto the next one are required. Just as in light optics, the phase space is conserved in the process of imaging. Figure 2.3-4 shows the processes occurring in the sample during an EELS experiment.

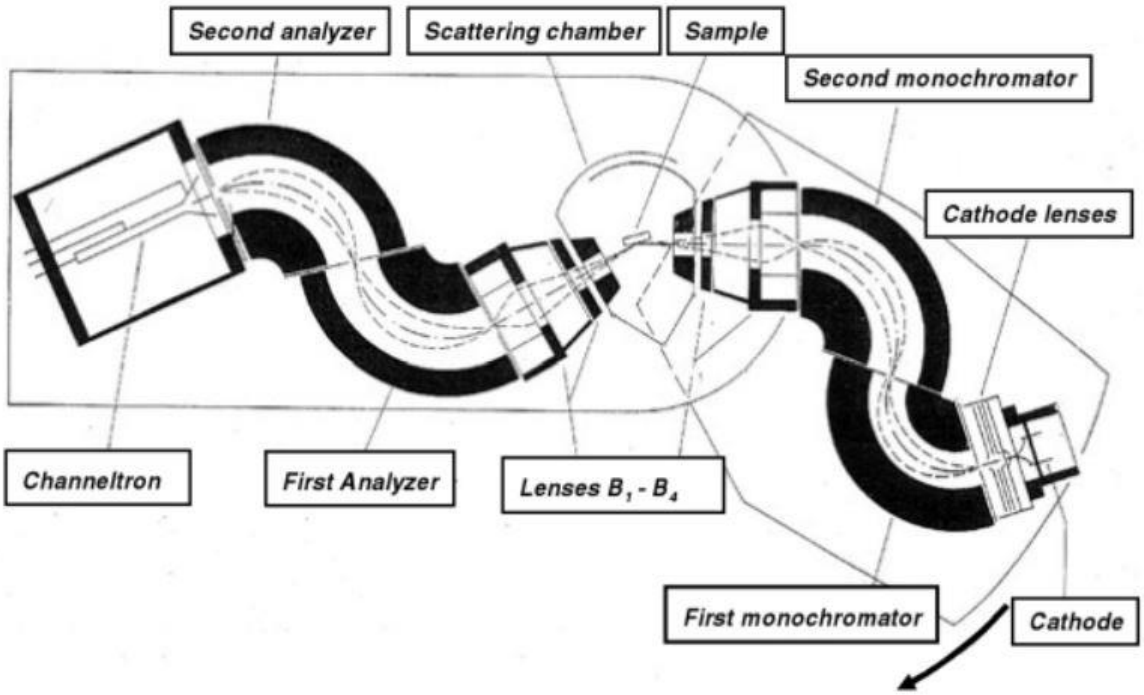

Figure 2.3-3. Electron spectrometer for inelastic scattering of electrons from surfaces.

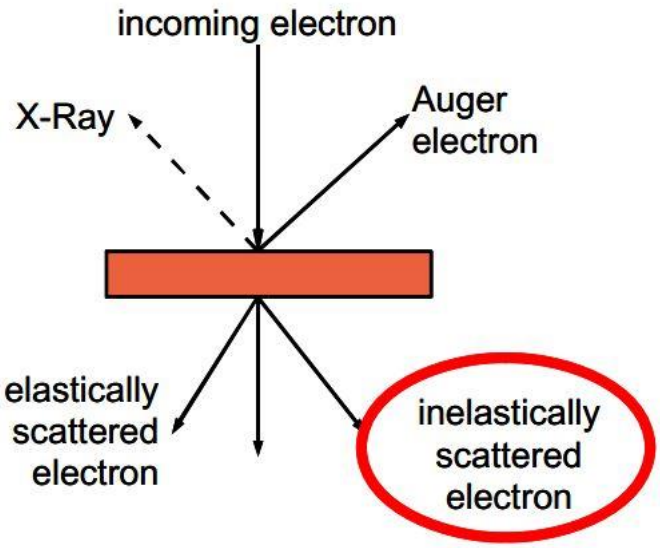

Figure 2.3-4. This figure summarizes all processes that happen in the sample during an EELS experiment (Jorissen, 2007).

2.3.4 Selected Area Electron Diffraction (SAED)

In 1976, Dorset and Hauptmann in Buffalo for the first time applied the direct methods to electron diffraction data. Selected area (electron) diffraction, is a crystallographic experimental technique that can be performed inside a TEM (Weirich, 2006). In this study, the SAED technique were used for identification of crystallography planes of carbon and metal.

2.3.4.1 SAED principles

Electron diffraction is an important tool for obtaining quantitative structural and crystallographic information about crystalline materials. The SAED advantage comparing to other methods is that it is possible to localized nanoparticles to determine their structure. However, the aperture is not as small as an individual nanoparticles. Electron beam acts as monochromatic electron wave, and the atoms in a crystal will act as scattering centers. Afterward, it will create a new wavelet that interferes with one another. The propagating electron wave through a crystal will be a diffraction pattern.

2.3.5 Energy Dispersive X-ray Microanalysis (EDX)

Energy-dispersive X-ray spectroscopy (EDS, EDX, or XEDS), sometimes called energy dispersive X-ray analysis (EDXA) or energy dispersive X-ray microanalysis (EDXMA), is an analytical technique used for the elemental analysis or chemical characterization of a sample (Nuruddin, 2010). It relies on an interaction of some source of X-ray excitation and a sample. Its characterization capabilities are due in large part to the fundamental principle that each element has a unique atomic structure allowing unique set of peaks on its X-ray emission spectrum (Montazer and Pakdel, 2010). The chemical mapping and elemental analysis of our samples have been obtained by using EDX equipped with TEM Jeol JEM 2100 of the CCiT-UB.

2.3.5.1 EDX principles

EDX makes use of the X-ray spectrum emitted by a solid sample bombarded with a focused beam of electrons to obtain a localized chemical analysis (Janaun, 2013). All elements from atomic number 4 (Be) to 92 (U) can be detected in principle, though not all instruments are equipped for 'light' elements (Z < 10) (Reed, 1995). Qualitative analysis involves the identification of the lines in the spectrum and is fairly straightforward owing to the simplicity of X-ray spectra; quantitative analysis (determination of the concentrations of the elements present) entails measuring line intensities for each element in the sample and for the same elements in calibration Standards of known composition (Reed, 1995).

By scanning the beam in a television-like and displaying the intensity of a selected X-ray line, element distribution images or 'maps' can be produced (Shaban, 2013). Also, images produced by electrons collected from the sample reveal surface topography or mean atomic number differences according to the mode selected (Wong, 2013). The scanning electron microscope produce electron images but can also be used for element mapping, and even point analysis, if an X-ray spectrometer is added.

2.3.6 Raman spectroscopy

Raman spectroscopy is a spectroscopic technique based on inelastic scattering of monochromatic light, usually from a laser source (Majumdar, 2012). Inelastic scattering means that the frequency of photons in monochromatic light changes upon interaction with a sample (Abdallah and Yang, 2012). In this study the Horiba Raman spectroscopy equipped with laser detector synapse CCD of the CCiT-UB was used for characterization. Raman provides details information regarding the carbon order disorder structure. For the carbon nanoparticles the so called D and G peaks allowed us to calculate carbon crystallinity degree; moreover the existence of mono and or multi-layer of graphene were confirmed from the 2D band in Raman spectra.

2.3.6.1 Raman principles

Photons of the laser light are absorbed by the sample and then reemitted. Frequency of the reemitted photons is shifted up or down in comparison with original monochromatic frequency, which is called the Raman effect and this shift provides information about vibrational, rotational and other low frequency transitions in molecules (Lukaszkowicz, 2011). Raman spectroscopy can be used to study solid, liquid and gaseous samples.

A Raman system typically consists of four major components (Sureshkannan, 2013):

1. Excitation source (Laser).
2. Sample illumination system and light collection optics.
3. Wavelength selector (Filter or Spectrophotometer).
4. Detector (Photodiode array, CCD or PMT).

A sample is normally illuminated with a laser beam in the ultraviolet, visible or near infrared range and scattered light is collected with a lens and is sent through interference filter or spectrophotometer to obtain Raman spectrum of a sample (Salkic, 2012).

2.3.7 Superconducting-quantum-interference-device (SQUID)

A SQUID is a very sensitive magnetometer used to measure extremely subtle magnetic fields, based on superconducting loops containing Josephson junctions (Piróth and Sólyom, 2008). Studies of nanoparticles magnetic properties have been done by employing a SQUID. Nanoparticles superparamagnetic behavior, saturation magnetization parameters and blocking temperature are important analysis information's derived from SQUID measurements.

2.3.7.1 SQUID principles

SQUIDs are sensitive enough to measure fields as low as 5 aT (5×10^{-18} T) within a few days of averaged measurements with a noise levels of 3 fT $Hz^{½}$ (Drung, 2007).

There are two main types of SQUID considering the number of weak links (Josephson junction) in the SQUID ring: direct current (DC) and radio frequency (RF), as is shown in Figure 2.3-5; DC SQUIDs work with two Josephson junction, which is more stable and sensitive, while RF SQUIDs can work with only one Josephson junction, which might make them cheaper to produce, but are less sensitive (Qi, 2011).

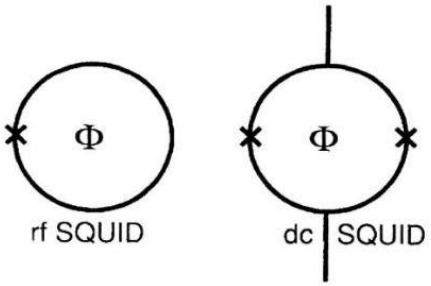

Figure 2.3-5. Schematic illustration of an rf and dc SQUID, The Josephson junctions are indicated by crosses. The magnetic flux Φ threads the superconducting loop of the SQUID, changing the impedance around (rf SQUID) or across (dc SQUID) the loop (Hämäläinen, 1993, Qi, 2011).

A SQUID uses the properties of electron-pair wave coherence and Josephson junctions to detect very small magnetic fields and it is considered as one of the most senstivie magnetometer, and used to characterize extremely weak magnetic signal, such as 10^{-6} and 10^{-5} emu (Zhu, 2008).

The sample magnetic signal is obtained via a superconducting pick-up coil. the flux transformer scheme uses a pickup loop as an antenna and a coupling coil on top of the SQUID that together form a superconducting closed circuit; when a magnetic field is coupled to the pick-up loop, flux quantization requires that the total flux in the transformer remains constant, as a result a presistent supercurrent is generated, producing a flux via the input coil in the SQUID (Seeber, 1998).

2.3.8 Surface analysis by Brunauer–Emmett–Teller

Brunauer–Emmett–Teller (BET) theory aims to explain the physical adsorption of gas molecules on a solid surface and serves as the basis for an important analysis technique for the measurement of the specific surface area of a material (Chen, 2012a). Porous material can be differentiated on the basis of pore dimensions. BET surface analysis is a useful tool to have information on pore structures of materials. The synthesis of spherical porous carbon microparticles are described in section 3.5. Surface area measurements are typically based on N_2 absorption at 77 K. BET model is preferable and reliable than Langmuir model to interpret the data. Because the assumption for Langmuir model is adsorbates pack in a monolayer, but the BET model accommodates multilayers (Koh, 2009). According to SEM images, obtained porous material have large enough pores to allow more than one adsorbed layer and the Langmuir surface area leads to overestimation. Thus BET surface area calculation have been considered.

Applications:

-Powder industry
-Adsorbent (zeolite, molecular sieve, activated carbon, silica gel, activated alumina, etc.);
-Catalyst (platinum, palladium and other metal catalysts);
-Ceramic materials (alumina, zirconia, silicon nitride, silicon carbide, quartz, etc.);
-Battery materials (lithium manganese oxide, graphite, polymer battery materials and alkaline materials);
-Magnetic powder materials (iron oxide, ferrite, etc.);
-Nano-powder materials (ceramic materials, metal materials, silver, iron, copper, tungsten powder, nickel powder and metal powder);
-Environmental Sciences (sediment, suspended solids, etc.);
-Others (such as ultra-fine fibers, porous fabric, polymer composites, etc.).

2.3.8.1 BET principle

Adsorption is defined as the adhesion of atoms or molecules of gas to a surface. In BET surface area analysis, nitrogen is usually used due to its high purity and strong interaction with most solids. The sample surface is cooled by using liquid N_2 to obtain detectable amounts of adsorption. Known amounts of nitrogen gas are then released stepwise into the sample cell. Relative pressures less than atmospheric pressure is achieved by creating conditions of partial vacuum. After the saturation pressure, no more adsorption occurs regardless of any further increase in pressure. Pressure transducers monitor the pressure changes due to the adsorption process. After the adsorption layers are formed, the sample is removed from the nitrogen atmosphere and heated to cause the adsorbed nitrogen to be released from the material and quantified. The data collected is displayed in the form of a BET isotherm, which plots the amount of gas adsorbed as a function of the relative pressure (Hwang and Barron, 2011).

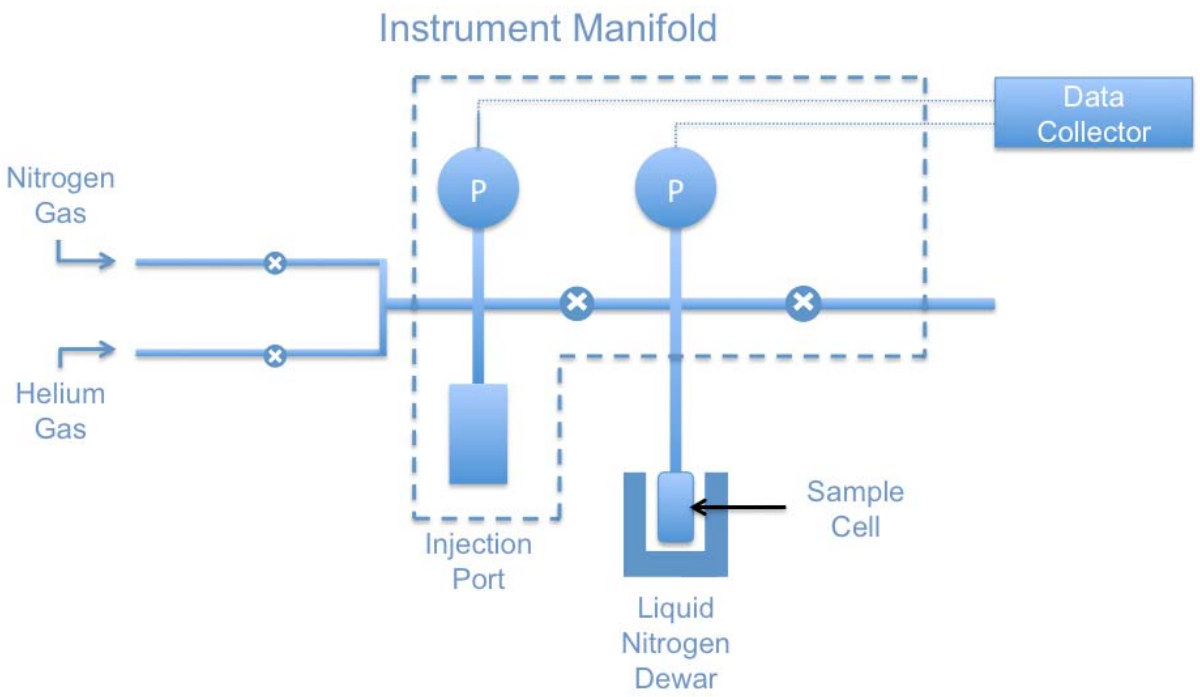

Figure 2.3-6. Schematic representation of the BET instrument. The degasser is not shown (Hwang and Barron, 2011).

III. Results

This chapter consists of six main sections. The first and two sections are the results obtained from liquid phase arc discharge reactor. Third, fourth and fifth sections are the results obtained from gas phase arc discharge reactor. The last section is illustration regarding potential applications of carbon-based nanoparticles.

3.1 Precise control over superparamagnetic iron core and carbon shell nanostructure

The study was initiated by synthesis of carbon coated iron nanoparticles by a liquid phase arc discharge reactor. The details of liquid phase arc discharge reactor is described in Arc Discharge experimental set-up (chapter 2.1). The effects of arc current, helium flow and ferrocene content have been studied by previous researchers in FEMAN group. They successfully obtained superparamagnetic nanoparticle and with relatively narrow size distribution. However, size controlling of carbon and iron remained a challenge and therefore considered as the objective of further research. In the following section an approach for controlling carbon encapsulated iron nanoparticle is presented.

Precise control over carbon nanostructure and magnetic nanoparticles in the form of core@shell structure are still challenging and important. Here we utilized the liquid phase arc discharge plasma reactor for synthesis and controlling the size of carbon encapsulated iron nanoparticles (CEINPs) at near-atmospheric pressure. The morphology and structural features of the iron/carbon were investigated using transmission electron microscopy (TEM) and high-resolution TEM. All the particles show a superparamagnetic behavior as determined by superconducting quantum interference device measurements. In order to evaluate the carbon shell protection and ensure the absence of iron oxide, selected area electron diffraction technique, energy-dispersive X-ray spectroscopy and electron energy loss spectroscopy were employed. Moreover, the degree of carbon order-disorder was studied by Raman spectroscopy. It is concluded that by changing gas composition of the arc discharge reactor used in the research project, morphological properties of CEINPs can be precisely controlled according to the application requirements.

The interest in magnetic nanoparticles (MNPs) has been stimulated by the properties and potential applications of these unique nanoparticles. MNPs comprise an important class of nanobiomaterials supporting various functional possibilities, such as agents for applications in imaging, cell labeling, drug delivery, gene delivery, hyperthermia (Xie, 2011), tissue engineering (Ishii, 2011) and DNA detection (Kerman,

2004). Moreover, MNPs exhibit great potential for applications including data storage (Reiss and Hütten, 2005), spintronics devices (Singamaneni, 2011) and water purification (Lin, 2008, Mayo, 2007). Many experimental and theoretical studies have been done to provide an understanding of synthesis mechanism. These studies investigate how parameters of the process influence nanoparticles properties such as shape, core and shell size distributions, magnetic properties, crystallinity and stability.

The stability is one of the main requirements for almost any application of MNPs. In our research, pure iron metal is the magnetic core of the produced particles. The instability, large aggregation, and rapid bio-degradation of the pure uncoated (naked) magnetic nanoparticles could be overcome by replacement of the naked magnetic nanoparticles by the encapsulated ones, since the intrinsic properties of the inner magnetic cores in this case are well protected by outer carbon shells (Galakhov, 2011). Coating metallic cores by silica (De Matteis, 2014, Roca, 2012), carbon (Luo, 2010, M. Reza Sanaee, 2013a, M. Reza. Sanaee, 2014) and precious-metal (Schärtl, 2010) are examples of popular inorganic coating approaches. Although to date most studies have been focused on the development of polymer or silica protective coatings, recently carbon-coated magnetic nanoparticles are receiving more attention, because carbon-based materials have many advantages over polymer or silica, such as high chemical and thermal stability, better conductivity, as well as biocompatibility of carbon-based materials (Wu, 2011b, Lu, 2007). It is noteworthy that in many cases the protecting shells not only stabilize the nanoparticles, but can also be used for further functionalization, for instance, with other nanoparticles or various ligands, depending on the desired application (Bakthavathsalam, 2013).

So far, several smart strategies have been employed to prepare carbon encapsulated iron, nickel, cobalt and magnetic oxides nanoparticles including hydrothermal reaction (Zhang, 2010), chemical vapor deposition (Cao, 2008), detonation synthesis (Lu, 2005), chemical vapor condensation (Wang, 2003), electron beam irradiation (Nishijo, 2005), laser ablation (Park, 2008) arc discharge (Aguilo-Aguayo, 2010, M. Reza. Sanaee, 2013) and co-carbonization (Huo, 2004). In contrast, each one of these synthesis methods has particular advantages according to their applications and uses. Herein, some of their importance and properties are

highlighted. Recently, in an important research report, Luo clearly suggest that their detonation synthesis route is capable of producing a variety of nanocrystalline particles, such as Fe-based oxides, graphite coated Fe, Fe-based carbides and their mixtures (Luo, 2012). According to their analysis, graphite coated Fe particles have a broad range from 8 to 40 nm in diameter and, therefore control over size distribution still remains a challenge (Luo, 2012). An excellent work has been done by El-Gendy which obtained carbon coated iron nanoparticles with core average size 16 nm by chemical vapor deposition method (El-Gendy, 2009). According to the given magnetic analysis, the particles show a blocking temperature above 400 K and hence superparamagnetic behavior is only evidenced and applicable above room and body temperature (El-Gendy, 2009). The combustion synthesis (autothermal process) has inherent advantages, including the use of low cost materials and the simplicity of the production protocol (Bystrzejewski, 2007) however, this method seems to not be suitable for encapsulating metallic nanoparticles by carbon. Borysiuk produced and compared carbon encapsulated iron nanoparticles (CEINPs) by using both, arc plasma and combustion synthesis methods. According to their experiments, the combustion sample has much higher content of carbon, indicating that the Fe particles were not totally covered by graphite layer and were dissolved in the etching process. In contrast, the Fe-containing particles are much more abundant in arc-plasma samples and they are covered by thicker graphite layers, effectively protecting them during etching process (Borysiuk, 2008). A hydrothermal process has been reported by Wang (Wang, 2006). They found that only Fe nanoparticles did not favor the formation of CEINPs due to the oxidation of Fe nanoparticle by H_2O during the reaction. Common challenges for synthesis of CEINPs are improving uniformity, enhancing coating protection and controlling particles compositions, shape and core/shell sizes. In addition, due to the lack of comprehensive understanding of the optimal parameters and formation mechanism most of the current fabrication process are empirical, which means a large number of experimental trials are required to optimize any given process. Arc discharge method is simple, cost effective rapid technique that can easily be carried out. However, maintaining and/or increasing quality in parallel with quantity of nanoparticles needs to be improved by arc discharge method. In addition, plasma instability, high temperature and chemical pollution during

the process are drawback examples of the arc discharge technique. A proper control of the synthesis parameters is essential and depends directly on the reactor design.

In present study, a modified arc-discharge reactor has been employed and designed in a way to minimize drawbacks. Our interest has been focused in the synthesis of carbon encapsulated iron nanoparticles with a precise control of particle size by using this method. Depending on the arc discharge reactor design, several parameters can effects morphological properties such as gas type, applied current, precursor material, cathode and anode material, pressure and temperature. In this study, as a new size control feature, different mixtures of argon and helium were used to form arc plasma. This control is an important issue for a vast range of applications from nano-scale electronic devices (Thomas and Swathi, 2012) to biomedical applications such as, drug delivery, hyperthermia and MRI imaging (Oh, 2010, Shang, 2014, Veiseh, 2010, Zhang, 2013b, M. Reza Sanaee, 2013b).

3.1.1 Method

Carbon encapsulated iron nanoparticle were synthetized by a liquid phase modified arc discharge apparatus (Sanaee and Bertran, 2015, Aguilo-Aguayo, 2013). The procedures are explained in section 2.1.1. Ar and/or He gas mixtures ([Ar]/[Ar + He] of 1, 0.75, 0.50 and 0.25) were introduced at set flow rate. Based on the utilized gas percentage, the CEINPs samples are named as presented in Table 3.1-1.

Table 3.1-1. Argon (Ar) and Helium (He) percentage that were used for synthesis process are presented along with the assigned CEINPs names.

Gas%	100% Ar	75% Ar + 25% He	50% Ar + 50% He	25% Ar + 75% He	0% Ar + 100% He
CEINPs Name	Ar100	Ar75	Ar50	Ar25	Ar0

CEINPs morphologies have been characterized by Jeol JEM 2100, Jeol JEM 2010F (equipped with GIF spectrometer) and Hitachi MT800 (equipped with Bruker

XFlash detector 4010) for high-resolution transmission electron microscopy (HTEM) and transmission electron microscope (TEM) images, electron energy-loss spectroscopy (EELS) and energy dispersive X-ray analysis (EDX). The magnetic properties of the CEINPs have been investigated by a superconducting quantum interference device (SQUID). The degree of carbon shell order-disorder was studied by Horiba Raman spectroscopy equipped with laser detector synapse CCD.

3.1.2 Results and discussion

Results are given of CEINPs synthesized in pure argon, pure helium and in several mixtures of these gases. The morphology of the synthesized particles was studied by TEM and HRTEM. The particles core sizes and average diameters were determined from the data obtained by TEM micrographs. Figure 3.1-1 shows representative the results of the TEM analysis. The HRTEM image in Figure 3.1-2 clarifies a clear core@shell structure and sharp interface between them and carbon shell hermetically closed to the iron core. It was observed that the structures of Fe@C are predominately spherical in all samples.

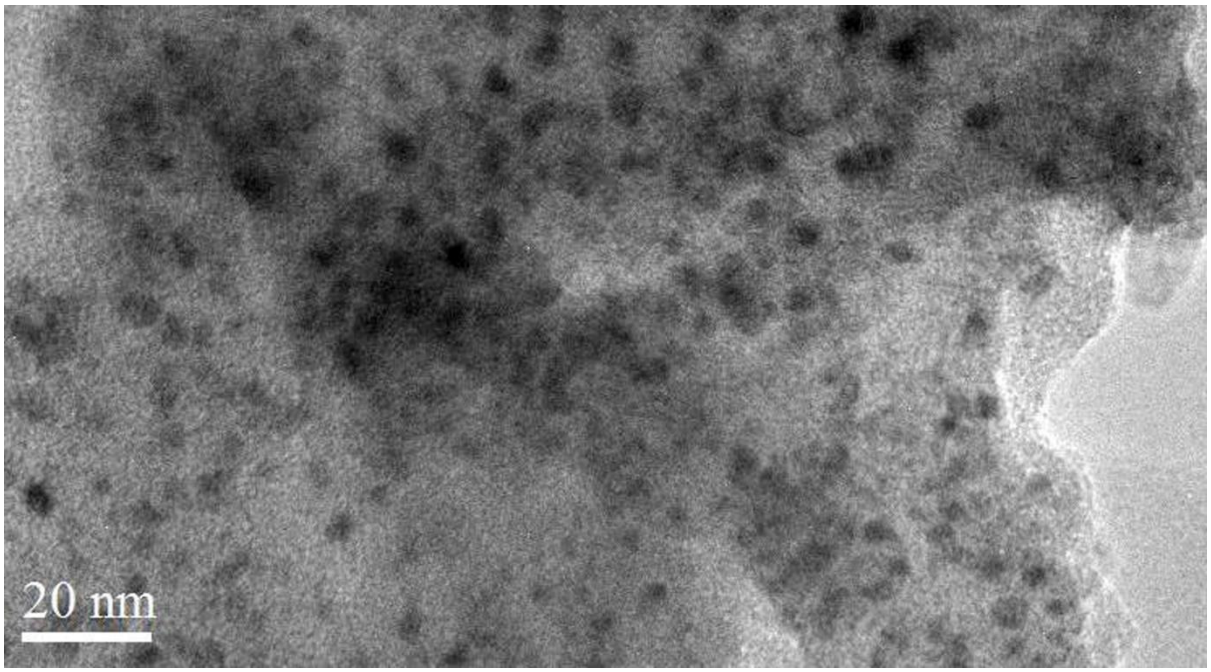

Figure 3.1-1. TEM image of CEINPs, the iron cores are visible in black spots.

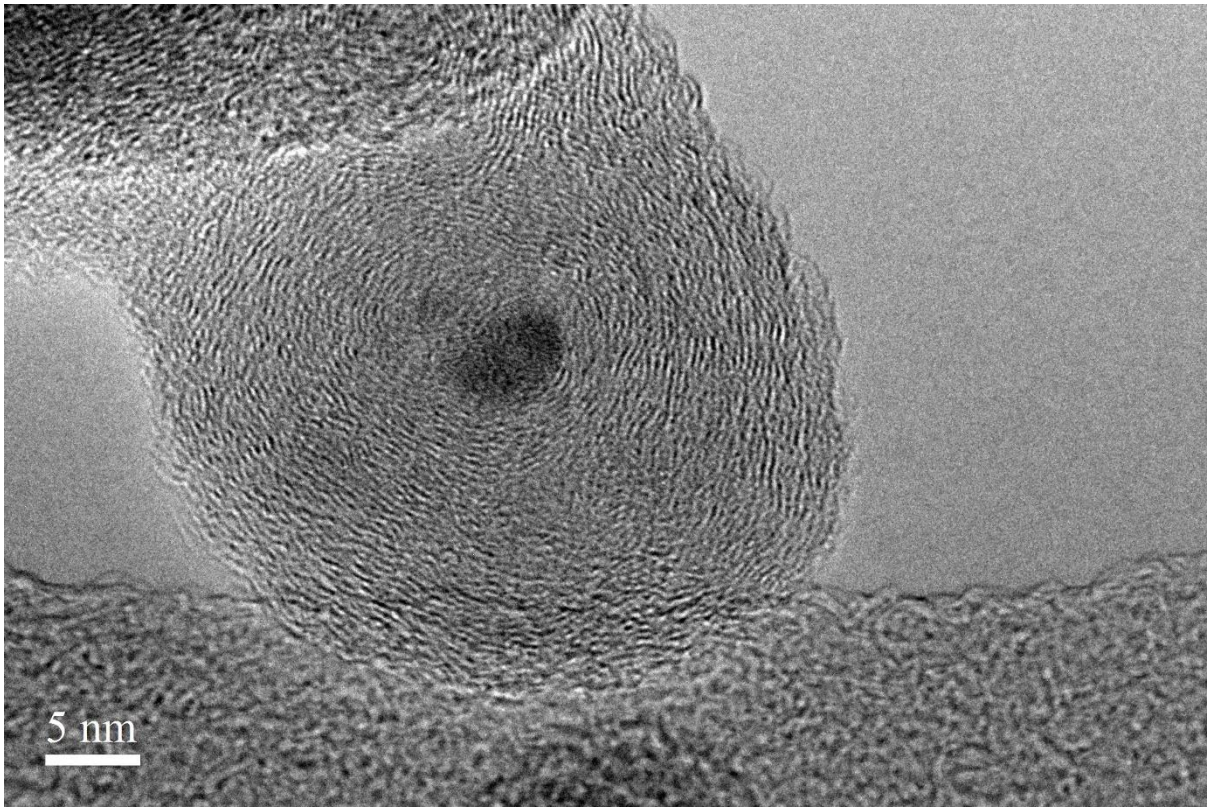

Figure 3.1-2. HRTEM image from a single iron core at carbon shell nanostructure.

Size distribution histograms of all samples are presented in Figure 3.1-3. A comparison between size distributions exhibits more particles monodispersion (Fe core size: 3.4 ± 0.7 nm) when 100% of argon is used Figure 3.1-3 (e). This result enhances the use of argon over helium in large scale production not only because of the monodispersion of obtained particles but also because of abundantly and cost reason.

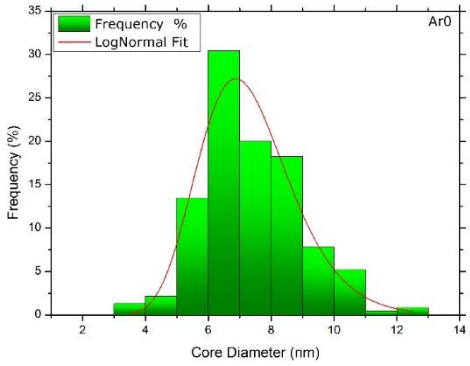

(a)

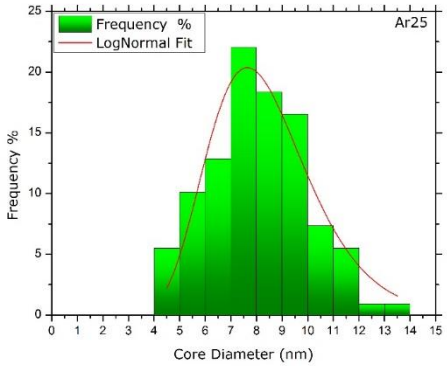

(b)

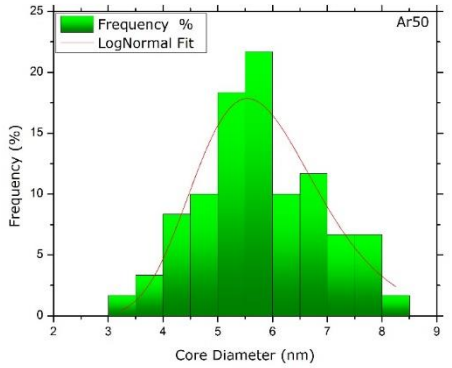

(c)

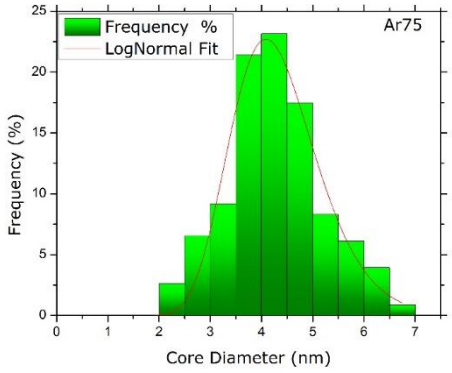

(d)

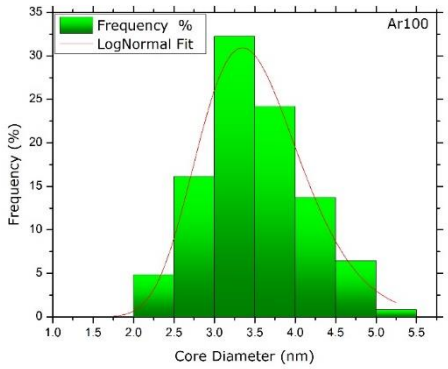

(e)

Figure 3.1-3. (a), (b), (c), (d) and (e) Iron core size distribution histogram of Ar0, Ar25, Ar50, Ar75 and Ar100 are presented; (e) comparatively best iron core size distribution obtained when pure argon is used.

HRTEM images of each synthesized CEINPs samples are presented in Figure 3.1-4. HRTEM analysis demonstrates the effect Ar/He gas ratio on CEINPs in both sizes of carbon shell and iron core. It is evident that the particle diameters are increasing as the percentage of argon increases. On the other hand, the core diameters are decreasing as the argon content increases. Increase in carbon shell thickness limits the distance between iron cores and avoid the magnetic interaction between them. In addition, a thicker carbon shell provides more protection for iron core from oxidation and made nanoparticles suitable candidates for aqueous environment. The nature of inert gas appears to be a sensitive parameter to control CEINPs diameter.

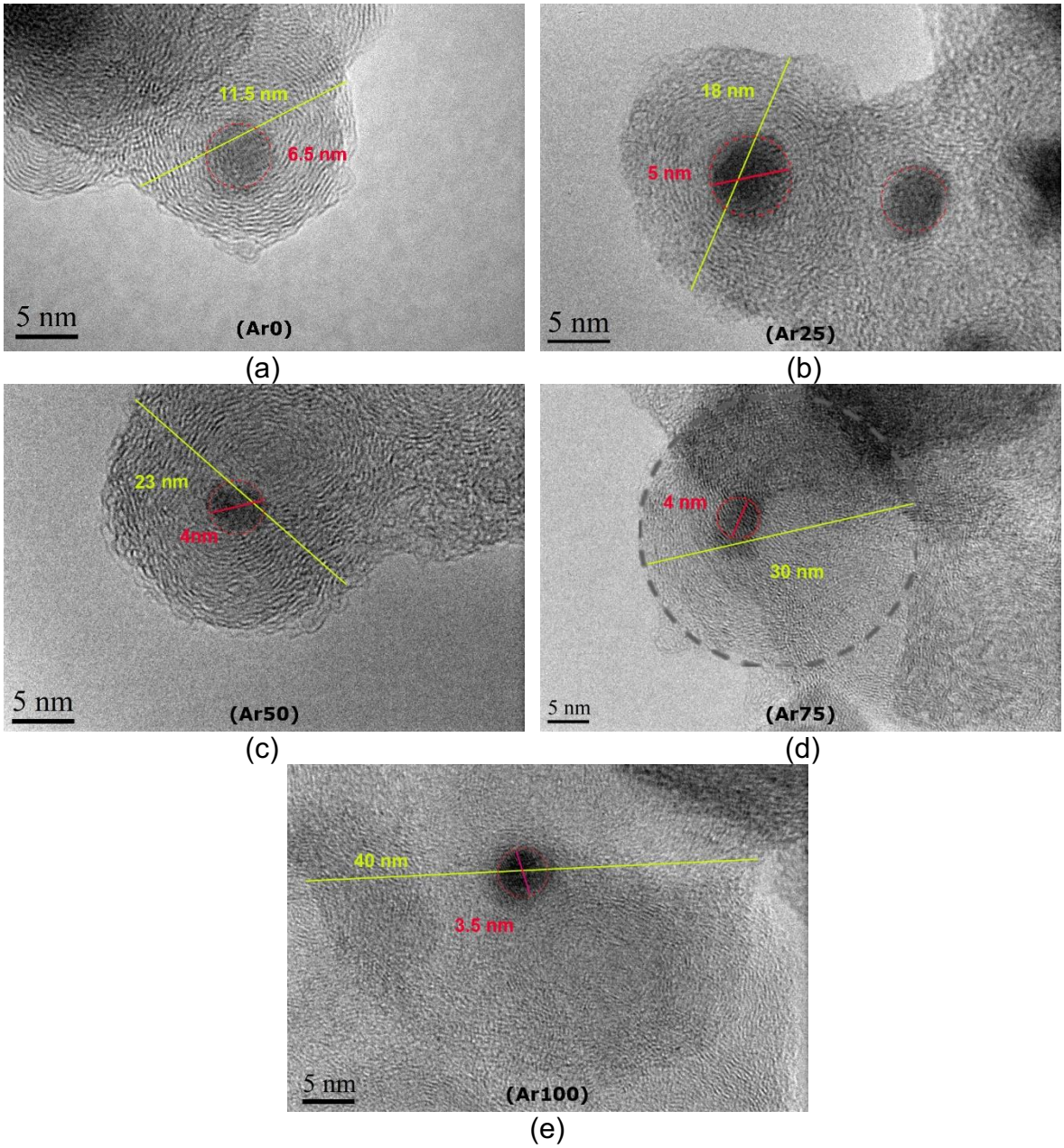

Figure 3.1-4. The size variations of CEINPs components are evident in HRTEM images. (a) 100% helium is used to synthesize Ar0 sample, by adding and increasing 25% argon, the carbon shell formed larger and iron core formed smaller as can be observed in (b) image, same trend are shown in (c), (d) and (e) images, respectively.

The synthesis of nanoparticles by thermal plasmas is an intricate heat and mass transfer process that involves a phase conversion in a few tens of milliseconds, as well as interactions between the thermofluid field, the induced electromagnetic field and the particle concentration field, all of which are described by numerous variables; Despite the strong industrial and scientific interest in the topic, the growth mechanism of the nanoparticles remains poorly understood (Shigeta and Murphy, 2011). In our

study, basic parameters are kept constant and only effects of the gas mixtures are studied to describe the growth mechanism from this perspective.

Four major phases are considered to describe the formation of CEINPs: evaporation, expansion, growth of iron core and carbon shell. The processes start with vaporization of precursor. The precursor is in form of a droplet, which crosses high enthalpy plasma spot and its surface starts evaporating. The plasma temperature decrease dramatically, this quenching causes the vapor to be highly supersaturated. Although inert gas does not undergo chemical reactions but it affects the plasma formation and consequently changes temperature gradient of plasma. Cracking of molecules occurred in expansion phase and carbon, iron and hydrogen are available. Haines and co-workers concluded that the sublimation rate of graphite rods under static argon is about two times higher than static helium (Haines and Tsai, 2002). Accordingly, higher argon concentration caused more availability of carbon species for larger carbon shell formation. Supersaturated vapor resulted in rapid production of nanoparticles. It seems that vapor pressure increases along with the plasma temperature, in our case that the plasma has been generated by argon and helium and their mixtures. Critical radius of carbon limits the iron core size, therefore as the carbon shell appears larger then iron core appears smaller. Thermal conductivity of argon is about eight times smaller than helium (Farhat, 2001). Varying the argon-helium gas ratio alters the heat transfer from central of the plasma to outside, and then, when argon concentration increases then temperature gradient increases or in other word cooling rate decreases. Accordingly, the critical radius of carbon shell and iron core change with gas ratio. Nanoparticle growth occurs in gas phase (Majetich, 1994) and lower thermal conductivity of argon prolong the formation time. Consequently, the carbon and iron dimensions change.

Naked metallic nanoparticles are highly chemical active and easy to be oxidized in air, which results in poor magnetism and dispersibility (Peng, 2011). One of the advantages of arc discharge technique is its capability to produce protected metallic nanoparticles simultaneously (at the same process). Carbon-coated nanoparticles are usually in the metallic state, and compared to the corresponding oxides, they have a higher magnetic moment (Chen, 2012b). Moreover, if there has been an incomplete

protection, the cores of such particles become oxidized, particles cannot be functionalized properly and their efficiency will be low. Primarily, selected area electron diffraction (SAED) technique is used to verify iron oxidation issue. The example of SAED patterns in Figure 3.1-5 for CEINPs were successfully indexed to pure iron (alpha iron) crystal structure as identified by diffraction rings corresponding to the (1 1 0) and (1 1 2) Fe crystalline planes. Electron diffraction from iron oxides was not detected in any of our samples. In general it should be noted that SAED images of CEINPs reveal diffuse rings that are due to the presence of both nanocrystalline and amorphous phases.

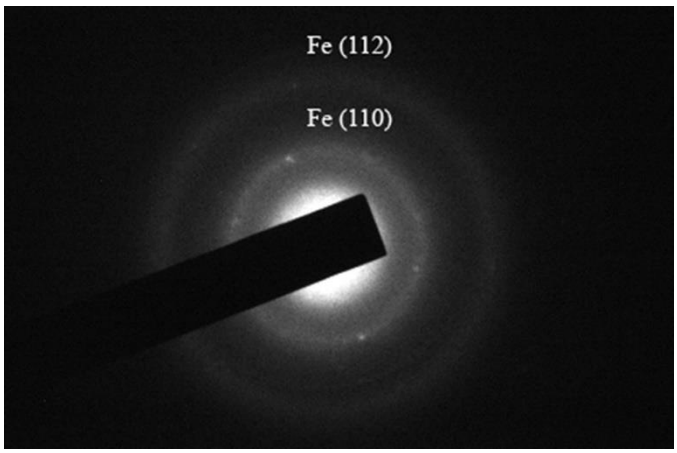

Figure 3.1-5. SAED pattern showed pure iron phases, no diffraction point of iron oxides was detected.

In addition, several points of CEINPs have been characterized by EDX analysis at micro scale and EELS analysis at nanoscale. An example of EDX spectrum and composition mapping along with corresponding sample image are presented in Figure 3.1-6. As it is shown in Figure 3.1-7, results of EELS analysis are in agreement with EDX analysis. Consequently, only iron peak has been observed from both EELS and EDX analysis and no trace of oxygen or other impurities have been found, which shows that all iron particles were well protected by carbon shells.

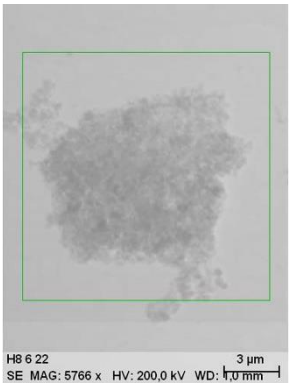

(a)

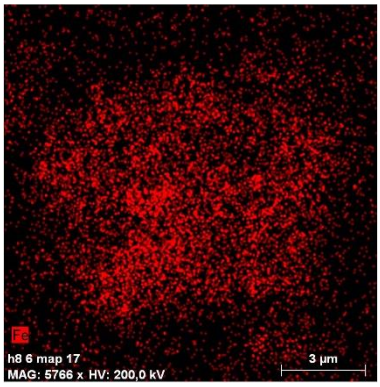

(b)

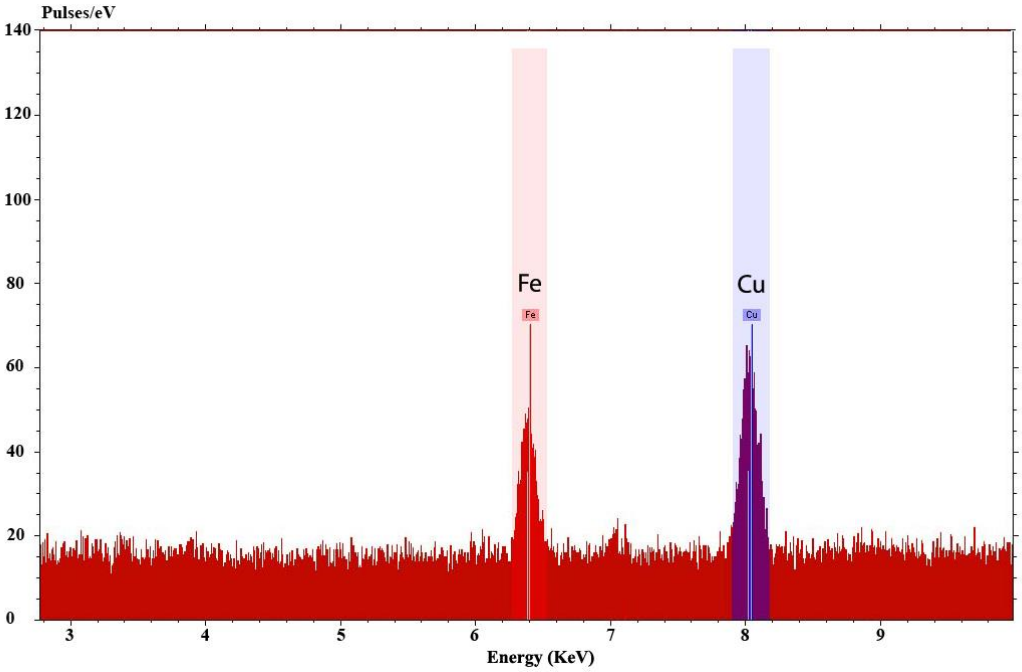

(c)

Figure 3.1-6. (a) TEM image at micro scale (b) Chemical mapping in conjunction with TEM image A, Reddish points accumulation represent appearance of iron in particles, (c) EDX spectrum, Red peak corresponds to Fe and blue peak is Cu from grid of the sample.

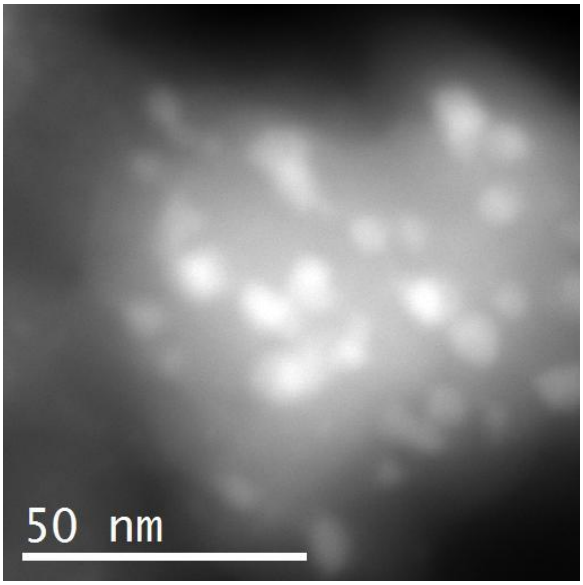

(a)

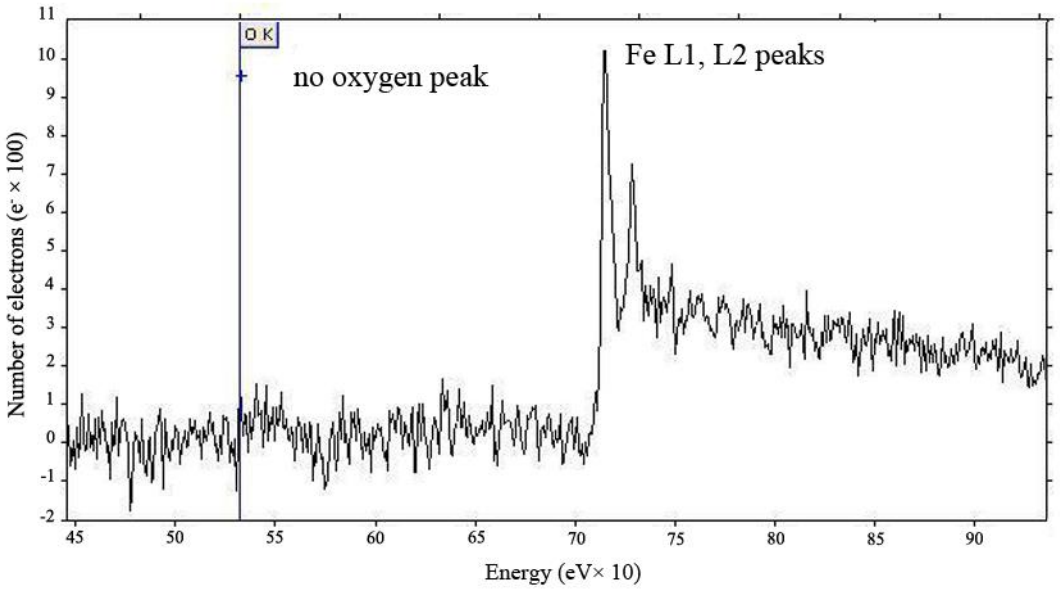

(b)

Figure 3.1-7. (a) An example of TEM image from EELS analysis, iron cores are visible in white circles, (b) EELS spectrum from image (a), only iron peaks were detected.

In principle, magnetic nanoparticles have attracted attention because of the possibility of manipulating them by an external magnetic force. superparamagnetic behavior provides multifunctional effects such as controlled heating capability under an alternating magnetic field, which is suitable for hyperthermic treatment of cancer (Ruiz-Hernandez, 2011). SQUID is employed to characterize magnetic properties of

the synthesized particles. The superparamagnetic state is defined for a system of no interacting single domain nanoparticles, whose susceptibility follows the Curie law and, its magnetization curve can be described by the Langevin function (Bittova, 2011). The normalized magnetizations M/M_s as a function of H/T ratio together with the Langevin fitting of the data for all samples at room temperature (300 K) have been analyzed and effective moment were calculated accordingly. Figure 3.1-8 is an example plot showing that these particles have a coercivity close to zero and have no hysteresis. The ratio of remnant to saturation magnetization at room temperature ranges from $M_r/M_s \sim 0.020$ to 0.05, which clearly indicates that all the samples are in a superparamagnetic state.

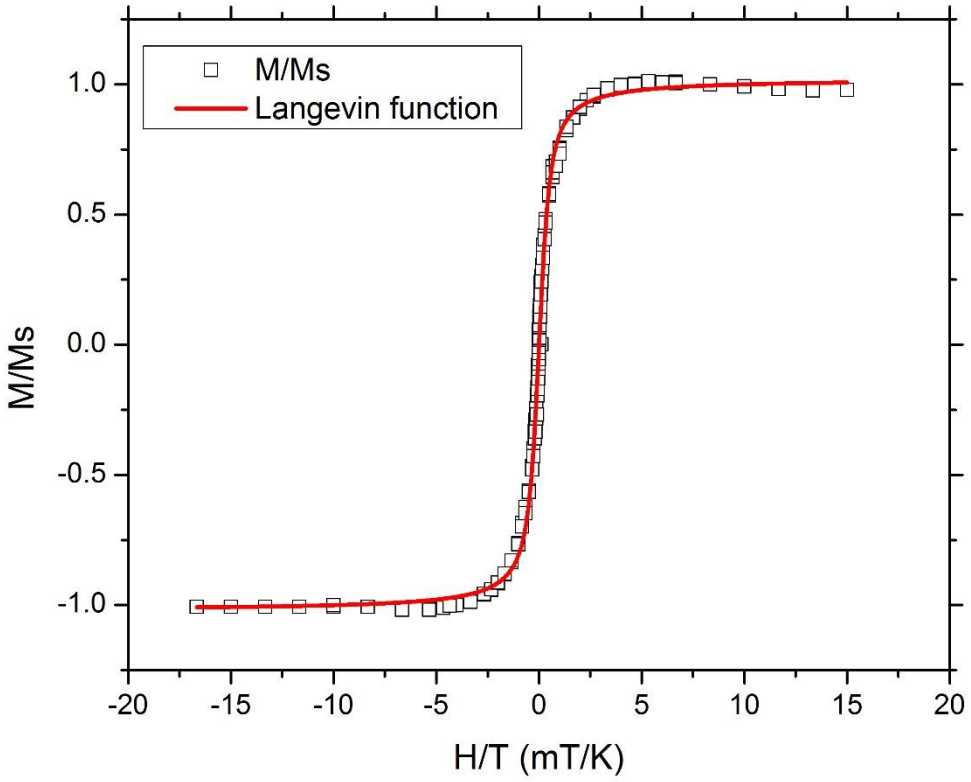

Figure 3.1-8. Temperature magnetization data to the saturation magnetization M_S, are reported as a function of the H/T ratio together with the Langevin fit of the data.

Figure 3.1-9 summarizes the dependence of normalized moment (μ) and saturation magnetization (emu/g) according to the mean iron core and carbon shell diameters. Saturation magnetization and moment (μ) are found to increase when the iron size is increasing and the carbon shell is decreasing. Similar trend and size

dependency for iron saturation magnetization were reported in the literatures (Seehra, 2010, Dutta, 2009, Sanchez, 2002). Saturation magnetization is mainly dependent on size, shape, surface effect, metal composition, crystalline magnetic anisotropy energy, as well as coating by non-magnetic materials (Sharif, 2013, Sato, 1987). The values of moment (μ) observed for samples grown under majority of argon appeared clearly lower than samples grown under high concentration of helium.

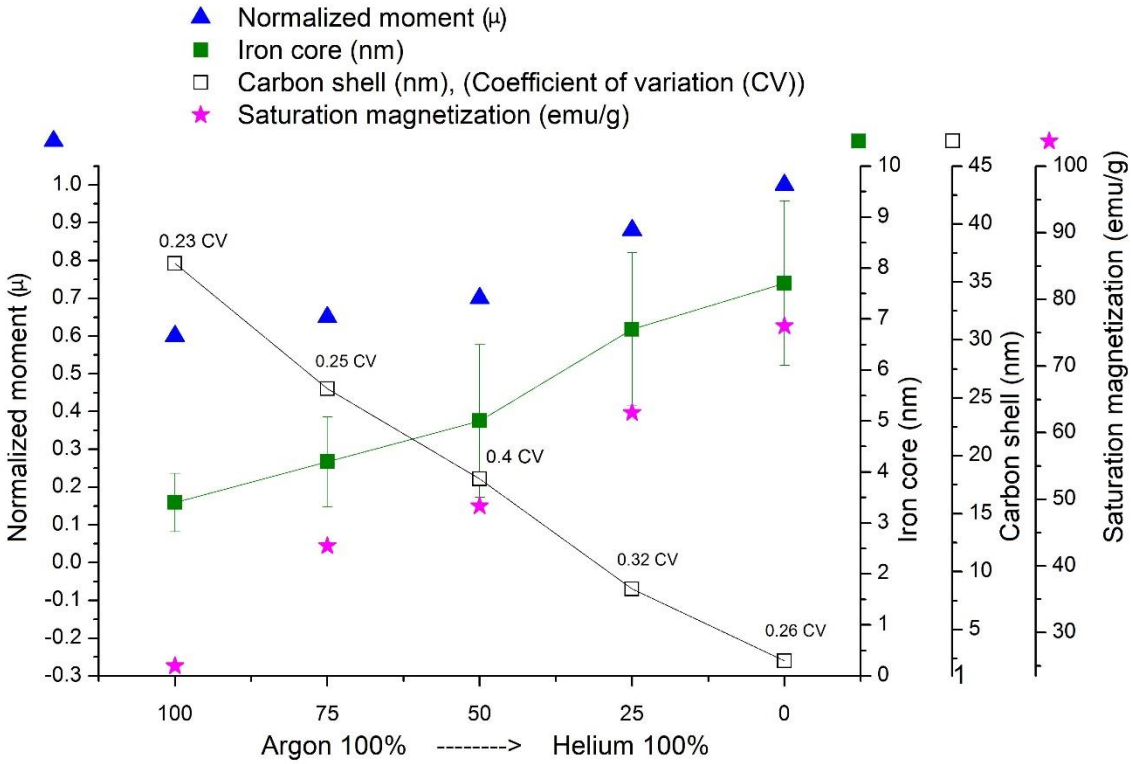

Figure 3.1-9. Effects of iron core and carbon shell sizes according to the normalized moment (μ) (Ar0 μ value is 8.93×10^-17 emu) and saturation magnetization (emu/g) versus gas ratio. The error bars correspond to iron core size dispersion and, carbon shell coefficient of variation (CV) is given for clarity.

Zero-field-cooling (ZFC) and field-cooling (FC) magnetization as a function of temperature measured at 100 Oe have been analyzed. ZFC and FC graphs are plotted in Figure 3.1-10. ZFC and FC magnetization measurement indicates the mean blocking temperature for each sample. The blocking temperature was determined as the peak temperature of the *M(T)* curve after ZFC (Shiratsuchi, 2003). For ZFC curves, as the temperature increases, the magnetization shows an increase because the magnetic moment is thermally activated along the magnetic field direction. For samples Ar100,

Ar75, Ar50, Ar25 and Ar0, the transition temperature from ferromagnetic to superparamagnetic state or blocking temperature, T_b, peaks can be observed in Figure 3.1-10 (a), (b), (c), (d) and (e) the ZFC curve at about 24 K, 26 K, 30 K, 41 K and 50 K, respectively. By contrast the T_b value of Ar0 is almost double of Ar100 T_b, due to the larger iron particles. This result is in agreement with TEM observations of iron core diameter. The finding that T_b increases as the size of the nanoparticles increases is consistent with conventional Stoner-Wohlfarth theory: the energy barrier, over which the magnetization of the nanoparticles should be thermally activated, increases as the size of the nanoparticles increases (Lee, 2005). Dependency between T_b and iron core size is plotted in Figure 3.1-11. Above blocking temperature, the particles are free to align with the field during the measuring time and ZFC curve superimposes with FC curve, this state is called superparamagnetic, because the particle behaves similarly to paramagnetic spin but with a much larger moment (Raj, 2005). ZFC and FC curves demonstrate that all samples are in superparamagnetic state above 260 K. Ar100 sample is superparamagnetic at low temperature (above 220 K), therefore it is a suitable CEINPs for specific applications that operate at extremely low temperature such as applications in aerospace industry.

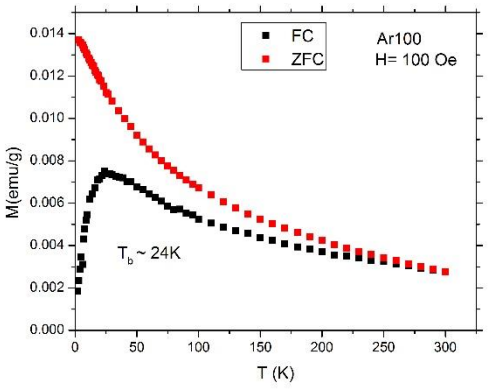

(a)

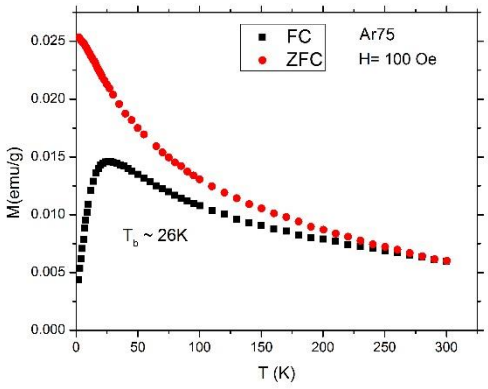

(b)

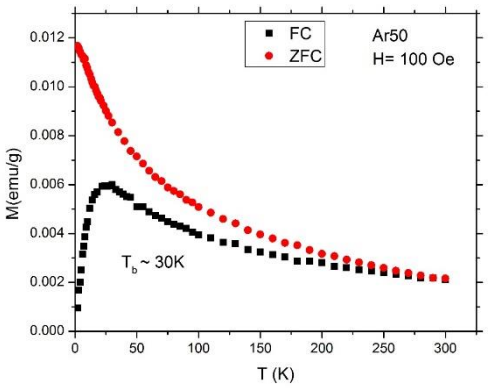

(c)

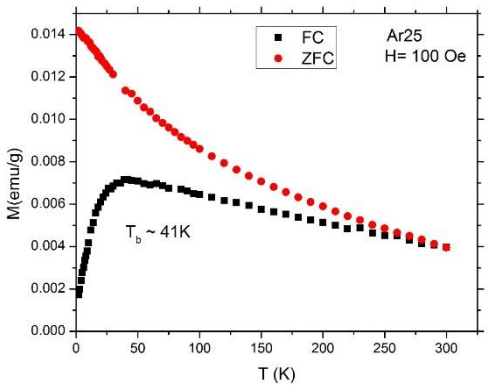

(d)

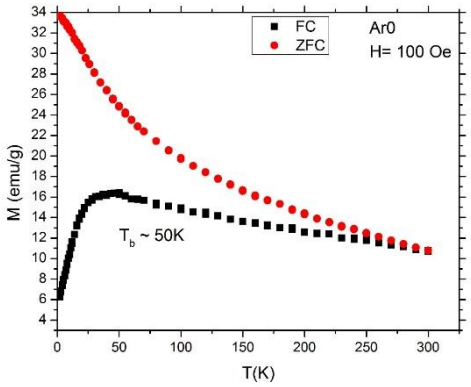

(e)

Figure 3.1-10. (a), (b), (c), (d) and (e) Zero-field-cooled and (*H* = 100 Oe) field-cooled magnetization curves of samples: Ar100, Ar75, Ar50, Ar25 and Ar0.

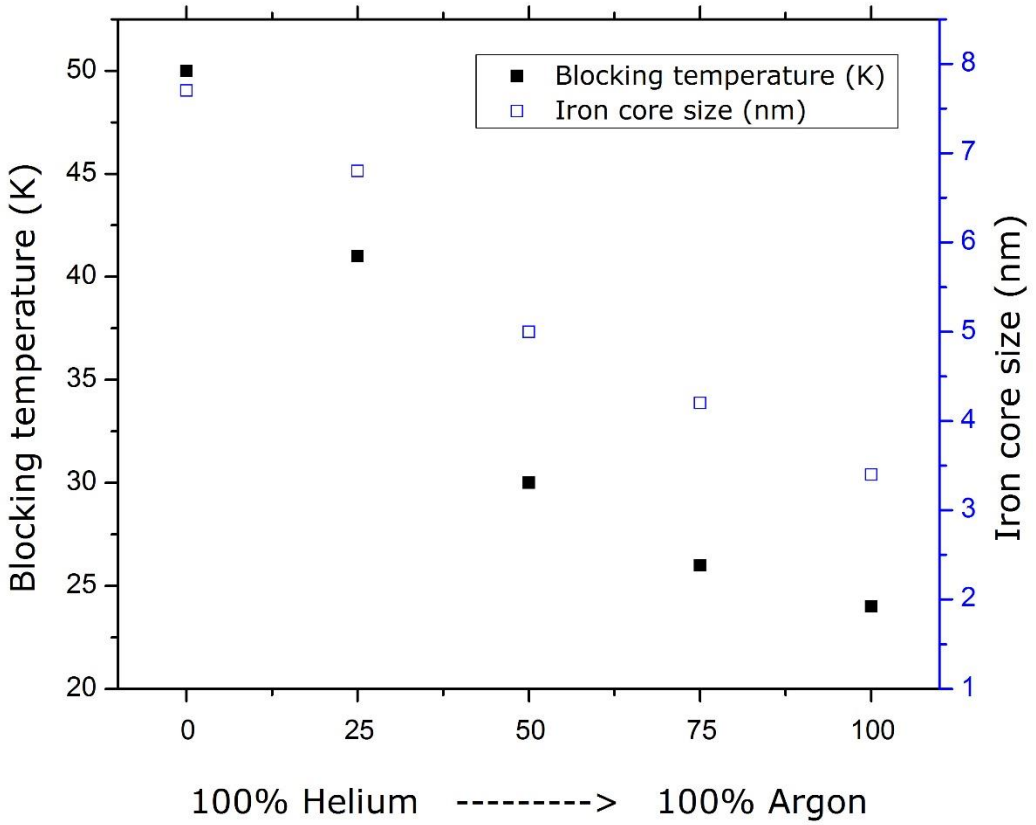

Figure 3.1-11. Dependency of iron core size and blocking temperature versus gas helium/argon.

More detailed information of carbon shell characteristics can be achieved by Raman spectroscopy; thereby the degree of carbon order-disorder is studied. The G-line and D-line Raman spectra peaks are observed around 1600 cm^{-1} and 1350 cm^{-1} respectively. The peak intensity ratio I_D/I_G is often used to determine the extent of structural disorder (e.g., I_D/I_G = 0 for a perfect, infinite graphene layer) in graphite and/or the size of the graphitic domains (Sethuraman, 2010). The Raman spectra are fitted with a Lorentzian function for further analysis; a typical spectrum is presented in Figure 3.1-12.

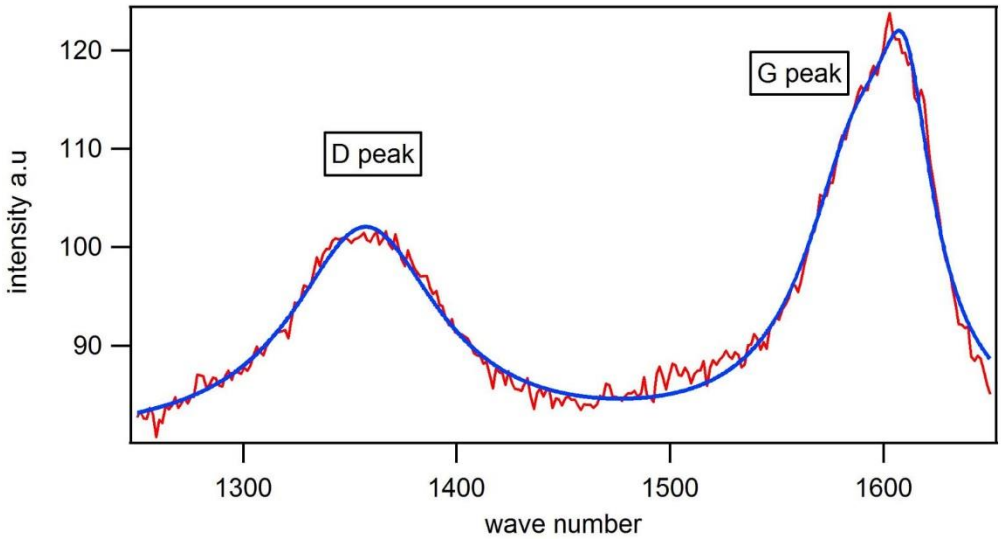

Figure 3.1-12. Raman spectrum fitted to a Lorentzian function, I_D/I_G<1.

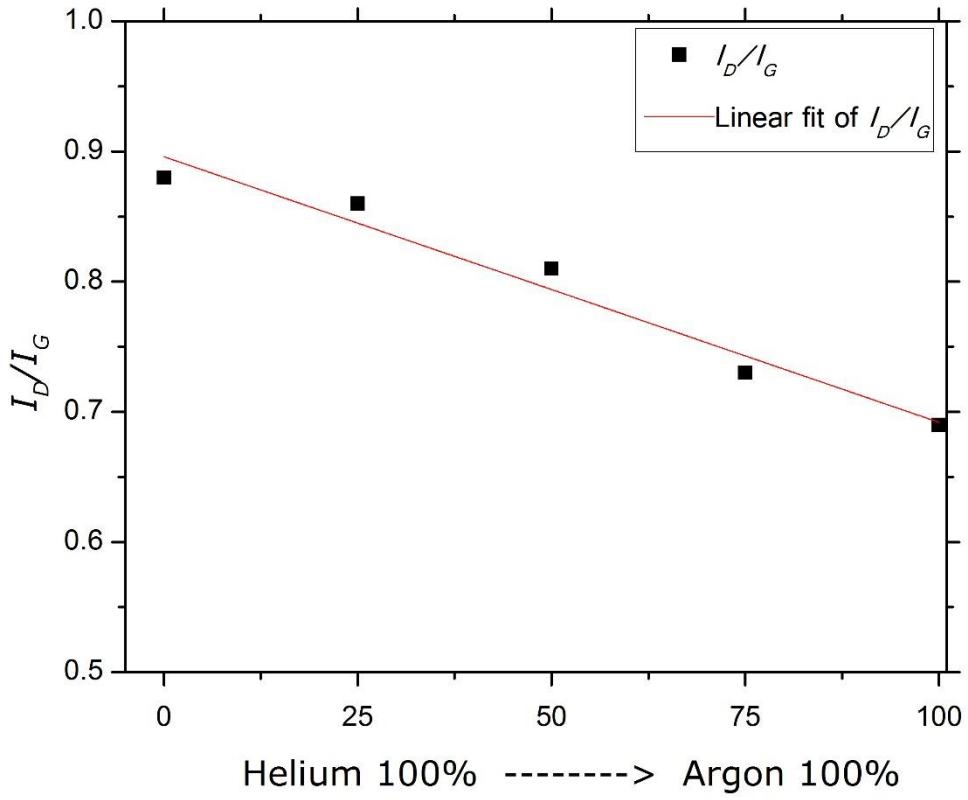

Figure 3.1-13. I_D/I_G packs vs argon and helium mixtures.

As it is shown in Figure 13 the ratio I_D/I_G is decreasing as the carbon thickness of iron core is getting larger and exhibits a higher degree of graphitization. This is probably due to the lower cooling rate of vapor when plasma is generated by argon

comparing to the helium generated plasma. Laplaze pointed out the great influence of the cooling rate of vapors on the structure and yield of nanostructured carbon material; they observed a fast cooling rate when plasma is generated by helium and lower with argon at close flow rate (Laplaze, 2002). Accordingly, our results show less defect and best crystallinity when pure argon is used. Crystalline carbon isolation made nanoparticles suitable for chemically activated environment and biological media. Huo explored the stability of carbon encapsulated iron nanorods by annealing experiments. Their ferric nanoparticles diffused and ejected from carbon shells via quasi-melting, they concluded that the ejection phenomenon may be related to the high activity of iron nanoparticles, exothermic oxidation reaction, as well as many defects of carbon shells (Huo, 2008). Therefore, it is expected that the Ar100 sample which shows less defected carbon shell provide more stability comparing to other samples.

3.1.3 Conclusions

Iron core at carbon shell nanostructures are synthesized successfully in a controlled manner. The nature of inert dragging gas and its composition appears to be a sensitive parameter to control CEINPs shell and core diameters. This is probably due to its influence on heat transfer and diffusion in the reactor. The argon/helium gas ratio alters the heat transfer from central of the plasma to outside. When argon concentration increases then the temperature gradient increases or in other word, cooling rate decreases, resulting in changes of the critical radius of carbon shell and iron core. Nanoparticle growth occurs in gas phase and, lower thermal conductivity of the gas enlarges the formation time. It is concluded that, by increasing ratios of argon to helium, carbon shell thickness increases from 2.3 nm to 36.6 nm and iron core size decreases from 7.7 nm to 3.4 nm. In addition, using pure argon, most size monodispersion is obtained. Diffraction points of iron oxide were not detected from SAED analysis. Moreover, both EELS analysis at nanoscale and EDX analysis at micro scale showed no trace of oxygen in iron cores. These results point to a high efficiency of carbon shell to isolate iron core from a possible external oxidation. Raman spectroscopy results indicate that the crystallinity of the carbon shell increases when pure argon is used. The size dependence of the effective moment and the saturation magnetization parameters of superparamagentic nanoparticles have been

demonstrated. All studied CEINPs exhibit superparamagnetic behavior above 260 K. And samples with smaller iron cores exhibit superparamagnetism above 220 K. This causes the blocking temperature of the particles grown without argon (T_b ~ 50 K) to be almost double than those grown in pure argon (T_b ~ 24 K), in agreement with T_b dependence vs TEM iron core diameter. The CEINPs characterization demonstrated that by changing gas composition of the arc discharge reactor used in the research project, morphological properties of carbon encapsulated iron nanoparticles can be controlled according to the different applications. The results of this contribution are one step forward to controlling carbon and iron core/shell and understanding growth mechanism.

3.2 Synthesis of carbon encapsulated mono and multi iron nanoparticles

(Journal of Nanomaterials, article ID 178524, 2014)

Investigation focused on synthesis process of carbon encapsulated iron nanoparticles. Our extensive study successfully leads to the synthesis of a new carbon encapsulated multi iron nanoparticles, which means that, to equal carbon shell size, the amount of iron distributed between multinucleated nanoparticle cores increases. Until now, all reported studies have been only on mono iron nanoparticles and the synthesis of multi iron core at carbon shell has not yet been reported. We will show the effect of carbon shell on saturation magnetization. As reported in the literature, the increase of the saturation magnetization of magnetic nanoparticles may permit a more effective development of multifunctional agents for simultaneous targeted cell delivery, magnetic resonance imaging (MRI) contrast enhancement, and targeted cancer therapy in the form of local hyperthermia. Specifically, because of the extremely narrow distance between multiple iron cores, a greater visibility will be compared to that of particles with a single iron core and, therefore, this type of nanoparticles has more priority to be used as contrast agent. On the other hand, it is noteworthy to mention that due to the carbon shell spherical shape and iron superparamagnetic behavior, their movement in body fluid can be smooth and controllable and hence the carbon encapsulated iron nanoparticles can be potentially used in drug delivery.

By changing certain parameters we have also changed the morphologies of spherical iron cores, and according to TEM images, we obtained oval shape iron cores as well. The following section introduces and describes the synthesis of mono and multi iron cores.

There has been an increasing interest in fabrication of magnetic based nanomaterials due to their potential applications in data storage (Reiss and Hütten, 2005), Li-ion battery (Yang and Wang, 2014), highly sensitive magnetic sensors (Zamfir, 2011) and spintronics devices (Singamaneni, 2011). Moreover, magnetic nanoparticles are attracting attention in both the medical and biological fields for applications including magnetic separation of biological entities (Colombo, 2012),

tissue engineering (Ishii, 2011) food analysis (Cao, 2012) therapeutic drug delivery (Veiseh, 2010), hyperthermia for tumor therapy (Yanase, 2012), contrast enhancement agents for magnetic resonance imaging applications (Na, 2009, Ruiz, 2013), water purification (Ambashta and Sillanpää, 2010) and catalysis (Zuo, 2009, Tsang, 2004). Most of the studies in these areas focus on particles based on oxides since magnetic nanoparticles, which are based on pure metallic materials are very sensitive to oxidation given their high specific surface area and reactivity (Bystrzejewski, 2011).

The key point of using magnetic nanoparticles is the possibility and capability to control them by an external magnetic field. Naked metallic nanoparticles are chemically highly active and are easily oxidized in air, resulting negative effects on magnetic properties. To avoid such consequences, well developed graphitic carbon layers can provide an effective barrier to maintain magnetic properties. Coating metallic cores by silica (Roca, 2012), carbon (Nowicka, 2012, M. Reza Sanaee, 2013a, M. Reza Sanaee, 2013b, Ji, 2014) and precious-metal (Schärtl, 2010) are examples of popular inorganic coating approaches. Compared to the polymer, silica, or Au layer, the carbon layer has many advantages, such as higher chemical and thermal stability, better conductivity, and higher biocompatibility (Wu, 2011b, Avalos-Belmontes, 2012, Uhm and Rhee, 2013). Moreover, carbon-coated nanoparticles are usually in the metallic state, and compared to the corresponding oxides, they have a higher magnetic moment (Chen, 2012b). In particular, at present, a hot topic is magnetic carbon coated metal (such as Fe, Co, Ni, Mn) composites that are always metal phases as the nucleus of core@shell structural composite nanomaterials (Luo, 2012).

In this research study, carbon encapsulated iron nanoparticles (CEINPs) were designed and produced in a way to make them suitable nanocarriers for biomedical applications. So far, different methods including arc discharge (M. Reza. Sanaee, 2013, M. Reza. Sanaee, 2012, Shen and Wang, 2011), hydrothermal reaction (Zhang, 2010), chemical vapor deposition (Cao, 2008), detonation synthesis (Lu, 2005), chemical vapor condensation (Wang, 2003), magnetron and iron-beam co-sputtering (Nishijo, 2005), laser ablation (Park, 2008) and co-carbonization (Huo, 2004) are used to synthesize core@shell structures in which metallic nanoparticles are encapsulated

by precious metals, polymers, silica, or carbon. However, each of these methods has particular advantages and disadvantages comparing to our method for the synthesis of CEINPs. Until now, all reported studies have been only on mono iron nanoparticles and the synthesis of multi iron core at carbon shell has not yet been reported (Chaudhary, 2014, Zhao, 2007, Luo, 2010, Bystrzejewski, 2011, Fedoseeva, 2012, Abdullaeva, 2012, Gupta, 2012, Sharma, 2012, Zhang, 2013a, Labędź, 2014, Mostofizadeh, 2011).

In current nanoparticle fabrication processes, control of the particle size and composition is still empirical, which means a large number of experimental trials are required to optimize any given process (Shigeta and Murphy, 2011). Plasma properties such as size, gradient temperature, thermal conductivity and cooling rate are mainly dependent on the used inert gases. Consequently, all parameters are kept constant to study the influences of helium and nitrogen on morphological properties as well as magnetic properties. Here, we present the synthesis of both CEINPs and carbon encapsulated multi iron nanoparticles. The morphological properties were studied by scanning electron microscopy (SEM) and transmission electron microscopy (TEM). In order to verify the absence of iron oxide, the samples were analyzed by selected area diffraction (SAED), electron energy loss spectroscopy (EELS) and energy-dispersive X-ray spectroscopy (EDX) techniques, and the diffraction was determined by fast Fourier transform (FFT) from the TEM images. In addition, carbon shell crystallinity was investigated by Raman spectroscopy. Afterward, the magnetic properties were obtained from superconducting quantum interference device (SQUID) characterization technique.

3.2.1 Method

A liquid phase modified arc discharge reactor was utilized (Enric Bertran, 2012, M. Reza. Sanaee, 2014, Aguilo-Aguayo, 2013). Nitrogen, helium and their mixtures were used to synthesis each samples, from 0% to 100% of N_2. Accordingly, each nanoparticle samples were named based on the nitrogen content, i.e. 75% N + 25% H is N75. The procedures are explained in section 2.1.1.

3.2.2 Results and Discussion

The Influence of nitrogen and helium mixtures on CEINPs morphologies and magnetic properties were studied. As it is shown in Figure 3.2-1(a), SEM image reflects the CEINPs in spherical and agglomeration form. TEM images in Figure 3.2-1(b), (c), (d), (e) and (f) show geometry of each individual nanoparticles from N0, N25, N50, N75 and N100 samples, respectively. Spherical iron nanoparticles show a mean diameter of 7.5 nm in N0 samples. By adding 25% and 50% nitrogen, mainly oval shape iron nanoparticles with mean dimensions of 7.6 nm × 6.5 nm and 8 nm × 5.6 nm were found in N25 and N50 samples, respectively. Afterwards, by adding 25% more nitrogen, iron nanoparticles tended to form comparatively smaller oval iron core with mean dimensions of 7.8 nm × 4.7 nm in N75 sample. Using only nitrogen leaded to the formation of carbon encapsulated multi iron nanoparticles (CEMINPs). Consequently, in case of N100 sample the majority of nanoparticles have small multi iron cores. In this last case, CEMINPs mainly consisted of spherical iron cores of 1 nm and 2 nm of diameter and one or two oval shaped iron cores of 4.3 nm × 2.5 nm.

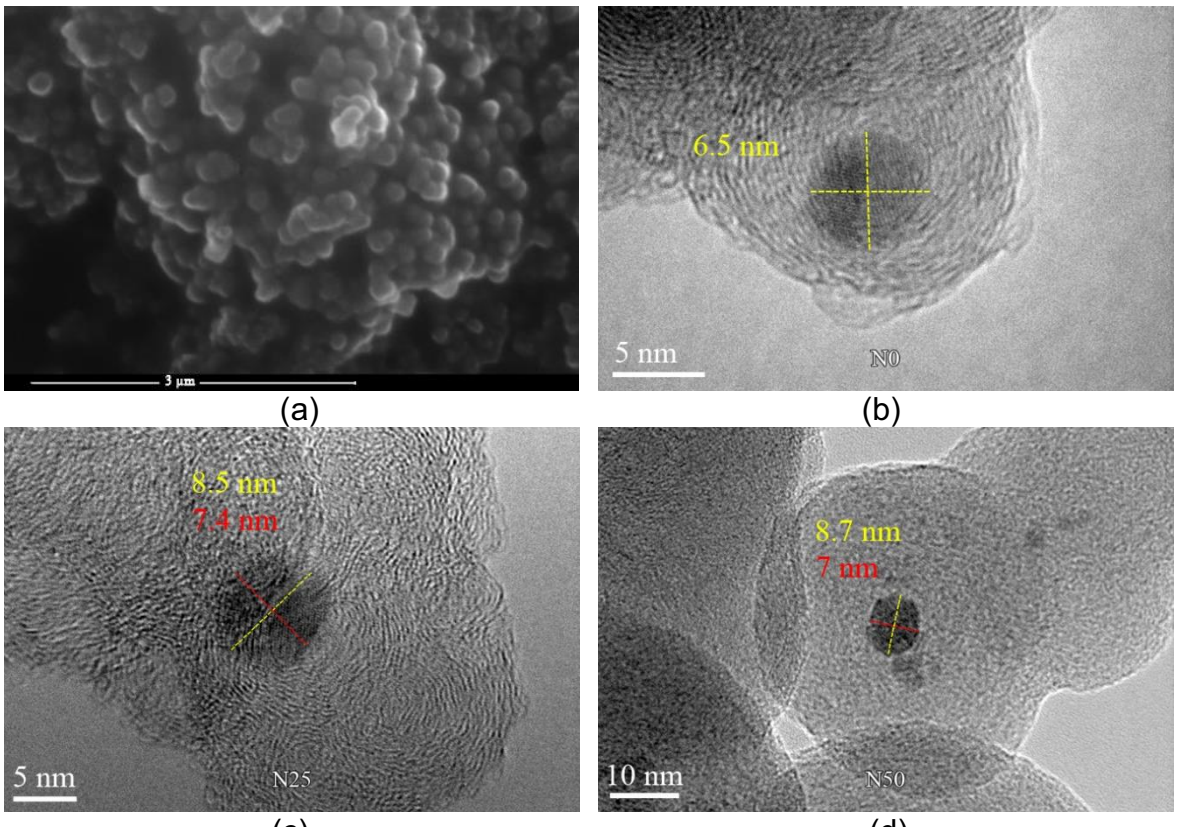

(a) (b)

(c) (d)

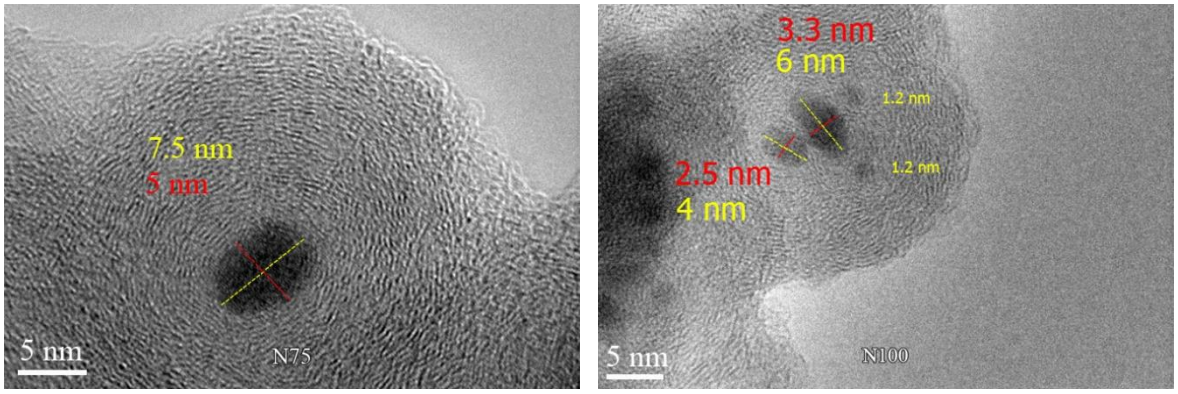

(e) (f)

Figure 3.2-1. (a) SEM image shows agglomeration of CEINPs produced under nitrogen. (b), (c), (d), (e), and (f) TEM images of CEINPs and CEMINPs are shown from N0, N25, N50, N75, and N100 samples, respectively. It is evident that the morphologies of carbon and iron were changed by increasing nitrogen ratio over helium. The increasing trend in carbon shell formation and the decreasing trend in iron formation are remarkable. The merging and formation of iron core nanoparticles from samples N100 to N0 revealed the role and effect of coalescence in during the formation of CEINPs and CEMINPs.

Figure 3.2-2(a) and 3.2-2(b) represent TEM images from N100 samples. However, as shown in Figure 3.2-2(c), a single iron particle with oval shape and dimensions of 3 nm × 9 nm was observed in N100 sample as well. In general, according to the TEM observations, as we increased nitrogen gas percentage versus helium to generate plasma, the iron cores were adopting an oval shape. Based on TEM observations extremely small iron particles of 1 to 3 nm do not form a bigger single iron core and instead formed multi iron core at carbon shell nanoparticle. Gutsch discussed the coalescence effect, which merge nanoparticles to form a bigger one in gas phase production of nanoparticles (Gutsch, 2002). The condition of nucleation occurs in iron supersaturation vapor, which permits to obtain the particles with stable growth. Afterwards, coalescence occurs when the concentration is high enough. Once the carbon shell formation begins, the iron cores growth and coalescence end. Obtained results highlighted the coalescence effects on formation of iron nanoparticles from sample N100 to N0. The presence of oval iron nanoparticles and multi iron cores shows the coalescence of the nucleus before starting carbon shell formation. The coalescence of only two iron particles was observed. This can be probably due to surpassing of the critical radius of carbon shell for the growth after the first iron coalescence.

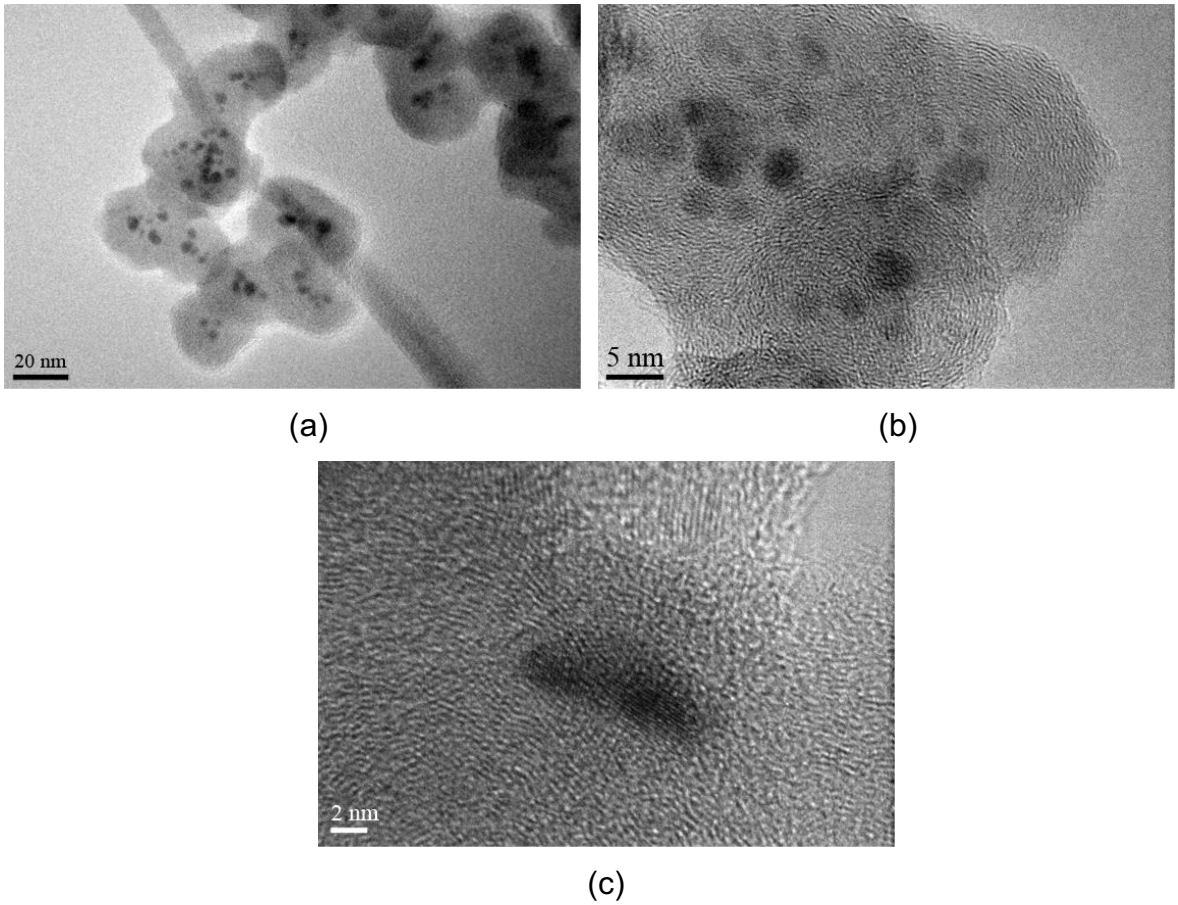

Figure 3.2-2. (a) Illustration of CEMINPs; the iron cores are located very close to each other. (b) Close observation of a few individual multi-iron cores at carbon shell nanoparticles. (c) Appearance of single oval shape iron nanoparticle in N100 samples; this is probably due to the coalescence between two particles.

The effect of nitrogen and helium in growth formation can be attributed to their differences in thermal conductivity and plasma temperature. Thermal conductivity of nitrogen is about 9 times smaller than helium. Thermal conductivity regulates the cooling rate and gradient of temperature. Thus comparatively nitrogen exhibits lower cooling rate and longer gradient of temperature over highly supersaturated vapor. Supersaturated vapor results in rapid production of numerous nanoparticles. In addition, relatively more carbon species are available in supersaturated vapor for carbon shell formation at higher temperature generated by nitrogen plasma rather than helium plasma. Accordingly, a decrease trend in carbon shell formation is obvious from sample N100 to N0 in Figure 3.2-1. It should be noted that the carbon shell formation limits the critical radius of iron. According to our observation, when iron particles are small enough (1-3 nm) they are trapped into a single carbon shell.

Since nitrogen is a diatomic gas, its plasma has higher energy contents for a given temperature than the atomic gases such as helium (Gerdeman and Hecht). Also because of high electronegativity of nitrogen, more energetic electrons are necessary to produce self-sustained arc discharge. Consequently, when nitrogen is used, due to the high temperature, the carbon electrodes were deformed during the experiment as shown in Figure 3.2-3.

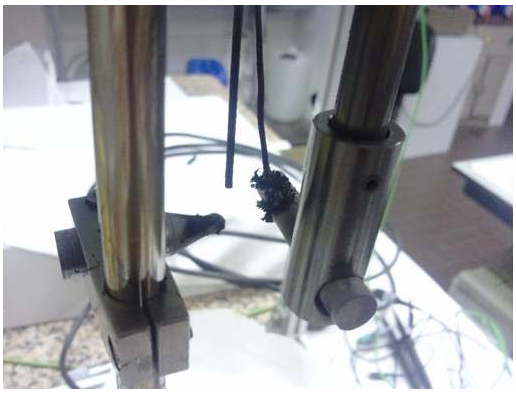

Figure 3.2-3. Deformation of carbon electrodes; the nanoparticles deposited on the carbon surface due to the high temperature of nitrogen plasma.

Regardless of inert gas type, in arc discharge processes the electron bombardment mainly is on the anode and therefore the carbon from the anode electrode was consumed and deformed. This deformation caused changes in plasma shape, made it unstable and prevented continuous synthesis. Moreover, it exerts a negative effect on formation and size distribution of CEINPs and CEMINPs. Figure 3.2-4(a) shows the size distribution of spherical iron core from N0 sample. In order to evaluate the size distribution of oval shape iron cores, the equivalent volume of sphere radius was considered and accordingly other sample size distributions were plotted in Figure 3.2-4(b), (c), (d) and (e). As the result, N0 sample reveals the narrower iron core size distribution, because by using only helium the cathode carbon electrode shows less morphology changes, comparatively.

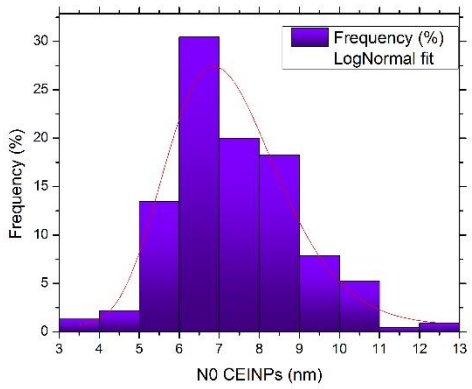

(a)

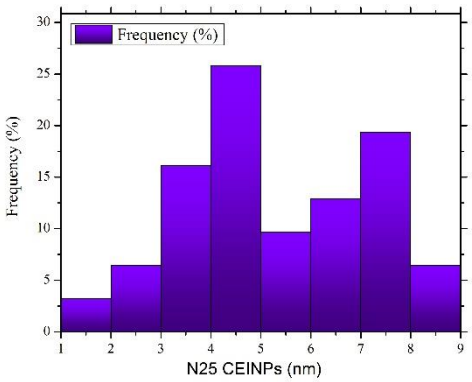

(b)

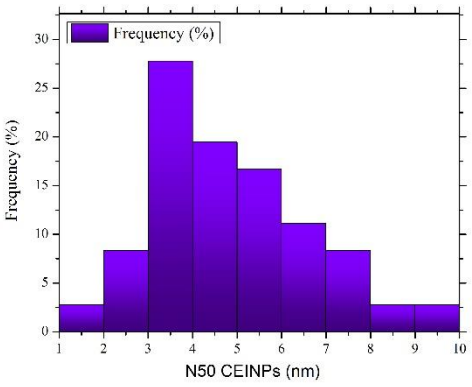

(c)

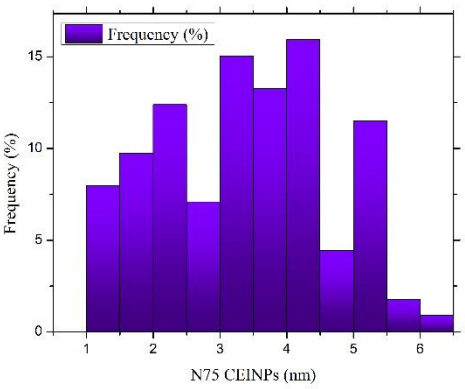

(d)

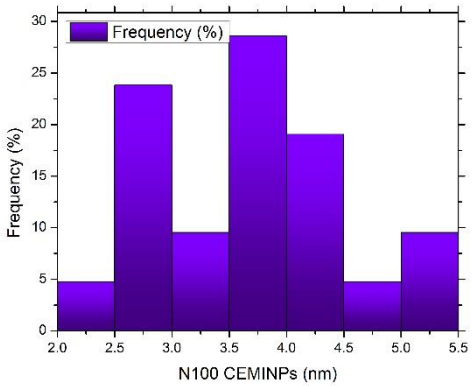

(e)

Figure 3.2-4. Iron core size distribution for all samples. (a) Iron cores of N0 sample show narrow size distribution and followed the lognormal curve. (b) In case of N25 sample, there are two size categories of nanoparticles from 1-6 and 6 to 9. (c) and (d) N50 and N75 are not showing narrow size distribution due to the deformation of carbon electrode and its influence on plasma formation in terms of size and stability. (e) N100 (CEMINPs) size distribution estimation is quiet broad due to the appearance of different iron core sizes in each carbon shell.

In spite of usefulness of presented method for CEINPs and CEMINPs synthesis, plasma instability and discontinuous synthesis are the main drawbacks.

An exploration of the deformed carbon electrode by SEM has been done. SEM image from carbon piece taken from anode electrode is presented in Figure 3.2-5. The image revealed the formation of agglomerates of spherical carbon particles. Spaces between particles are clearly visible, and evidence the formation of porous carbon. The morphology of carbon deposited on the anode is the result of an intense electron bombardment, which produces voids and densely packed particle agglomerates on a seemingly porous superstructure like to cauliflower (Figure 3.2-5). Thinner carbon deposition on cathode was observed probably due to the neutral nanoparticles and positive radicals of carbon. Moreover, the cathode suffers a significant ion bombardment (for example CH_3^+ (Gordiets, 2011)). In addition, according to the given growth mechanism of CEINPs, the nitrogen plasma has a higher temperature compared to helium plasma, which results in higher availability of carbon species. According to our observation, higher contribution of nitrogen shows an increase in deposition of carbon related structure on the electrodes.

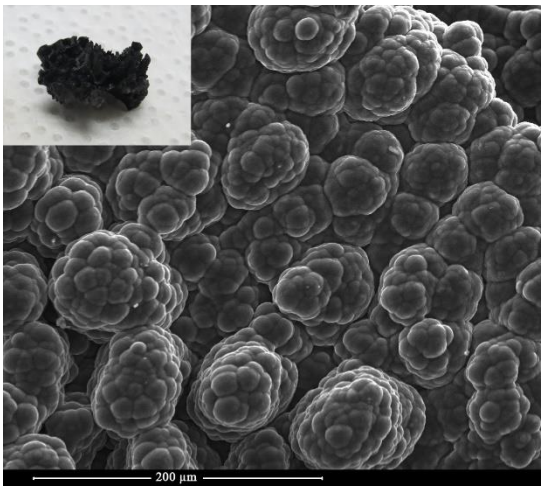

Figure 3.2-5. SEM image of CEINPs deposited on anode electrode when nitrogen plasma is used. The inset image is the carbon piece in question. Carbon spherical formation (cauliflower like superstructure) and the pores between them are clearly visible. Possibly nanopores also exist but cannot be observed at this resolution.

Due to the importance of iron core sufficient protection and in order to show the efficiency of carbon shells against the oxidation of core, samples and their images were evaluated by SAED and FFT techniques, respectively. SAED is shown in

Figure 3.2-6(a), diffraction points of iron are indexed to α-Fe crystal structure as identified by diffraction rings corresponding to the (-1,0,1) and (0,-1,1) planes. However, as it is shown in Figure 3.2-6 (b) from FFT analysis, trace of iron carbide was detected in interface between core and shell. Most importantly, diffraction points of iron oxides were not detected in any of our samples.

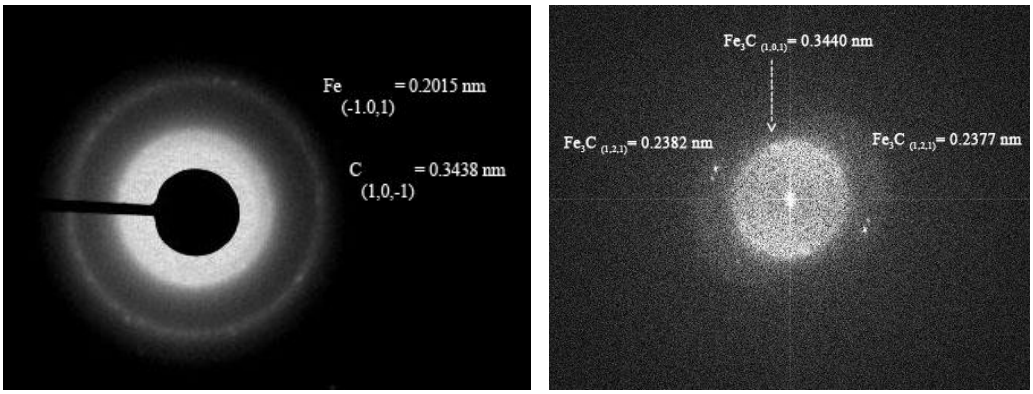

(a) (b)

Figure 3.2-6. (a) SAED image reveals diffuse rings due to the presence of both nanocrystalline and amorphous phases. (b) FFT analysis of images shows trace of iron carbide.

In addition, nanoparticles were analyzed by EELS and EDX along with chemical mapping. Figure 3.2-7 represents an example of EELS analysis at nanoscale and EDX together with chemical mapping at micro scale. As the result, absences of oxygen are confirmed in iron cores; therefore carbon shell properly sealed the iron cores in all samples. In addition, the less defects in carbon shell provides higher protection efficiency.

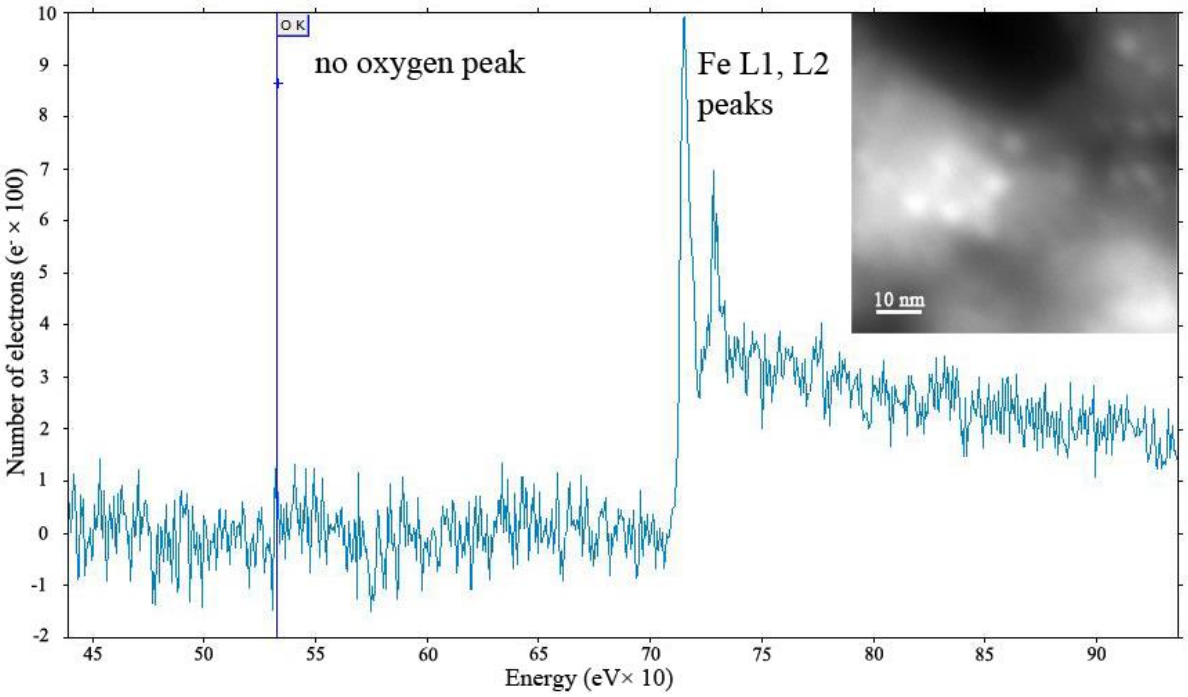

(a)

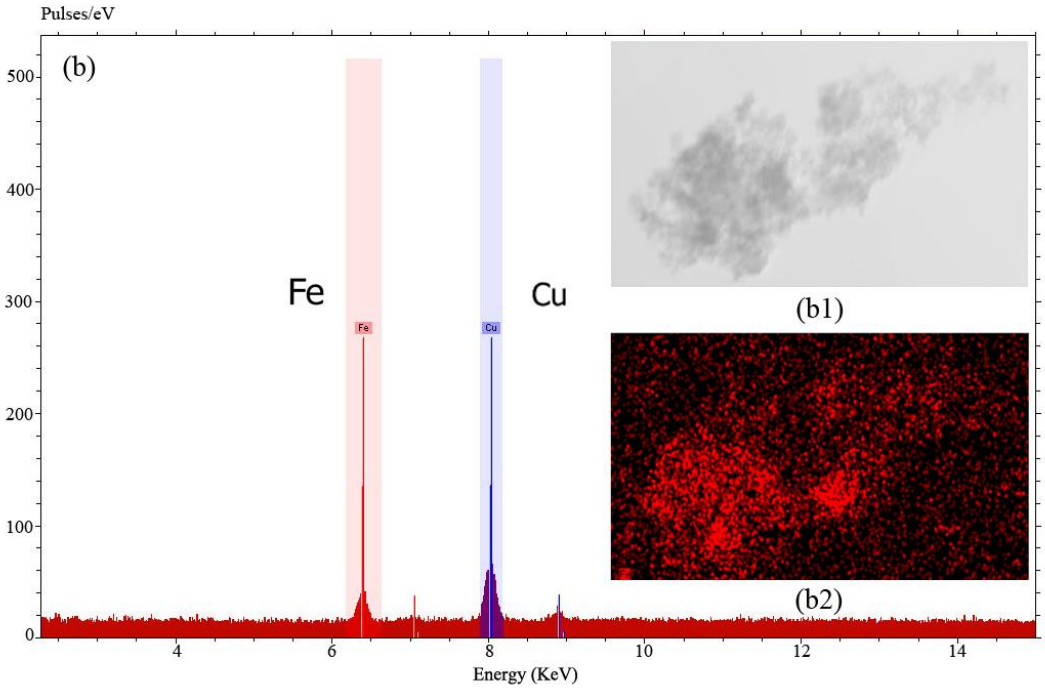

(b)

Figure 3.2-7. (a) Spectra of EELS analysis at nanoscale and associated TEM image is in the inset. EELS analysis shows no oxygen peak. (b) EDX analysis at microscale shows only Fe peak without oxygen peak as well (Cu peak is due to the grid). EDX associated TEM image is in (b1) inset, and associated chemical mapping is in (b2) inset. Red spots represent Fe.

Accordingly, carbon shells order/disorder structure was analyzed by Raman spectroscopy. The D-band of metal/C nanoparticles are considered to be a disorder-induced feature owing to lattice distortion or amorphous carbon background signal (Lee, 2012). The peak intensity ratio I_D/I_G is often used to determine the extent of structural disorder in graphite and/or the size of the graphitic domains (Sethuraman, 2010). Thus, the decoupled I_D/I_G is considered. D and G peaks are located near ~1350 and ~1600 cm^{-1}, respectively. Raman spectra peak−height ratios I_D/I_G were determined from Lorentzian fittings as the example spectrum shown in Figure 3.2-8(a). The carbon shells crystallinity degree (I_D/I_G) was obtained for each sample accordingly and was lower than one for all samples, indicating high carbon crystallinity. Comparison of I_D/I_G ratio of each sample in Figure 3.2-8(b) reveals slight decrease in I_D/I_G ratio as more nitrogen is used. This means that the graphitization degree of the samples increases slightly with increasing nitrogen gas concentration. Zhao studied carbon nanostructures production by an AC arc discharge plasma process at atmospheric pressure and concluded that the value of I_D/I_G decreases from 1.2 to 0.6 with the increasing arc discharge current (Zhao, 2011). In contrast, in their study the temperature increases along with the arc discharge electric current elevates, while in our study the electric current was kept constant and the temperature was regulated according to the gas mixture N_2/He at near atmospheric pressure. Nitrogen exhibits higher plasma temperature in comparison with helium plasma and, the lowest I_D/I_G corresponds to N100 sample (I_D/I_G ~ 0.81), when only nitrogen was used.

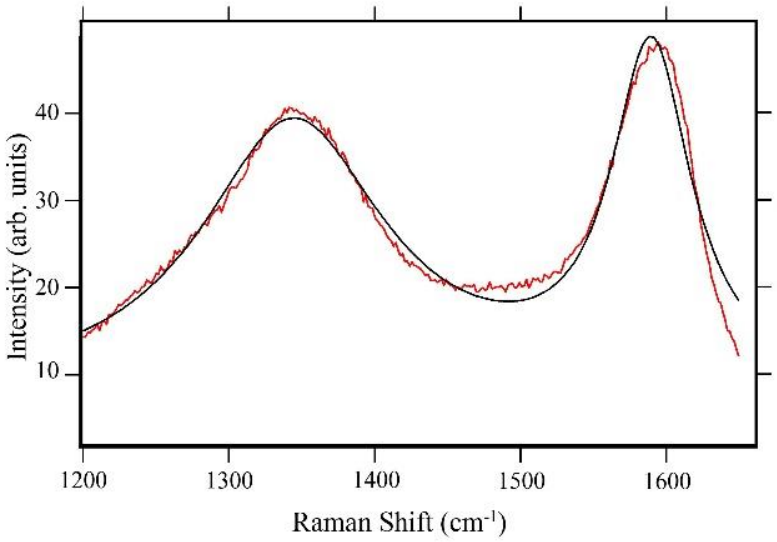

(a)

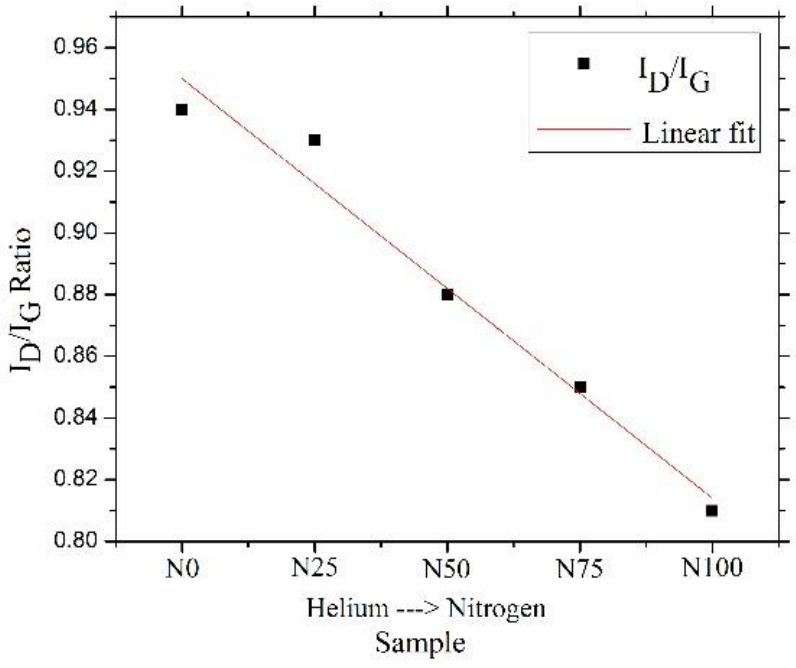

(b)

Figure 3.2-8. (a) Micro-Raman spectra of N100 sample fitted to a Lorentzian function; D and G peaks are located near ~1350 and ~1600 cm^{-1}. (b) This graph shows the I_D/I_G ratio for each sample. By using only helium (N0), the number of defects is always higher than samples that were obtained by using nitrogen and/or its mixture with helium.

Afterwards, the magnetic properties were characterized by a superconducting quantum interference device (SQUID). CEINPs and CEMINPs magnetic behaviors were investigated at 300 K. Figure 3.2-9 represents the comparison of normalized hysteresis curves for N100, N75, N50, N25 and N0 samples.

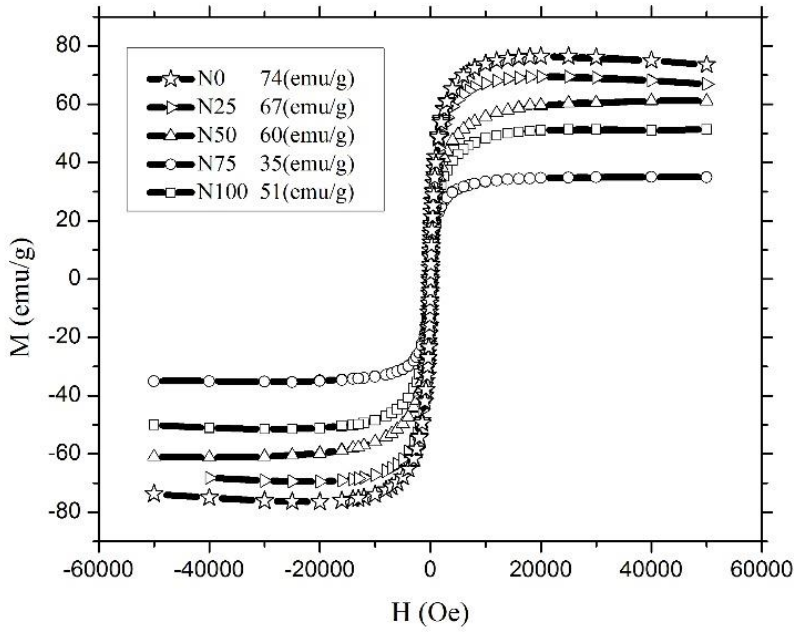

Figure 3.2-9. Hysteresis curves comparison of N0, N25, N50, N75, and N100 samples. The saturation magnetization, M_{sat}, are 74, 67, 60, 35, and 51 (emu/g), respectively.

The saturation magnetization, M_{sat}, for the nanocrystalline ferrites, in general is found to be lower compared to their bulk value, which is attributed to surface spin effects (Dahotre and Singh, 2014). Saturation magnetization largely depends on size, shape, metal composition, crystalline magnetic anisotropy energy, as well as coating by non-magnetic materials (Gutsch, 2002, Sato, 1987). N0 sample exhibits a higher saturation magnetization than samples generated in presence of nitrogen. Therefore, from morphological point of view, as the iron cores are reforming from spherical shape to smaller oval shape, the saturation magnetization decreases. Size dependency of saturation magnetization is reported in the literature (Dutta, 2009, Seehra, 2010, Sanchez, 2002). Interestingly, in spite of smaller iron cores, the multi iron cores nanoparticles (N100 sample) exhibit a higher saturation magnetization than single oval shape nanoparticles in N75 sample. Jafari studied the effects of carbon shell on the structural and magnetic properties of Fe_3O_4 and concluded that the magnetization of

Fe_3O_4 nanoparticles was reduced after coating with carbon (Jafari, 2014). Bittova carried out a research study on the effects of coating on dipolar inter particle interactions and showed the reduction of saturation magnetization after coating as well (Bittova, 2010). The single iron core is mainly located in the center of a large carbon shell while the multi iron cores are distributed in a carbon shell. Therefore probably carbon shell has less negative magnetic effect to multi iron cores, comparatively. Increasing the saturation magnetization of magnetic nanoparticles may permit more effective development of multifunctional agents for simultaneous targeted cell delivery, magnetic resonance imaging contrast enhancement, and targeted cancer therapy in the form of local hyperthermia (Hadjipanayis, 2008). Zero-field-cooling (ZFC) and field-cooling (FC) curves exhibit the main attributes of a superparamagentic system. ZFC and FC magnetization curves from N100 sample are plotted in Figure 3.2-10(a). All the samples were in superparamagnetic state at room temperature. Multi iron core nanoparticles blocking temperature ($T_B \approx 30$ K) of N100 sample is lower than other samples, followed by N75, N50 43 K, N25 and N0 with 36 K, 43 K, 45 K and 55 K respectively. The T_B values versus median size from size distribution analysis are plotted in Figure 3.2-10(b). The finding that T_B decreases as the size of the nanoparticles decreases is consistent with conventional Stoner-Wohlfarth theory (Lee, 2005): the energy barrier, over which the magnetization of the nanoparticles should be thermally activated, increases as the size of the nanoparticles increases. Consequently, the lowest T_B value of CEMINPs confirms the existence of smaller iron nanoparticles comparing to the other samples. The sum of multi iron cores in each carbon shell is greater than a single oval shape in N75 sample but its T_B value is lower. This is an interesting characteristic of CEMINPs. The result of low T_B value opens the possibility of using superparamagnetic particles in applications that required high standard and needs to operate at very low temperatures such as sensors in aerospace industry. Moreover, magnetic properties results of CEMINPs and CEINPs are important because in principle, the interest in magnetic particles is all due to the possibility to governing, heating and detecting them by an external magnetic field for biomedical applications.

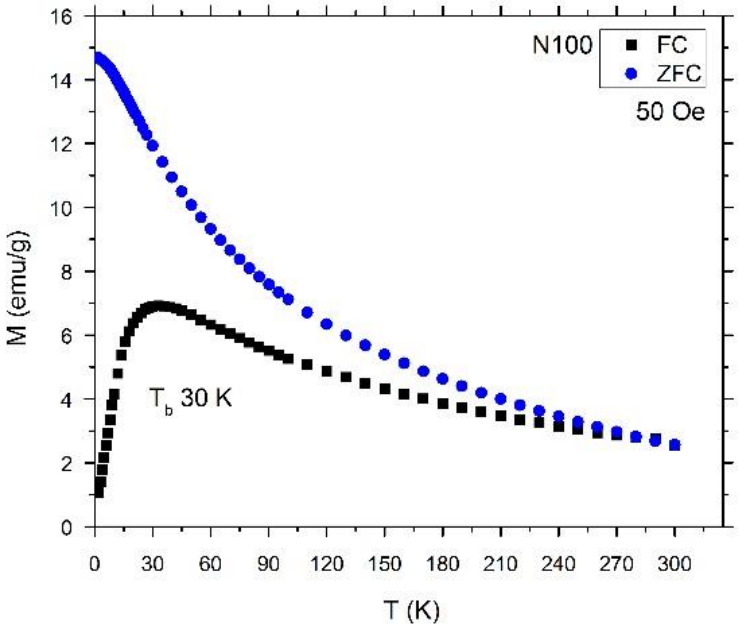

(a)

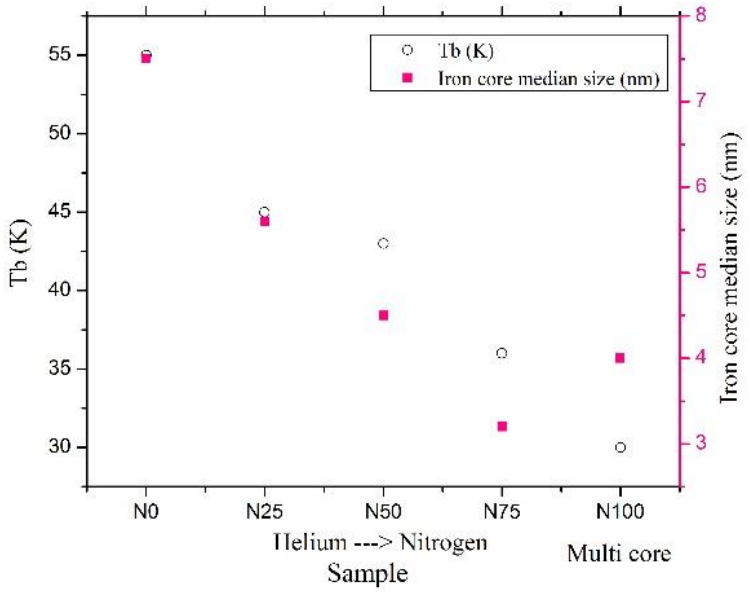

(b)

Figure 3.2-10. (a) Zero-field-cooled and field-cooledmagnetization curve ofmulti-iron core nanoparticles measured at 50Oe. This type of nanoparticles exhibit a low blocking temperature (30 K) and become in superparamagnetic state above 240K. (b) This graph shows the changes between blocking temperature and iron median size for each sample.

3.2.3 Conclusions

Mono and multi iron nanoparticles encapsulated in carbon shell were controllably synthesized using a new modified arc discharge reactor. Influence of nitrogen on plasma evidenced higher concentration of carbon species and changes the morphologies of CEINPs and CEMINPs. Moreover, the nature of gas has influence on yield of nanoparticles, in particular, nitrogen plasma provided highest yield in our study. The diffraction points of iron oxide were not detected from SAED and FFT techniques. In addition, EELS analysis at nanoscale and EDX analysis at micro scale showed no trace of oxygen in iron cores, hence samples were well protected by carbon shells. Based on the Raman spectroscopy results, high carbon crystallinity is observed when only nitrogen is used. Sufficient iron core protection along with low defects of carbon shell structure promote very small pores and therefore minimize the possibility of iron oxidation, degradation and or possible toxicity, hence both CEINPs and CEMINPs are suitable for high chemically active environment. All the particles show a superparamagnetic behavior at room temperature as determined by SQUID measurements. Lowest blocking temperature of 30 K evidenced the synthesis of smaller multi cores than mono core nanoparticles. Interestingly, although multi iron cores are smaller than single iron core in CEINPs (N75), they exhibit higher saturation magnetization. One of the reasons can be the existence of a few iron cores in a single carbon shell and therefore carbon shell has a lower negative effect on magnetic properties. Owing to the extremely close distance (around 2 nm) between iron cores in CEMINPs, there will be higher visibility comparing to CEINPs and, therefore, this type of nanoparticles have more priority to be used as contrast agent. On the other hand, it is noteworthy to mention that due to the carbon shell spherical shape and iron superparamagnetic behavior, their movement in body fluid can be smooth and controllable and hence the CEINPs can be potentially used in drug delivery. It is concluded that the gas nature of the reactor plasma used in the research project has a significant effect on the morphological properties of CEINPs. Accordingly, by this method CEINPs and CEMINPs can be synthesized based on the desired applications.

3.3 Influences of precursor concentration and gas flow on carbon encapsulated iron nanoparticles formation

(Journal of Nanomaterials, article ID 450183, 2015)

The objective of the present experiment is to study the gas flow influence on carbon coated iron nanoparticles and also to improve the protection against the oxidation that usually appears in core@shell nanoparticles. Spherical iron nanoparticles coated with a carbon shell were obtained by a modified gas phase arc-discharge reactor. Oxidized iron nanoparticles involve a loss of the magnetic characteristics and also changes in the chemical properties. Our nanoparticles show superparamagnetic behavior and high magnetic saturation owing to the high purity α-Fe of core and to the high core sealing, provided by the carbon shell. In this modified gas phase reactor, a liquid iron precursor was injected in the plasma spot, dragged by an inert gas flow. A fixed arc-discharge current of 40A was used to secure a stable discharge, and several samples were produced at different conditions. Transmission electron microscopy indicated an iron core diameter between 5 and 9 nm. Selected area electron diffraction provided evidences of a highly crystalline and dense iron core. The magnetic properties were studied up to 5K temperature using a SQUID. The results reveal a superparamagnetic behavior, a narrow size distribution (σg = 1.22), and an average diameter of 6 nm for nanoparticles having a blocking temperature near 40K.

Superparamagnetic particles appear to be important agents for a variety of applications in the fields of drug delivery, magnetic resonance imaging (MRI), and cancer treatments like hyperthermia. This is due to the special magnetic characteristic of these particles. That is the reason of our interest in studying the size limits under which the nanoparticles present a superparamagnetic behavior (Martínez-Boubeta, 2006). In order to synthesize nanoparticles in the vapor phase, appropriate conditions should be created. Like in the case described in the capillary theory of nucleation and under supersaturation conditions, a vapor phase mixture in thermal plasma (arc-discharge) can become thermodynamically unstable giving place to a nucleation process (Kharisov, 2012). From that and setting particular conditions, it is possible to produce solid phase homogeneous particles in the vapor phase surrounding the hot spot of the arc-discharge. The method varies depending on the phase of the precursor

that we are interested to use. Here, the precursor is injected into thermal plasma, which provides the necessary conditions to induce reactions that lead to supersaturation and particle nucleation. Under the condition of thermal plasma, the precursor decomposes in radicals, atoms, and ions forming a high temperature ionized gas. The high concentration of species and high temperatures in the plasma arc induce a diffusion process associated with a fast quenching of gas species. During this process, the gas species react and condense to form particles in a similar way to a vaporized material when cooled down by mixing with a cool gas or expanded through a nozzle (Swihart, 2003). Fe is one of the most common materials used for the formation of magnetic nanoparticles. It is due to its superparamagnetic behavior, which is easily controlled by the nanometric size of the magnetic core, and because the Fe is suitable for biomedical applications. The use of a carbon shell is intended to achieve the required biocompatibility and prevents oxidation of the iron core and formation of agglomerations of nanoparticles (Sounderya and Zhang, 2008). The structural and morphological characteristics like shape and size distribution were studied using transmission electron microscopy (TEM) and selected area electron diffraction (SAED). The absence of oxygen was preliminarily evidenced by the energy-dispersive X-ray analysis (STEM EDX). The magnetic characteristics were determined using a superconducting quantum interference device (SQUID).

3.3.1 Method

In order to facilitate the study of magnetic behavior and other characteristics of core@shell nanoparticles, we modified an arc-discharge reactor in order to operate for longer time and produce large amounts of them. The scheme of the reactor is shown in Figure 3.3-1. To facilitate the complete collection of the produced nanoparticles we dragged them out of the arc-discharge chamber, by a laminar flow of an inert gas (He) to a flask cooled by liquid nitrogen. The precursor was carried by the gas phase. Helium is used to drag the microdroplets of precursor. The carbon electrodes can be rotated and moved in order to avoid problems that the consumption of carbon electrode could cause. One of the electrodes has a sharp conical tip shape (cathode) and the other has a cylindrical shape with an approximate diameter of 4 cm, and can rotate and move backward and forward (anode). The plasma is being

generated by a power supply to produce an arc DC current of 40 A. The pressure was kept stable at near-atmospheric conditions (5-8 × 10^4Pa). The run period of one experiment was 30 min. Although, to obtain more quantity of product, in principle we can extend the time, it requires having stable conditions during the production process. We used pure He to drag the precursor compound because plasma becomes more stable (Ando and Zhao, 2006). We investigated the effects of two technological parameters, the concentration of the Fe precursor into the solvent isooctane and the total gas flow (He). Both the isooctane and the Fe precursor (ferrocene) were of a purity of 99.9%. In our study, we define residence time as the period that one particle of the precursor is spending inside the plasma zone. The time that gas atoms and precursor radicals stay inside the plasma zone depends on the gas flow rate. This has an effect on the size of the particles as the longer they stay inside the plasma zone, the larger they grow (Vardelle, 2001).

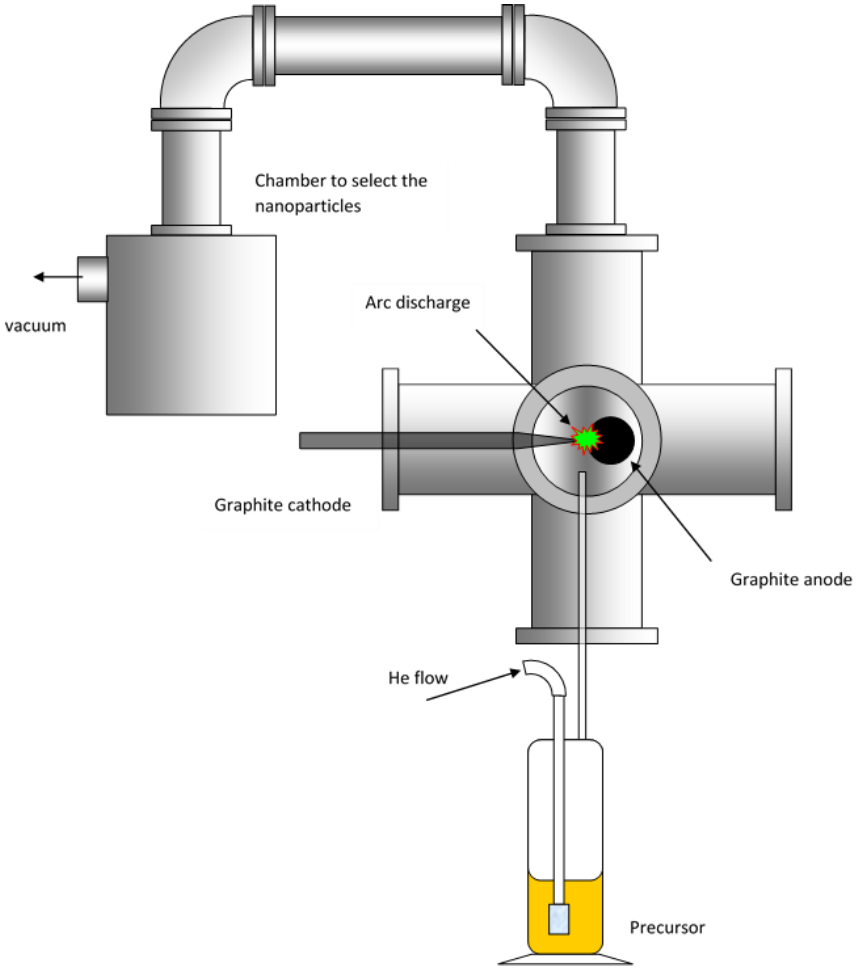

Figure 3.3-1. General picture of the gas phase arc discharge reactor used for the synthesis of the iron core encapsulated in carbon nanoparticles.

The velocity u and the He flow rate, Φ, are related through the equation:

$$u = \frac{4\Phi}{\pi d^2} \qquad (1)$$

Where d is the internal diameter of the cannula through which the gas is targeted in the plasma zone (~3 mm). By measuring the size of the plasma zone h (~5 mm) we can estimate the residence time:

$$\tau = \frac{h}{u} \qquad (2)$$

Table 3.3-1 shows the different residence times for several values of He flow rate. Different concentrations of Fe precursor into the isooctane, from 1% to 4% w/w, were used to determine the effect on the size of the particles and on the total amount of the obtained product.

Table 3.3-1. Flow rate and resulting velocity and residence time for a precursor vapor with 1% of ferrocene concentration.

He flow rate, Φ (sccm)	Precursor vapor velocity, U (cm/s)	Residence time, τ (ms)
30 ± 2	7.07 ± 0.50	71 ± 1.5
60 ± 2	14.13 ± 0.50	35 ± 1.5
120 ± 2	28.28 ± 0.50	18 ± 1.5

3.3.2 Results and Discussion

Images of nanoparticles were observed by TEM (JEOL 2100) in high resolution mode, using 200 kV and a probe size of 0.5 nm. Prior to TEM observations, the formed nanoparticles were diluted in methanol and then magnetically filtrated. The size distribution of the nanoparticles follows the lognormal function described by Granqvist and Buhrman (Granqvist and Buhrman, 1976):

$$f(D) = \frac{1}{\sqrt{2D}ln\sigma g}\exp\left(-\frac{ln^2(D/\bar{D})}{2ln^2\sigma g}\right) \qquad (3)$$

Here, D is the particle diameter, $\bar{D}$ is the diameter geometric mean, which in a lognormal distribution is equal to its median, and σg is the geometric standard deviation (dimensionless), which describes how spread out are the set of core diameters from the geometric mean. Figure 3.3-2 shows several pictures as example of the obtained particles for different flows and concentrations. Figure 3.3-2(a) shows

a TEM image of nanoparticles obtained with a precursor flow of 30 sccm, in a concentration of 1% w/w. Actually, this is the only sample that presents an important difference in the size distribution from all the others (average diameter of 8.18 nm). When the precursor concentration was doubled to 2%w/w, the iron core average size decreased to 5.43nm (Figure 3.3-2(b)). Figure 3.3-2(a) shows how the carbon forms a shell around the Fe core. The shell of carbon in this sample was measured to be between 4 and 6 nm thick. After doubling the precursor concentration to 4% w/w, the size of these particles remains quite constant to 5.34 nm, but the total amount of particles and density of Fe cores increase (Figure 3.3-2(c)). From Table 3.3-2, when the precursor concentration is kept to 1%w/w, an increase of the He flow produces a decrease in the iron core size. Residence time can explain this behavior only for conditions of low precursor concentrations. At higher precursor concentrations, residence time seems to have no influence on the iron core size. This behavior could be associated with the increase of the nucleation inducing an increase in the particle concentration, as evidenced by comparing Figure 3.3-2(b) and (c). This phenomenon could be related to the reduction of the supersaturation conditions, establishing a competitive mechanism limiting the resulting iron core size.

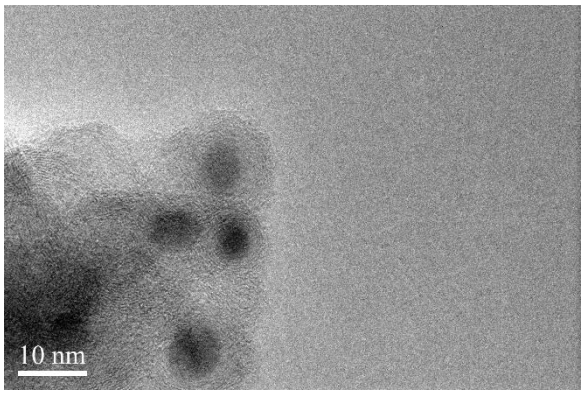

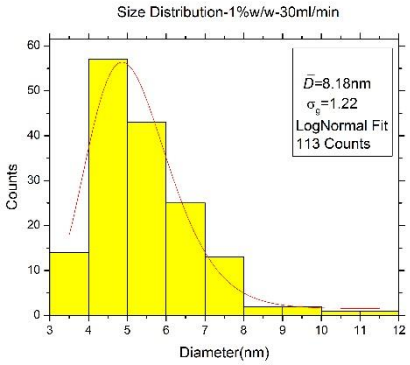

(a)

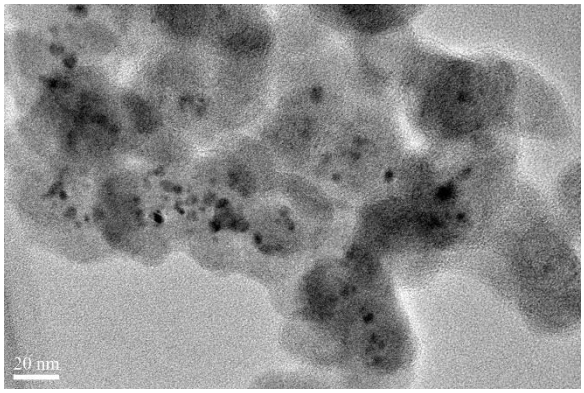

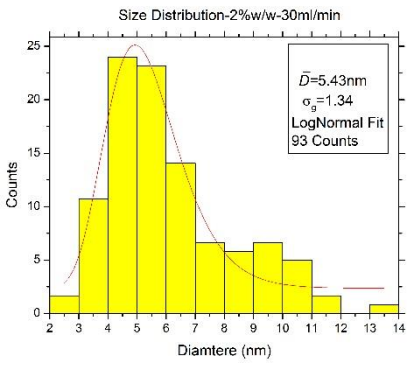

(b)

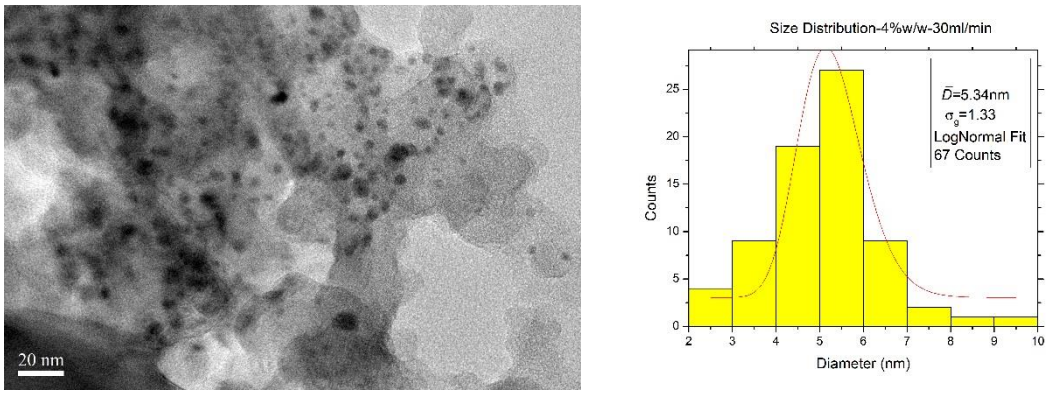

(c)

Figure 3.3-2. TEM images of iron encapsulated in carbon nanoparticles produced by arc-discharge (40 ± 5 A of current) using different flows and concentrations accompanied by their size distribution histograms. (a) 30 sccm with a concentration of 1% w/w, (b) 30 sccm with a precursor concentration of 2% w/w, and (c) 30 sccm with a concentration of 4% w/w.

Table 3.3-2. The iron core diameter average and its standard deviation of all our samples in relation to the two set parameters, He flow rate and ferrocene/isooctane concentration. Samples with 1.1 < σ_g < 1.4 are quite monodisperse. Samples having σ_g above 1.4 (He flow of 60 sccm and low ferrocene concentration) are bimodal.

Iron core size (nm)/geometric standard deviation, σ_g			
He flow rate (sccm)	[Ferrocene/isooctane] 1% w/w	[Ferrocene/isooctane] 2% w/w	[Ferrocene/isooctane] 4% w/w
30	8.18/1.22 Figure 3.3-2(a)	5.43/1.34 Figure 3.3-2(b)	5.34/1.33 Figure 3.3-2(c)
60	6.23/1.47	6.12/1.46	5.22/1.22
120	5.22/1.25	___	___

Another detail in the micrographs of Figure 3.3-2 is the absence of coalescence. This indicates a low concentration of nucleus during the growth process for the conditions listed in Table 3.3-2. By treating all the size distribution results with ORIGIN tools, D and σ_g were determined. The diameter of the nanoparticles was determined by ImageJ, a free software tool for image processing and analysis. Figure 3.3-3 shows the histogram of the size distribution for the nanoparticles, which were synthesized under a precursor flow of 60 sccm and a ferrocene concentration of 4% w/w. The resulting geometric size average is 5.22 nm and the geometric standard deviation 1.22.

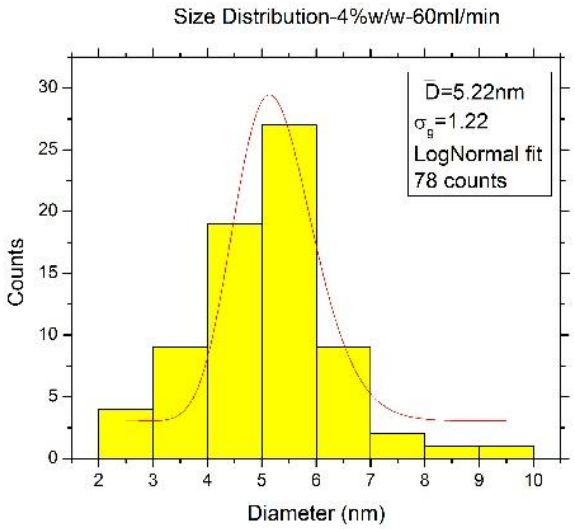

Figure 3.3-3. Histogram of the size distribution for iron nanoparticles grown under precursor concentration of 4% w/w and He flow of 60 sccm. The iron core is 5.22 nm and the geometric standard deviation σ=1.22.

All the studied samples (Table 3.3-2) present a size distribution of the iron core between 5.22 nm and 8.18 nm. This could be due to the stabilization of the growth of the carbon shell after reaching the critical radius of a carbon sphere. Under this hypothesis, the formation of a stable carbon shell would limit the Fe core growth. According to the studies reported by Kuznetsov (Kuznetsov, 2001), the nucleation of carbon on the surface of the metal catalyst is something common for all kinds of carbon deposits. The difference in morphology of the carbon deposits depends on the reaction conditions and on the nature of the metal catalyst. A thermodynamic analysis of the effect of different reaction parameters on the critical radius of the carbon nucleus was performed and, it showed that an increase in the temperature can be responsible for the formation of smaller nuclei.

Another interesting fact supporting the formation of a carbon shell surrounding the iron nanoparticles is that the use of metals, which are characterized by a higher metal-carbon energy bond, yields nanotubes of smaller radius (Kuznetsov, 2001). In these studies, the critical radius of the carbon is related to the change in Gibbs free energy during the nucleation (Kuznetsov, 2001). The only sample that seems not to follow this assumption is the one grown under conditions of 1% w/w of Fe concentration and precursor flow of 30 sccm. This result could be related to the higher residence time associated with a low flow rate, which leads to an increase in the core

size and a delay in reaching the conditions of carbon supersaturation located outside the hot plasma region.

To discuss the size distribution of our samples we can rely on the geometric standard deviation, σ_g. The results of size and dispersion of iron cores along with their experimental parameters are listed in Table 3.3-2. A geometric standard deviation lower than 1.1 indicates a monodisperse size distribution, whereas for values above 1.4 indicates a wide distribution of size. Between these two values the size distribution is considered quite monodispersed. When the dispersion is larger than 1.4, the size distribution is considered to be bimodal (Merkus, 2009). Table 3.3-2 lists the level of dispersion of the different samples.

The absence of oxygen in the spectrum was preliminarily evidenced by the energy-dispersive X-ray analysis (STEM-EDX). Oxygen peak is not present in the spectrum in the expected energy (O-Kα at 525 eV), which indicates a low level of oxygen. In addition, a HRTEM picture of an iron encapsulated in carbon nanoparticle was explored (Figure 3.3-4). To obtain the crystal structure of the iron core and the carbon shell, we calculated its fast Fourier transform (inset of Figure 3.3-4). The only phases evidenced from this figure were the α-Fe (d-spacing = 0,202nm) and the iron carbide (d-spacing = 0,221 nm). No diffraction points of iron oxides were detected (Aguilo-Aguayo, 2010) in any of our samples. The phases of iron carbide probably are located in the interface between the iron core and the carbon shell. As we comment below from the magnetic measurements, the content of the iron carbide phase is minor if compared with the α-Fe.

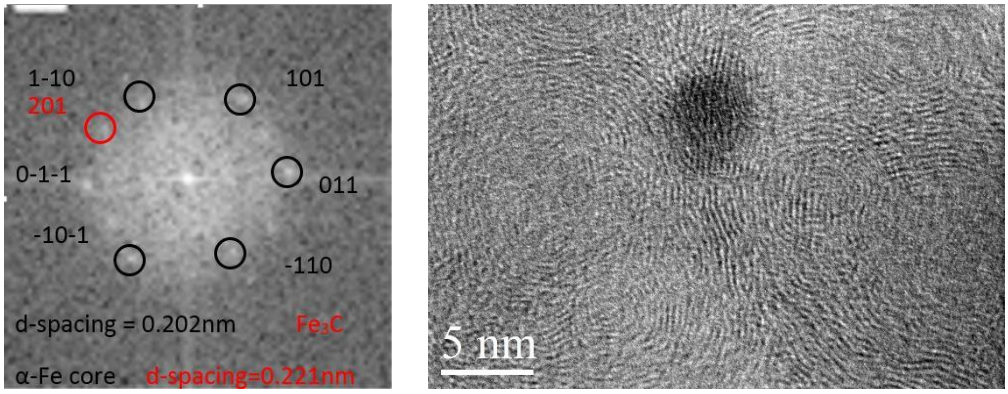

Figure 3.3-4. TEM image of a nanoparticle. In the small picture we can see the calculated FFT diffraction pattern from which we obtain the crystalline structure of the iron core. Here it corresponds to the α-phase.

In addition carbon shell appears surrounding completely the iron cores forming crystalline domains with a structure similar to the fullerene one. This result suggests that iron core is completely sealed into the cover shell, which is of great importance and interest in biomedical applications (Bakoglidis, 2012).

SQUID measurements were used to investigate the magnetic characteristics of our samples. Two hysteresis loops (Figure 3.3-5) of different samples were studied to compare their characteristics. Samples of Figure 3.3-5 (a) and (b) were produced by means of a precursor gas flow of 30 sccm and with a precursor concentration of 1% w/w and 2% w/w, respectively. From the hysteresis loop measured by SQUID at 5 K we have obtained the coercive field HC. For the sample of the 2% w/w concentration having a diameter 5.43 nm, this is 0.03T and, for the sample of 1% w/w with a diameter of 8.18 nm, it is 0.05 T. These results come in agreement with other results, which indicates the influence of the size on the magnetization when it comes to superparamagnetic nanoparticles (Han, 2006).

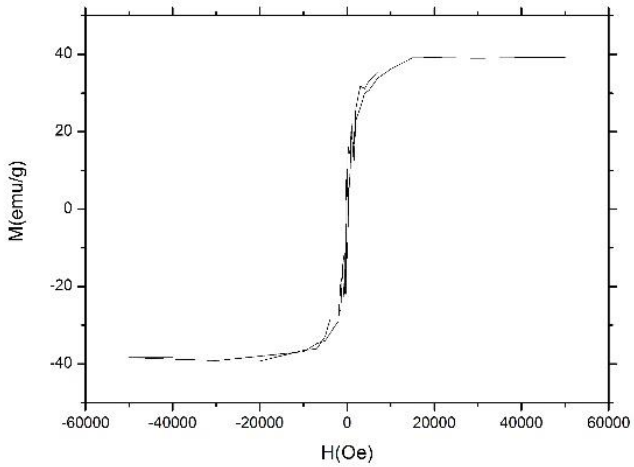

(a)

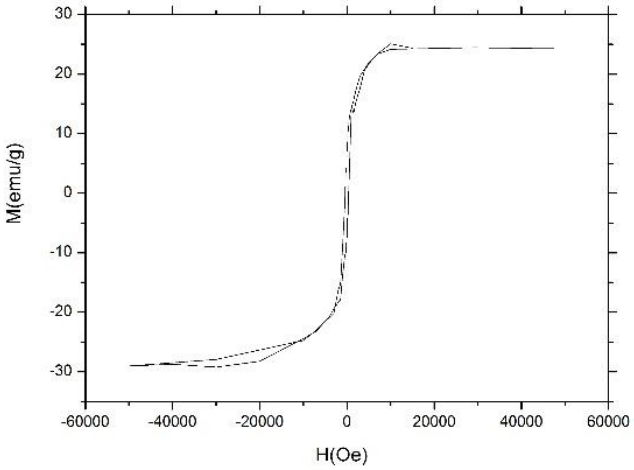

(b)

Figure 3.3-5. The hysteresis loops measured at 5K for samples with different precursor concentrations: (a) 1% w/w and (b) 2% w/w. Both were obtained at a precursor gas flow of 30 sccm.

Subsequently we compare the values of the coercive field with those reported in the bibliography for magnetic nanoparticles encapsulated in carbon nanotubes (Gozzi, 2006). We have calculated the critical radius of the iron consisting of uniaxial nanoparticles. To achieve this, we use the Neel- Arrhenius equation (Néel, 1949) for blocking temperatures T_B = 40 K and k_B = 1.380·10^{-23} J/K assumed. Then, from the equation:

$$T_B = \frac{K.V}{K_B.log(t_m/t_0)} \qquad (4)$$

Where the factor log (t_m/t_0) = 25, tm is the measuring time of the SQUID (100 s), and t_0 is the characteristic relaxation time. The value K is the anisotropy energy density (K = 4.8 × 10^4 J/m^3 for Fe bulk) and the volume is as follows:

$$V = \frac{4\pi}{3}\frac{d^3}{8} \qquad (5)$$

Where d is the diameter of the core. From the above relations the critical radius is calculated to be 4.09 nm. The theoretical graph shows the connection of the radius of the nanoparticles to H_C and the comparison with the values of the samples shows an agreement. To obtain the curve, the following equation is used (Cullity and Graham, 2011):

$$H_c = H_{CO}\left[1 - \left(\frac{D_P}{D}\right)^{3/2}\right] \qquad (6)$$

In this equation, H_{CO} is the field that should be applied in order to demagnetize the bulk material, D_P is the critical radius belowwhich our particles become superparamagnetic, and D is the real radius of the sample. For particles of 5.43 nm we expect a coercive field H_c = 0.035 T. The coercive field from our sample of this size is measured to be 0.030T, which is a value very close to the theoretical one. For nanoparticles of a diameter around 8.1 nm the theoretical value of H_c is expected to be 0.053 T. The value of our sample of this diameter is 0.050 T, which is also in agreement with the theoretical one. In the case of very small nanoparticles, one can observe superparamagnetic behavior related to the fact that a demagnetization effect arises from the additional energy of the magnetic fields outside the graphitic carbon encapsulation (Uhm, 2010).

SQUID measurements of a sample in concentration of 1%, in a precursor gas flow of 60 sccm, and in temperatures of 5 and 300 K were taken. In Figure 3.3-6 the normalized magnetization versus the applied field can be seen. The ratio of remnant to saturation magnetization both at 5 K and in room temperature is 0.9, less than 0.25, which is the value for the paramagnetic materials, so the carbon-coated iron nanoparticles are superparamagnetic materials (Jin, 2013).

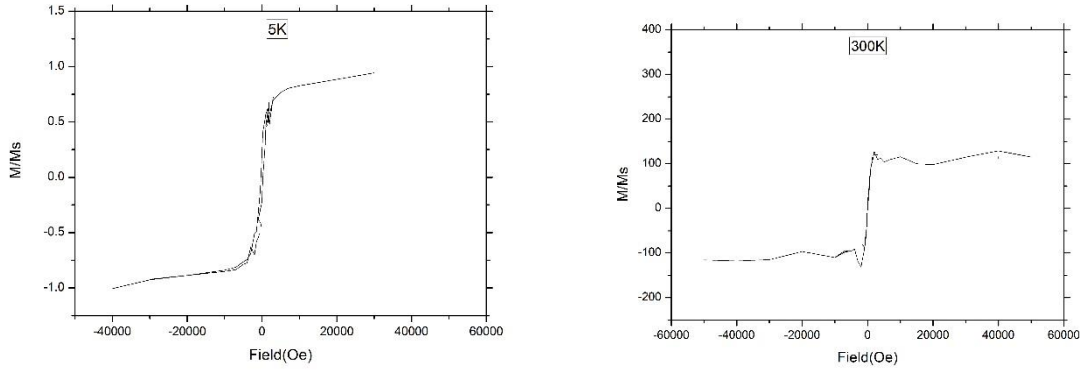

(a) (b)

Figure 3.3-6. Graphs of the normalized magnetization M/M_s ratio with the field in 5 K and room temperature.

From the zero field cooled and the field cooled curve it can be seen that the nanoparticles are superparamagnetic in room temperature. The blocking temperature appears near 40 K, where the maximum of the ZFC magnetization is localized. Gittleman's model describes blocking temperature and the critical volume that separates nanoparticles from the blocked state ($V > V_P$) and superparamagnetic state ($V_P > P$) (Gittleman, 1974). Also, as the peak of the zero field cooled curve is quite narrow, we can assume that the size distribution is narrow as well (Figure 3.3-7) (Hansen and Mørup, 1999).

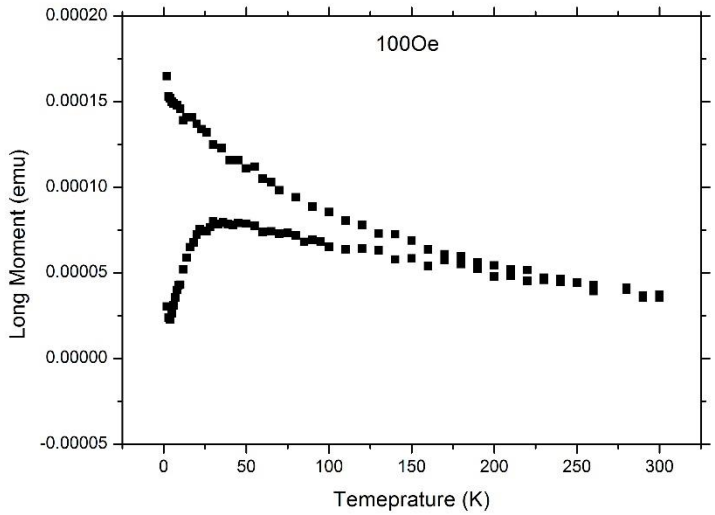

Figure 3.3-7. Zero fields cooled and the field cooled magnetization curves for 100Oe field.

3.3.3 Conclusions

Morphological and structural characterization revealed a quite good monodispersion as well as the α-phase crystallinity of the iron core, the iron carbide phase, and the absence of oxygen. These are very important factors when it comes to large scale productions, necessary for biomedical applications. The iron core is completely shielded by carbon. The magnetic characterization revealed the superparamagnetic behavior of the particles in temperatures above 300 K. Further research will be done concerning the improvement of the collection process of the nanoparticles in order to have the highest amounts possible per experimental round.

3.4 Synthesis of carbon nanoparticles decorated by fullerenes

The functionalization of carbon nanoparticles is limited due to their amorphous carbon structure. In this section, we developed a new approach for decorating carbon nanoparticles by fullerenes, which facilitates and extends the possibilities for functionalizing carbon nanoparticles.

Fullerene materials have received a wide attention due to their possible biomedical applications. The major limitations in practical applications of carbon nanoparticles are broad size distribution and functionalization. The arc discharge is a well-known technique for synthesis of carbon based materials. Here, we report the synthesis of carbon nanoparticles decorated by fullerenes (CNDFs) in one step (without adding additional fullerene), by a modified gas phase arc discharge method. The precursor component and carrier gas used in the delivery system in this modified gas phase arc discharge method allows a simple and continuous synthesis of carbon nanoparticles, which improves their size monodispersion. CNDFs characterization by SEM confirmed the spherical shape of nanoparticles with an averaged diameter of 50.4 nm, which is a suitable dimension for biomedical applications. Fullerenes were observed and analyzed by high resolution transmission electron microscopy. The carbon structures along the periphery were thin enough for observation of single molecules with fullerenic structure. Beside other applications and advantages of fullerenes, in this case, they can facilitate and extend the possibilities of functionalization of the carbon nanoparticles.

Carbon nanoparticles are nontoxic, biocompatible, and nonimmunogenic, which allows them to be used extensively in cellular delivery (Fang, 2010). The poor cellular penetration of many small molecules and proteins can be overcome by conjugation to a nanomaterial carrier, whose size, shape, and surface chemistry can be engineered for optimal cellular uptake (Ganeshkumar, 2013). It has been reported that the particle size and shape are key variables determining the rates and mechanisms of cellular uptake (Yan, 2006). A theoretical model has been developed by Decuzzi for the receptor mediated endocytosis of non-spherical particles, showing

that elongated particles lying in parallel to the cell membrane, and would not internalized to the cell, in contrast spherical particles internalized to the cell more easily (Decuzzi and Ferrari, 2008). Consequently, carbon nanoparticle synthesis in spherical shape is our interest. Difficulties of carbon nanoparticles functionalization can be overcome by conjugation to fullerene molecules. Decoration of nanoparticles by fullerenes extends and facilitates the possibilities of functionalization in view to possible applications to biomedicine and drug delivering. Accordingly, we set our objective to produce spherical carbon nanoparticles decorated with fullerene molecules on the surface. Arc discharge is well known for bottom-up growth of the whole family of carbon allotropes named fullerene. Fullerenes materials have received wide attention due to their biomedical applications such as photodynamic therapy, magnetic resonance imaging and also their capability to act as 'radical sponges' in various schemes (Partha and Conyers, 2009, Wang, 2014). So far, different methods such as laser ablation (Wu, 2011a), arc discharge (Churilov, 2013), electron beam evaporation (Thakur, 2011), diffusion flame (Goel, 2012) and ion beam sputtering (Chuanchen, 1994) are used for the synthesis of fullerene and carbon nanoparticles separately. Recently, Wang commented that spherical nanocarbon materials have properties that make them promising as nano-medicines and therapeutic agents and the major limitations of realizing the practical applications of fullerenes are high cost and low production yield. It will be important to develop a large scale method for the synthesis and purification of these structures (Wang, 2014).

By extensive trial experiments, the arc discharge reactor parameters have been optimized for synthesis of carbon nanoparticles based on drug delivery requirements in terms of size and shape. In the present contribution, we report single step synthesis of spherical carbon nanoparticle, decorated with fullerene on its surface, using a modified gas phase arc discharge reactor working at near atmospheric pressure. The precursor component and its delivery system allowed a facile and continuous synthesis of carbon nanoparticles to improve their size monodispersion. CNDFs have been studied by scanning electron microscopy (SEM) and high resolution transmission electron microscopy (HTEM).

3.4.1 Method

The arc discharge reactor was setup in a way to synthetize CNDFs s by continues flow of gas and precursor. In order to obtain stable and proper size, argon was selected and used as the inert carrier gas. The current was set constant (40 A) by a controlled DC power supply. Plasma was generated between two movable arms (electrodes) of pure graphite 99.99%. A small flow of argon (60 sccm) drag the precursor solution and separate gas flow (1600 sccm) deliver the CNDFs soot to the collection chamber. Precursor was prepared by solving ferrocene (99.5% purity) in benzene (99.9% purity). A high temperature resistance alumina thin tube was used for injecting to precursor gas to the plasma flame between electrodes. Finally, the collected CNDFs were washed four times in ethanol and kept in ethanol for their characterization.

3.4.2 Results and Discussion

Nanoparticles size distribution has an important impact in biomedical applications. In a review, Gaumet pointed out that biodistribution depends on the physicochemical properties of particles, especially size and the global message from the literature is that small particles have an enhanced ability to reach their target cell in drug delivery system (Gaumet, 2008). According to our previous experiments (Sanaee and Bertran, 2015), the carbon electrodes transformation leads to the broad size distribution synthesis of carbon encapsulated iron nanoparticles and also affect plasma in terms of stability and size, which are important parameters for the formation of nanoparticles by gas phase arc discharge method. The modified reactor facilitates the continuous delivery of precursor by gas flow. In this way, the precursor evaporation rate at room temperature and also the gas flow regulates the precursor delivery to plasma precisely. Consequently, the geometry of carbon electrodes relatively remains unchanged. This is important to achieve uniformity in the synthesis of nanoparticles (NPs). The SEM images of Figure 3.4-1 (a) indicate the spherical shape of the obtained CNDFs. Thus, these CNDFs can be more easily internalized to the cell than elongated particles (Ferrari, 2008, Decuzzi, 2009) due to their spherical shape. Accordingly, size distribution of CNDFs are estimated and plotted in Figure 3.4-1 (b).

Narrow size distribution of CNDFs is important due to the fact that this parameter directly influences the efficiency of the operation in view of their potential applications, especially in drug delivery system.

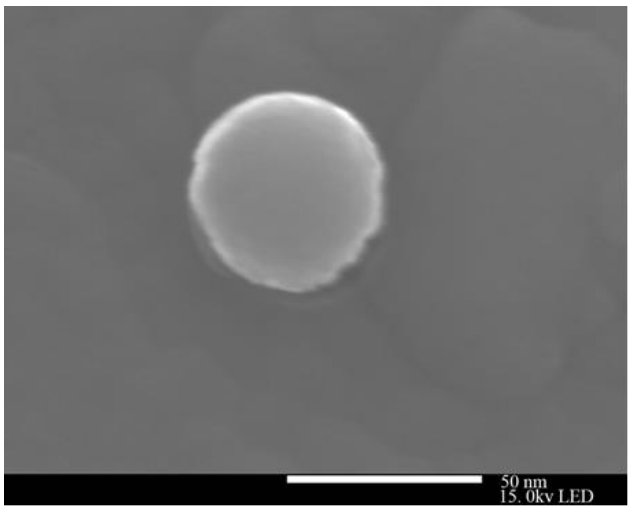

(a)

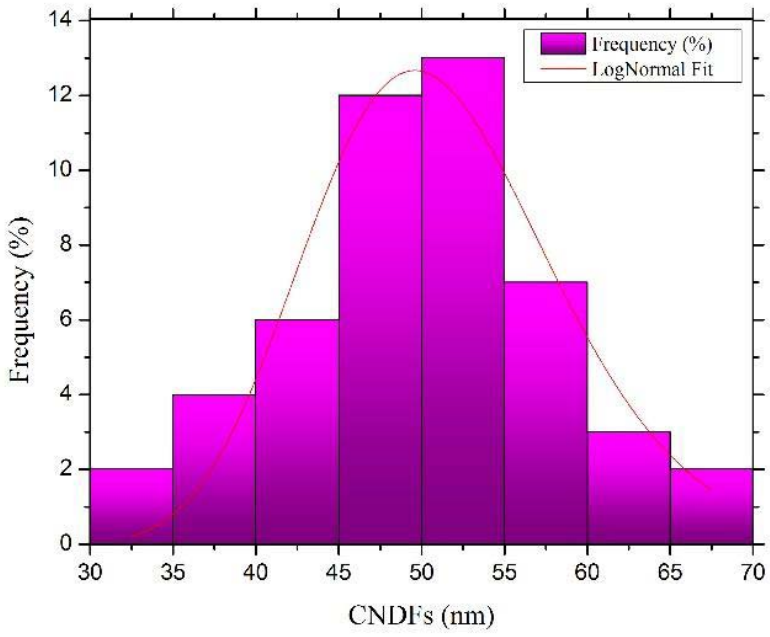

(b)

Figure 3.4-1. (a) SEM image of CNDFs in a group, which shows particles in spherical shape (b) Particle size distribution histogram of CNDFs is following a logarithmic-linear distribution with mean spherical carbon diameter of 50.4 nm.

The CNDFs size analysis shows a mean size of 50.4 nm and standard deviation is 7.8. From morphological point of view, the obtained CNDFs have optimum diameter 50 nm for endocytic uptake (Gao, 2005). Endocytosis is an energy-using process by which cells absorb molecules (such as proteins) by engulfing them (Peate and Nair, 2015). Moreover, it's worthy to mention that M. Ferrari, discussed the possibility of using nanoparticles themselves to be used as anticancer agents, even if they do not carry drugs (Ferrari, 2008). Nanoparticles of different sizes are taken up by cancer cells with different efficiency as shown graphically in Figure 3.4-2.

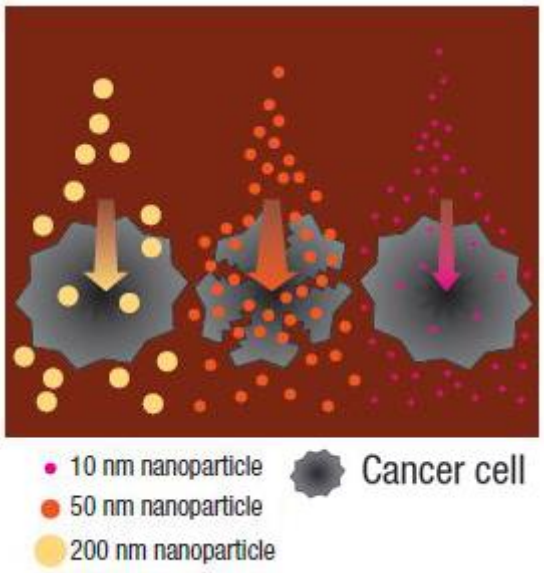

Figure 3.4-2. 50 nm nanoparticles are taken up by cancer cells with higher efficiency than 10 nm and 200 nm nanoparticles (Ferrari, 2008).

Obtained CNDFs shows high quality in terms of size distribution and shape and promises as an efficient nanocarriers.

Fullerene detection and size analysis have been done by high resolution transmission electron microscopy (HRTEM) technique. As explained by Goel an ability to observe an individual fullerene molecule by HRTEM is of interest for several reasons. Such a technique would offer a possible means for extending the detection and analysis of fullerenes to lower limits of detection than can be attained by conventional chemical analysis. In addition the HRTEM technique would be useful also for the detection and characterization of fullerenes which are too strongly bound to, or within, the material with which they are condensed in the synthesis process (Goel,

2004). Also, Chuvilin revealed direct transformation of single fullerene molecules from graphene by HRTEM technique (Chuvilin, 2010). Figure 3.4-3 shows carbon nanoparticles carrying fullerene molecules on the surface.

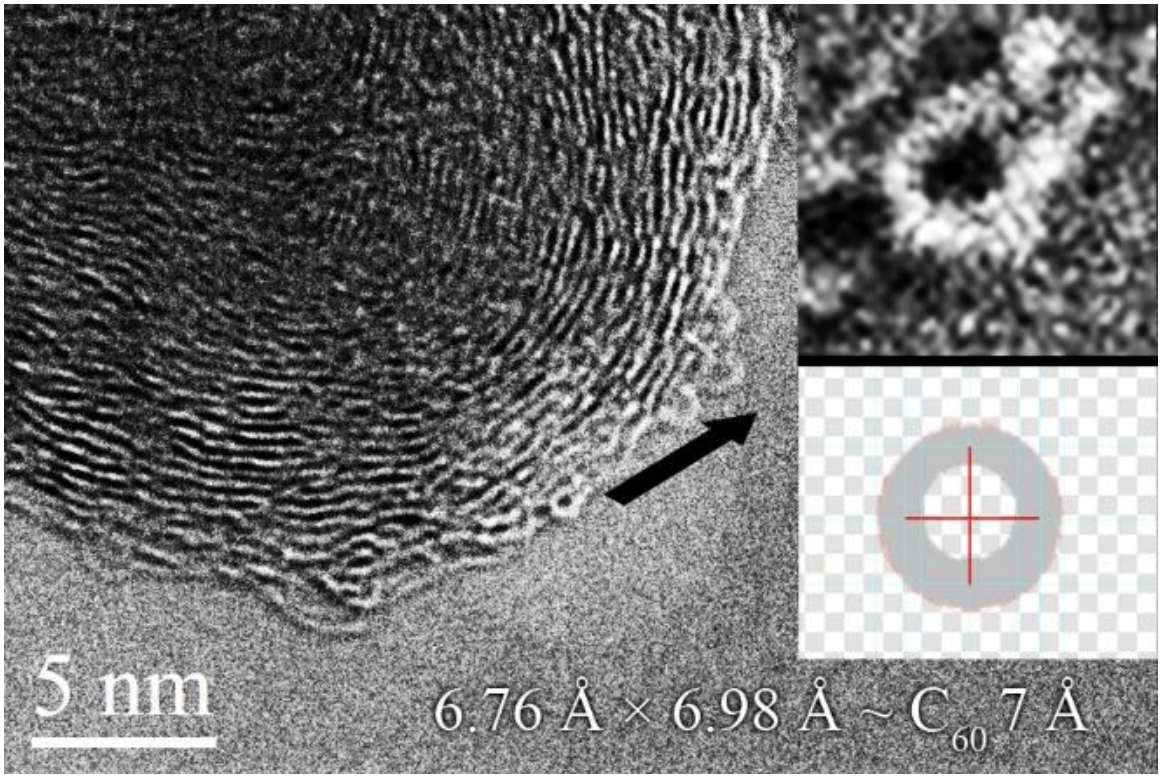

(a)

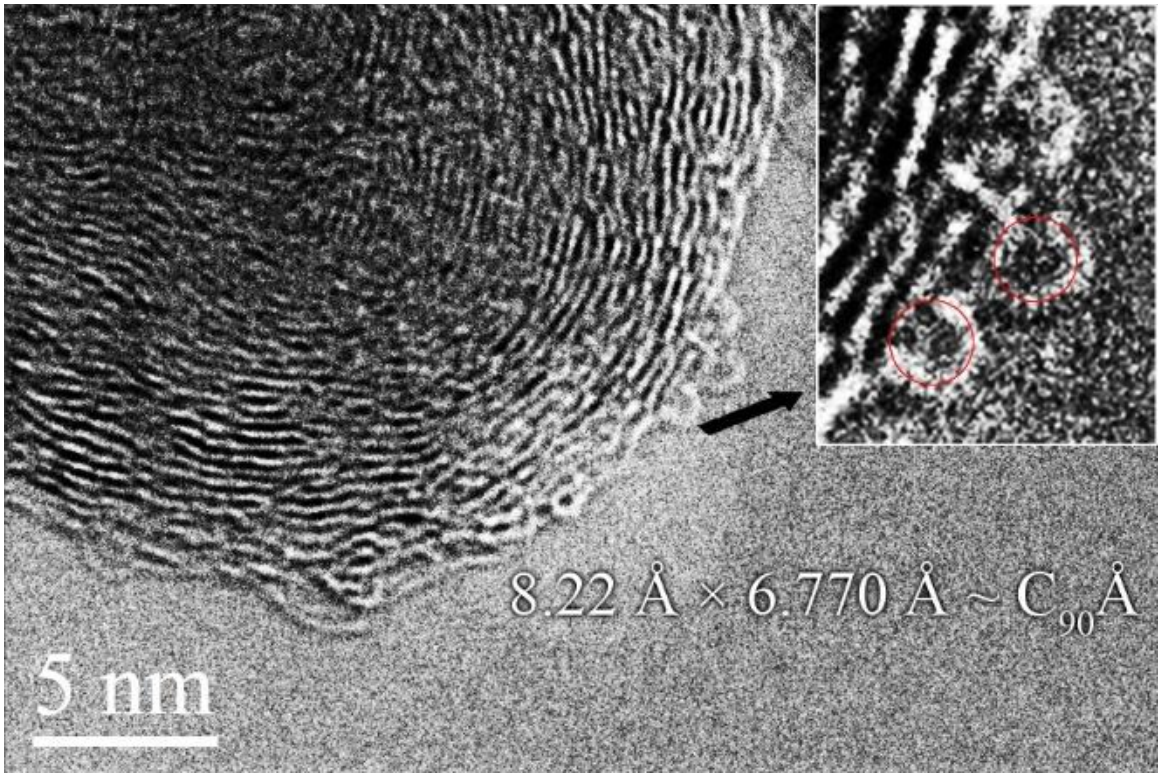

(b)

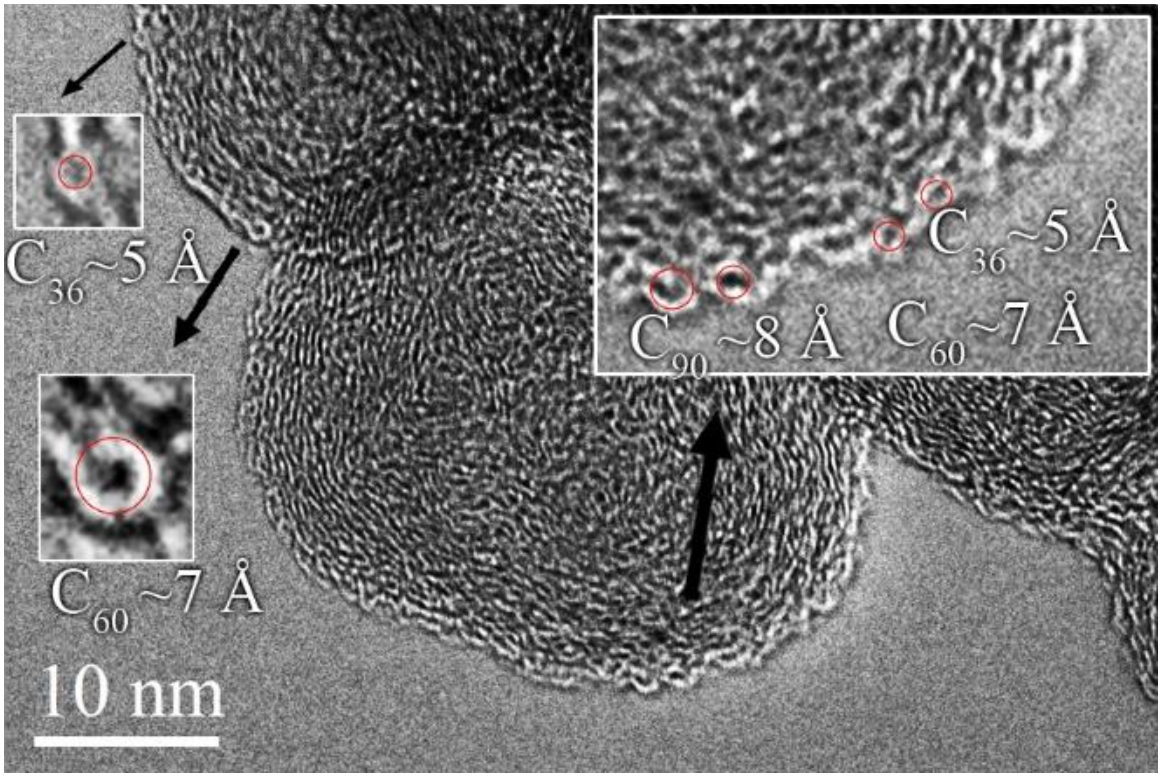

(c)

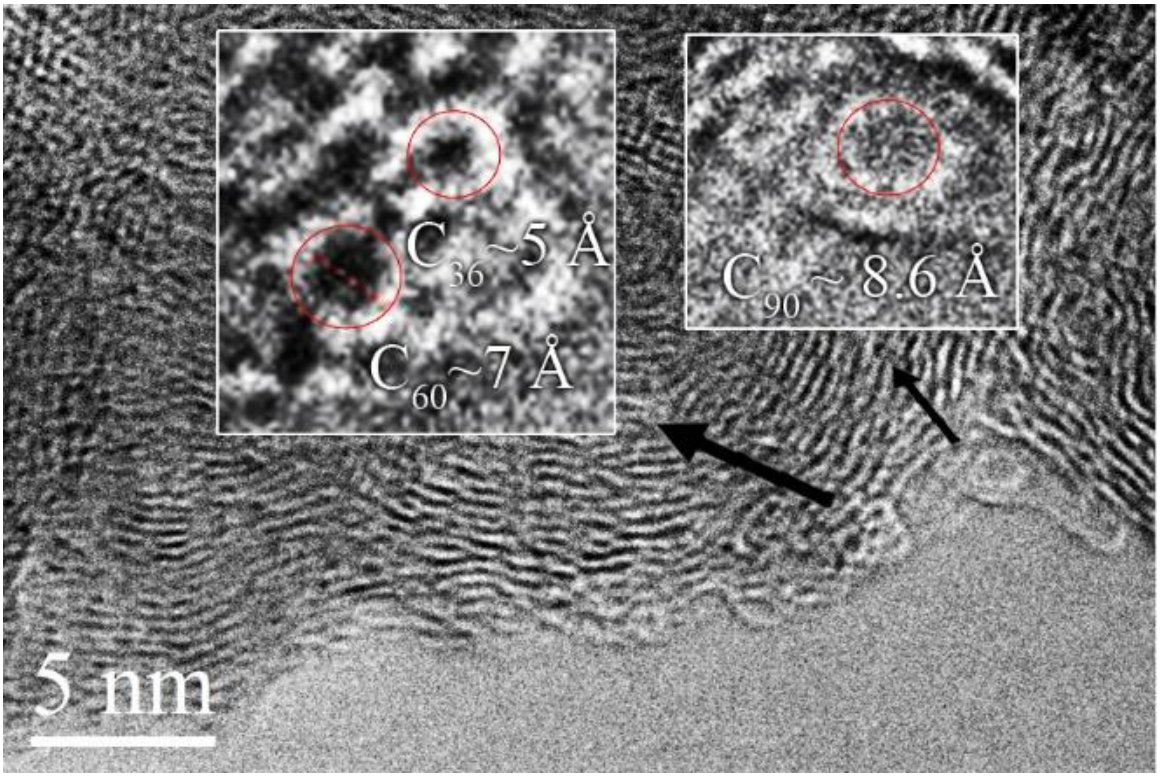

(d)

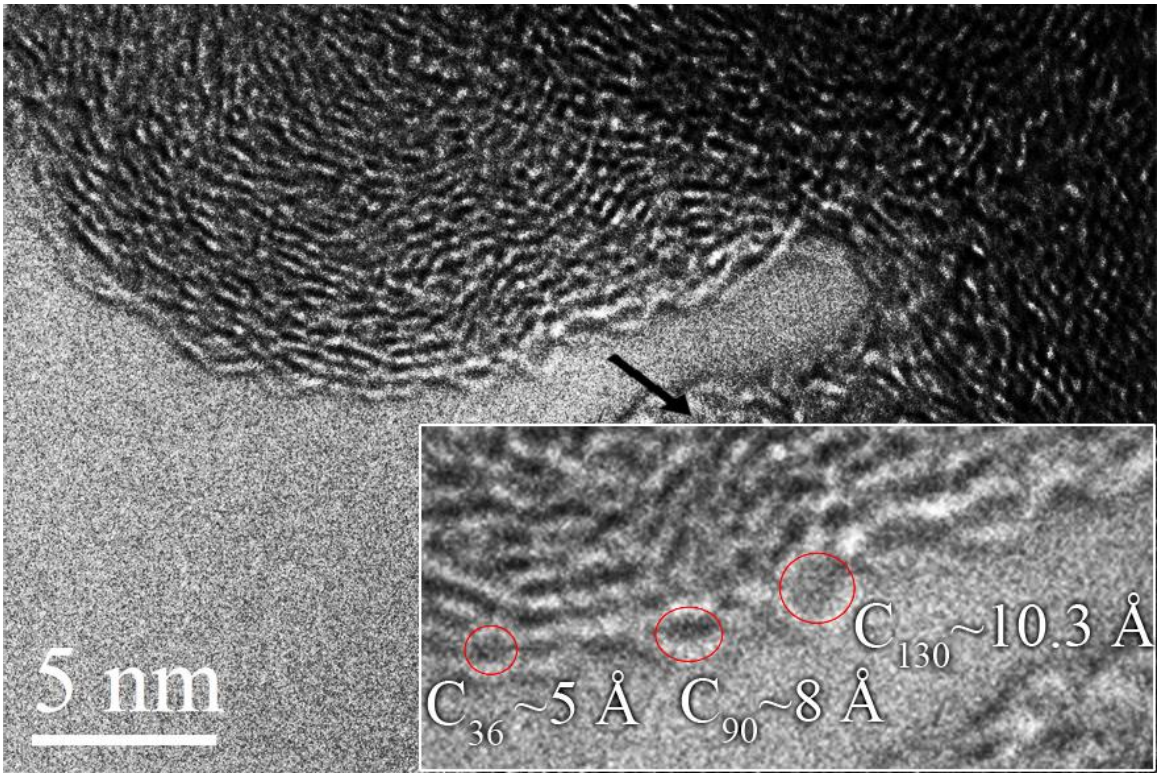

(e)

Figure 3.4-3. Showing the HTEM images from CNDFs; the fullerene closed cage are observed clearly and measured. The black dashes indicate fullerenes structure. (a) and (b) The inset

show the accurate measurement method of fullerene by HTEM (c), (d) and (e) HTEM showing fullerenes of C_{36}, C_{60}, C_{90} and C_{130} on carbon nanoparticles surface.

It should be noted that only carbon structures along the periphery of nanoparticles were thin enough for observation and for getting an accurate measurements of the structure. Accordingly, average diameters of selected structures include 5.2 Å, 7 Å, 8 Å, 10.3 Å, which correspond to C_{36}, C_{60}, C_{90} and C_{130}, respectively. The present decorated CNDFs by fullerenes have a great potential for drug delivery because fullerenes can facilitate the functionalization of carbon nanoparticles. There are many reports regarding the possibilities of fullerenes functionalization (Beheshtian, 2012, Itami, 2011, Shi, 2014a, Bandi, 2014, Cataldo, 2014). The attachment of these molecules to a carbon nanoparticle opens the possibilities of taking advantage from characteristics of both fullerenes and carbon nanoparticles. CNDFs can be used as vehicles or carriers, in order to selectively pass fullerenes through membranes, which will be regulated by the total size of carbon nanoparticle 50.4 nm.

The formation of fullerenes (carbon-caged nanomaterials) still remains unknown. Argon carrying precursor to cross the hot plasma region and forming highly supersaturated vapor containing carbon species and iron. By increasing ferrocene concentration to maximum in benzene, the fullerene appeared on the surface of carbon nanoparticles. This result shows that the precursor containing ferrocene is the iron source in the process, which acts as catalyst for obtaining CNDFs. Different catalysts like Cu, Ni, Co and Fe were used by different researchers to produce and enhance the rate of formation of fullerenes as well as the nanomaterials (Ahmad, 2008, Ahmad, 2005, José-Yacamán, 1993, Ma and Tennent, 2011). Our results also confirm their finding. Dunk studied the C_{60} growth and other higher fullerenes by direct exposure to carbon vapor produced from graphite or C-enriched amorphous carbon (Dunk, 2012). Their results show that fullerenes smaller than C_{60} do not form, other than from very minor fragmentation of the parent C_{60}, suggesting that the growth process is bottom-up. In our case, the CNDFs containing fullerenes obtained from supersaturated vapor and suggest the growth of bottom-up approach. Accordingly, the appearance of small fullerene C_{36} and big fullerene C_{130} is due to direct interaction of

atomic carbon with fullerenes during growth that allows an easy rearrangement of the bonds which, in turn, enable the efficient formation of the different isomers of fullerene.

3.4.3 Conclusions

Carbon nanoparticles carrying fullerene molecules on the surface have been obtained directly in one step by a modified arc discharge reactor. Gas phase delivery of precursor to plasma and precursor compounds improved size distribution of CNDFs. SEM observations showed that CNDFs have spherical shape, 50.4 nm, which is an optimum diameter for endocytic uptake and therefore CNDFs have a suitable morphology for drug delivery. Different fullerene molecule structures along the periphery of CNDFs were detected by HRTEM analysis. Obtained results indicated that the modified gas phase arc discharge technique is suitable for engineering nanostructure materials such as CNDFs for biomedical applications.

3.5 Synthesis of spherical porous carbon microparticles by gas phase arc discharge method

Porous carbon materials with various pore sizes and pore structures have been synthesized using different methods. However, there are only a few reports regarding the synthesis of porous carbon nanosphere/microparticle. In this section, we will introduce a new spherical porous carbon microparticles (PCMPs) material with no agglomeration. The synthesis process is by gas phase arc discharge reactor that previously used for the synthesis of carbon particles decorated by fullerene. The synthesis process is by gas phase arc discharge reactor that was previously used for the synthesis of carbon particles decorated by fullerene. The morphology of PCMPs has been studied by SEM and, BET analysis provided the surface area.

Porous carbon materials have received a great deal of attention and have been widely applied to gas separation, water purification, catalyst supports, and electrodes for electrochemical double layer capacitors, adsorbent, drug/gene carriers and fuel cells (Qiao and Zhao, 2009).

According to the International Union of Pure and Applied Chemistry recommendation, porous carbon materials can be classified into three types based on their pore sizes: microporous < 2 nm, 2 nm < mesoporous < 50 nm, and macroporous > 50 nm (Lee, 2006).

The following are representative traditional methods. I) Chemical activation, physical activation, and a combination of the physical and chemical activation processes. II) Catalytic activation of carbon precursors using metal salts or organometallic compounds. III) Carbonization of polymer blends composed of a carbonizable polymer and a pyrolyzable polymer IV) Carbonization of a polymer aerogel synthesized under supercritical drying conditions (Lee, 2006). Most porous carbons were prepared by carbonization of raw natural materials (e.g., wood, coal, petroleum pitches, coconut shell) (Skrabalak, 2009). Carbons are either microporous (pore size <2 nm) or low surface area solids with broad pore-size distributions; Meso- (pore size 2-20 nm) and macroporous (>20 nm) carbons have gained recent

prominence for applications involving large molecules (e.g., separations) and high diffusion rates (e.g., electrodes for double-layer capacitors, catalyst supports) (Skrabalak and Suslick, 2006). It should be noted that most of the studies for synthesis of porous materials are not in the form of spherical and individual particles and the porosity analysis is from a piece of material and therefore surface analysis of porous micro particles should not be compared with other porous carbon materials. Porous carbon materials have been synthesized using various methods. Most research efforts emphasize the use of templates and their subsequent removal to produce meso- and macro-porous carbons with controlled periodic open-framework (Su, 2008). Template carbonization is considered a unique and versatile method for preparation of the porous carbons with controlled pore structure and texture (Ania, 2007). Generally, a variety of templates including zeolites, mesoporous silica or aluminosilicates, crystal colloids and metal-organic frameworks, ultrasonic spray pyrolysis were used to prepare nano porous carbon materials (Wang, 2009). However, using templates for producing porous carbon is tedious, requiring multiple synthetic steps, caustic chemical treatments, and long curing times (Xia, 2008). Meanwhile, the scale-up has also proven difficult and is not cost-effective due to the destruction of (relatively) expensive templates. Moreover removing the inorganic templates often requires corrosive chemicals, such as hydrofluoric acid, which greatly limits the possibilities for industrial scale-up (Huang, 2011, Xia, 2011, Skrabalak and Suslick, 2006). Skrabalak reported a chemical approach named ultrasonic spray pyrolysis for the generation of meso- and macroporous carbon powders (Skrabalak and Suslick, 2006). Silica and carbon aerogels in the form of microparticles are traditionally obtained from monoliths by milling. With respect to the porous particles, a lack of particle sphericity and the absence of particle size uniformity, required for many drug delivery applications, are expected to be obtained when using conventional milling techniques (García-González, 2011). Therefore a novel synthesis method and improvement to produce porous particles is still required.

Here, we report a single step synthesis of spherical porous carbon microparticles (PCMPs) by a modified gas phase arc discharge reactor. We propose a new method in gas phase, environmental friendly, with insignificant by-product comparing to chemical methods. The morphology of PCMPs has been characterized

by scanning electron microscopy (SEM) and the surface area measurement has been done by BET analysis.

3.5.1 Method

BET method using Micromeritics Tristar 3000 using N_2 as the adsorbate at 77 K. Before measuring the surface area, the sample was outgassed at 300^0C for 4 hours to remove gas molecules from the pores. A scanning electron microscope operated at an accelerating voltage of 15 keV was used to observe the PCMP networks. Gas phase arc discharge reactor and process conditions are the same as CNDFs synthesis described in section 3.4.1. PCMPs accumulated at the bottom of the test tube after 30 min and were easily separated from nanoparticles, alternatively, they can be separated by centrifugation in less time.

3.5.2 Results and discussion

Catalytic activation of carbon precursors using metal salts or organometallic compounds are common for carbon porous material synthesis. Ferrocene contains 30% iron by weight and can be used as a precursor of iron in fuel additives (Zhao, 2014). Moreover, in our previous experiments we have used ferrocene widely for synthesis of carbon encapsulated mono and multi iron cores. De Fina, evaluated the chemistry of ferrocene and solubility in organic solvent (De Fina, 2001), list of solvents are shown in appendix D. Ferrocene solubility among 46 tested organic solvents ranges from 0.09% to 18.61%. The highest solubility rate corresponds to benzene. Therefore, the precursor compounds were prepared by mixing benzene and ferrocene by sonication. Inert gases such as argon, nitrogen and helium are commonly used for ionization and generating plasma. According to our previous investigations, the plasma characteristics such as size, stability, thermal conductivity and temperature have a meaningful influence on formation of carbon particles. For the synthesis of PCMPs argon is chosen in order to have stable plasma between electrodes. Moreover, argon plasma produces enough temperature for reaching to carbon supersaturated vapor condition, which is important for obtaining porous structure. Moreover as

reported by Sanaee same method has been used for synthesis of carbon particles decorated with fullerene molecules. Perhaps, fullerenes have had influence in the formation of PCMPs, as recently Dunk studies have reported and revealed that fullerene growth is likely to be involved in the formation of other carbon nanostructures from carbon vapor. The narrow size distribution is one of the main requirements for almost any application of PCMPs. Subsequently, PCMPs have been studied by SEM as shown in Figure 3.5-1.

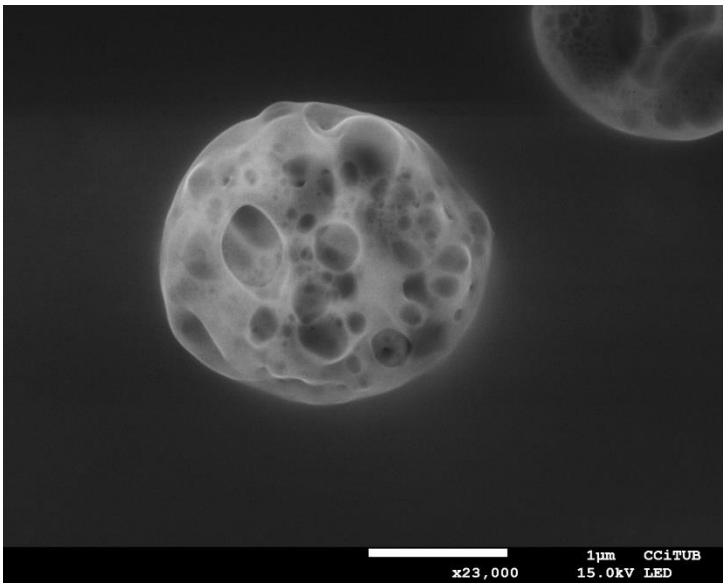

Figure 3.5-1. SEM image from an individual spherical PCMP, large pores are clearly visible.

According to the SEM analysis carbon particles reported in the literature are agglomerated (Ray, 2009, Simon-Deckers, 2009, Chen, 2007). The agglomeration of carbon particles is a common disadvantage, and further surface functionalization is necessary to separate them. Interestingly, based on SEM images in Figure 3.5-2 (a) and (b) obtained PCMPs are completely separated from each other's and indicating no agglomeration. More importantly, the size distribution analysis shows narrow size distribution of PCMPs as shown in Figure 3.5-2 (c). Particles size distribution is very important as addressed by Gaumet (Gaumet, 2008). Thus, for example, biodistribution depends on the physicochemical properties of particles, especially size. Practically, one of the major limitations of using particles is their broad size distribution. Due to the unique characteristics of PCMPs such as narrow size distribution, porosity, high surface area and carbon thermal and chemical stability, these particles are potentially

suitable for drug delivery. The nano porous structure involves that each one of these particles of 2.1 μm of size (Figure 3.5-2 (a) and (b)) is a nano-system and can be loaded by drug molecules for carrying them to the tumor. Furthermore, these nanosystems can enable release of drug in controlled time intervals, by activating the particles by external thermal activation or irradiation.

The specific surface of PCMPs is independent of the specific surface of loaded nanoparticles, in other words, specific surface depends on the size and density of porous, which is independent from the size of microparticles. This provides an additional advantage to limit the movement of the nanoparticles to cross specific cellular membranes such as blood-brain barrier.

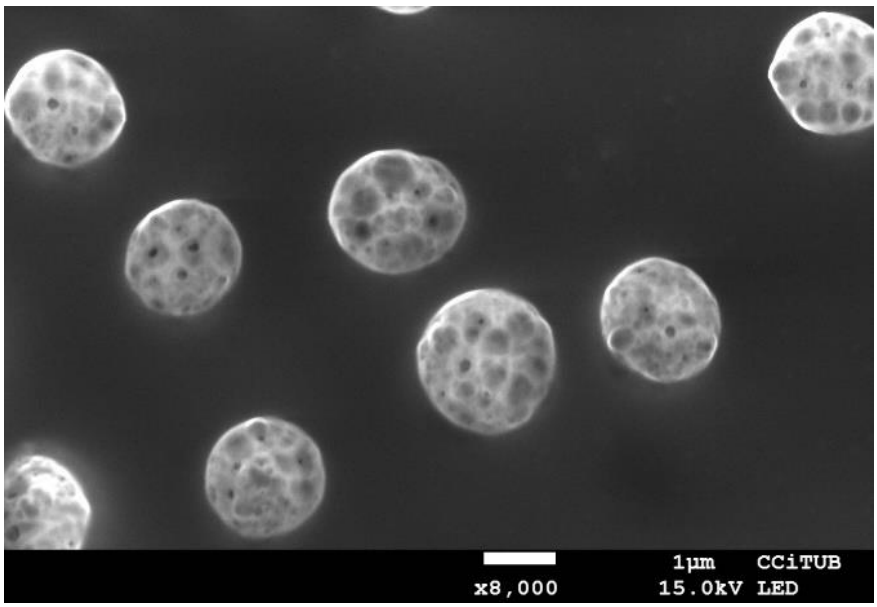

(a)

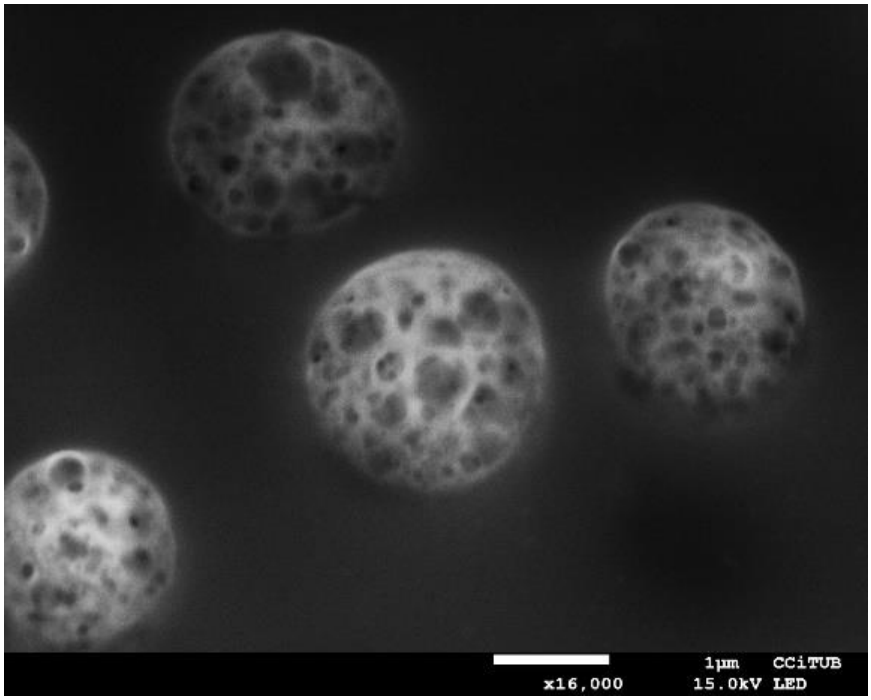

(b)

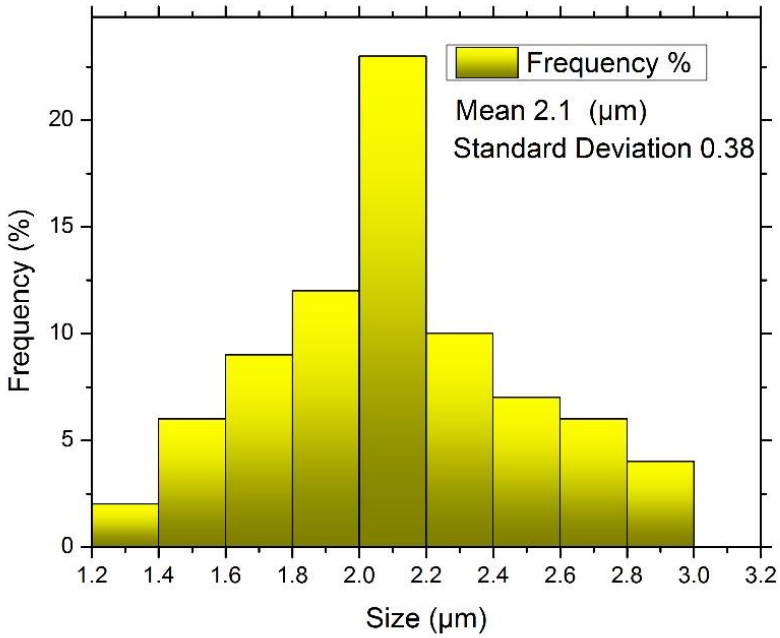

(c)

Figure 3.5-2. (a) and (b) show SEM images from a group of PCMPs, nano-pores are visible, there is no carbon agglomeration or any other impurity, (c) Size distribution histogram of PCMPs, showing narrow size distribution with mean diameter of 2.1 μm.

There are reports for using particles for releasing the drug in controlled manner and certain time intervals (Thakur, 2014, Wang, 2013, McBride, 2013). Surface area measurements are typically based on N_2 absorption at 77 K. The Langmuir or Brunauer-Emmer-Teller (BET) model is typically used to interpret the data. The basic assumption for the Langmuir model is that adsorbates pack in a monolayer, whereas the BET model accommodates multilayers (Koh, 2009). Based on SEM observation in Figure 3.5-2(a), (b) and Figure 3.5-1 obtained PCMPs have large enough pores to allow more than one adsorbed layer, in this case the Langmuir surface area leads to overestimation, and the BET surface area calculation is more reliable. For this reason, the porosity of PCMPs structure was determined by its nitrogen adsorption revealing a specific surface area of 153.4 ± 4.2 m^2/g. BET analysis summary report is presented in Table 3.5-1. In addition, the BET analysis data are provided in Appendix Table B-1, Table B-2 and Table B-3. Surface area of obtained PCMPs structure is slightly higher than recent reported surface area of micro porous particles (Dai, 2013). The porosity of the PCMPs structure was assessed quantitatively by nitrogen adsorption desorption measurements. According to the fife types of adsorption isotherms described by Brunauer (Brunauer, 1940). The PCMPs nitrogen adsorption–desorption isotherms in Figure 3.5-3(a) indicates the multilayer adsorption. The average pore width (nm) versus pore volume (cm^3/g) is plotted in Figure 3.5-3 (b). The pore sizes range between 1.6 nm to 109.3 nm. The adsorption average pore size is 9.05 nm. Interestingly, the pore volumes are almost in a flat range while the pore sizes are different (Figure 3.5-3(b)), this is an interesting balance between average pore sizes (up to 73.9 nm) and pore volume. In typical particles, BET analysis results show a monolayer adsorption, in contrast, in our case using porous micro particles, BET analysis has evidenced the multilayer adsorption mechanism. Multilayer adsorption can enhance the total amount of absorbed drug molecules in this kind of particles. These characteristics offer the possibility of using PCMPs to carry a higher concentration of drug to delivery to the target site.

Table 3.5-1. Summary report of BET analysis; the sample was kept at 300 ^{0}C for 4 hours to remove gas molecules from the pores.

Summary Report
Surface Area
Single point surface area at p/p° = 0.299413190: 100 .2124 m²/g
BET Surface Area: 153.4895 m²/g
BJH Adsorption cumulative surface area of pores between 1.5000 nm and 300.0000 nm width: 139.6790 m²/g
BJH Desorption cumulative surface area of pores between 1.5000 nm and 300.0000 nm width: 128.8150 m²/g
Pore Volume
Single point adsorption total pore volume of pores less than 140.4108 nm width at p/p° = 0.986022467: 0 .347585 cm³/g
BJH Adsorption cumulative volume of pores between 1.5000 nm and 300.0000 nm width: 0.331326 cm³/g
BJH Desorption cumulative volume of pores between 1.5000 nm and 300.0000 nm width: 0.154029 cm³/g
Pore Size
Adsorption average pore width (4V/A by BET): 9.05822 nm
BJH Adsorption average pore width (4V/A): 9.4882 nm
BJH Desorption average pore width (4V/A): 4.7829 nm

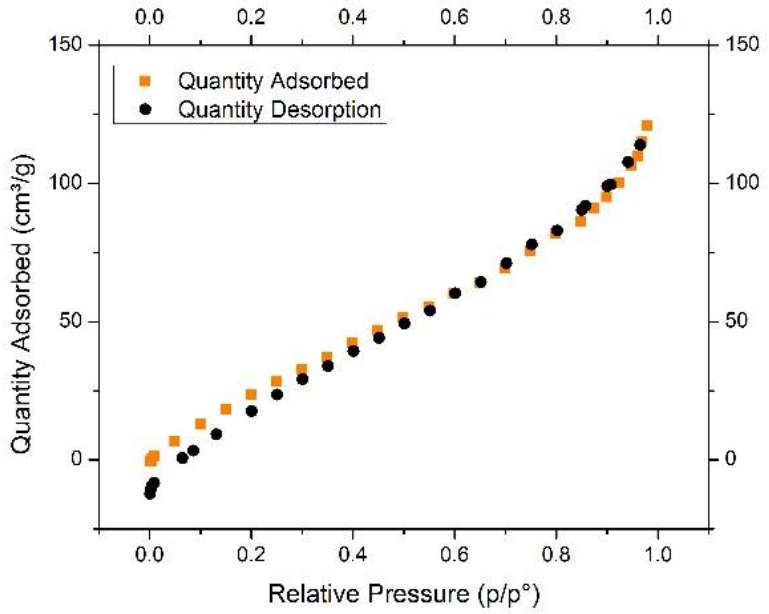

(a)

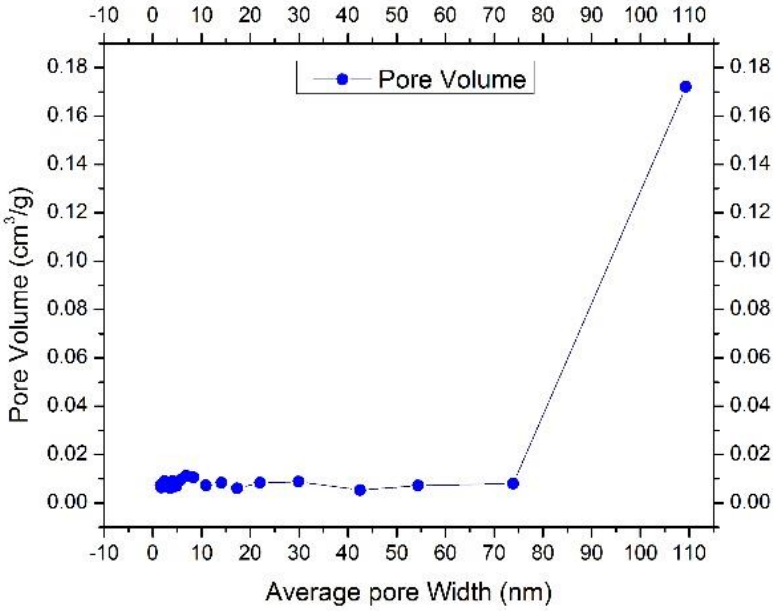

(b)

Figure 3.5-3. (a) Quantity adsorbed (cm^3/g) versus relative pressure (p/p^0) showing isotherm corresponding multi-layer adsorption so called S-shaped or sigmoid isotherm. (b) Pore volume versus average pore width (nm) indicates that pore sizes ranges from 1.6 to 109.3 nm averagely and the pore volume show almost a flat range up to 73.9 nm pore width showing that majority of the pores are a few nanometers. The pore width average size of 109.3 nm, which exceptionally has volume higher than other pores, can be seen from SEM images as well, probably it is the gate to other smaller pores.

Beside biomedical applications, due to the unique morphology and as well as electrical conductivity, the PCMPs can be suitable for advanced detection at nanoscale for lab on a chip devices. Both electrical conductivity and possibility to attract and trap the substances through the pores can enable PCMPs structure to be used as a detector in lab on a chip devices, because the trapped substances will alter the signal and electrical properties of PCMPs. The pores narrow size distribution is not a concern for all applications necessarily. For instance filtration by similar pore sizes can lead to the blockage in early stages, while different pore sizes can filter particles of different sizes with less possibility of blockage. It's noteworthy to mention that owing to the proper PCMPs size, potentially it is suitable for placing them into micro fluids for precise filtration of possible micro/nano contamination through micro fluid channels.

3.5.3 Conclusions

The PCMPs material structure described here are has been prepared through a new, facile synthetic method based on a gas phase arc discharge technology. SEM images show PCMPs spherical shape with no agglomeration. According to SEM images, the size distribution of PCMPs is narrow with mean diameter of 2.1 μm. BET analysis shows a specific surface area of 153.4 ± 4.2 m^2/g. The unique properties of PCMPs show great promise as a carrier for drug delivery system; and for lab on a chip devices.

3.6 Applications

There are wide ranges of potential applications for carbon encapsulated iron nanoparticles (CEINPs), carbon nanoparticles decorated by fullerenes (CNDFs) and porous carbon micro particles (PCMPs) as explained in chapter I, section 1.7. “Potential applications”. This section is about primary experiments that have been done in order to show potential applications of obtained particles in both biomedical and non-biomedical applications.

We have already demonstrated the synthesis of CEINPs in precise and controlled manner, which means that we can determine both carbon shell and iron core sizes at nanoscale based on desired application. Herein, we briefly studied their potential usage for treatment of eye floaters. Moreover, the growth of graphene has been studied by using CEINPs.

In addition, we engineered a new CNDFs successfully based on described drug delivery requirements in important literature. The details and possible applications are described in “carbon particles decorated by fullerene” section.

PCMPs are new structures that have not been reported yet. Many interesting applications are predictable for such a carbon porous material. Their unique characteristics are described in section of “Synthesis of spherical porous carbon microparticle by gas phase arc discharge method”. Here our investigation shows their interesting transformation on copper substrate by using chemical vapor deposition technique.

3.6.1 Possibility of using CEINPs for treatment of eye floaters

Floaters are suspended in the vitreous humour, the thick fluid or gel that fills the eye. Vitreous floaters are a common complaint in the ophthalmic care setting. Vitreous floaters are most commonly caused by posterior vitreous detachment, vitreous syneresis and asteroid hyalosis; while these symptoms are considered physiological in nature they can be of considerable inconvenience to many patients (Delaney, 2002). Such as it has been described by Sendrowski, today the best treatment options for symptomatic vitreous floaters remain conservative ones, with close follow-up and education. Time and patient reassurance will, for the most part, result in reduction or resolution of initial symptoms and has, over time, shown to be a sound treatment option. In terms of ‘‘off-label’’ treatment, laser and surgical options for vitreous floaters have not been adequately defined (Sendrowski and Bronstein, 2010). Consequently, it is necessary to investigate new possibilities for floaters treatment.

Here we propose the use of CEINPs for filtering floaters through the vitreous humour. The vitreous has a viscosity two to four times that of pure water, giving it a gelatinous consistency. It also has a refractive index of 1.336 (Land and Fernald, 1992). Viscosity of water is 8.94×10^{-4} (Pa.s) at 25 °C and the viscosity of blood is normally to 4×10^{-3} Pa.s at 37 °C (Land and Fernald, 1992, Elert, 1998). Thus, we can estimate that viscosity of blood is 3.3 – 4.5 times greater than water and is similar to the viscosity of vitreous humour. Red blood cells are a standard size of about 11.5-14.5 μm. It is possible to add CEINPs to blood and then via a magnet the particles can drag red blood cells and then can be observed by microscope.

Liua characterized starch by polarized light microscope and electron microscopes (Liu, 2009). A drop of the starch particle suspension was spread onto the copper grids coated with a carbon support film, and then coated with gold for observation at 20 kV. Figure 3.6-1 shows starch and blood. Blood substances are known, they can be distinguished under electron microcopy for test.

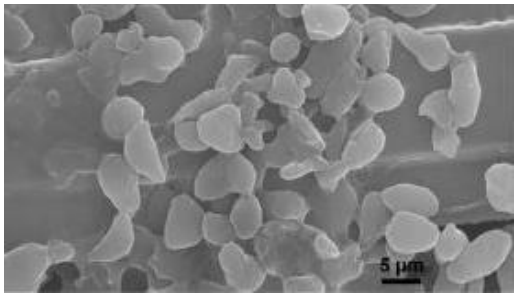

(a)

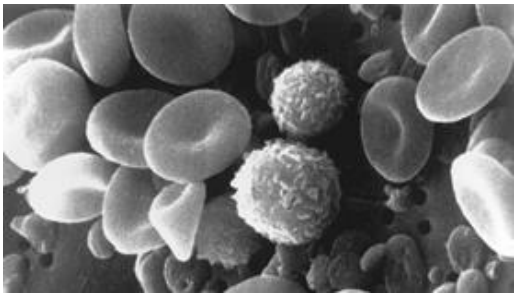

(b)

Figure 3.6-1. (a) Shows starch under electron microscopy (Liu, 2009), (b) Shows blood substances under electron microscopy (Bruce Wetzel 1989).

However, we could not supply blood for our test. Instead we followed another approach for illustration. The floaters actual sizes are often no more than 100 μm. Rice starch is relatively small (about 2 μm) while potato starches have larger granules (up to 100 μm) (Visakh and Thomas, 2010), therefore potato starch is a suitable representative for floater. Initial attempt have been done and we used CEINPs for dragging potato starches by a magnet. A light microscope was employed for observation. In the sequence images of Figure 3.6-2 we can clearly see the movement of CEINPs and starch. As a primary test, we shown potential use of CEINPs for treatment of eye floaters.

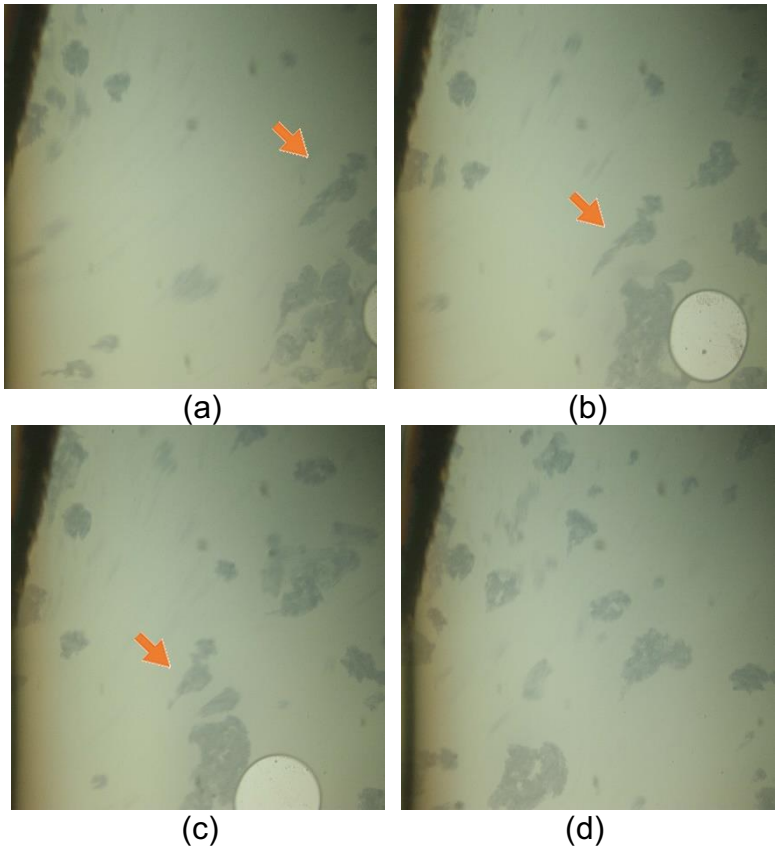

Figure 3.6-2. Images of CEINPs and starch under microscope, sequence images of (a), (b), (c) and (d) showing the movement of starch and CEINPs due to the magnetic attraction, respectively.

3.6.2 Graphene growth by using carbon encapsulated iron nanoparticles

Large-area graphene growth is required for the development and production of graphene applications such as electronic devices. The remarkable properties of graphene reported so far include high values of its Young's modulus (~1,100 GPa), fracture strength (125 GPa), thermal conductivity (~5,000 $Wm^{-1}K^{-1}$), mobility of charge carriers (200,000 $cm^2V^{-1}s^{-1}$) and specific surface area (calculated value, 2,630 m^2g^{-1}), plus fascinating transport phenomena such as the quantum Hall effect (Park and Ruoff, 2009).

Graphene has been made by four different methods: 1st was chemical vapor deposition (CVD) and epitaxial growth, such as the decomposition of ethylene on nickel surfaces (Eizenberg and Blakely, 1979). 2nd was micromechanical exfoliation of graphite, which is also known as the 'Scotch tape' or peel-off method (Novoselov, 2004, Lu, 1999). 3rd method was epitaxial growth on electrically insulating surfaces

such as SiC and the 4th was the creation of colloidal suspensions (Berger, 2006). CVD on Cu foils has already shown great promise. Recently, Victor M. Ferrier presented doctoral thesis entitled “Fabrication and characterization of macroscopic graphene layers on metallic substrates” in FEMAN group (Freire Soler, 2014); Large area synthesis of graphene still remained a challenge. Ferrier reactor and method have been utilized for using carbon encapsulated iron nanoparticles (CEINPs) to growth graphene on copper in clean room. Figure 3.6-3 shows CVD reactor in clean room. It has been proposed that CVD growth of graphene on Ni occurs by a C segregation or precipitation process, whereas graphene on Cu grows by a surface adsorption process (Li, 2009). It is desirable to have graphene on silicon for many applications for instance transferring graphene from metal substrates to insulators is a critical step for realizing electronic applications (Yu, 2008b) therefore, researchers use exfoliation method to transfer graphene on silicon substrate. Another method is to put a layer of copper or nickel by sputtering technique on silicon substrate before graphene growth. Until now, there is no any direct method to obtain graphene on silicon substrate directly. In order to study the influences of CEINPs for graphene growth, both copper and silicon substrates were used. Initially, one drop of CEINPs was put on two pieces of silicon separately. Two samples were considered. The concentration of second sample was one tenth of first sample. The scanning electron microscopy (SEM) images of silicon first and second samples before the CVD are shown in Figure 3.6-4(a) and (b). It is clear that the distance between CEINPs is increased as the concentration is decreased.

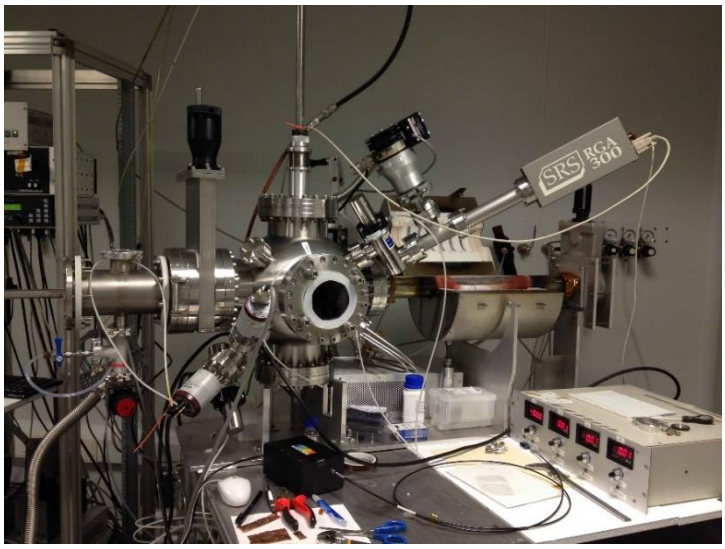

Figure 3.6-3. CVD reactor in clean room condition (Freire Soler, 2014).

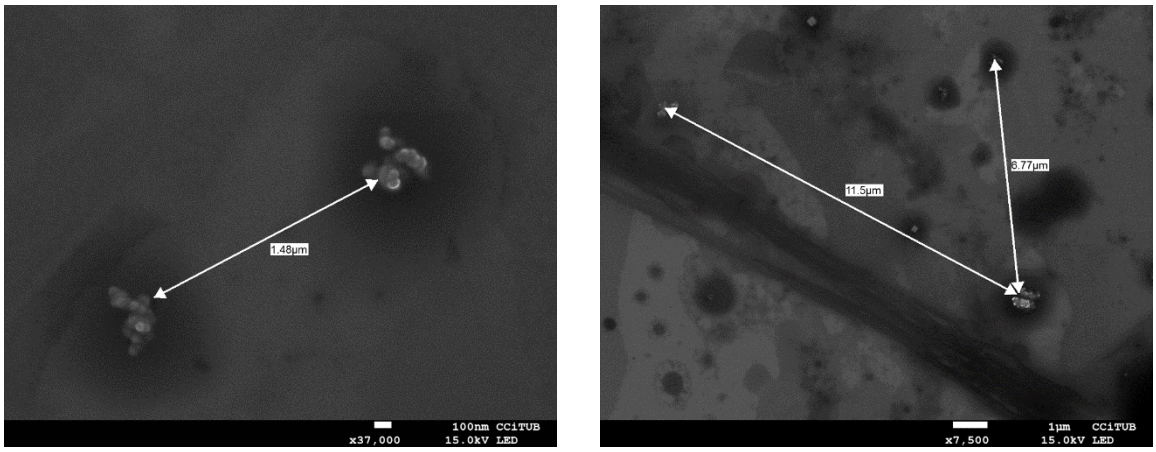

(a) (b)

Figure 3.6-4. SEM images of first and second samples, the distance between CEINPs is 1.48 micrometer in first sample and averagely 9 micrometer in second samples.

Afterward, the graphene growth condition process has been done on the two silicon substrates by CVD method in clean room. The CVD growth condition is summarized in Table 3.6-1. As the result a graphene like carbon on silicon substrate has been obtained and the corresponding SEM images of each sample are shown in Figure 3.6-5(a) and (b). However, it is not feasible to distinguish between the graphene like layer of the two samples, because we could not localize the CEINPs on the substrate before and after the growth. Using AZ5214E photoresist for creating an indexed pattern on silicon can solve this issue. This graphene like layer is not spread everywhere on the substrate and most probably its initial growth has been from CEINPs, and the iron particles act as catalysis for the growth. Interestingly, CEINPs can be seen in spherical form before forming a complete layer on silicon in Figure 3.6-5(c). It was not feasible to localize it by Raman spectroscopy, because Raman equipped with light microscope and it was not possible to observe the graphene like layer. However, energy-dispersive X-ray spectroscopy (EDX) analysis were performed and confirmed that the material is carbon as it was expected. The EDX analysis and corresponding SEM images are shown in Figure 3.6-5(d), (e) and (f), respectively. The carbon peak in EDX analysis of Figure 3.6-5(d) is weak, due to the fact that carbon has a low Z number (6) and the X-Rays emitted are fast absorbed by the detector window. Consequently, the detectability of carbon is very low by EDX and signal is weak. The SEM images in Figure 3.6-5 are very similar to the graphene

transferred to silicon substrate reported in the literature (Xiang, 2011). Therefore, by taking into account the EDX analysis, observed carbon layers are deemed to be graphene.

Table 3.6-1. CVD process conditions of CEINPs on copper and silicon substrates, the pretreatment was performed for copper substrate in order to remove the copper oxides.

CVD Method Copper substrate	
Pretreatment	Generating Plasma: CH_2 Pressure: 20 Pa H_2 Flow: 20sccm Duration: 10 min
Copper and silicon substrates	
CVD Growth	CH_4 Flow: 5sccm H_2 Flow: 20sccm Temperature: 1040 ^{0}C Total pressure: 20 Pa Duration: 20 min

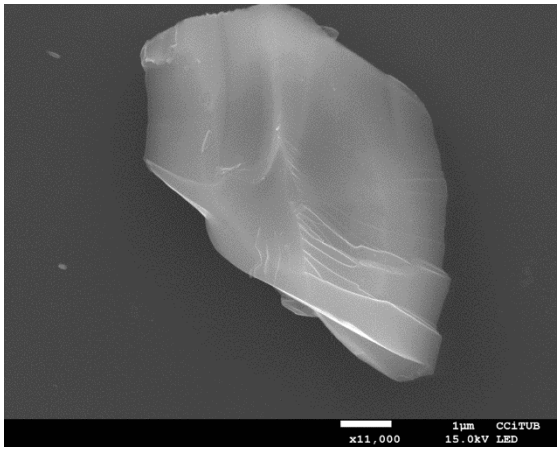

(a)

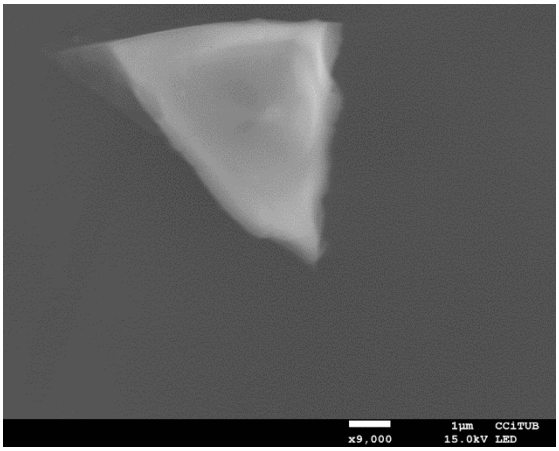

(b)

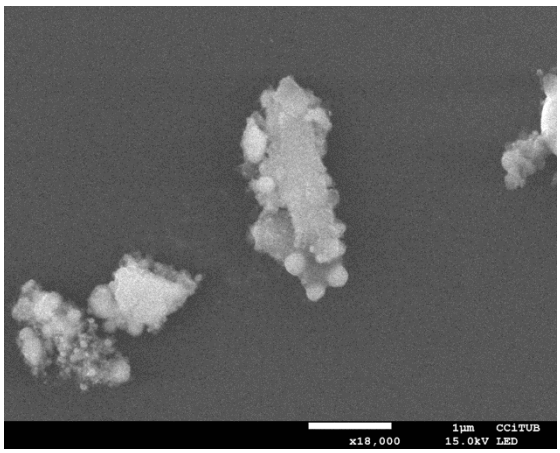

(c)

(d)

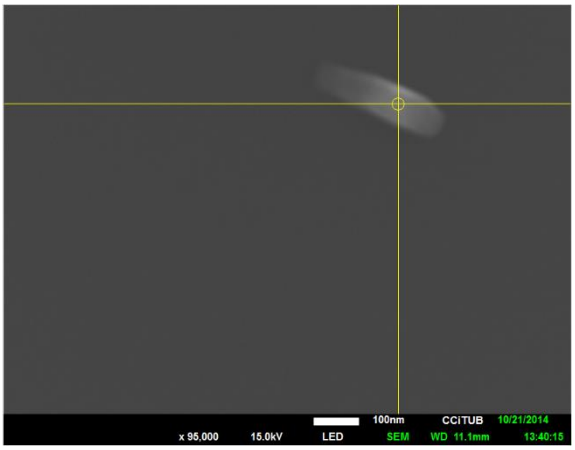

(e)

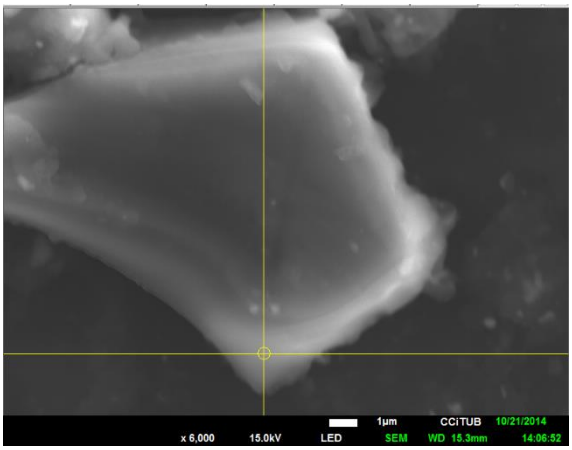

(f)

Figure 3.6-5. (a) Carbon layer that deemed to be graphene on silicon substrate by using CEINPs from the first sample and (b) the layer from the second sample. (c) Shows initial formation of carbon layer and the spherical CEINPs can be seen at the bottom left corner. (d) EDX analysis shows the carbon peak from selected points by cross in (e) and (f) SEM images.

Metals surface oxidation have negative effect for growing nanotubes (Shahzad, 2014), similarly our failure experiments confirmed the same result. For this reason, before using CVD a hydrogen pre-treatment have been done on copper substrates and the copper oxides were removed. It should be noted that influences of different concentrations of CEINPs on copper foil were not verifiable because the copper foil was not flat. An example of graphene obtained on copper foil by using CEINPs is shown Figure 3.6-6.

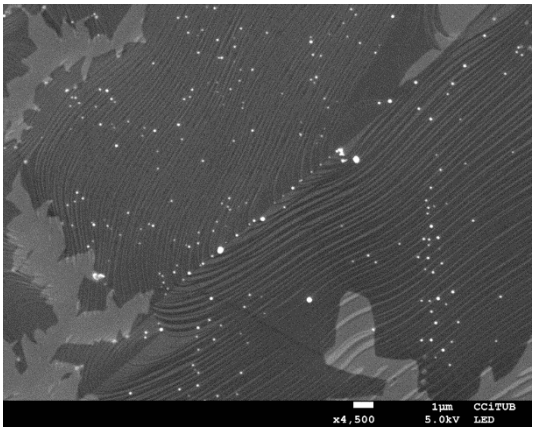

Figure 3.6-6. Graphene growth on copper foil by using CEINPs.

Recently Han concluded that highly crystalline graphene can be obtained on well-controlled surface morphology of the copper substrate (Han, 2011). Therefore, we have investigated the growth of graphene by using CEINPs on a complete flat copper with (1 1 1) plane. A drop of CEINPs in Milli-Q water evaporated and spreads on the copper surface shows an inhomogeneous distribution of CEINPs as shown in Figure 3.6-7(a). In order to evaluate the graphene quality and the effects of CEINPs four regions of rectangular shapes have been selected and marked as 1×2 mm in Figure 3.6-7(a) and (b). After CVD process the graphene growth have been analyzed by SEM and Raman spectroscopy. Forth marked regions were located by Raman spectroscopy, which was equipped with a light microscope and the associated spectra for each region were obtained for comparison and shown in Figure 3.6-7(c). SEM image in Figure 3.6-7(d) shows an example of graphene and CEINPs from this copper surface. The two most intense features are the G peak at 1580 cm^{-1} and the 2D band at 2700 cm^{-1}, which were observed for the fourth regions. CEINPs concentration of region (I) is high as observed by SEM in Figure 3.6-7(a) and Its Raman spectrum (Figure 3.6-7(c) 2D peak (I) is sharp and triple than the G peak providing evidence of high quality and monolayer graphene. The CEINPs concentration in region (II) (Figure 3.6-7(a)) is also high and, in contrast, it appears with a more homogeneous distribution than region (I), the Raman spectra of (II) region (Figure 3.6-7(c)) is sharp and high as well, pointing to good quality monolayer graphene. The CEINPs amount in regions (III) and (IV) are low and the graphene in these two regions are far from high concentration of CEINPs (Figure 3.6-7(b) and Figure 3.6-7(c)) and the corresponding Raman spectra shows small 2D peaks pointing to multilayer graphene. However it is

still graphene since the G peak is not greater than the 2D, (copper substrate is 1×1 cm). The comparison between Raman spectrums of graphite and mono and multi layers of graphene are described by Ferrari in details (Ferrari, 2006). The analysis of SEM images together with Raman spectrum revealed that CEINPs allowed the formation of monolayer graphene whereas, with less or no CEINPs concentration the graphene grows in multilayer form. The incorporation of iron cores of CEINPs as catalyst should be taken into account. As a conclusion, using CEINPs for improving the growth of graphene can become an alternative via. It is a new feature for controlling the mono and multi-layers growth of graphene in large copper surface.

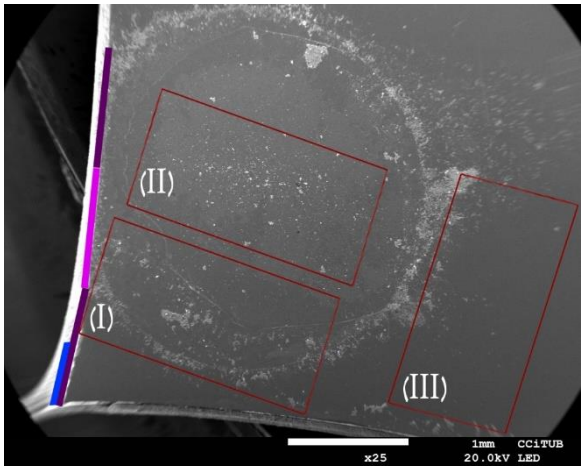

(a)

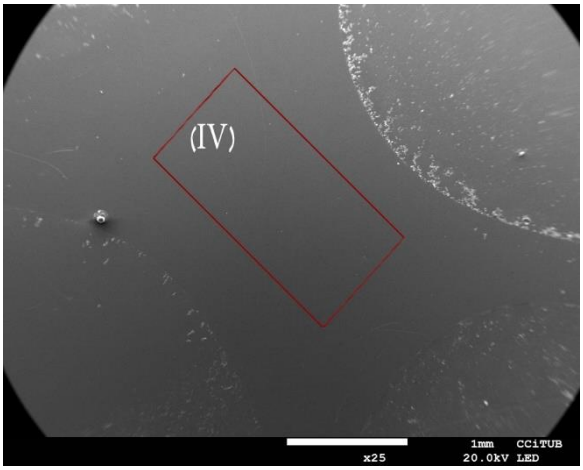

(b)

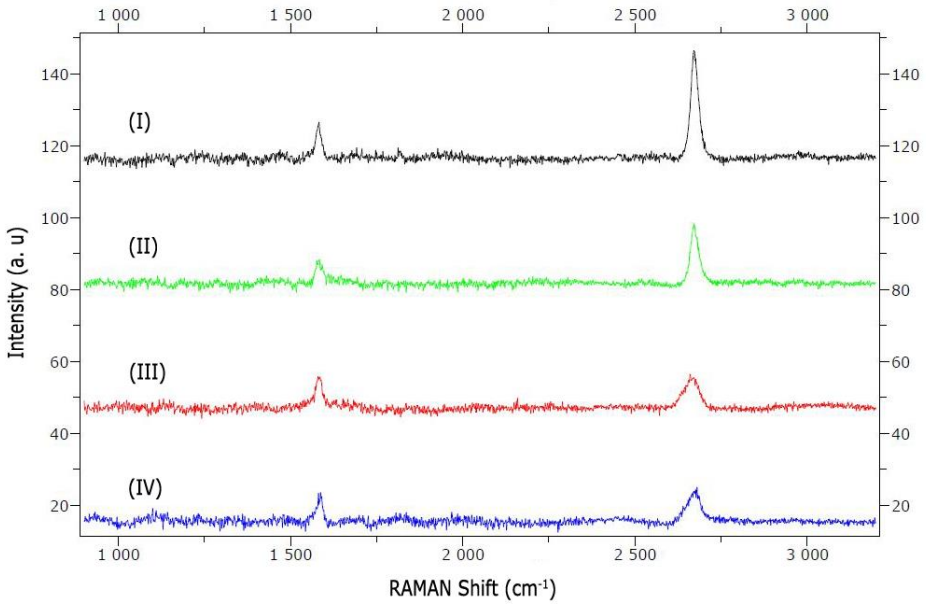

(c)

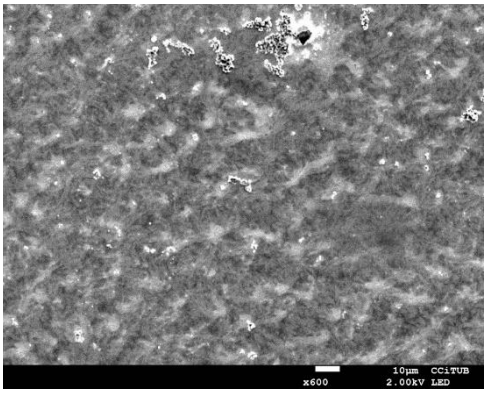

(d)

Figure 3.6-7. (a) SEM images of CEINPs samples on copper surface, the three rectangular regions of 1×2 mm with different CEINPs concentration that have been selected for the experiment (b) SEM image showing the center of copper surface, where, the CEINPs borders are visible in white and the forth region is shown in rectangular shape. (C) Raman spectra for each selected region of (I), (II), (III) and (IV). (d) SEM image showing graphene and CEINPs on copper surface.

The same CVD method has been applied on porous carbon microparticles (PCMPs) on copper substrate. PCMPs show a new carbon structure like an O ring, such as shown in Figure 3.6-8(a) together with associated EDX analysis that shows carbon peak in Figure 3.6-8(b). It is noteworthy to mention that PCMPs contains spherical closed cages of fullerene molecules. In an important research study Dunk results shed new light on the fundamental processes that govern self-assembly of carbon networks, and they commented that fullerene growth is likely involved in the formation of other carbon nanostructures (Dunk, 2012). Probably, the fullerenes play a role for the PCMPs rearrangement to O ring form. The sizes of O rings are smaller than PCMPs and it seems that the porous are filled as there is no visible porous on the O rings structure at this magnification in Figure 3.6-8(a). The small particles in Figure 3.6-8 (a) are mostly due to segregation of silicon contamination from the bulk (reactor glass tube) to the surface, Wang observed similar silicon particles on copper using CVD (Wang, 2015). The small particles on copper substrate observed in SEM image of Figure 3.6-9 (a) and was analyzed by EDX and shown silicon peak Figure 3.6-9 (b).

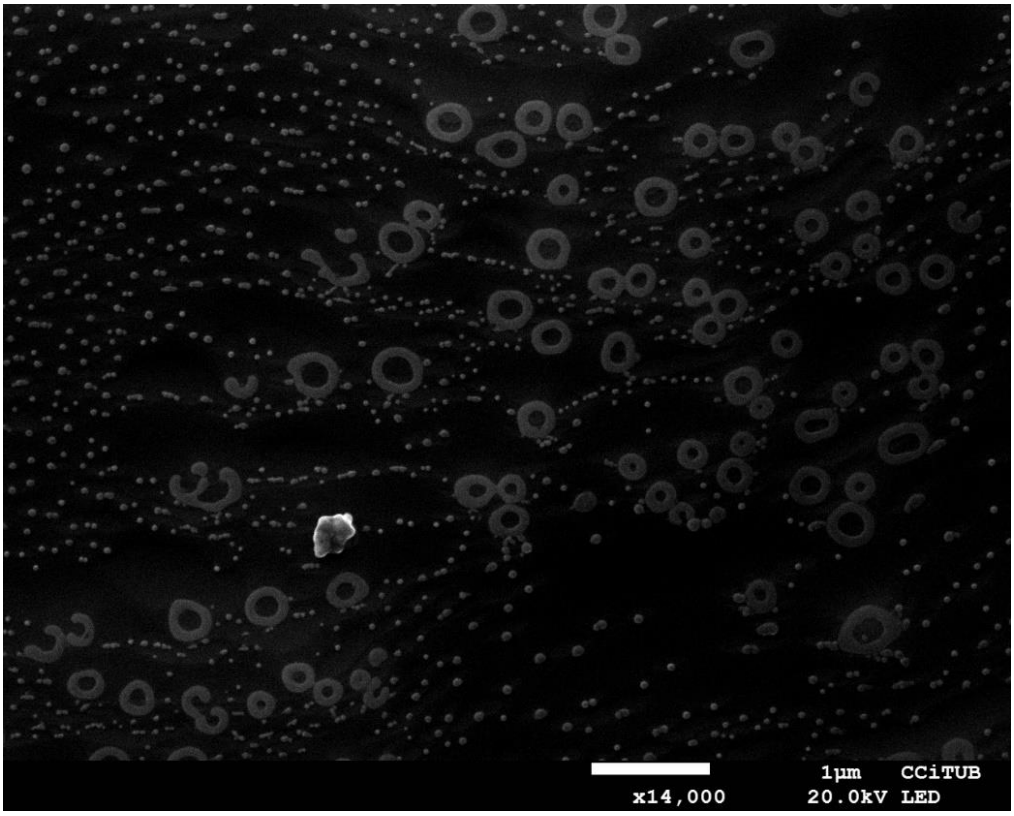

(a)

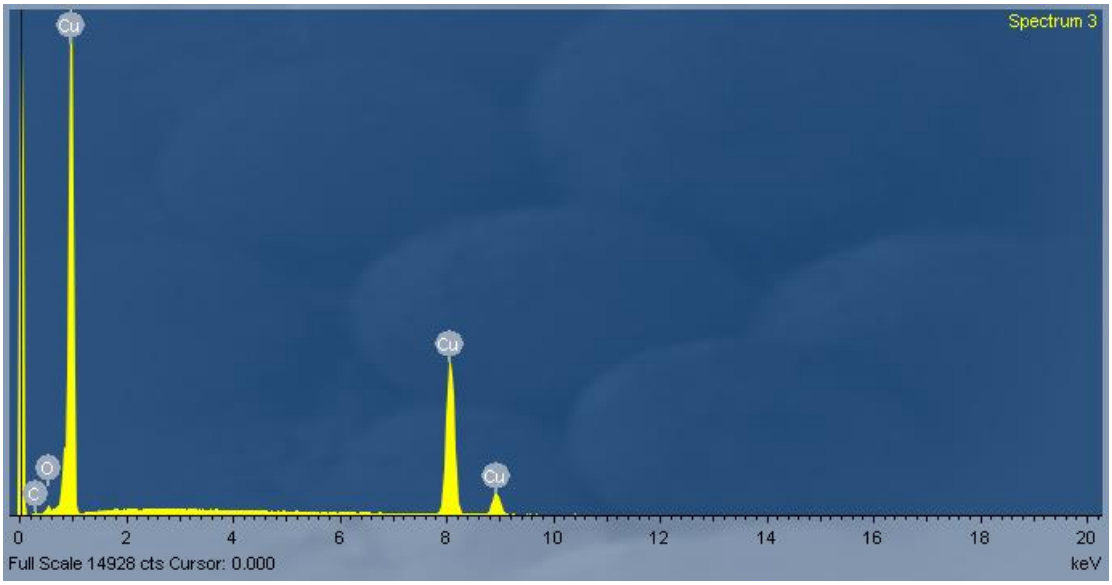

(b)

Figure 3.6-8. (a) Transformation of PCMPs on copper substrate by CDV method. EDX elemental analysis confirms the carbon peak from the O rings. (b) Associated EDX analysis of (a) SEM image, shows carbon peak and the Cu peaks from the copper substrate and oxygen as well.

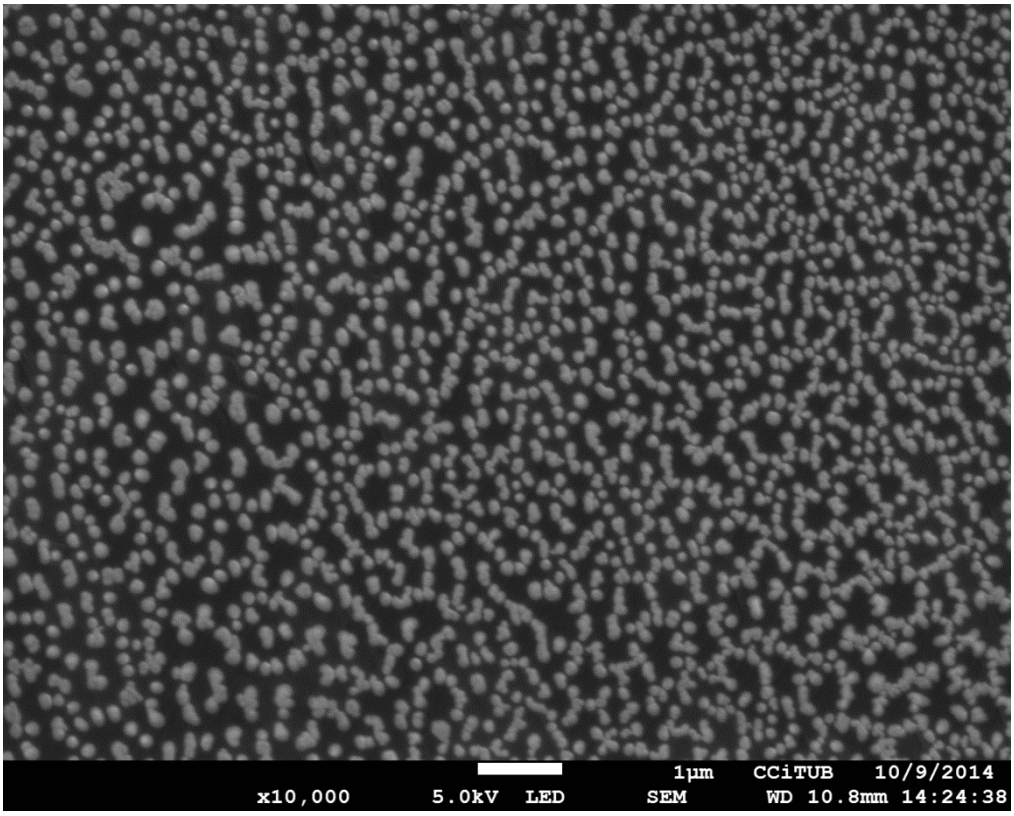

(a)

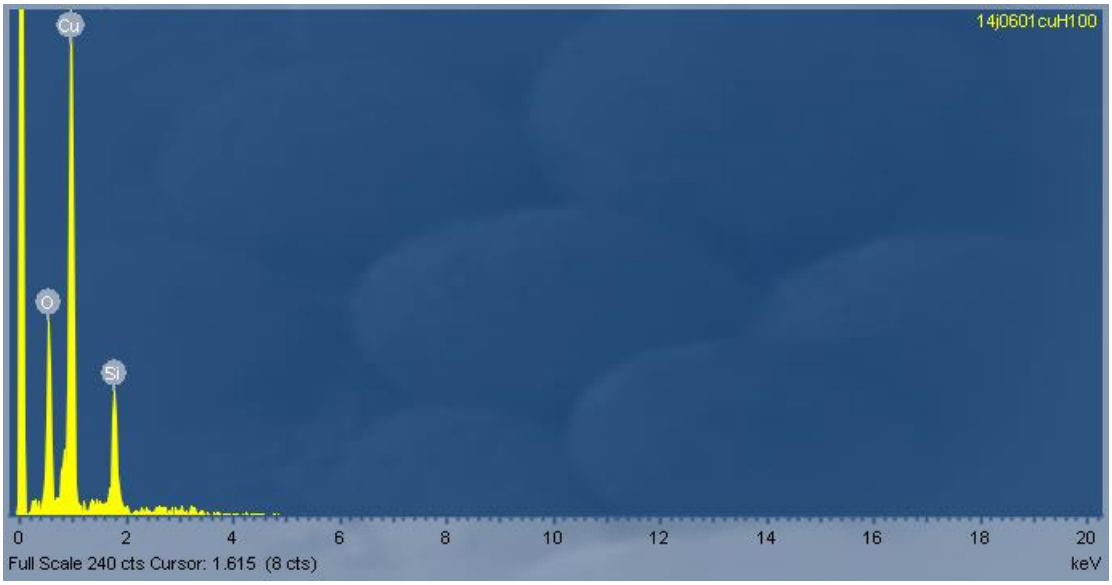

(b)

Figure 3.6-9. (a) This is the SEM image of copper surface, which was used for the graphene growth but it is contaminated by many particles (b) The EDX analysis of those particles in image (a) revealed silicon peak.

IV. Conclusions

- Carbon encapsulated iron nanoparticles were synthesized successfully in a controlled manner by a new liquid phase arc discharge reactor.

- The argon-helium gas ratio alters the heat transfer from central of the plasma to outside. When argon concentration increases then the temperature gradient increases or in other words, the cooling rate decreases, resulting in changes of the critical radius of carbon shell and iron core. Nanoparticle growth occurs in gas phase and lower thermal conductivity of the gas enlarges the formation time.

- It is concluded that by increasing ratios of argon to helium, carbon shell thickness increases from 2.3 nm to 36.6 nm and iron core decreases from 7.7 nm to 3.4 nm.

- Diffraction points of iron oxide were not detected from SAED analysis. Moreover, both EELS analysis at nanoscale and EDX analysis at micro scale showed no trace of oxygen in iron cores. These results point to a high efficiency of carbon shell to isolate iron core from a possible external oxidation.

- Raman spectroscopy results indicate that the crystallinity of the carbon shell increases when pure argon is used.

- The size dependence of effective moment and saturation magnetization parameters of superparamagentic nanoparticles has been demonstrated.

- Ar0, Ar25, Ar50 and Ar75 samples exhibit superparamagnetic behavior above 260 K.

- ZFC and FC curves demonstrate that Ar100 sample is superparamagnetic at low temperature (above 220 K / -53 ^{0}C), therefore it is a suitable CEINPs for specific applications that operate at extremely low temperature such as applications in aerospace industry.

- The blocking temperature of the particles grown without argon (T_b ~ 50 K) is almost double than that grown in pure argon (T_b ~ 24 K), in agreement with T_b dependence vs TEM iron core diameter.

- A new multi iron nanoparticles encapsulated in carbon shell were synthesized.

- Interestingly, although multi iron cores are smaller than iron core in CEINPs (N75), they exhibit a higher saturation magnetization. One of the reasons can be the existence of a few iron cores in a single carbon shell and therefore carbon shell has lower negative effect on magnetic properties.

- Owing to the extremely close distance (around 2 nm) between iron cores in CEMINPs, there will be higher visibility comparing to CEINPs and therefore, this type of nanoparticles has more priority to be used as contrast agent. On the other hand, it is noteworthy to mention that due to the carbon shell spherical shape and iron superparamagnetic behavior, their movement in body fluid can be smooth and controllable, and hence, the CEINPs can be potentially used in drug delivery.

- It is concluded that the gas nature of the reactor plasma used in the research project has a significant effect on the morphological properties of CEINPs. Accordingly, by this method CEINPs and CEMINPs can be synthesized based on the desired applications. The results of this contribution are one step forward to controlling carbon and iron core@shell and understanding growth mechanism.

- By adjusting the precursor concentration (1% w/w) and gas flow (30sccm), carbon encapsulated iron nanoparticles have been obtained by using gas phase arc discharge reactor.

- Morphological and structural characterization revealed a quite monodispersion as well as the α-phase crystallinity of the iron core, the iron carbide phase, and the absence of oxygen. These are very important factors when it comes to large scale productions, necessary for biomedical applications.

- Carbon nanoparticles decorated by fullerene (CNDFs) molecules on the surface have been obtained directly in one step by a new modified gas phase arc discharge reactor.

- Gas phase delivery of precursor to plasma and precursor compounds improved size distribution of CNDFs.

- SEM observations show that CNDFs are of spherical shape, 50.4 nm, which is optimum diameter for endocytic uptake and therefore have suitable morphology for drug delivery. In addition, CNDFs can be internalized to the cell more easily than elongated particles due to their spherical shape.

- Different fullerene molecules structures, including C_{36}, C_{60}, C_{90} and C_{130}, along the periphery of CNDFs, were detected by HTEM analysis. Obtained results indicate that arc discharge technique is suitable for engineering nanostructure materials such as CNDFs for biomedical applications.

- A new spherical porous carbon microparticles (PCMPs) structure has been obtained through a new and facile synthetic method.

- SEM images show PCMPs spherical shape with no agglomeration.

- According to SEM images, the size distribution of PCMPs is narrow with a mean diameter of 2.1 μm.

- In typical particles, BET analysis results show monolayer adsorption. In contrast, in our case, using porous microparticles, BET analysis has evidenced a multilayer adsorption mechanism.

- BET analysis shows specific surface area of 153.4 ± 4.2 m^2/g. The unique properties of PCMPs show a great promise as a carrier for drug delivery system and for lab on a chip devices.

- It was shown the possibility of using carbon encapsulated iron nanoparticle for treatment of eye floaters.

- Large multi-mono graphene (1×1 cm) has been obtained on copper substrate by using CEINPs and CVD method.

- Raman spectroscopy results revealed that the use of high concentration of CEINPs enhances the quality of graphene and leads to the growth of mono layer on copper substrate.

References

ABDALLAH, W. A. & YANG, Y. 2012. Raman spectrum of asphaltene. *Energy & Fuels,* 26**,** 6888-6896.

ABDULLAEVA, Z., OMURZAK, E., IWAMOTO, C., GANAPATHY, H. S., SULAIMANKULOVA, S., LILIANG, C. & MASHIMO, T. 2012. Onion-like carbon-encapsulated Co, Ni, and Fe magnetic nanoparticles with low cytotoxicity synthesized by a pulsed plasma in a liquid. *Carbon,* 50**,** 1776-1785.

AFRAZEH, M. 2007. Rozaneh Magazine. Available: http://www.rozanehmagazine.com/MayJune2007.html/Aculture.html 2015.

AGUILO-AGUAYO, N., INESTROSA-IZURIETA, M. J., GARCÍA-CÉSPEDES, J. & BERTRAN, E. 2010. Morphological and magnetic properties of superparamagnetic carbon-coated Fe nanoparticles produced by arc discharge. *Journal of nanoscience and nanotechnology,* 10**,** 2646-2649.

AGUILO-AGUAYO, N., LIU, Z., BERTRAN, E. & YANG, J. 2013. Thermal-Induced Structural Evolution of Carbon-Encapsulated Iron Nanoparticles Generated by Two Different Methods. *The Journal of Physical Chemistry C,* 117**,** 19167-19174.

AGUILO-AGUAYO, N. *Production and characterisation of carbon-encapsulated iron nanoparticles by arc-discharge plasma. Doctoral thesis, Universitat de Barcelona, 2012.*

AHMAD, B., AHMAD, M., RIAZ, M., AHMAD, N. & AHMAD, S. 2005. Effect of surface temperature on the concentration of C 60/C 70 molecules in dc arc discharge fullerene generator. *Materials chemistry and physics,* 94**,** 52-57.

AHMAD, B., RIAZ, M., AHMAD, M., NAWAZ, S. & AHMAD, S. 2008. Synthesis and characterization of higher fullerene (C 84) in dc arc discharge using Cu as a catalyst. *Materials Letters,* 62**,** 3367-3369.

AI, Z., DENG, K., WAN, Q., ZHANG, L. & LEE, S. 2010. Facile microwave-assisted synthesis and magnetic and gas sensing properties of Fe3O4 nanoroses. *The Journal of Physical Chemistry C,* 114**,** 6237-6242.

AMBASHTA, R. D. & SILLANPÄÄ, M. 2010. Water purification using magnetic assistance: a review. *Journal of hazardous materials,* 180**,** 38-49.

AMER, M. S. 2010. *Raman spectroscopy, fullerenes and nanotechnology*, Royal Society of Chemistry.

ANDO, Y. & ZHAO, X. 2006. Synthesis of carbon nanotubes by arc-discharge method. *New diamond and frontier carbon technology,* 16**,** 123-138.

ANIA, C. O., KHOMENKO, V., RAYMUNDO-PIÑERO, E., PARRA, J. B. & BEGUIN, F. 2007. The large electrochemical capacitance of microporous doped carbon obtained by using a zeolite template. *Advanced Functional Materials,* 17**,** 1828-1836.

AVALOS-BELMONTES, F., RAMOS-DEVALLE, L., RAMÍREZ-VARGAS, E., SÁNCHEZ-VALDES, S., MÉNDEZ-NONEL, J. & ZITZUMBO-GUZMÁN, R. 2012. Nucleating effect of carbon nanoparticles and their influence on the thermal and chemical stability of polypropylene. *Journal of Nanomaterials,* 2012**,** 104.

BAKER, R. 1989. Catalytic growth of carbon filaments. *Carbon,* 27**,** 315-323.

BAKER, R., BARBER, M., HARRIS, P., FEATES, F. & WAITE, R. 1972. Nucleation and growth of carbon deposits from the nickel catalyzed decomposition of acetylene. *Journal of catalysis,* 26**,** 51-62.

BAKOGLIDIS, K., SIMEONIDIS, K., SAKELLARI, D., STEFANOU, G. & ANGELAKERIS, M. 2012. Size-dependent mechanisms in AC magnetic hyperthermia response of iron-oxide nanoparticles. *Magnetics, IEEE Transactions on,* 48**,** 1320-1323.

BAKTHAVATHSALAM, P., RAJENDRAN, V. K., SARAN, U., CHATTERJEE, S. & ALI, B. M. J. 2013. Immunomagnetic nanoparticle based quantitative PCR for rapid detection of Salmonella. *Microchimica Acta,* 180**,** 1241-1248.

BANDI, V., EL-KHOULY, M. E., OHKUBO, K., NESTEROV, V. N., ZANDLER, M. E., FUKUZUMI, S. & D'SOUZA, F. 2014. Bisdonor–azaBODIPY–Fullerene Supramolecules: Syntheses, Characterization, and Light-Induced Electron-Transfer Studies. *The Journal of Physical Chemistry C,* 118**,** 2321-2332.

BEAN, C. & LIVINGSTON, J. 1959. Superparamagnetism. *Journal of Applied Physics,* 30**,** S120-S129.

BECKER, R. & DÖRING, W. 1935. The kinetic treatment of nuclear formation in supersaturated vapors. *Ann. Phys,* 24**,** 752.

BEHESHTIAN, J., PEYGHAN, A. A. & BAGHERI, Z. 2012. Theoretical investigation of C 60 fullerene functionalization with tetrazine. *Computational and Theoretical Chemistry,* 992**,** 164-167.

BERGER, C., SONG, Z., LI, X., WU, X., BROWN, N., NAUD, C., MAYOU, D., LI, T., HASS, J. & MARCHENKOV, A. N. 2006. Electronic confinement and coherence in patterned epitaxial graphene. *Science,* 312**,** 1191-1196.

BITTOVA, B., POLTIEROVA-VEJPRAVOVA, J., ROCA, A., MORALES, M. & TYRPEKL, V. Effects of coating on magnetic properties in iron oxide nanoparticles. Journal of Physics: Conference Series, 2010. IOP Publishing, 072012.

BITTOVA, B., VEJPRAVOVA, J. P., KALBAC, M., BURIANOVA, S., MANTLIKOVA, A., DANIS, S. & DOYLE, S. 2011. Magnetic properties of iron catalyst particles in HiPco single wall carbon nanotubes. *The Journal of Physical Chemistry C,* 115**,** 17303-17309.

BOGUE, R. 2010. Quantum dots: a bright future for photonic nanosensors. *Sensor Review,* 30**,** 279-284.

BORYSIUK, J., GRABIAS, A., SZCZYTKO, J., BYSTRZEJEWSKI, M., TWARDOWSKI, A. & LANGE, H. 2008. Structure and magnetic properties of carbon encapsulated Fe nanoparticles obtained by arc plasma and combustion synthesis. *Carbon,* 46**,** 1693-1701.

BRENNER, J., HARKNESS, J., KNICKELBEIN, M., KRUMDICK, G. & MARSHALL, C. 1997. Microwave plasma synthesis of carbon-supported ultrafine metal particles. *Nanostructured materials,* 8**,** 1-17.

BRUCE WETZEL, H. S. 1989. *SEM blood cells* [Online]. National Cancer Institute. Available: http://en.wikipedia.org/wiki/White_blood_cell#/media/File:SEM_blood_cells.jpg 2015].

BRUNAUER, S., DEMING, L. S., DEMING, W. E. & TELLER, E. 1940. On a theory of the van der Waals adsorption of gases. *Journal of the American Chemical Society,* 62**,** 1723-1732.

BUTT, H.-J., GRAF, K. & KAPPL, M. 2006. *Physics and chemistry of interfaces*, John Wiley & Sons.

BYSTRZEJEWSKI, M. 2011. Synthesis of carbon-encapsulated iron nanoparticles via solid state reduction of iron oxide nanoparticles. *Journal of Solid State Chemistry,* 184**,** 1492-1498.

BYSTRZEJEWSKI, M., HUCZKO, A., LANGE, H., CUDZIŁO, S. & KICINSKI, W. 2007. Combustion synthesis route to carbon-encapsulated iron nanoparticles. *Diamond and related materials,* 16**,** 225-228.

BYSTRZEJEWSKI, M., KLINGELER, R., GEMMING, T., BÜCHNER, B. & RÜMMELI, M. 2011. Synthesis of carbon-encapsulated iron nanoparticles by pyrolysis of iron citrate and poly (vinyl alcohol): a critical evaluation of yield and selectivity. *Nanotechnology,* 22**,** 315606.

BYSTRZEJEWSKI, M., PYRZYNSKA, K., HUCZKO, A. & LANGE, H. 2009. Carbon-encapsulated magnetic nanoparticles as separable and mobile sorbents of heavy metal ions from aqueous solutions. *Carbon,* 47**,** 1201-1204.

CABRIOLU, R., KASHCHIEV, D. & AUER, S. 2012. Breakdown of nucleation theory for crystals with strongly anisotropic interactions between molecules. *The Journal of chemical physics,* 137**,** 204903.
CAO, H., HUANG, G., XUAN, S., WU, Q., GU, F. & LI, C. 2008. Synthesis and characterization of carbon-coated iron core/shell nanostructures. *Journal of Alloys and Compounds,* 448**,** 272-276.
CAO, M., LI, Z., WANG, J., GE, W., YUE, T., LI, R., COLVIN, V. L. & WILLIAM, W. Y. 2012. Food related applications of magnetic iron oxide nanoparticles: enzyme immobilization, protein purification, and food analysis. *Trends in Food Science & Technology,* 27**,** 47-56.
CATALDO, F., GARCÍA-HERNÁNDEZ, D. A. & MANCHADO, A. 2014. Sonochemical Synthesis of Fullerene C60/Anthracene Diels-Alder Mono and Bis-adducts. *Fullerenes, Nanotubes and Carbon Nanostructures,* 22**,** 565-574.
CHATURVEDI, S. & DAVE, P. N. 2013. Design process for nanomaterials. *Journal of Materials Science,* 48**,** 3605-3622.
CHAUDHARY, R. P., MOHANTY, S. K. & KOYMEN, A. R. 2014. Novel method for synthesis of Fe core and C shell magnetic nanoparticles. *Carbon,* 79**,** 67-73.
CHAZELAS, C., COUDERT, J.-F., JARRIGE, J. & FAUCHAIS, P. 2006. Synthesis of ultra fine particles by plasma transferred arc: Influence of anode material on particle properties. *Journal of the European Ceramic Society,* 26**,** 3499-3507.
CHEN, C.-N., CHEN, Y.-L. & TSENG, W. J. 2007. Surfactant-assisted de-agglomeration of graphite nanoparticles by wet ball mixing. *Journal of materials processing technology,* 190**,** 61-64.
CHEN, C., DING, G., ZHANG, D., JIAO, Z., WU, M., SHEK, C.-H., WU, C. L., LAI, J. K. & CHEN, Z. 2012a. Microstructure evolution and advanced performance of Mn_3O_4 nanomorphologies. *Nanoscale,* 4**,** 2590-2596.
CHEN, J., HERRICKS, T. & XIA, Y. 2005. Polyol synthesis of platinum nanostructures: control of morphology through the manipulation of reduction kinetics. *Angewandte Chemie,* 117**,** 2645-2648.
CHEN, Z., HONG, G., WANG, H., WELSHER, K., TABAKMAN, S. M., SHERLOCK, S. P., ROBINSON, J. T., LIANG, Y. & DAI, H. 2012b. Graphite-coated magnetic nanoparticle microarray for few-cells enrichment and detection. *ACS nano,* 6**,** 1094-1101.
CHOI, M. K. & PYUN, J. 2008. Light intensity and its fluctuations on a layered microsphere: Effects of shell thickness acting as a quantum well. *Current Applied Physics,* 8**,** 603-611.
CHUANCHEN, S., HAIBIN, G. & DUFEI, F. 1994. Extraction of C60 cluster ion beam. *Review of scientific instruments,* 65**,** 1405-1407.
CHURILOV, G. N., KRÄTSCHMER, W., OSIPOVA, I. V., GLUSHENKO, G. A., VNUKOVA, N. G., KOLONENKO, A. L. & DUDNIK, A. I. 2013. Synthesis of fullerenes in a high-frequency arc plasma under elevated helium pressure. *Carbon,* 62**,** 389-392.
CHUVILIN, A., KAISER, U., BICHOUTSKAIA, E., BESLEY, N. A. & KHLOBYSTOV, A. N. 2010. Direct transformation of graphene to fullerene. *Nature chemistry,* 2**,** 450-453.
COEY, J., VENKATESAN, M., FITZGERALD, C., DOUVALIS, A. & SANDERS, I. 2002. Ferromagnetism of a graphite nodule from the Canyon Diablo meteorite. *Nature,* 420**,** 156-159.
COLOMBO, M., CARREGAL-ROMERO, S., CASULA, M. F., GUTIÉRREZ, L., MORALES, M. P., BÖHM, I. B., HEVERHAGEN, J. T., PROSPERI, D. & PARAK, W. J. 2012. Biological applications of magnetic nanoparticles. *Chemical Society Reviews,* 41**,** 4306-4334.
CULLITY, B. D. & GRAHAM, C. D. 2011. *Introduction to magnetic materials*, John Wiley & Sons.
CURIE, M. 2013. *Pierre Curie: With Autobiographical Notes by Marie Curie*, Courier Corporation.

DAHOTRE, S. & SINGH, L. 2014. Superparamagnetism and FMR study of Nano Mn-Zn Ferrite. *Advances in Applied Science Research,* 5.
DAI, W., KIM, S. J., SEONG, W.-K., KIM, S. H., LEE, K.-R., KIM, H.-Y. & MOON, M.-W. 2013. Porous carbon nanoparticle networks with tunable absorbability. *Scientific reports,* 3.
DE FINA, K. M., EZELL, C. & ACREE JR, W. E. 2001. Solubility of ferrocene in organic nonelectrolyte solvents. Comparison of observed versus predicted values based upon mobile order theory. *Physics and Chemistry of Liquids,* 39**,** 699-710.
DE MATTEIS, L., FERNÁNDEZ-PACHECO, R., CUSTARDOY, L., GARCÍA-MARTÍN, M. L., DE LA FUENTE, J. S. M., MARQUINA, C. & IBARRA, M. R. 2014. Influence of a Silica Interlayer on the Structural and Magnetic Properties of Sol–Gel TiO2-Coated Magnetic Nanoparticles. *Langmuir,* 30**,** 5238-5247.
DECUZZI, P. & FERRARI, M. 2008. The receptor-mediated endocytosis of nonspherical particles. *Biophysical journal,* 94**,** 3790-3797.
DECUZZI, P., PASQUALINI, R., ARAP, W. & FERRARI, M. 2009. Intravascular delivery of particulate systems: does geometry really matter? *Pharmaceutical research,* 26**,** 235-243.
DELANEY, Y., OYINLOYE, A. & BENJAMIN, L. 2002. Nd: YAG vitreolysis and pars plana vitrectomy: surgical treatment for vitreous floaters. *Eye,* 16**,** 21-26.
DESAI, A. & HAQUE, M. 2007. Mechanical properties of ZnO nanowires. *Sensors and Actuators A: Physical,* 134**,** 169-176.
DING, F. & BOLTON, K. 2006. The importance of supersaturated carbon concentration and its distribution in catalytic particles for single-walled carbon nanotube nucleation. *Nanotechnology,* 17**,** 543.
DRUNG, D., ASSMANN, C., BEYER, J., KIRSTE, A., PETERS, M., RUEDE, F. & SCHURIG, T. 2007. Highly sensitive and easy-to-use SQUID sensors. *Applied Superconductivity, IEEE Transactions on,* 17**,** 699-704.
DUNK, P. W., KAISER, N. K., HENDRICKSON, C. L., QUINN, J. P., EWELS, C. P., NAKANISHI, Y., SASAKI, Y., SHINOHARA, H., MARSHALL, A. G. & KROTO, H. W. 2012. Closed network growth of fullerenes. *Nature communications,* 3**,** 855.
DUTTA, P., PAL, S., SEEHRA, M., SHAH, N. & HUFFMAN, G. 2009. Size dependence of magnetic parameters and surface disorder in magnetite nanoparticles. *Journal of Applied Physics,* 105**,** 07B501-07B501-3.
EGERTON, R. 2009. Electron energy-loss spectroscopy in the TEM. *Reports on Progress in Physics,* 72**,** 016502.
EIZENBERG, M. & BLAKELY, J. 1979. Carbon monolayer phase condensation on Ni (111). *Surface Science,* 82**,** 228-236.
EL-GENDY, A., IBRAHIM, E., KHAVRUS, V., KRUPSKAYA, Y., HAMPEL, S., LEONHARDT, A., BÜCHNER, B. & KLINGELER, R. 2009. The synthesis of carbon coated Fe, Co and Ni nanoparticles and an examination of their magnetic properties. *Carbon,* 47**,** 2821-2828.
ELERT, G. 1998. Viscosity. *The Physics Hypertextbook,* 2014.
ENRIC BERTRAN, N. A.-A., MARÍA JOSÉ INESTROSA-IZURIETA. 2012. *Method and Reactor for the Production of Carbon-Coated Nano-particles.*
FANG, Y., GU, D., ZOU, Y., WU, Z., LI, F., CHE, R., DENG, Y., TU, B. & ZHAO, D. 2010. A Low-Concentration Hydrothermal Synthesis of Biocompatible Ordered Mesoporous Carbon Nanospheres with Tunable and Uniform Size. *Angewandte Chemie International Edition,* 49**,** 7987-7991.
FARHAT, S., DE LA CHAPELLE, M. L., LOISEAU, A., SCOTT, C. D., LEFRANT, S., JOURNET, C. & BERNIER, P. 2001. Diameter control of single-walled carbon nanotubes using argon–helium mixture gases. *The Journal of Chemical Physics,* 115**,** 6752-6759.
FEDOSEEVA, Y. V., BULUSHEVA, L., OKOTRUB, A., VYALIKH, D., HUO, J., SONG, H., ZHOU, J. & CHEN, X. 2012. Effect of oxidation and heat treatment on the morphology

and electronic structure of carbon-encapsulated iron carbide nanoparticles. *Materials Chemistry and Physics,* 135**,** 235-240.
FERRARI, A., MEYER, J., SCARDACI, V., CASIRAGHI, C., LAZZERI, M., MAURI, F., PISCANEC, S., JIANG, D., NOVOSELOV, K. & ROTH, S. 2006. Raman spectrum of graphene and graphene layers. *Physical review letters,* 97**,** 187401.
FERRARI, M. 2008. Nanogeometry: beyond drug delivery. *Nature nanotechnology,* 3**,** 131-132.
FEYNMAN, R. P. 1960. There's plenty of room at the bottom. *Engineering and science,* 23**,** 22-36.
FREIRE SOLER, V. M. 2014. Fabrication and Characterization of Macroscopic Graphene Layers on Metallic Substrates. *Doctoral thesis, Universitat de Barcelona, 2014.*
FRIEDLANDER, S. 1983. DYNAMICS OF AEROSOL FORMATION BY CHEMICAL REACTION*. *Annals of the New York Academy of Sciences,* 404**,** 354-364.
GALAKHOV, V. R., BULING, A., NEUMANN, M., OVECHKINA, N. A., SHKVARIN, A. S., SEMENOVA, A., UIMIN, M., YERMAKOV, A. Y., KURMAEV, E. & VILKOV, O. 2011. Carbon states in carbon-encapsulated nickel nanoparticles studied by means of X-ray absorption, emission, and photoelectron spectroscopies. *The Journal of Physical Chemistry C,* 115**,** 24615-24620.
GANESHKUMAR, M., PONRASU, T., SATHISHKUMAR, M. & SUGUNA, L. 2013. Preparation of amphiphilic hollow carbon nanosphere loaded insulin for oral delivery. *Colloids and Surfaces B: Biointerfaces,* 103**,** 238-243.
GAO, H., SHI, W. & FREUND, L. B. 2005. Mechanics of receptor-mediated endocytosis. *Proceedings of the National Academy of Sciences of the United States of America,* 102**,** 9469-9474.
GARCÍA-GONZÁLEZ, C., ALNAIEF, M. & SMIRNOVA, I. 2011. Polysaccharide-based aerogels—Promising biodegradable carriers for drug delivery systems. *Carbohydrate Polymers,* 86**,** 1425-1438.
GAUMET, M., VARGAS, A., GURNY, R. & DELIE, F. 2008. Nanoparticles for drug delivery: the need for precision in reporting particle size parameters. *European journal of pharmaceutics and biopharmaceutics,* 69**,** 1-9.
GEDYE, R. N., SMITH, F. E. & WESTAWAY, K. C. 1988. The rapid synthesis of organic compounds in microwave ovens. *Canadian Journal of Chemistry,* 66**,** 17-26.
GERDEMAN, D. & HECHT, N. Arc Plasma Technology in Materials Science', 1972. New York, Springer Verlag.
GHOSH CHAUDHURI, R. & PARIA, S. 2011. Core/shell nanoparticles: classes, properties, synthesis mechanisms, characterization, and applications. *Chemical reviews,* 112**,** 2373-2433.
GHOSH, S. K. 2011. Kubo gap as a factor governing the emergence of new physicochemical characteristics of the small metallic particulates. *Assam University Journal of Science and Technology,* 7**,** 114-121.
GITTLEMAN, J., ABELES, B. & BOZOWSKI, S. 1974. Superparamagnetism and relaxation effects in granular Ni-Si O 2 and Ni-Al 2 O 3 films. *Physical Review B,* 9**,** 3891.
GOEL, A., HOWARD, J. B. & VANDER SANDE, J. B. 2004. Size analysis of single fullerene molecules by electron microscopy. *Carbon,* 42**,** 1907-1915.
GOEL, A., HOWARD, J. B. & VANDER SANDE, J. B. 2012. Fullerenic structures and such structures tethered to carbon materials. Google Patents.
GORDIETS, B., INESTROSA-IZURIETA, M. J., NAVARRO, A. & BERTRAN, E. 2011. Nanoparticles in SiH4-Ar plasma: Modelling and comparison with experimental data. *Journal of Applied Physics,* 110**,** 103302.
GOZZI, D., LATINI, A., CAPANNELLI, G., CANEPA, F., NAPOLETANO, M., CIMBERLE, M. R. & TROPEANO, M. 2006. Synthesis and magnetic characterization of Ni nanoparticles and Ni nanoparticles in multiwalled carbon nanotubes. *Journal of alloys and compounds,* 419**,** 32-39.

GRANQVIST, C. & BUHRMAN, R. 1976. Log-normal size distributions of ultrafine metal particles. *Solid State Communications,* 18**,** 123-126.
GRUDZINSKI, I. P., BYSTRZEJEWSKI, M., CYWINSKA, M. A., KOSMIDER, A., POPLAWSKA, M., CIESZANOWSKI, A. & OSTROWSKA, A. 2013. Cytotoxicity evaluation of carbon-encapsulated iron nanoparticles in melanoma cells and dermal fibroblasts. *Journal of Nanoparticle Research,* 15**,** 1-18.
GUNJI, T., HIRAMA, K., TSUKADA, S. & ABE, Y. 2014. Preparation and properties of a fullerene/polysiloxane hybrid from chemically modified fullerene and polymethoxysiloxane. *Journal of Sol-Gel Science and Technology,* 72**,** 80-84.
GUPTA, V., PATRA, M. K., SHUKLA, A., SAINI, L., SONGARA, S., JANI, R., VADERA, S. R. & KUMAR, N. 2012. Synthesis of core–shell iron nanoparticles from decomposition of Fe–Sn nanocomposite and studies on their microwave absorption properties. *Journal of Nanoparticle Research,* 14**,** 1-10.
GUTSCH, A., KRAMER, M., MICHAEL, G., MUHLENWEG, H., PRIDOHL, M. & ZIMMERMANN, G. 2002. Gas-phase production of nanoparticles. *Kona,* 20**,** 24-37.
HADJIPANAYIS, C. G., BONDER, M. J., BALAKRISHNAN, S., WANG, X., MAO, H. & HADJIPANAYIS, G. C. 2008. Metallic iron nanoparticles for MRI contrast enhancement and local hyperthermia. *Small,* 4**,** 1925-1929.
HAFNER, B. 2007. Scanning electron microscopy primer. *Characterization Facility, University of Minnesota-Twin Cities***,** 1-29.
HAINES, J. & TSAI, C. 2002. Graphite sublimation tests for the muon collider/neutrino factory target development program. *ORNL/TM-2002/27, Oak Ridge National Laboratory, Oak Ridge, Tennessee*.
HÄMÄLÄINEN, M., HARI, R., ILMONIEMI, R. J., KNUUTILA, J. & LOUNASMAA, O. V. 1993. Magnetoencephalography—theory, instrumentation, and applications to noninvasive studies of the working human brain. *Reviews of modern Physics,* 65**,** 413.
HAN, B., RHEE, C., LEE, M. & UHM, Y. 2006. Synthesis of nano crystalline Ni and Fe by levitational gas condensation method. *Magnetics, IEEE Transactions on,* 42**,** 3779-3781.
HAN, G. H., GUNES, F., BAE, J. J., KIM, E. S., CHAE, S. J., SHIN, H.-J., CHOI, J.-Y., PRIBAT, D. & LEE, Y. H. 2011. Influence of copper morphology in forming nucleation seeds for graphene growth. *Nano letters,* 11**,** 4144-4148.
HANSEN, M. F. & MORUP, S. 1999. Estimation of blocking temperatures from ZFC/FC curves. *Journal of Magnetism and Magnetic Materials,* 203**,** 214-216.
HARTONO, S. B., YU, M., GU, W., YANG, J., STROUNINA, E., WANG, X., QIAO, S. & YU, C. 2014. Synthesis of multi-functional large pore mesoporous silica nanoparticles as gene carriers. *Nanotechnology,* 25**,** 055701.
HERITAGE, A. 2000. The American Heritage dictionary of the English language. Houghton Mifflin Company.
HERNANDEZ, A. V., TORCHYNSKA, T., VAZQUEZ, A. Q., MATSUMOTO, Y., KHOMENKOVA, L. & SHCHERBINA, L. Emission and structure investigations of Si nano-crystals embedded in amorphous silicon. Journal of Physics: Conference Series, 2007. IOP Publishing, 1231.
HORNYAK, G. L., DUTTA, J., TIBBALS, H. F. & RAO, A. 2011. *Introduction to nanoscience*, Crc Press.
HUANG, L., WANG, M., DAI, T., SPERANDIO, F. F., HUANG, Y.-Y., XUAN, Y., CHIANG, L. Y. & HAMBLIN, M. R. 2014. Antimicrobial photodynamic therapy with decacationic monoadducts and bisadducts of [70] fullerene: in vitro and in vivo studies. *Nanomedicine,* 9**,** 253-266.
HUANG, S., WOODSON, M., SMALLEY, R. & LIU, J. 2004. Growth mechanism of oriented long single walled carbon nanotubes using “fast-heating” chemical vapor deposition process. *Nano Letters,* 4**,** 1025-1028.

HUANG, W., ZHANG, H., HUANG, Y., WANG, W. & WEI, S. 2011. Hierarchical porous carbon obtained from animal bone and evaluation in electric double-layer capacitors. *Carbon,* 49**,** 838-843.
HUCZKO, A., BYSTRZEJEWSKI, M., LANGE, H., FABIANOWSKA, A., CUDZILO, S., PANAS, A. & SZALA, M. 2005. Combustion synthesis as a novel method for production of 1-D SiC nanostructures. *The Journal of Physical Chemistry B,* 109**,** 16244-16251.
HUCZKO, A., LANGE, H., CHOJECKI, G., CUDZILO, S., ZHU, Y. Q., KROTO, H. W. & WALTON, D. R. 2003. Synthesis of novel nanostructures by metal-polytetrafluoroethene thermolysis. *The Journal of Physical Chemistry B,* 107**,** 2519-2524.
HUO, J., SONG, H. & CHEN, X. 2004. Preparation of carbon-encapsulated iron nanoparticles by co-carbonization of aromatic heavy oil and ferrocene. *Carbon,* 42**,** 3177-3182.
HUO, J., SONG, H., CHEN, X. & CHENG, B. 2008. From carbon-encapsulated iron nanorods to carbon nanotubes. *The Journal of Physical Chemistry C,* 112**,** 5835-5839.
HWANG, N. & BARRON, A. R. 2011. BET surface area analysis of nanoparticles. *The Connexions project***,** 1-11.
HWANG, W. S., TRUONG, P. L. & SIM, S. J. 2012. Size-dependent plasmonic responses of single gold nanoparticles for analysis of biorecognition. *Analytical biochemistry,* 421**,** 213-218.
IBACH, H. 2006a. *Physics of surfaces and interfaces*, Springer.
IBACH, H. 2006b. Vibrational Excitations at Surfaces. *Physics of Surfaces and Interfaces***,** 309-377.
IIJIMA, S. 1991. Helical microtubules of graphitic carbon. *nature,* 354**,** 56-58.
ISHII, M., SHIBATA, R., NUMAGUCHI, Y., KITO, T., SUZUKI, H., SHIMIZU, K., ITO, A., HONDA, H. & MUROHARA, T. 2011. Enhanced angiogenesis by transplantation of mesenchymal stem cell sheet created by a novel magnetic tissue engineering method. *Arteriosclerosis, thrombosis, and vascular biology,* 31**,** 2210-2215.
ITAMI, K. 2011. Molecular catalysis for fullerene functionalization. *The Chemical Record,* 11**,** 226-235.
JACOBS, C. & MÜLLER, R. H. 2002. Production and characterization of a budesonide nanosuspension for pulmonary administration. *Pharmaceutical research,* 19**,** 189-194.
JAFARI, A., BOUSTANI, K. & SHAYESTEH, S. F. 2014. Effect of carbon shell on the structural and magnetic properties of Fe3O4 superparamagnetic nanoparticles. *Journal of Superconductivity and Novel Magnetism,* 27**,** 187-194.
JANAUN, J., ABANG, S. & ANWAR, A. M. Synthesis and characterization of carbon-based catalyst derived from seaweed. Clean Energy and Technology (CEAT), 2013 IEEE Conference on, 2013. IEEE, 19-22.
JI, X., HUANG, X., ZHAO, Q., WANG, A. & LIU, X. 2014. Facile Synthesis of Carbon-Coated Zn 2 SnO 4 Nanomaterials as Anode Materials for Lithium-Ion Batteries. *Journal of Nanomaterials,* 2014.
JIN, C., HAIYAN, Z., LIPING, L. & LIB, Z. 2013. SUPER-PARAMAGNETIC CARBON COATED IRON NANOPARTICLES AND BIOLOGICAL MAGNETIC INDUCTION HEATING PROPERTIES. *DIGEST JOURNAL OF NANOMATERIALS AND BIOSTRUCTURES,* 8**,** 43-51.
JORISSEN, K. 2007. *Ab initio berekening van relativistische elektronenergieverliesspectra The ab initio calculation of relativistic electron energy loss spectra.* University of Antwerp.
JOSÉ-YACAMÁN, M., MIKI-YOSHIDA, M., RENDON, L. & SANTIESTEBAN, J. 1993. Catalytic growth of carbon microtubules with fullerene structure. *Applied physics letters,* 62**,** 202-204.
JOSHI, N. 2008. *Study of the Melting of Transition Metal Nanoclusters and Their Application to the Vapor-liquid-solid (VLS) Model*, ProQuest.

KACHAN, S. & PONYAVINA, A. 2001. Resonance absorption spectra of composites containing metal-coated nanoparticles. *Journal of Molecular Structure,* 563**,** 267-272.
KERMAN, K., MATSUBARA, Y., MORITA, Y., TAKAMURA, Y. & TAMIYA, E. 2004. Peptide nucleic acid modified magnetic beads for intercalator based electrochemical detection of DNA hybridization. *Science and technology of Advanced Materials,* 5**,** 351-357.
KHARISOV, B. I., DIAS, H. R., KHARISSOVA, O. V., JIMÉNEZ-PÉREZ, V. M., PEREZ, B. O. & FLORES, B. M. 2012. Iron-containing nanomaterials: synthesis, properties, and environmental applications. *RSC Advances,* 2**,** 9325-9358.
KOH, K., WONG-FOY, A. G., & MATZGER, A. J. 2009. A porous coordination copolymer with over 5000 m2/g BET surface area. *Journal of the American chemical society*, 131(12), 4184-4185.
KOPRINAROV, N., KONSTANTINOVA, M., PCHELAROV, G. & MARINOV, M. 1997. Carbon macrostructures obtained at AC arc discharge. *Journal of crystal growth,* 171**,** 111-118.
KRÄTSCHMER, W. & HUFFMAN, D. R. 1992. Fullerites: New forms of crystalline carbon. *Carbon,* 30**,** 1143-1147.
KREYLING, W. G., SEMMLER-BEHNKE, M. & MÖLLER, W. 2006. Ultrafine particle-lung interactions: does size matter? *Journal of Aerosol Medicine,* 19**,** 74-83.
KRUIS, F. E., FISSAN, H. & PELED, A. 1998. Synthesis of nanoparticles in the gas phase for electronic, optical and magnetic applications—a review. *Journal of Aerosol Science,* 29**,** 511-535.
KUZNETSOV, V. L., USOLTSEVA, A. N., CHUVILIN, A. L., OBRAZTSOVA, E. D. & BONARD, J.-M. 2001. Thermodynamic analysis of nucleation of carbon deposits on metal particles and its implications for the growth of carbon nanotubes. *Physical Review B,* 64**,** 235401.
LABĘDŹ, O., GRABIAS, A., KASZUWARA, W. & BYSTRZEJEWSKI, M. 2014. Influence of Al on synthesis and properties of carbon-encapsulated iron nanoparticles. *Journal of Alloys and Compounds,* 603**,** 230-238.
LAND, M. F. & FERNALD, R. D. 1992. The evolution of eyes. *Annual review of neuroscience,* 15**,** 1-29.
LANGE, H., SIODA, M., HUCZKO, A., ZHU, Y., KROTO, H. & WALTON, D. 2003. Nanocarbon production by arc discharge in water. *Carbon,* 41**,** 1617-1623.
LAPLAZE, D., ALVAREZ, L., GUILLARD, T., BADIE, J. & FLAMANT, G. 2002. Carbon nanotubes: dynamics of synthesis processes. *Carbon,* 40**,** 1621-1634.
LAURENT, C., FLAHAUT, E., PEIGNEY, A. & ROUSSET, A. 1998. Metal nanoparticles for the catalytic synthesis of carbon nanotubes. *New J. Chem.,* 22**,** 1229-1237.
LEE, J., KIM, J. & HYEON, T. 2006. Recent progress in the synthesis of porous carbon materials. *Advanced Materials,* 18**,** 2073-2094.
LEE, S. J., JUNG, J., KIM, M. A., KIM, Y.-R. & PARK, J. K. 2012. Synthesis of highly stable graphite-encapsulated metal (Fe, Co, and Ni) nanoparticles. *Journal of Materials Science,* 47**,** 8112-8117.
LEE, Y., LEE, J., BAE, C. J., PARK, J. G., NOH, H. J., PARK, J. H. & HYEON, T. 2005. Large-scale synthesis of uniform and crystalline magnetite nanoparticles using reverse micelles as nanoreactors under reflux conditions. *Advanced Functional Materials,* 15**,** 503-509.
LEFEBVRE, A. H. 1998. *Gas turbine combustion*, CRC press.
LESLIE-PELECKY, D. L. & RIEKE, R. D. 1996. Magnetic properties of nanostructured materials. *Chemistry of materials,* 8**,** 1770-1783.
LI, M., CUSHING, S. K., WANG, Q., SHI, X., HORNAK, L. A., HONG, Z. & WU, N. 2011. Size-dependent energy transfer between CdSe/ZnS quantum dots and gold nanoparticles. *The Journal of Physical Chemistry Letters,* 2**,** 2125-2129.
LI, X., CAI, W., COLOMBO, L. & RUOFF, R. S. 2009. Evolution of graphene growth on Ni and Cu by carbon isotope labeling. *Nano letters,* 9**,** 4268-4272.

LIN, K.-S., CHANG, N.-B. & CHUANG, T.-D. 2008. Fine structure characterization of zero-valent iron nanoparticles for decontamination of nitrites and nitrates in wastewater and groundwater. *Science and Technology of Advanced Materials,* 9**,** 025015.
LIU, D., WU, Q., CHEN, H. & CHANG, P. R. 2009. Transitional properties of starch colloid with particle size reduction from micro-to nanometer. *Journal of Colloid and Interface Science,* 339**,** 117-124.
LIU, X. H., ZHONG, L., HUANG, S., MAO, S. X., ZHU, T. & HUANG, J. Y. 2012. Size-dependent fracture of silicon nanoparticles during lithiation. *Acs Nano,* 6**,** 1522-1531.
LO, J.-C., LU, J.-C. & TENG, M.-H. 2011. A new crucible design of the arc-discharge method for the synthesis of graphite encapsulated metal (GEM) nanoparticles. *Diamond and Related Materials,* 20**,** 330-333.
LU, A. H., SALABAS, E. E. L. & SCHÜTH, F. 2007. Magnetic nanoparticles: synthesis, protection, functionalization, and application. *Angewandte Chemie International Edition,* 46**,** 1222-1244.
LU, X., YU, M., HUANG, H. & RUOFF, R. S. 1999. Tailoring graphite with the goal of achieving single sheets. *Nanotechnology,* 10**,** 269.
LU, Y., ZHU, Z. & LIU, Z. 2005. Carbon-encapsulated Fe nanoparticles from detonation-induced pyrolysis of ferrocene. *Carbon,* 43**,** 369-374.
LUKASZKOWICZ, K. 2011. *Review of nanocomposite thin films and coatings deposited by PVD and CVD technology*, INTECH Open Access Publisher.
LUO, N., LI, X., WANG, X., YAN, H., ZHANG, C. & WANG, H. 2010. Synthesis and characterization of carbon-encapsulated iron/iron carbide nanoparticles by a detonation method. *Carbon,* 48**,** 3858-3863.
LUO, N., LIU, K., LIU, Z., LI, X., CHEN, S., SHEN, Y. & CHEN, T. 2012. Controllable synthesis of carbon coated iron-based composite nanoparticles. *Nanotechnology,* 23**,** 475603.
M. REZA SANAEE, N. A.-A., ENRIC BERTRAN 2013a. Synthesis of carbon encapsulated iron nanoparticles for applications in biomedicine. *Journal of Nanomedicine and Nanotechnology.* Las Vegas, USA.
M. REZA SANAEE, S. C., V. M. FREIRE, N. AGUILO-AGUAYO, E. BERTRAN. Design and synthesis of carbon encapsulated iron nanoparticle for drug delivery. 10th International conference on Nano Bio and Med, 2013b Bilbao, Spain. Phantoms foundation, 212,213.
M. REZA. SANAEE, O. A., E. BERTRAN. Influence of plasma reactor parameters on carbon coating of iron nanoparticle. International conference on Nanoscience and Nanotechnology 11-14 March 2014 Madrid, Spain. Phantoms foundation, 9.
M. REZA. SANAEE, S. C., N. AGUILO-AGUAYO, E. BERTRAN. Influences of argon-helium mixtures on the carbon-coated iron nanoparticles produced by a modified arc discharge. 9th International Conference on Nanoscience and Nanotechnologies 2012 Thessaloniki, Greece. Artion, 12.
M. REZA. SANAEE, S. C., V. M. FREIRE, N. AGUILO-AGUAYO, E. BERTRAN. Study of carbon encapsulated iron nanoparticles produced by a modified arc discharge by applying nitrogen, argon and helium. International Conference on Nanoscience and Nanotechnology 23-26 April 2013 Bilbao, Spain. Phantoms foundation, 160,161.
MA, J. & TENNENT, H. 2011. Fullerenes are deposited onto a metal catalyst precursor or metal catalyst of iron, cobalt, manganese, nickel, or molybdenum; metal catalyst precursor/fullerene is reduced in presence of carbon containing gas; sublimation of fullerene and growing single walled carbon nanotubes; uniform diameter. Google Patents.
MAJETICH, S., SCOTT, J., BRUNSMAN, E. & MCHENRY, M. Formation of nanoparticles in a carbon arc. MRS Proceedings, 1994. Cambridge Univ Press, 29.
MAJUMDAR, M. G. 2012. Analysis of Stress-Coupled Magneto-Electric Effect in BaTiO3-CoFe2O4 Composites using Raman Spectroscopy. *International Journal of Scientific & Engineering Research,* 3**,** 1-7.

MALIK, H. K. & SINGH, A. K. 2010. *Engineering physics*, Tata McGraw Hill Education Private Limited.
MARTÍNEZ-BOUBETA, C., SIMEONIDIS, K., ANGELAKERIS, M., PAZOS-PÉREZ, N., GIERSIG, M., DELIMITIS, A., NALBANDIAN, L., ALEXANDRAKIS, V. & NIARCHOS, D. 2006. Critical radius for exchange bias in naturally oxidized Fe nanoparticles. *Physical Review B,* 74**,** 054430.
MAYO, J., YAVUZ, C., YEAN, S., CONG, L., SHIPLEY, H., YU, W., FALKNER, J., KAN, A., TOMSON, M. & COLVIN, V. 2007. The effect of nanocrystalline magnetite size on arsenic removal. *Science and Technology of Advanced Materials,* 8**,** 71-75.
MCBRIDE, A. A., PRICE, D. N., LAMOUREUX, L. R., ELMAOUED, A. A., VARGAS, J. M., ADOLPHI, N. L. & MUTTIL, P. 2013. Preparation and characterization of novel magnetic nano-in-microparticles for site-specific pulmonary drug delivery. *Molecular pharmaceutics,* 10**,** 3574-3581.
MCBRIDE, J. R. 2015. Ajit D. Kelkar, Daniel JC Herr and James G. Ryan: Nanoscience and Nanoengineering: Advances and Applications. *Journal of Cluster Science***,** 1-3.
MCNAUGHT, A. D. & MCNAUGHT, A. D. 1997. *Compendium of chemical terminology*, Blackwell Science Oxford.
MERKUS, H. G. 2009. *Particle size measurements: fundamentals, practice, quality*, Springer Science & Business Media.
MEYERS, M. A., MISHRA, A. & BENSON, D. J. 2006. Mechanical properties of nanocrystalline materials. *Progress in Materials Science,* 51**,** 427-556.
MNYUSIWALLA, A., DAAR, A. S. & SINGER, P. A. 2003. 'Mind the gap': science and ethics in nanotechnology. *Nanotechnology,* 14**,** R9.
MOHAMUD, R., XIANG, S. D., SELOMULYA, C., ROLLAND, J. M., O'HEHIR, R. E., HARDY, C. L. & PLEBANSKI, M. 2013. The effects of engineered nanoparticles on pulmonary immune homeostasis. *Drug metabolism reviews,* 46**,** 176-190.
MOKARI, T., SZTRUM, C. G., SALANT, A., RABANI, E. & BANIN, U. 2005. Formation of asymmetric one-sided metal-tipped semiconductor nanocrystal dots and rods. *Nature Materials,* 4**,** 855-863.
MONTAZER, M. & PAKDEL, E. 2010. Reducing photoyellowing of wool using nano TiO2. *Photochemistry and photobiology,* 86**,** 255-260.
MOODY, M. P. & ATTARD, P. 2002. Homogeneous nucleation of droplets from a supersaturated vapor phase. *The Journal of chemical physics,* 117**,** 6705-6714.
MOSTOFIZADEH, A., LI, Y., SONG, B. & HUANG, Y. 2011. Synthesis, properties, and applications of low-dimensional carbon-related nanomaterials. *Journal of nanomaterials,* 2011**,** 16.
MUSEUM, B. 2012. *Nanotechnology is ancient history* [Online]. Thegaurdian. Available: http://www.theguardian.com/nanotechnology-world/nanotechnology-is-ancient-history 2015].
NA, H. B., SONG, I. C. & HYEON, T. 2009. Inorganic nanoparticles for MRI contrast agents. *Advanced Materials,* 21**,** 2133-2148.
NANDA, K., MAISELS, A., KRUIS, F., FISSAN, H. & STAPPERT, S. 2003. Higher surface energy of free nanoparticles. *Physical review letters,* 91**,** 106102.
NAZAROV, M. 2011. *New Generation of Europium-and Terbium-Activated Phosphors: From Syntheses to Applications*, CRC Press.
NÉEL, L. 1949. Théorie du traînage magnétique des ferromagnétiques en grains fins avec applications aux terres cuites. *Ann. géophys,* 5**,** 99-136.
NING, L., XIAOJIE, L., XIAOHONG, W., HONGHAO, Y., FEI, M. & WEI, S. 2009. Preparation and magnetic behavior of carbon-encapsulated iron nanoparticles by detonation method. *Composites Science and Technology,* 69**,** 2554-2558.
NISHIJO, J., OKABE, C., BUSHIRI, J., KOSUGI, K., NISHI, N. & SAWA, H. 2005. Formation of carbon-encapsulated metallic nano-particles from metal acetylides by electron beam

irradiation. *The European Physical Journal D-Atomic, Molecular, Optical and Plasma Physics,* 34**,** 219-222.
NOVOSELOV, K. S., GEIM, A. K., MOROZOV, S., JIANG, D., ZHANG, Y., DUBONOS, S., GRIGORIEVA, I. & FIRSOV, A. 2004. Electric field effect in atomically thin carbon films. *science,* 306**,** 666-669.
NOWICKA, A. M., KOWALCZYK, A., BYSTRZEJEWSKI, M., DONTEN, M. & STOJEK, Z. 2012. Carbon-encapsulated iron nanoparticles used to generate magnetic field and to enhance substrate transport at electrode surface. *Electrochemistry Communications,* 20**,** 4-6.
NURUDDIN, M., BAYUAJI, R., MASILAMANI, M. & BIYANTO, T. 2010. Sidoarjo mud: A potential cement replacement material. *Civil Engineering Dimension,* 12**,** 18-22.
OH, W.-K., YOON, H. & JANG, J. 2010. Size control of magnetic carbon nanoparticles for drug delivery. *Biomaterials,* 31**,** 1342-1348.
PARADA 2006. Microwave-assisted synthesis and magnetic study of nanosized Ni/NiO materials.
PARK, J., JEONG, S., JEONG, M., KIM, J. & CHO, B. 2008. Synthesis of carbon-encapsulated magnetic nanoparticles by pulsed laser irradiation of solution. *Carbon,* 46**,** 1369-1377.
PARK, S. & RUOFF, R. S. 2009. Chemical methods for the production of graphenes. *Nature nanotechnology,* 4**,** 217-224.
PARTHA, R. & CONYERS, J. L. 2009. Biomedical applications of functionalized fullerene-based nanomaterials. *International journal of nanomedicine,* 4**,** 261.
PEATE, I. & NAIR, M. 2015. *Anatomy and Physiology for Nurses at a Glance*, John Wiley & Sons.
PENG, R., ZHANG, W., RAN, Q., LIANG, C., JING, L., YE, S. & XIAN, Y. 2011. Magnetically switchable bioelectrocatalytic system based on ferrocene grafted iron oxide nanoparticles. *Langmuir,* 27**,** 2910-2916.
PIRÓTH, A. & SÓLYOM, J. 2008. *Fundamentals of the Physics of Solids: Volume II: Electronic Properties*, Springer Science & Business Media.
POMOGAILO, A. D. & KESTEL'MAN, V. N. 2006. *Metallopolymer nanocomposites*, Springer Science & Business Media.
QI, L. 2011. *MEG study on the prediction of motion trajectory.*
QI, W., WANG, M. & XU, G. 2003. Comment on “Size effect on the lattice parameters of nanoparticles”. *Journal of materials science letters,* 22**,** 1333-1334.
QIAO, Y. & ZHAO, X. 2009. Electrorheological effect of carbonaceous materials with hierarchical porous structures. *Colloids and Surfaces A: Physicochemical and Engineering Aspects,* 340**,** 33-39.
RAJ, B. 2005. *Frontiers in Materials Science*, Universities Press.
RAMESH, P. D. & RAO, K. J. 1995. Microwave-assisted synthesis of aluminum nitride. *Advanced Materials,* 7**,** 177-179.
RAO, J. P., GRUENBERG, P. & GECKELER, K. E. 2015. Magnetic zero-valent metal polymer nanoparticles: Current trends, scope, and perspectives. *Progress in Polymer Science,* 40**,** 138-147.
RASHID, M. H., RAULA, M. & MANDAL, T. K. 2011. Polymer assisted synthesis of chain-like cobalt-nickel alloy nanostructures: Magnetically recoverable and reusable catalysts with high activities. *Journal of Materials Chemistry,* 21**,** 4904-4917.
RAY, S., SAHA, A., JANA, N. R. & SARKAR, R. 2009. Fluorescent carbon nanoparticles: synthesis, characterization, and bioimaging application. *The Journal of Physical Chemistry C,* 113**,** 18546-18551.
REED, S. J. 1995. Electron probe microanalysis. *Microprobe techniques in the earth sciences.* Springer.
REISS, G. & HÜTTEN, A. 2005. Magnetic nanoparticles: applications beyond data storage. *Nature materials,* 4**,** 725-726.

REITZ, R. D. 1987. Modeling atomization processes in high-pressure vaporizing sprays. *Atomisation Spray Technology,* 3**,** 309-337.
ROCA, A., CARMONA, D., MIGUEL-SANCHO, N., BOMATI-MIGUEL, O., BALAS, F., PIQUER, C. & SANTAMARIA, J. 2012. Surface functionalization for tailoring the aggregation and magnetic behaviour of silica-coated iron oxide nanostructures. *Nanotechnology,* 23**,** 155603.
RODUNER, E. 2006. Size matters: why nanomaterials are different. *Chemical Society Reviews,* 35**,** 583-592.
RUIZ-HERNANDEZ, E., BAEZA, A. & VALLET-REGI, M. A. 2011. Smart drug delivery through DNA/magnetic nanoparticle gates. *ACS nano,* 5**,** 1259-1266.
RUIZ, A., SALAS, G., CALERO, M., HERNANDEZ, Y., VILLANUEVA, A., HERRANZ, F., VEINTEMILLAS-VERDAGUER, S., MARTINEZ, E., BARBER, D. & MORALES, M. 2013. Short-chain PEG molecules strongly bound to magnetic nanoparticle for MRI long circulating agents. *Acta biomaterialia,* 9**,** 6421-6430.
SAITO, Y. 1995. Nanoparticles and filled nanocapsules. *Carbon,* 33**,** 979-988.
SAITO, Y., YOSHIKAWA, T., OKUDA, M., FUJIMOTO, N., YAMAMURO, S., WAKOH, K., SUMIYAMA, K., SUZUKI, K., KASUYA, A. & NISHINA, Y. 1994. Cobalt particles wrapped in graphitic carbon prepared by an arc discharge method. *Journal of Applied Physics,* 75**,** 134-137.
SALKIC, S. 2012. Monitoring Photocatalytic Degradation of X-Ray Contrast Media with Raman Spectroscopy.
SANAEE, M. R. & BERTRAN, E. 2015. Synthesis of Carbon Encapsulated Mono-and Multi-Iron Nanoparticles. *Journal of Nanomaterials,* 2015.
SANCHEZ, R., RIVAS, J., VAQUEIRO, P., LOPEZ-QUINTELA, M. & CAEIRO, D. 2002. Particle size effects on magnetic properties of yttrium iron garnets prepared by a sol–gel method. *Journal of magnetism and magnetic materials,* 247**,** 92-98.
SANTO, N., FASCIO, U., TORRES, F., GUAZZONI, N., TREMOLADA, P., BETTINETTI, R., MANTECCA, P. & BACCHETTA, R. 2014. Toxic effects and ultrastructural damages to Daphnia magna of two differently sized ZnO nanoparticles: Does size matter? *Water research,* 53**,** 339-350.
SANTORO, F., DASGUPTA, S., SCHNITKER, J., AUTH, T., NEUMANN, E., PANAITOV, G., GOMPPER, G. & OFFENHAUSSER, A. 2014. Interfacing electrogenic cells with 3d nanoelectrodes: position, shape, and size matter. *ACS nano,* 8**,** 6713-6723.
SATO, T., IIJIMA, T., SEKI, M. & INAGAKI, N. 1987. Magnetic properties of ultrafine ferrite particles. *Journal of Magnetism and Magnetic Materials,* 65**,** 252-256.
SCHÄRTL, W. 2010. Current directions in core–shell nanoparticle design. *Nanoscale,* 2**,** 829-843.
SCHWEITZER, J. 2014. *Scanning Electron Microscope* [Online]. Purdue University. Available: http://www.purdue.edu/ehps/rem/rs/sem.htm 2015].
SCOTT, J. H. J. & MAJETICH, S. A. 1995. Morphology, structure, and growth of nanoparticles produced in a carbon arc. *Physical Review B,* 52**,** 12564.
SEEBER, B. 1998. *Handbook of applied superconductivity*, CRC press.
SEEHRA, M., SINGH, V., DUTTA, P., NEELESHWAR, S., CHEN, Y., CHEN, C., CHOU, S. & CHEN, C.-C. 2010. Size-dependent magnetic parameters of fcc FePt nanoparticles: applications to magnetic hyperthermia. *Journal of Physics D: Applied Physics,* 43**,** 145002.
SENDROWSKI, D. P. & BRONSTEIN, M. A. 2010. Current treatment for vitreous floaters. *Optometry-Journal of the American Optometric Association,* 81**,** 157-161.
SERAPHIN, S., ZHOU, D. & JIAO, J. 1996. Filling the carbon nanocages. *Journal of applied physics,* 80**,** 2097-2104.
SETHURAMAN, V. A., HARDWICK, L. J., SRINIVASAN, V. & KOSTECKI, R. 2010. Surface structural disordering in graphite upon lithium intercalation/deintercalation. *Journal of Power Sources,* 195**,** 3655-3660.

SHABAN, S. E., IBRAHIEM, N. M., EL-MONGY, S. A. & ELSHEREAFY, E. E. 2013. Validation of scanning electron microscope (SEM), energy dispersive X-ray (EDX) and gamma spectrometry to verify source nuclear material for safeguards purposes. *Journal of Radioanalytical and Nuclear Chemistry,* 296**,** 1219-1224.

SHAH, R. R., O'HAGAN, D. T., AMIJI, M. M. & BRITO, L. A. 2014. The impact of size on particulate vaccine adjuvants. *Nanomedicine,* 9**,** 2671-2681.

SHAHZAD, H. 2014. Carbon Nanotubes Deposited by Hot Wire Plasma CVD and water assisted CVD for Energetic and Environmental Applications.

SHANG, L., NIENHAUS, K. & NIENHAUS, G. U. 2014. Engineered nanoparticles interacting with cells: size matters. *J Nanobiotechnol,* 12.

SHARIF, M. J., YAMAUCHI, M., TOH, S., MATSUMURA, S., NORO, S.-I., KATO, K., TAKATA, M. & TSUKUDA, T. 2013. Enhanced magnetization in highly crystalline and atomically mixed bcc Fe–Co nanoalloys prepared by hydrogen reduction of oxide composites. *Nanoscale,* 5**,** 1489-1493.

SHARMA, M., MANTRI, S. & BAHADUR, D. 2012. Study of carbon encapsulated iron oxide/iron carbide nanocomposite for hyperthermia. *Journal of Magnetism and Magnetic Materials,* 324**,** 3975-3980.

SHEA, W. R. 1983. *Nature Mathematized: Historical and Philosophical Case Studies in Classical Modern Natural Philosophy*. *Nature mathematized*, Springer Science & Business Media.

SHEN, L. & WANG, N. 2011. Effect of nitrogen pressure on the structure of Cr-N, Ta-N, Mo-N, and WN nanocrystals synthesized by arc discharge. *Journal of Nanomaterials,* 2011**,** 52.

SHI, J., LIU, Y., WANG, L., GAO, J., ZHANG, J., YU, X., MA, R., LIU, R. & ZHANG, Z. 2014a. A tumoral acidic pH-responsive drug delivery system based on a novel photosensitizer (fullerene) for in vitro and in vivo chemo-photodynamic therapy. *Acta biomaterialia,* 10**,** 1280-1291.

SHI, J., WANG, L., GAO, J., LIU, Y., ZHANG, J., MA, R., LIU, R. & ZHANG, Z. 2014b. A fullerene-based multi-functional nanoplatform for cancer theranostic applications. *Biomaterials,* 35**,** 5771-5784.

SHIGETA, M. & MURPHY, A. B. 2011. Thermal plasmas for nanofabrication. *Journal of Physics D: Applied Physics,* 44**,** 174025.

SHIRATSUCHI, Y., YAMAMOTO, M., ENDO, Y., LI, D. & BADER, S. 2003. Superparamagnetic behavior of ultrathin Fe films grown on Al2O3 (0001) substrates. *Journal of applied physics,* 94**,** 7675-7679.

SIMON-DECKERS, A., LOO, S., MAYNE-L'HERMITE, M., HERLIN-BOIME, N., MENGUY, N., REYNAUD, C., GOUGET, B. & CARRIÈRE, M. 2009. Size-, composition-and shape-dependent toxicological impact of metal oxide nanoparticles and carbon nanotubes toward bacteria. *Environmental science & technology,* 43**,** 8423-8429.

SINGAMANENI, S., BLIZNYUK, V. N., BINEK, C. & TSYMBAL, E. Y. 2011. Magnetic nanoparticles: recent advances in synthesis, self-assembly and applications. *Journal of Materials Chemistry,* 21**,** 16819-16845.

SKRABALAK, S. E. 2009. Ultrasound-assisted synthesis of carbon materials. *Physical Chemistry Chemical Physics,* 11**,** 4930-4942.

SKRABALAK, S. E. & SUSLICK, K. S. 2006. Porous carbon powders prepared by ultrasonic spray pyrolysis. *Journal of the American Chemical Society,* 128**,** 12642-12643.

SONG, Q. & ZHANG, Z. J. 2004. Shape control and associated magnetic properties of spinel cobalt ferrite nanocrystals. *Journal of the American Chemical Society,* 126**,** 6164-6168.

SONO-TEK. 2015. *Ultrasonic Atomization Technology* [Online]. Sono-Tek Corporation. Available: http://www.sono-tek.com/ultrasonic-nozzle-technology/ 2012].

SOUNDERYA, N. & ZHANG, Y. 2008. Use of core/shell structured nanoparticles for biomedical applications. *Recent Patents on Biomedical Engineering,* 1**,** 34-42.

SU, J.-W., FU, S.-J., GWO, S. & LIN, K.-J. 2008. Fabrication of porous carbon nanotube network. *Chemical Communications*, 5631-5632.
SURESHKANNAN, G., KUMAR, G. M. & SARAVANAN, M. 2013. Characterization and experimental investigation of TiN micro tubular coil heater using Raman spectroscopy. *Archives of Metallurgy and Materials,* 58, 641-645.
SWIHART, M. T. 2003. Vapor-phase synthesis of nanoparticles. *Current Opinion in Colloid & Interface Science,* 8, 127-133.
TAYLOR, A., KRUPSKAYA, Y., COSTA, S., OSWALD, S., KRÄMER, K., FÜSSEL, S., KLINGELER, R., BÜCHNER, B., BOROWIAK-PALEN, E. & WIRTH, M. P. 2010a. Functionalization of carbon encapsulated iron nanoparticles. *Journal of Nanoparticle Research,* 12, 513-519.
TAYLOR, A., KRUPSKAYA, Y., KRÄMER, K., FÜSSEL, S., KLINGELER, R., BÜCHNER, B. & WIRTH, M. P. 2010b. Cisplatin-loaded carbon-encapsulated iron nanoparticles and their in vitro effects in magnetic fluid hyperthermia. *Carbon,* 48, 2327-2334.
TENG, M.-H., HSIAO, C.-I. & HSIAO, Y.-L. 2009. Formation mechanism of microcrystalline spherical graphite particles in solidified nickel. *Diamond and Related Materials,* 18, 396-398.
THAKUR, P., KUMAR, A., GAUTAM, S. & CHAE, K. 2011. Electronic charge transfer in cobalt doped fullerene thin films and effect of energetic ion impacts by x-ray absorption spectroscopy. *Thin Solid Films,* 519, 8401-8405.
THAKUR, R. R. S., MCMILLAN, H. L. & JONES, D. S. 2014. Solvent induced phase inversion-based in situ forming controlled release drug delivery implants. *Journal of Controlled Release,* 176, 8-23.
THOMAS, R. & SWATHI, R. 2012. Organization of metal nanoparticles for surface-enhanced spectroscopy: a difference in size matters. *The Journal of Physical Chemistry C,* 116, 21982-21991.
TONEZZER, M. & HIEU, N. 2012. Size-dependent response of single-nanowire gas sensors. *Sensors and Actuators B: Chemical,* 163, 146-152.
TSANG, S. C., CAPS, V., PARASKEVAS, I., CHADWICK, D. & THOMPSETT, D. 2004. Magnetically Separable, Carbon-Supported Nanocatalysts for the Manufacture of Fine Chemicals. *Angewandte Chemie,* 116, 5763-5767.
TSAPIS, N., BENNETT, D., JACKSON, B., WEITZ, D. A. & EDWARDS, D. 2002. Trojan particles: large porous carriers of nanoparticles for drug delivery. *Proceedings of the National Academy of Sciences,* 99, 12001-12005.
UHM, Y. R. & RHEE, C. K. 2013. Synthesis and Magnetic Properties of Ni and Carbon Coated Ni by Levitational Gas Condensation (LGC). *Journal of Nanomaterials,* 2013.
UHM, Y. R., RHEE, C. K., LEE, H. M. & KIM, C. S. 2010. Magnetic properties and dispersion stability of carbon encapsulated Fe nano particles.
VARDELLE, M., FAUCHAIS, P., VARDELLE, A., LI, K.-I., DUSSOUBS, B. & THEMELIS, N. 2001. Controlling particle injection in plasma spraying. *Journal of Thermal Spray Technology,* 10, 267-284.
VARGA, G. & KRÖLL, M. New Product Development for Nanomaterials Systems and Solutions.
VEHKAMÄKI, H. 2006. *Classical nucleation theory in multicomponent systems*, Springer Science & Business Media.
VEISEH, O., GUNN, J. W. & ZHANG, M. 2010. Design and fabrication of magnetic nanoparticles for targeted drug delivery and imaging. *Advanced drug delivery reviews,* 62, 284-304.
VISAKH, P. & THOMAS, S. 2010. Preparation of bionanomaterials and their polymer nanocomposites from waste and biomass. *Waste and Biomass Valorization,* 1, 121-134.

WAN, F., MØLLER, E. H., YANG, M. & JØRGENSEN, L. 2012. Formulation technologies to overcome unfavorable properties of peptides and proteins for pulmonary delivery. *Drug Discovery Today: Technologies,* 9**,** e141-e146.
WANG, C., XU, H., LIANG, C., LIU, Y., LI, Z., YANG, G., CHENG, L., LI, Y. & LIU, Z. 2013. Iron oxide@ polypyrrole nanoparticles as a multifunctional drug carrier for remotely controlled cancer therapy with synergistic antitumor effect. *ACS nano,* 7**,** 6782-6795.
WANG, H., GAO, Q., HU, J. & CHEN, Z. 2009. High performance of nanoporous carbon in cryogenic hydrogen storage and electrochemical capacitance. *Carbon,* 47**,** 2259-2268.
WANG, J., HU, Z., XU, J. & ZHAO, Y. 2014. Therapeutic applications of low-toxicity spherical nanocarbon materials. *NPG Asia Materials,* 6**,** e84.
WANG, Z.-J., WEINBERG, G., ZHANG, Q., LUNKENBEIN, T., KLEIN-HOFFMANN, A., KURNATOWSKA, M., PLODINEC, M., LI, Q., CHI, L. & SCHLOEGL, R. 2015. Direct Observation of Graphene Growth and Associated Copper Substrate Dynamics by In-Situ Scanning Electron Microscopy. *ACS nano*.
WANG, Z., XIAO, P. & HE, N. 2006. Synthesis and characteristics of carbon encapsulated magnetic nanoparticles produced by a hydrothermal reaction. *Carbon,* 44**,** 3277-3284.
WANG, Z., ZHANG, Z., CHOI, C. & KIM, B. 2003. Structure and magnetic properties of Fe (C) and Co (C) nanocapsules prepared by chemical vapor condensation. *Journal of alloys and compounds,* 361**,** 289-293.
WEDER, G. 2010. *Living cell adhesion measured by force spectroscopy.* University of Neuchâtel, Switzerland, 2006.
WEIRICH, T. E., LÁBÁR, J. L. & ZOU, X. 2006. *Electron crystallography: Novel approaches for structure determination of nanosized materials*, Springer Science & Business Media.
WEISS, J., TAKHISTOV, P. & MCCLEMENTS, D. J. 2006. Functional materials in food nanotechnology. *Journal of food science,* 71**,** R107-R116.
WICKSON, F. 2008. Narratives of nature and nanotechnology. *Nature nanotechnology,* 3**,** 313-315.
WILLIAMS, D. B. & CARTER, C. B. 1949. Transmission electron microscopy: a textbook for materials science. 1996. New York: Plenum Press.
WILLIAMS, D. B. & CARTER, C. B. 2009. The Transmission electron microscope. *Transmission Electron Microscopy.* Springer.
WONG, J. M., HUSTON, R. B., VIZCAINO, C. & LOWRING, J. B. 2013. Composition for acid gas tolerant removal of mercury from a flue gas. Google Patents.
WU, H., YANG, R., SONG, B., HAN, Q., LI, J., ZHANG, Y., FANG, Y., TENNE, R. & WANG, C. 2011a. Biocompatible inorganic fullerene-like molybdenum disulfide nanoparticles produced by pulsed laser ablation in water. *ACS nano,* 5**,** 1276-1281.
WU, P., DU, N., ZHANG, H., YU, J. & YANG, D. 2011b. Carbon nanocapsules as nanoreactors for controllable synthesis of encapsulated iron and iron oxides: magnetic properties and reversible lithium storage. *The Journal of Physical Chemistry C,* 115**,** 3612-3620.
XIA, X.-H., TU, J.-P., MAI, Y.-J., WANG, X.-L., GU, C.-D. & ZHAO, X.-B. 2011. Self-supported hydrothermal synthesized hollow Co_3O_4 nanowire arrays with high supercapacitor capacitance. *Journal of Materials Chemistry,* 21**,** 9319-9325.
XIA, X., TU, J., ZHANG, J., HUANG, X., WANG, X., ZHANG, W. & HUANG, H. 2008. Enhanced electrochromics of nanoporous cobalt oxide thin film prepared by a facile chemical bath deposition. *Electrochemistry Communications,* 10**,** 1815-1818.
XIANG, H., ZHANG, K., JI, G., LEE, J. Y., ZOU, C., CHEN, X. & WU, J. 2011. Graphene/nanosized silicon composites for lithium battery anodes with improved cycling stability. *Carbon,* 49**,** 1787-1796.
XIE, J., LIU, G., EDEN, H. S., AI, H. & CHEN, X. 2011. Surface-engineered magnetic nanoparticle platforms for cancer imaging and therapy. *Accounts of chemical research,* 44**,** 883-892.

YAN, A., LAU, B. W., WEISSMAN, B. S., KÜLAOTS, I., YANG, N. Y., KANE, A. B. & HURT, R. H. 2006. Biocompatible, hydrophilic, supramolecular carbon nanoparticles for cell delivery. *Advanced Materials,* 18**,** 2373-2378.

YANASE, S., NOMURA, J., MATSUMURA, Y., KATO, H. & TAGAWA, T. 2012. Hyperthermia enhances the antitumor effect of photodynamic therapy with ALA hexyl ester in a squamous cell carcinoma tumor model. *Photodiagnosis and photodynamic therapy,* 9**,** 369-375.

YANG, D.-P., GAO, F., CUI, D.-X. & YANG, M. 2009. Microwave rapid synthesis of nanoporous Fe3O4 magnetic microspheres. *Current Nanoscience,* 5**,** 485-488.

YANG, Z. & WANG, S. 2014. High Cycling Performance Cathode Material: Interconnected LiFePO 4/Carbon Nanoparticles Fabricated by Sol-Gel Method. *Journal of Nanomaterials,* 2014.

YIN, X., NG, B. W.-H. & ABBOTT, D. 2012. Terahertz sources and detectors. *Terahertz Imaging for Biomedical Applications.* Springer.

YONEMOTO, Y. & KUNUGI, T. 2011. *Macroscopic Gas-Liquid Interfacial Equation Based on Thermodynamic and Mathematical Approaches*, INTECH Open Access Publisher.

YU, M. K., JEONG, Y. Y., PARK, J., PARK, S., KIM, J. W., MIN, J. J., KIM, K. & JON, S. 2008a. Drug-loaded superparamagnetic iron oxide nanoparticles for combined cancer imaging and therapy in vivo. *Angewandte Chemie International Edition,* 47**,** 5362-5365.

YU, Q., LIAN, J., SIRIPONGLERT, S., LI, H., CHEN, Y. P. & PEI, S.-S. 2008b. Graphene segregated on Ni surfaces and transferred to insulators. *Applied Physics Letters,* 93**,** 113103.

ZAMFIR, L.-G., GEANA, I., BOURIGUA, S., ROTARIU, L., BALA, C., ERRACHID, A. & JAFFREZIC-RENAULT, N. 2011. Highly sensitive label-free immunosensor for ochratoxin A based on functionalized magnetic nanoparticles and EIS/SPR detection. *Sensors and Actuators B: Chemical,* 159**,** 178-184.

ZENG, S., CAI, M., LIANG, H. & HAO, J. 2012. Size-dependent colorimetric visual detection of melamine in milk at 10 ppb level by citrate-stabilized Au nanoparticles. *Anal. Methods,* 4**,** 2499-2505.

ZHANG, H., LIANG, C., LIU, J., TIAN, Z. & SHAO, G. 2013a. The formation of onion-like carbon-encapsulated cobalt carbide core/shell nanoparticles by the laser ablation of metallic cobalt in acetone. *Carbon,* 55**,** 108-115.

ZHANG, J. 2015. Growth of Close Packed Semiconducting Single-walled Carbon Nanotube Arrays Using Oxygen-Deficient TiO2 Nanoparticles as Catalysts. *Nano letters*.

ZHANG, J., ZHU, Y., LI, J., ZHU, M., TAO, C. & HANAGATA, N. 2013b. Preparation and characterization of multifunctional magnetic mesoporous calcium silicate materials. *Science and Technology of Advanced Materials,* 14**,** 055009.

ZHANG, S., NIU, H., HU, Z., CAI, Y. & SHI, Y. 2010. Preparation of carbon coated Fe 3 O 4 nanoparticles and their application for solid-phase extraction of polycyclic aromatic hydrocarbons from environmental water samples. *Journal of Chromatography A,* 1217**,** 4757-4764.

ZHANG, Y., TAO, N. & LU, K. 2008. Mechanical properties and rolling behaviors of nano-grained copper with embedded nano-twin bundles. *Acta Materialia,* 56**,** 2429-2440.

ZHANG, Z.-C., XU, B. & WANG, X. 2014. Engineering nanointerfaces for nanocatalysis. *Chemical Society Reviews,* 43**,** 7870-7886.

ZHAO, H., GE, Y., ZHANG, T., ZHANG, J., TAN, J. & ZHANG, H. 2014. Unregulated emissions from diesel engine with particulate filter using Fe-based fuel borne catalyst. *Journal of Environmental Sciences,* 26**,** 2027-2033.

ZHAO, J. 2014. Molecular Dynamics Simulations of Silver-induced Crystallization in Silicon Nanocluster.

ZHAO, M., SONG, H., CHEN, X. & LIAN, W. 2007. Large-scale synthesis of onion-like carbon nanoparticles by carbonization of phenolic resin. *Acta Materialia,* 55**,** 6144-6150.

ZHAO, S., HONG, R., LUO, Z., LU, H. & YAN, B. 2011. Carbon nanostructures production by AC arc discharge plasma process at atmospheric pressure. *Journal of Nanomaterials,* 2011**,** 14.

ZHONG, W. 2013. *An introduction to healthcare and medical textiles*, DEStech Publications, Inc.

ZHU, H. 2008. *Materials design and synthesis for desirable magnetic and optical properties*, ProQuest.

ZUO, X., PENG, C., HUANG, Q., SONG, S., WANG, L., LI, D. & FAN, C. 2009. Design of a carbon nanotube/magnetic nanoparticle-based peroxidase-like nanocomplex and its application for highly efficient catalytic oxidation of phenols. *Nano Research,* 2**,** 617-623.

Appendix

A. Tips to modify and improve the liquid phase plasma arc discharge equipment

The following descriptions are five tips to modify and improve the liquid phase plasma arc discharge equipment.

1. Changing the injector of the reactor

Instead of dropping the solution (ferrocene, the iron source) to the plasma zone, it can be possible to inject the solution to form a soft spray of microsized droplets by using spray or atomizer nozzle. A spray is a dynamic collection of drops dispersed in a gas. The aim is to increase dramatically the surface area of drops which contains iron molecules, as the result the evaporation rate increases. This approach has been used in fuel injectors for gasoline and diesel engines and atomizers for jet engines (gas turbines) (Lefebvre, 1998); atomizers for injecting heavy fuel oil into combustion air in steam boiler injectors, and rocket engine injectors. Drop size is critical because the large surface area of a finely atomized spray enhances fuel evaporation rate. Dispersion of the fuel into the combustion air is critical to maximize the efficiency of these systems and minimize emissions of pollutants (Reitz, 1987).

This approach will decrease the temperature fluctuation, also constant and controllable temperature is expected comparably. Dispersion of ferrocene into the plasma zone and combustion, helium could be critical to maximize the efficiency and minimize emissions of pollutants in our arc discharge equipment. These futures promote the monodispersion of nanoparticle and more quantity of nanoparticle is expected.

There are different types of spray and atomizer available such as the ultrasonic spray nozzle technology shown in Figure A-1.

Figure A-1. Ultrasonic atomizer suitable for delivering precursor (Sono-Tek, 2015).

2. Reverse installation of liquid phase reactor

In order to optimize the process, it's recommended to install the Arc Discharge Equipment in reverse position as shown in Figure A-2. Since the pressure is constant and the warm vapor goes up and then we will collect most of the particles from the glass surface of the chamber, in this way we can collect more particles comparing to the current one. In fact, we avoid the accumulation of the waste particles on the metallic surface, so we save considerable amount of nanoparticles; moreover, the cleaning will be easier and it helps overall maintenance of the system. Probably, such a modification will not affect the quality of the nanoparticle and therefor previously achieved results can be repeated.

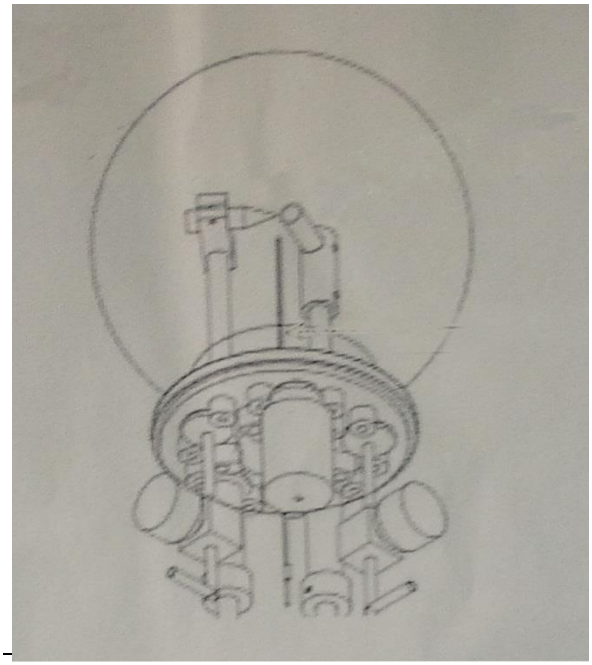

Figure A-2. The reactor with the inverse position, (new injector is required as explained previously, otherwise its necessary to change the current injector position).

3. Changing the glass chamber

It's desirable to install a bigger glass chamber to produce more quantity of particles. One of the weaknesses of the current method is removing the particles from the glass chamber. Currently a brush and ethanol are used to remove particles form the glass surface of the chamber and we lose amounts of nanoparticles. An alternative is to design a new glass chamber. A glass chamber concept model is represented in Figure A-3. In this new method removable test tubes can be provided, which will be put into ultrasound bath to remove the attached particle from the glass surface. By this method we minimize loses of nanoparticles.

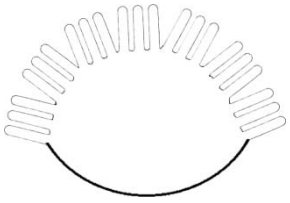

Figure A-3. Glass chamber concept model.

4. Cooling system

After reversing the system, its recommend using instant ice pack to cool down the system; since nanoparticles diffuse to cooler region (Aguilo-Aguayo, 2012), we can attract and collect more particles from glass surface of the chamber.

5. Temperature measurement

Currently, it’s not easy to fit the thermometer probe, sometimes after setting the probe and closing the chamber we see that it is not connected. Since the chamber is made of glass its recommend using a non-contact infrared thermometer to measure the temperature and or using Optical Emission Spectroscopy to make use of the optical emission of the line radiation of excited atoms or ions in plasma.

B. BET analysis data

BET analysis data from PCMPs are provided, as the following:

Table B-1. Isotherm Tabular Report.

Isotherm Tabular Report				
Relative Pressure (p/p°)	Absolute Pressure (mmHg)	Quantity Adsorbed (cm^3/g STP)	Elapsed Time (h:min)	Saturation Pressure (mmHg)
0.001742399	1.32685	-0.6177	00:38	761.50647
0.002783455	2.11962	-0.3786	00:40	
0.005161446	3.93047	0.2915	00:42	
0.009922908	7.55636	1.2417	00:43	
0.049603577	37.77345	6.8299	00:45	
0.099667419	75.89738	12.9795	00:46	
0.149512080	113.85442	18.3908	00:47	
0.199575911	151.97835	23.5564	00:48	
0.249480845	189.98128	28.5433	00:50	
0.299413190	228.00508	32.8587	00:51	
0.349312653	266.00385	37.2080	00:52	
0.399146333	303.95251	42.2420	00:53	
0.449062247	341.96381	46.9339	00:55	
0.498841143	379.87076	51.5013	00:56	
0.548806390	417.91962	55.2239	00:57	
0.598535954	455.78900	60.1756	00:59	
0.648479280	493.82117	64.2692	01:00	
0.698186963	531.67389	69.5307	01:01	
0.748119308	569.69769	75.7326	01:02	
0.797991379	607.67560	81.7463	01:04	
0.847874352	645.66180	86.3488	01:05	
0.873643232	665.28497	91.2305	01:06	
0.898842241	684.47418	95.0902	01:07	
0.923624869	703.34631	100.3555	01:09	
0.948692432	722.43542	106.2949	01:10	
0.959366000	730.56342	110.0003	01:11	
0.969349150	738.16565	114.9505	01:12	
0.979419986	745.83466	120.8250	01:14	
0.986022467	750.86249	224.7125	01:15	
0.965141087	734.96118	113.9617	01:16	
0.941679019	717.09467	107.7344	01:17	
0.907247468	690.87482	99.6817	01:19	
0.900398364	685.65918	99.0465	01:20	
0.857528805	653.01373	91.8313	01:21	
0.850323592	647.52692	90.4122	01:22	

0.802122659	610.82159	82.9389	01:23	
0.752004044	572.65594	77.9369	01:25	
0.702088210	534.64471	71.1412	01:26	
0.651843519	496.38306	64.3883	01:27	
0.601648200	458.15900	60.2888	01:28	
0.551661072	420.09348	53.9607	01:30	
0.501405440	381.82349	49.3565	01:31	
0.451286825	343.65784	44.1916	01:32	
0.401162720	305.48801	39.3613	01:34	
0.351076967	267.34738	33.9456	01:35	
0.300980253	229.19841	29.1086	01:36	
0.250932852	191.08699	23.5808	01:37	
0.200819708	152.92551	17.6393	01:39	
0.131540164	100.16869	9.2083	01:40	
0.085898077	65.41194	3.3098	01:41	
0.064748203	49.30618	0.5749	01:43	
0.009122938	6.94718	-8.2664	01:47	
0.004843650	3.68847	-9.4125	01:49	
0.002493055	1.89848	-10.5878	01:53	
0.001041056	0.79277	-12.2403	02:04	

BJH Adsorption Pore Distribution Report

t = 3.54[-5/ln(p/p°)]^0.333
Width Range: 1.5000 nm to 300.0000 nm
Adsorbate Property Factor: 0.95300 nm
Density Conversion Factor: 0.0015468
Fraction of Pores Open at Both Ends: 0.00

Table B-2. BJH Adsorption Pore Distribution Report.

Pore Width Range (nm)	Average Width (nm)	Incremental Pore Volume (cm^3/g)	Cumulative Pore Volume (cm^3/g)	Incremental Pore Area (m^2/g)	Cumulative Pore Area (m^2/g)
139.7 - 95.3	109.3	0.172046	0.172046	6.297	6.297
95.3 - 64.3	73.9	0.008067	0.180113	0.437	6.734
64.3 - 48.7	54.4	0.007227	0.187339	0.532	7.266
48.7 - 38.7	42.5	0.005404	0.192743	0.508	7.774
38.7 - 26.1	29.9	0.008808	0.201551	1.177	8.951
26.1 - 19.7	22.0	0.008324	0.209875	1.515	10.466
19.7 - 15.7	17.3	0.006088	0.215963	1.411	11.877
15.7 - 13.0	14.1	0.008334	0.224297	2.361	14.238
13.0 - 9.7	10.9	0.007205	0.231501	2.652	16.889
9.7 - 7.7	8.4	0.010602	0.242103	5.025	21.915
7.7 - 6.3	6.8	0.011295	0.253398	6.615	28.530
6.3 - 5.3	5.7	0.009458	0.262856	6.656	35.185
5.3 - 4.5	4.8	0.007002	0.269857	5.810	40.995
4.5 - 3.9	4.1	0.009046	0.278903	8.732	49.727
3.9 - 3.4	3.6	0.006213	0.285116	6.913	56.640
3.4 - 3.0	3.1	0.008185	0.293301	10.431	67.071
3.0 - 2.6	2.8	0.008337	0.301638	12.125	79.195
2.6 - 2.3	2.4	0.008925	0.310563	14.795	93.991
2.3 - 2.0	2.1	0.006920	0.317483	13.096	107.087
2.0 - 1.7	1.8	0.006422	0.323905	13.941	121.028
1.7 - 1.5	1.6	0.007421	0.331326	18.651	139.679

.

BJH Desorption Pore Distribution Report

t = 3.54[-5/ln(p/p°)]^0.333
Width Range: 1.5000 nm to 300.0000 nm
Adsorbate Property Factor: 0.95300 nm
Density Conversion Factor: 0.0015468
Fraction of Pores Open at Both Ends: 0.00

Table B-3. BJH Desorption Pore Distribution Report.

Pore Width Range (nm)	Average Width (nm)	Incremental Pore Volume (cm^3/g)	Cumulative Pore Volume (cm^3/g)	Incremental Pore Area (m^2/g)	Cumulative Pore Area (m^2/g)
56.5 - 33.9	39.8	0.010809	0.010809	1.086	1.086
33.9 - 21.4	24.8	0.014168	0.024978	2.281	3.367
21.4 - 19.9	20.6	0.001047	0.026025	0.204	3.571
19.9 - 13.8	15.7	0.012826	0.038851	3.259	6.830
13.8 - 13.1	13.4	0.002561	0.041411	0.762	7.592
13.1 - 9.8	11.0	0.013459	0.054870	4.911	12.503
9.8 - 7.7	8.5	0.008681	0.063551	4.101	16.605
7.7 - 6.2	6.8	0.012460	0.076012	7.323	23.928
6.2 - 5.2	5.6	0.012358	0.088370	8.786	32.714
5.2 - 4.4	4.7	0.006756	0.095126	5.700	38.414
4.4 - 3.8	4.1	0.011487	0.106613	11.343	49.758
3.8 - 3.3	3.5	0.007611	0.114223	8.716	58.474
3.3 - 2.8	3.0	0.008684	0.122907	11.466	69.940
2.8 - 2.5	2.6	0.007711	0.130618	11.699	81.639
2.5 - 2.2	2.3	0.008646	0.139264	15.067	96.706
2.2 - 1.9	2.0	0.006939	0.146203	13.921	110.627
1.9 - 1.6	1.7	0.007826	0.154029	18.188	128.815

Summary Report

Surface Area

Sample Mass: 0.0015 g

Analysis Adsorptive: N_2

Analysis Bath Temp.: 77.350 K

Single point surface area at p/p° = 0.299413190: 100 .2124 m^2/g

BET Surface Area: 153.4895 m^2/g

BJH Adsorption cumulative surface area of pores between 1.5000 nm and 300.0000 nm width: 139.6790 m^2/g

BJH Desorption cumulative surface area of pores between 1.5000 nm and 300.0000 nm width: 128.8150 m²/g

Pore Volume

Single point adsorption total pore volume of pores less than 140.4108 nm width at p/p°=0.986022467:0 .347585 cm³/g

BJH Adsorption cumulative volume of pores between 1.5000 nm and 300.0000 nm width: 0.331326 cm³/g

BJH Desorption cumulative volume of pores between 1.5000 nm and 300.0000 nm width: 0.154029 cm³/g

Pore Size

Adsorption average pore width (4V/A by BET): 9.05822 nm

BJH Adsorption average pore width (4V/A): 9.4882 nm

BJH Desorption average pore width (4V/A): 4.7829 nm

C. Summary of samples

A summary of useful data from carbon encapsulated iron nanoparticles (CEINPs) synthesis process by gas phase arc discharge reactor (section 2.1.2.3) are presented in the following table. Inert gas was Helium, because it can generate plasma in current lower than 40 ampere. Small flow referred to the gas flow that deliver the precursor and the large flow referred to the gas flow that deliver obtained particle to collection system.

Table C-1. Summary of samples from gas phase arc discharge reactor.

Pressure	Concentration Ferrocene	Channel diameter	Current	Small Flow Rate	Large Flow Rate	Precursor Type 1: Isooctane 2: Benzene
mbar	wt%	mm	A	sccm	sccm	Type
0	0.5	6.0	40	120	300	2
Observation: Voltage 15-16 V, Plasma unstable, small amount of CEINPs obtained, due to the low gas flow rate from big flow outlet, NPs did not pass the beads properly. Precursor consumption: 22 ml in 8 min						
-100	3.5	6.0	20	120	1200	1
Observation: Voltage 14-15 V, Plasma semi stable, very small amount of CEINPs obtained. Precursor consumption: 12 ml in 15 min.						
0	0.5	3.0	20	30	300	1
Observation: Voltage 12-14 V, small but stable plasma, no CEINPs obtained. Precursor consumption: 20 ml in 17 min.						
0	0.5	3.0	40	120	1200	1
Observation: Voltage 17-18 V, plasma stable, when rotating plasma lost, a bit CEINPs collected from outer layer of ceramic tube, and also glass beads. Precursor consumption: 20 ml in 17 min.						
0	3.5	3.0	20	30	1200	2
Observation: Voltage 12-15 V, stable plasma, due to the very close distance between ceramic tube and electrode, a carbon piece was formed between them and blocked ceramic tube, CEINPs obtained. Precursor consumption: 6 ml in 15 min.						
-100	0.5	3.0	20	120	1200	2
Observation: Voltage 13-15 V, not stable for the first 15 min and semi stable plasma in last minutes, it was difficult to control the pressure, CEINPs obtained, Precursor consumption: 13 ml in 25 min.						
0	3.5	6	20	120	300	1
Observation: Voltage 8-15 V, not stable plasma, no CEINPs obtained, Precursor consumption: 4 ml in 5 min.						
-100	3.5	3	40	120	300	2
Observation: Voltage 13-15 V, stable plasma, Obtained CEINPs, Precursor consumption: 8 ml in 15 min.						
-100	0.5	6	40	30	1200	1
Observation: Voltage 19-20 V,stable plasma, no CEINPs obtained, Precursor consumption: -						
-100	0.5	6	20	30	300	2

Observation: Voltage 18-19 V, stable plasma, by rotating the electrode plasma stopped, small amound of CEINPs obtained, Precursor consumption: 10 ml in 15 min.						
-100	3.5	3	40	30	300	1
Observation: Voltage 14-6 V, unstable plasma, no CEINPs obtained, difficult to control pressure. Precursor consumption: 11 ml in 15 min						
0	3.5	6	40	30	1200	2
Observation: Voltage 20-25 V, not stable plasma, last 5 minutes of synthesis run the plasma became stable, CEINPs obtained from the beads and also from ceramic tube, due to the very close distance between ceramic tube and electrode, a carbon piece was formed between them and blocked ceramic tube. Precursor consumption: 8 ml in 15 min.						

A summary of useful data from carbon encapsulated iron nanoparticles (CEINPs) synthesis process by liquid phase arc discharge reactor are shown in the following table. The details of this reactor are described in section 2.1.1.

Table C-2. Summary of samples from liquid phase arc discharge reactor.

Gas type	Gas flow sccm	Atmospheric pressure (yes/No)	Current A	Precursor Type Isooctane +Ferrocene (Yes/No)	Precursor Concentration %	Precursor Flow rate (sccm)	Fe@C obtained Yes/No	Syntehsis run (min)
He	1600	Yes	25	yes	0.5	1	yes	10
Comment: Magnetic nanoparticles obtained through filtration								
He	1600	no	40	yes	0.5	1	yes	6:30
Comment: Syringe problem, due to the tube blockage and high temperature								
He	1600	no	40	yes	0.5	1	yes	5
Comment Comment: Syringe problem, due to the tube blockage and high temprature								
He	1600	no	40	yes	0.5	1	yes	5
Comment: Problem with electrode sharpness and plasma								
He	500	yes	30	yes	0.5	1	yes	10
Comment: Magnetic nanoparticles obtained through filtration								
He	500	yes	30	yes	0.5	1	yes	10
Comment: Repeated, status ok								
He	500	yes	30	yes	0.5	1	yes	10
Comment: Repeated three times. decreasing flow rate and current made plasma stable								
He	500	yes	40	yes	0.5	2	yes	5
Comment: Repeated two times								
He	1600	yes	15, 20,25, 30, 40	-	-	-	-	-
Comment: 15 and 20 Ampere no stable plasma, for the rest Plasma generated and its light was measured by spectroscopy								
He	1600	yes	45,55,	-	-	-	-	-
Comment: Plasma generated and plasma measured by spectroscopy								

He	500	yes	30	-	-	-	-	-
Comment: Stable plasma generated								
Ar	500	yes	40	-	-	-	-	10
Comment: Plasma generated stable								
He	500	yes	40	-	-	-	-	10
Comment: Plasma generated stable								
Ar	500	yes	40	yes	3.5	3	yes	5
Comment: Repeated 3 time, status ok.								
Ar	1600	yes	25, 40	yes	3.5	1	yes	5
Comment: Difficult to control pressure, repeated three times								
Ar 50%, He 50%	1600	yes	25	yes	-	-	-	-
Comment: Plasma generated								
Ar 50%, He 50%	1600	yes	40	yes	3.5	1	no	5
Comment: Nanoparticles not obtained because of the syringe and pressure problems								
He 1600		yes	30	yes	0.5	1	no	10
Comment: We used tungsten electrode, and it was melted								
He	500	yes	30	-	-	-	-	--
Comment: Sharp carbon electrodes were used, stable plasma generated								
He	1600	yes	40	Only isooctane	-	-	-	-
Comment: Different geometry of carbon electrodes were examined, one sharp carbon electrode and one carbon rod show high light, and bigger plasma achieved comparing to using two carbon rods only. Plasma without adding isooctane shows a little electrode deformation,								
He	1600	yes	40	yes	3.5	1	yes	10
Comment: CEINPs obtained, the size distribution is broad. Comparing the 0.5% precursor concentration								
Ar 1600		yes	40	no precursor	-	-	-	-
Comment: Ampere set to 25, Stable plasma								
Ar	1600	yes	40	no precursor	-	-	-	-
Comment: Ampere set to 40, stable plasma, comparing to 25 Ampere more light and bigger plasma where observed.								
He	1600	yes, (30)	40	no precursor	-	-	-	-
Comment: Stable plasma, Ampere 25								
He	1600	yes, (30)	40	yes	0.5	1	no	-
Comment: Stable plasma, Ampere 25, electrodes were not in correct position, no precursor evaporation.								
Ar	1600	yes	25	yes	0.5	1	yes	10
Comment: Not stable plasma								
Ar	1600	yes	40	yes	0.5	1	yes	10
Comment: stable plasma								
Ar 50%, He 50%	1600	yes	25	yes	0.5	1	yes	10
Comment: Filtration process demonstrated that obtained nanoparticles are magnetic.								

Ar	1600	yes	40	yes	0.5	1	yes	5
Comment: Filtration process demonstrated that obtained nanoparticles are magnetic.TEM analysis shows 3 nm of iron nanoparticles								
He	1600	yes	40	yes	0.5	1	yes	5
Comment: Filtration process demonstrated that obtained nanoparticles are magnetic. TEM analysis shows 7 nm of iron nanoparticles								
Ar 75%-He 25%	1600	yes	40	yes	0.5	1	-	5
Comment: Syringe pump problem								
Ar 75%-He 25%	1600	yes	40	yes	0.5	1	-	5
Comment: Vacuum pump problem								
He	1600	yes	15	-	-	-	-	10
Comment: not stable plasma								
He	1600	yes	20	-	-	-	-	10
Comment: semi stable plasma and measured by optical emission spectroscopy (OES)								
He	1600	yes	25	-	-	-	-	10
Comment: stable plasma and measured by OES								
He	1600	yes	30	-	-	-	-	10
Comment: Stable plasma and measured by OES								
He	1600	yes	40	-	-	-	-	10
Comment: stable plasma and measured by OES								
Ar	1600	yes	15	-	-	-	-	10
Comment: no stable								
Ar	1600	yes	20	-	-	-	-	10
Comment: no plasma								
Ar	1600	yes	25	-	-	-	-	10
Comment: no plasma								
Ar	1600	yes	30	-	-	-	-	10
Comment: not stable plasma								
Ar	1600	yes	40	-	-	-	-	10
Comment: stable plasma, measured by OES								
Ar	1600	yes	40	Yes	0.5	1	yes	10
Comment: core@shell structure, superparamagnetic, details are in section 3.1								
Ar 75%-He 25%	1600	yes	40	Yes	0.5	1	yes	10
Comment: core@shell structure, superparamagnetic, details are in section 3.1								

Ar50 %- He50 %	1600	yes	40	yes	0.5	1	yes	10
Comment: core@shell structure, superparamagnetic, details are in section 3.1								
Ar25 %- He75 %	1600	yes	40	yes	0.5	1	yes	10
Comment: core@shell structure, superparamagnetic, details are in section 3.1								
Ar0%- He10 0%	1600	yes	40	yes	0.5	1	yes	10
Comment: core@shell structure, superparamagnetic, details are in section 3.1 and 3.2								
N100 %	1600	yes	40	yes	0.5	1	yes	10
Comment: Comment: core@shell structure, superparamagnetic, details are in section 3.2								
N75% - He25 %	1600	yes	40	yes	0.5	1	yes	10
Comment: Comment: core@shell structure, superparamagnetic, details are in section 3.2								
N50% - He50 %	1600	yes	40	yes	0.5	1	yes	10
Comment: Comment: core@shell structure, superparamagnetic, details are in section 3.2								
N25% - He75 %	1600	Yes	40	yes	0.5	1	yes	10
Comment: Comment: core@shell structure, superparamagnetic, details are in section 3.2								

D. Solubility of Ferrocene in organic solvents

Table D-1. Solubility of Ferrocene in Organic Non-Electrolyte Solvents

Solvent	Solvent Mol. Wt.	Mole Fraction Solubility	% Sol.	% Fe
n-Hexane	86.178	0.022600	4.75%	1.43%
n-Heptane	100.205	0.024890	4.52%	1.36%
n-Octane	114.232	0.027130	4.34%	1.30%
n-Nonane	128.259	0.029010	4.15%	1.25%
n-Decane	142.286	0.030970	4.01%	1.20%
n-Hexadecane	226.448	0.039630	3.28%	0.98%
Cyclohexane	98.189	0.033000	6.07%	1.82%
Methylcyclohexane	113.224	0.033720	5.42%	1.63%
Cyclooctane	109.192	0.046800	7.72%	2.32%
2,2,4-Trimethylpentane	114.232	0.021790	3.50%	1.05%
t-Butylcyclohexane	154.297	0.036120	4.32%	1.30%
Benzene	78.114	0.087586	18.61%	5.59%
Toluene	92.141	0.083210	15.49%	4.65%
Ethylbenzene	106.168	0.077030	12.76%	3.83%
o-Xylene	106.168	0.080140	13.24%	3.98%
m-Xylene	106.168	0.074360	12.34%	3.70%
p-Xylene	106.168	0.077850	12.89%	3.87%
Dibutyl ether	130.232	0.051070	7.14%	2.14%
Methyl t-butyl ether	88.151	0.041200	8.31%	2.50%
1,4-Dioxane	88.108	0.068300	13.40%	4.02%
Methanol	32.043	0.003298	1.88%	0.57%
Ethanol	46.070	0.005976	2.37%	0.71%
1-Propanol	60.097	0.008917	2.71%	0.81%
2-Propanol	60.097	0.007078	2.16%	0.65%
1-Butanol	74.124	0.001181	0.30%	0.09%
2-Butanol	74.124	0.010270	2.54%	0.76%
2-Methyl-1-propanol	74.124	0.009621	2.38%	0.71%
2-Methyl-2-propanol	74.124	0.009215	2.28%	0.68%
1-Pentanol	88.151	0.013520	2.81%	0.84%
2-Pentanol	88.151	0.012630	2.63%	0.79%
3-Methyl-1-butanol	88.151	0.012250	2.55%	0.77%
2-Methyl-2-butanol	88.151	0.015540	3.22%	0.97%
1-Hexanol	102.178	0.017350	3.11%	0.94%
2-Methyl-1-pentanol	102.178	0.014260	2.57%	0.77%
4-Methyl-1-pentanol	102.178	0.013430	2.42%	0.73%
1-Heptanol	116.205	0.020500	3.24%	0.97%
1-Octanol	130.232	0.022150	3.13%	0.94%
2-Ethyl-1-hexanol	130.232	0.016670	2.36%	0.71%
1-Decanol	158.286	0.027670	3.24%	0.97%
2-Ethyl-1-hexanol	130.232	0.016670	2.36%	0.71%
1-Decanol	158.286	0.027670	3.24%	0.97%
Cyclopentanol	86.135	0.017740	3.75%	1.13%
Butyl acetate	116.162	0.055800	8.65%	2.60%

Ethyl acetate	88.108	0.043000	8.67%	2.60%
Methyl acetate	74.081	0.032580	7.80%	2.34%
2,3-Dichloroethane	98.960	0.077350	13.61%	4.09%
1-Chlorobutane	92.569	0.059620	11.30%	3.39%
1-Chlorooctane	148.677	0.060620	7.47%	2.24%
Tetrachloromethane	153.823	0.06920	8.25%	2.48%
2-Propanone	95.550	0.02400	4.57%	1.37%
Acetonitrile	41.050	0.00756	3.34%	1.00%
Dimethyl sulfoxide	78.130	0.01410	3.29%	0.99%
Carbon disulfide	76.140	0.06690	14.91%	4.48%
Pyridine	79.100	0.07048	15.13%	4.54%

Scientific contributions

M. Reza Sanaee and Enric Bertran. "Synthesis of Carbon Encapsulated Mono-and Multi-Iron Nanoparticles." Journal of Nanomaterials, 450183 (2015) (published on line at http://www.hindawi.com/journals/jnm/aa/450183/)

S. Chaitoglou, M. Reza Sanaee, N. Aguilo-Aguayo, and E. Bertran "Arc-Discharge synthesis of iron encapsulated in carbon nanoparticles for biomedical applications." Journal of Nanomaterials 2014 (2014): 9.

M. Reza Sanaee, S. Chaitoglou, E. Bertran “Precise control over the core and shell sizes of carbon encapsulated superparamagnetic iron nanoparticles synthesized by arc discharge method”, Journal of Nanoparticles Research (Submitted).

M. Reza Sanaee and Enric Bertran “Synthesis of carbon nanoparticles decorated by fullerenes”, (manuscript); Patent consideration.

M. Reza Sanaee and Enric Bertran “Synthesis of spherical porous carbon microparticle by arc discharge method” (manuscript); Patent consideration.

Conference contributions

M. Reza Sanaee, official invitation as speaker of Sector 5-2: Nanoparticles at 4th Annual World Congress of Advanced Materials, May 27-29, 2015 (WCAM-2015), Chongqing, China.

M. Reza Sanaee official invitation as speaker at the 5th International Conference on Nanotek and Expo (Nanotek-2015) on during November 16-18, 2015 San Antonio, USA.

M. Reza Sanaee, S. Chaitoglou and Enric Bertran “Synthesis of fullerene on the surface of carbon nanoparticle by arc discharge method” in Proceedings of the International Conference on Trends in Nanotechnology, Phantoms Foundation, Barcelona, Spain, October 27-31, 2014.

S. Chaitoglou, A. Musheghyan, V-M Freire, M. Reza Sanaee, E. Pascual, J-L Andújar and E.Bertran, “The hidden influence of the flux of gas on the growth of graphene layers by low pressure chemical vapor deposition” in Proceedings of the International Conference on Trends in Nanotechnology, Phantoms Foundation, Barcelona, Spain, October 27-31, 2014.

M. Reza Sanaee and Enric Bertran “New Arc discharge possibilities for carbon coated pure iron nanoparticle continuous production” in Proceeding of Sisena Jornada IN2UB, Barcelona, Spain, June 5, 2014.

M. R. Sanaee, O. Arteaga, and E. Bertran, “Influence of plasma reactor parameters on carbon coating of iron nanoparticle,” in Proceedings of the International Conference on Nanoscience and Nanotechnology, p. 9, Phantoms Foundation, Madrid, Spain, March 11-14, 2014.

M. Reza Sanaee, Enric Bertran, "Synthesis of carbon encapsulated iron nanoparticles for applications in biomedicine," Proceedings of 3rd international conference on Nanotek, Journal of Nanomedicine and Nanotechnology, Ed., pp. 219, December 2-4, 2013.

M. Reza. Sanaee and E. Bertran “Coating control of carbon encapsulated iron nanoparticles synthesized by a modified arc discharge plasma” Accepted at 3rd Nano Today Conference, Biopolis, Sigrapour, December 8-11, 2013.

M. Reza Sanaee, V. M. Freire, N. Aguil, E. Bertran, and N.Aguil´o-Aguayo, “Study of carbon encapsulated iron nanoparticles produced by a modified arc discharge by applying nitrogen” in Proceedings of the 10th International Conference on Nano Spain, pp. 160–161, Phantoms Foundation, Bilbao, Spain, April 23-26, 2013.

V.-M. Freire, S. Chaitoglou, A. Ramírez, M. Reza Sanaee, E. Pascual, J.-L. Andújar, E. Bertran “Exploring new ways of chemical vapor deposition technology to produce graphene” in Proceedings of ImagineNano International Conference on Graphene. PP. 79, Phantoms Foundation, Bilbao, Spain, April 23-26, 2013.

S. Chaitoglou, M. Reza Sanaee, N. Aguilo-Aguayo, E. Bertran “Arc-Discharge Synthesis of Fe@C Nanoparticles for General Applications” in Proceedings of the 10th International Conference on Nano Spain, pp. 101, Phantoms Foundation, Bilbao, Spain, April 23-26, 2013.

M. Reza Sanaee, V. M. Freire, N. Aguil, E. Bertran, and N.Aguil´o-Aguayo, “Design and synthesis of carbon encapsulated iron nanoparticle for drug delivery,” in Proceedings of the 10th International Conference on Nano Bio and Med, pp. 212–213, Phantoms Foundation, Bilbao, Spain, April 23-26, April 23-26, 2013.

M. R. Sanaee, S. Chaitoglou, N. Aguil´o-Aguayo, and E. Bertran, “Influences of argon-helium mixtures on the carbon-coated iron nanoparticles produced by amodified arc discharge,” in Proceedings of the 9th International Conference on Nanoscience and Nanotechnologies, p. 12,Artion, Thessaloniki, Greece, 30June-7July 2012.

E. Escribano, M. Reza Sanaee, M. Llinàs, G. Calderó, C. Solans and MJ García-Celma, “Diffusion and skin permeation of clindamycin from a highly concentrated emulsion” in Proceeding of IV Jornada IN2UB, Barcelona, Spain, November 14, 2011.

Resumen en castellano

El concepto de la nanotecnología se atribuye al ganador del premio Nobel Richard Feynman, científico visionario, quien dio una muy famosa conferencia en 1959 (publicada en 1960), en la que dijo: "los principios de la física, por lo que yo puedo ver, no están en contra de la posibilidad de maniobrar los objetos átomo por átomo "(Feynman, 1960). En ese momento, se recibieron las palabras de Feynman como pura ciencia ficción, sin embargo, a día de hoy, tenemos instrumentos que permiten precisamente lo que Feynman ya había predicho: La creación de estructuras de átomos en movimiento de forma individual.

La nanotecnología se puede encontrar en la naturaleza. Desde los hermosos colores de algunas mariposas y polillas (los cuales surgen de las nanoestructuras de las alas) a los impresionantes vasos fabricados en cristal y con inclusiones metálicas realizados por los antiguos imperios Persa 1000 aC, Egipto, Romano 400 dC.

En principio, los resultados finales del presente trabajo de investigación conduce a la síntesis de nanoestructuras del tipo core@shell, consistentes en nanopartículas de hierro encapsulado en carbono, en nanopartículas de carbono decoradas con fullerenos y micropartículas de carbono porosas esféricas como material y herramienta para aplicaciones biomédicas. Actualmente, nos encontramos en un frente contra enfermedades peligrosas y destructivas como el cáncer, y la nanotecnología se presenta como una herramienta que nos puede ayudar a establecer un control de este tipo de dolencias. Este trabajo se enmarca en la Nanotecnología y tiene por objetivo el estudio y preparación de nanopartículas a base de carbono que puedan ser útiles para ciertas aplicaciones aplicaciones médicas o biomédicas y otras del ámbito de la nanotecnología más general.

Las nanopartículas magnéticas presentan un gran interés debido a sus propiedades únicas, especialmente en la administración de fármacos, hipertermia, resonancia magnética y separación de células. En muchas situaciones clínicas, las dosis de

medicación son elevadas, como resultado de una absorción alterada del fármaco o de una administración inespecífica a los tejidos. El objetivo final de la terapia de administración de fármacos y drogas magnéticamente controlada es el suministro selectivo de moléculas de fármaco de forma local, en el tejido enfermo, sin la necesidad de realizar un incremento concurrente del nivel de fármaco en los tejidos sanos.

Aunque ha habido muchos avances importantes en la síntesis de nanopartículas magnéticas, el mantenimiento de la estabilidad de estas partículas durante mucho tiempo es un problema importante. La estabilidad es un requisito fundamental para casi cualquier aplicación de las nanopartículas magnéticas. Especialmente los metales puros, tales como Fe, Co y Ni y sus aleaciones metálicas, son muy sensibles a la oxidación por el oxígeno del aire y otros agentes oxidantes, que pueden desactivar significativamente las propiedades magnéticas de esos metales. La principal dificultad para el uso de metales puros o aleaciones surge precisamente de su inestabilidad frente a la oxidación. Por lo tanto, es necesario desarrollar estrategias eficaces para mejorar la estabilidad química de las nanopartículas magnéticas. El método más sencillo parece ser la protección mediante una capa impenetrable, de modo que el oxígeno no pueda alcanzar la superficie de las partículas magnéticas. La estabilización y la protección de las partículas están a menudo estrechamente asociadas entre sí. Aunque hasta la fecha la mayoría de los estudios se han centrado en el desarrollo de revestimientos protectores de sílice o poliméricos, las nanopartículas magnéticas revestidas de carbono están recibiendo recientemente más atención, porque los materiales a base de carbono tienen importantes ventajas frente a los materiales poliméricos o de sílice, tales como alta estabilidad química y térmica, mejor conductividad eléctrica, así como biocompatibilidad de los materiales a base de carbono. Por lo tanto, el carbono es un candidato adecuado y preferible para formar una concha alrededor de un metal puro para la síntesis de las nanoestructuras core@shell. Es de destacar que, en muchos casos, las conchas de protección no sólo estabilizan las nanopartículas, sino que también se pueden utilizar para una funcionalización adicional, por ejemplo con otras nanopartículas o varios enlaces, dependiendo de la aplicación buscada.

Uno de los objetivos más importantes de la nanotecnología es el control de la materia a escala nanométrica. El control del tamaño es crucial para casi todas las aplicaciones potenciales de las nanopartículas. Se han realizado muchos estudios y examinado el papel del tamaño de las nanopartículas en las aplicaciones a sensores en biomedicina basados en nanopartículas. En cuanto a las aplicaciones para la administración de fármacos, Decuzzi en una interesante revisión contestado a esta pregunta: ¿Importa realmente la Geometría? Llegaron a la conclusión de que, la caracterización de la biodiversidad endotelial y el control preciso del tamaño y la forma de micro/nanofabricación han promovido un cambio de paradigma en la administración sistémica de partículas para aplicaciones biomédicas: la geometría y las propiedades físico-químicas de superficie contribuyen sustancialmente al diseño óptimo del sistema de partículas; La geometría afecta el transporte y la biodistribución de las partículas a nivel vascular; la fuerza de adhesión y la tasa de internalización en el nivel celular; la geometría favorece la acumulación de partículas en la proximidad de los vasos sanguíneos (dinámica de marginación) para mejorar la sensibilidad de la biodiversidad de la pared endotelial; la geometría afecta a la fuerza de adhesión a las células para mejorar la especificidad de la diana.

En consecuencia, en este estudio de investigación, el objetivo es desarrollar un enfoque para controlar la síntesis de nanopartículas de hierro encapsulado en carbono (CEINPs) en forma de nanoestructuras core@shell. En consecuencia, es necesaria la comprensión y el revelado del mecanismo de crecimiento de las nanopartículas de hierro encapsulado por carbono para llevar a cabo la caracterización. Por otra parte, las aplicaciones biomédicas son otro de los objetivos que pueden ser alcanzados con la ingeniería de las nanopartículas de carbono.

Hasta ahora, las estrategias que se han empleado para preparar nanopartículas a base de carbono, particularmente de hierro, y de otros sistemas encapsulados de carbono de nanopartículas de níquel, cobalto y óxidos magnéticos incluyen la síntesis mediante detonación, deposición química en fase vapor, síntesis por combustión, procesado hidrotérmico, síntesis de plasma de microondas y descarga de arco. Cada uno de estos métodos de síntesis tiene ventajas particulares en vistas a sus aplicaciones y usos.

La revisión de la literatura muestra claramente que la mayoría de los trabajos reportados se centran en materiales inorgánicos en lugar de compuestos orgánicos. Los materiales inorgánicos se pueden clasificar en tres grupos diferentes,, (i) metal, (ii) óxido de metal o metaloide, y (iii) calcogenuro metálico y sales.

Un problema común con el método de síntesis mediante descarga de arco es la inestabilidad del plasma. A fin de mejorar la estabilidad del plasma, que es crucial para obtener tamaños de núcleo más pequeños, así como las desviaciones estándar más pequeños, Aguilo-Aguayo decidió utilizar un precursor metálico mediante un compuesto organometálico en estado líquido en lugar de pepitas de Fe sólidas. La inyección del precursor en ese sistema era una innovación en la tecnología de plasma de descarga de arco y ello permitió mejorar la calidad de las nanopartículas (tamaños más pequeños, distribución más estrecha del tamaño), para controlar mejor la composición y el carbono encapsulación Fe, para obtener un mayor rendimiento de nanopartículas que el reactor anterior, así como para trabajar a presiones atmosféricas y reducir así los costes relacionados con el sistema de vacío. Además, mejoraron el procedimiento para recoger y manipular las nanopartículas en solución, que es el modo más seguro. Debido a las ventajas de ese nuevo reactor, se ha seguido utilizando con algunas modificaciones para la investigación realizada en ese estudio. Este reactor modificado se denominó reactor de descarga de arco en fase líquida.

Uno de los desafíos más habituales en la síntesis de las nanopartículas de carbono es la mejora de la uniformidad, la mejora de la protección mediante el revestimiento de las nanopartículas core@shell y el control de su composición, forma y tamaño del núcleo/corteza. Además, debido al desconocimiento de los parámetros óptimos y a la falta de comprensión global del mecanismo de formación, la mayor parte de los procesos de fabricación de nanopartículas core@shell son empírico, lo que significa que se requiere un gran número de ensayos experimentales para optimizar cualquier proceso dado. El método de descarga de arco, en general,es una técnica sencilla, rápida y rentable que puede llevarse a cabo fácilmente. Sin embargo, el aumento de la calidad junto con el mantenimiento en paralelo de la cantidad de nanopartículas

obtenidas necesita ser mejorado. Por otra parte, la inestabilidad del plasma, las elevadas temperaturas y la contaminación química durante el proceso son ejemplos de los inconvenientes que presenta la técnica de descarga de arco. En este sentido, es esencial un control adecuado de los parámetros de síntesis, los cuales son directamente dependientes del diseño del reactor.

Las debilidades que presentaba el reactor de descarga de arco en fase líquida son diversas: fugas de aire, descargas inestables de corriente, deformación de los electrodos, variaciones en el tiempo de residencia a temperaturas elevadas durante el experimento, la pobre productividad asociada al proceso de recolección de las partículas y a la baja tasa de síntesis. Con el fin de resolver estos problemas se barajaron diversas soluciones que condujeron al diseño de un nuevo reactor. Una vez concretado el diseño se construyó un reactor, totalmente nuevo en base a la experiencia previa y a la resolución de los problemas encontrados en las dos versiones anteriores. El nuevo reactor no sólo mejoró el proceso de síntesis de nanopartículas de hierro encapsuladas en carbono sino que ha dado lugar a un sistema más versátil con posibilidades para la síntesis de dos nuevos materiales: nanopartículas de carbono decoradas mediante fullerenos y micropartículas porosas esféricas.

Entre las características del nuevo reactor modificado destacamos la inyección del precursor de hierro a través de un gas de arrastre que inyecta los vapores del precursor justo en el centro de la descarga de arco. Esta nueva técnica proporciona significantes mejoras respecto del anterior diseño (reactor de descarga de arco en fase líquida) y lo hemos denominado reactor de descarga de arco en fase gaseosa.

Las principales conclusiones de este estudio son las siguientes:

• Se han sintetizado con éxito nanopartículas de hierro encapsulado en carbono de una manera controlada mediante el uso de un reactor de descarga de arco en fase líquida.

• La relación de gas argón-helio altera la transferencia de calor desde el centro del plasma hacia el exterior. Cuando aumenta la concentración de argón el gradiente de temperatura aumenta o en otras palabras, disminuye la velocidad de enfriamiento,

resultando en cambios del radio crítico de la concha de carbono y del núcleo de hierro. El crecimiento de nanopartículas se produce en fase gaseosa y una menor conductividad térmica del gas hace aumentar el tiempo de formación.

• Se concluye que al aumentar la relación de argón respecto a helio, el espesor de la envoltura de carbono aumenta de 2,3 nm a 36,6 nm y el diámetro del núcleo de hierro disminuye desde 7,7 nm a 3,4 nm.

El análisis SAED no proporcionó ningun rastro de la presencia de óxido de hierro en los núcleos de las nanopartículas. Por otra parte, tanto el análisis EELS a escala nanométrica como el análisis EDX en la microescala no mostraron ningún rastro de oxígeno en los núcleos de hierro de las nanopartículas. Estos resultados apuntan a una elevada eficiencia de la envoltura de carbono para aislar el núcleo de hierro de una posible oxidación externa.

• Los resultados de la espectroscopia Raman indican que la cristalinidad de la envoltura de carbono aumenta cuando se utiliza argón puro.

• Se han demostrado las dependencias del momento efectivo y de los parámetros de magnetización de saturación de las nanopartículas superparamagnéticas con el tamaño de las nanopartículas.

• Las curvas ZFC y FC demuestran que al utilizar una atmósfera del 100% de argón, las nanopartículas resultantes son superparamagnéticas a baja temperatura (por encima de 220K/-53ºC), por lo tanto son CEINPs adecuadas para aplicaciones específicas que operan a muy baja temperatura, tales como las de la industria aeroespacial.

• La temperatura de bloqueo de las partículas obtenidas sin argón (T_b ~ 50K) es casi el doble que las preparadas en argón puro (T_b ~ 24 K), de acuerdo con la dependencia de T_b con el tamaño del núcleo de hierro, determinado mediante TEM.

• Se sintetizaron nuevas nanopartículas con núcleos múltiples de hierro encapsulados con una envoltura de carbono.

• Curiosamente, a pesar de que las nanopartículas con múltiples núcleos de hierro, más pequeños que el núcleo de hierro en las CEINPs (N75) de un solo núcleo, las nanopartículas multinucleares exhiben una mayor magnetización de saturación. Una de las razones puede ser la presencia de estructuras con un par de núcleos de hierro en una única envoltura de carbono, la cual da lugar a un efecto negativo menor sobre las propiedades magnéticas.

• Debido a la muy corta distancia (alrededor de 2 nm) entre los núcleos de hierro en las nanopartículas multinucleares, CEMINPs, habrá una mayor visibilidad en procesos de formación de imagen en comparación con las CEINPs y por lo tanto las CEMINPs son preferibles como agente de contraste. Por otra parte, es importante mencionar que, debido a la forma esférica de la envoltura de carbono y al comportamiento superparamagnético del núcleo de hierro de los CEINPs, su movimiento en el fluido corporal es suave y controlable y muy adecuado en procesos de administración de fármacos.

• Se llegó a la conclusión de que la naturaleza del gas del reactor de plasma utilizado en el proyecto de investigación tiene un efecto significativo sobre las propiedades morfológicas de las CEINPs. De acuerdo con ello, y conforme a las aplicaciones deseadas, las CEINPs y CEMINPs se pueden sintetizar con este método simplemente ajustando los parámetros tecnológicos correspondientes. Los resultados de esta contribución son un paso adelante en el control de la morfología de la envoltura de carbono y del núcleo de hierro y en la comprensión del mecanismo de crecimiento de las nanopartículas.

• Se han obtenido nanopartículas de hierro encapsuladas en carbono mediante un reactor de descarga de arco en fase gaseosa, ajustando la concentración de precursor (1% w/w) y el flujo de gas (30 sccm) de.

• La caracterización morfológica y estructural reveló una notable monodispersión de los núcleos de hierro así como la presencia en el núcleo de hierro cristalizado en la fase α, la presencia de la fase de carburo de hierro y la ausencia de oxígeno. Estos son factores muy importantes cuando se trata de producciones a gran escala, necesarias para aplicaciones biomédicas.

• Se han obtenido nanopartículas de carbono decoradas con moléculas de tipo fullereno en la superficie (CNDFs) directamente y en un solo paso con el nuevo reactor modificado de descarga de arco en fase gaseosa.

• El suministro en fase gaseosa de compuestos precursores al plasma mejoraron la distribución del tamaño de CNDFs.

• Las observaciones mediante SEM muestraron que las CNDFs presentan forma esférica con 50,4 nm de diámetro, la cual es óptima para la captación endocítica y tienen una morfología adecuada para la administración de fármacos. Además, las CNDFs puede ser internalizadas en la célula más fácilmente que las partículas alargadas debido a su forma esférica.

• Las diferentes estructuras de fullereno, C_{36}, C_{60}, C_{90} y C_{130}, encontradas en la superficie de las CNDFs fueron detectados mediante análisis HRTEM. Los resultados obtenidos indican que la técnica de descarga de arco en fase gaseosa es adecuada para la ingeniería de materiales nanoestructurados tales como las CNDFs para aplicaciones biomédicas.

• La técnica de descarga de arco de fase gaseosa es un método fácil y sintético que permite producir un nuevo material basado en micropartículas esféricas de carbono poroso (PCMPS).

• Las imágenes de SEM muestran las PCMPS con una forma esférica y sin aglomeración.

• Las imágenes de SEM muestran que la distribución del tamaño de las PCMPS es estrecho y con un diámetro medio de 2,1 μm.

• Mientras que, en general, el análisis de BET de partículas muestra una adsorción monocapa, en nuestro caso, utilizando micropartículas porosas, el análisis BET ha evidenciado un mecanismo de adsorción de múltiple capa..

• El análisis BET de las PCMPS ha proporcionado una superficie específica de 153,4 ± 4,2 m^2/g. Las propiedades únicas de las PCMPS muestran su gran potencial como portadoras para la administración de fármacos; y para los dispositivos del tipo lab-on-a-chip..

• Se ha demostrado la posibilidad de usar carbón encapsulado de nanopartículas de hierro para el tratamiento de las miodesopsias.

• Grandes dominios de grafeno multi-mono (1 × 1 cm) se han obtenido sobre sustratos de cobre utilizando CEINPs y mediante deposición química en fase vapor.

• Los resultados de la espectroscopia Raman revelaron que el uso de una elevada concentración de CEINPs mejora la calidad del grafeno y conduce al crecimiento de una monocapa de grafenp sobre el sustrato de cobre.